UC Davis

UC Davis Electronic Theses and Dissertations

Title

Energy Harvesting and Storage Solutions Through Electrochemistry: From Catalysts for Alternative Fuel Production to Absorber Layers for Advanced Solar Cells

Permalink

https://escholarship.org/uc/item/3jq5q1ph

Author

Brayfield, Cassondra Marie

Publication Date

2023

Peer reviewed|Thesis/dissertation

Energy Harvesting and Storage Solutions Through Electrochemistry

By

CASSONDRA MARIE BRAYFIELD
DISSERTATION

Submitted in fulfillment of the requirements for the degree of

DOCTOR OF PHILOSOPHY

in

Material Science and Engineering

in the

COLLEGE OF ENGINEERING

of the

UNIVERSITY OF CALIFORNIA

DAVIS

Approved:

_____

Subhash Risbud, Chair

_____

Seyed Amirhossein

_____

Klaus van Benthem

Committee in Charge

2023

Declaration:

Full names: Cassondra Marie Brayfield

Student Number: 914452320

Qualification: Doctor of Philosophy

I hereby declare that the above-mentioned treatise/dissertation/thesis is my own work and that it has not previously been submitted for assessment to another University or for another qualification.

Cassondra Marie Brayfield

2 August 2023

Energy Harvesting and Storage Solutions

Through Electrochemistry:

From Catalysts for Alternative Fuel Production to Absorber Layers for Advanced Solar Cells

By: Cassondra Brayfield

Contents

1. **Abstract:**

With the global market transitioning from fossil fuels to more carbon neutral methods of energy harvesting and storage such as alternative fuel production and solar cell engineering, this work discusses two methods for improving energy harvesting (via photovoltaic solar energy absorption) and storage (via synthesized catalysts which require relatively low applied voltage to produce fuels including hydrogen gas and liquid formate). The catalysts produced for this study include a novel application of the addition of external ligands and consequently a secondary coordination sphere (SCS) onto an organometallic cluster center to form an electrocatalyst cluster. By incorporating an SCS, preliminary results have shown enhancement of the reaction rate and catalytic activity due to interactions that work to stabilize charged intermediates by improving the efficiency of substrate binding.

Currently, the specific mechanisms responsible for these stabilization effects are not fully understood, but it is most likely related to the increased negative or positive charge character which the clusters take on due to the addition of the SCS ligands. By employing a combination of cyclic voltammetry (CV), constant potential electrolysis (CPE), infrared (IR) spectroscopy, and IR spectroelectrochemistry (SEC), and by using several different cluster compositions with various net charges, we have achieved proper benchmarking of the electrocatalyst system. This type of characterization gives researchers the ability to probe the effects of various SCSs, cluster geometries, and charge environments on the catalytic performance in hydrogen evolution reactions (HERs) and in carbon dioxide reduction reactions (CO_2RRs).

A series of six iron carbonyl clusters modified with net positive, net negative, or un-charged ligand SCSs were synthesized and, to deconvolute the thermodynamic and kinetic effects, electrochemically reacted with various organic acid substrates. It was found that in all cases when a phosphine ligand is added to an iron-based organometallic cluster center ($Fe_4N(CO)_{12}$) there is some increase in the reaction rate and turn-over frequency (TOF) with respect to overpotential (η), but in the case where the addition of a ligands creates a net positive charge on the catalyst, this reaction rate improvement is much more significant. While in HER, hydrogen is the desired product, in a CO_2RR, a common product is formate and further experimentation is proposed to introduce modified E. coli bacteria to an aqueous CPE cell to further investigate if the formate produced can be further processed by the organic media to produce other useful commodity fuels such as isobutanol or pyruvate bioplastics.

For the improvement of energy harvesting techniques with solar cell devices, recent studies explore a variety of layer materials and deposition methods such as the window layer, back mirror layer, back surface field layer, and perhaps the most important and functional layer, the absorber layer. Sb_2Se_3 has been proposed as a promising option as the absorber layer used in photovoltaic devices. While many deposition methods have been explored to achieve a conformal and homogeneous film, very little work has been done on Sb_2Se_3 electrochemical deposition techniques. This work explores a variety of parameters which can be tuned to affect the morphology of the film as well as composition and performance.

The three main parameters explored to deposit Sb_2Se_3 onto fluorine-doped tin oxide (FTO) substrates include temperature of deposition, pre-deposition surface treatments, and pre- and

post-deposition annealing treatments. Many characterization techniques were performed including but not limited to, scanning electron microscopy (SEM), energy-dispersive X-ray spectroscopy (EDS), X-ray diffraction (XRD), surface photovoltage (SPV) measurements, Ultraviolet-visible (UV-Vis) spectroscopy, and photoelectrochemical (PEC) measurements of these micro/nanoparticle films. These results show that not only was the target film composition, Sb_2Se_3, achieved, but also it can be improved by a hydrophilization and $KMnO_4$ surface treatments and by a post-deposition annealing treatment during which the deposited films are annealed at 300°C to 400°C for 3 hours in an argon atmosphere in the presence of pristine selenium powder. As each parameter is separately compared to a control sample, the work explores the precise effect of each parameter on the composition, morphology, band gap, and performance of the Sb_2Se_3 films. Once optimal deposition parameters and treatments were identified, further pre-deposition annealing treatments were performed displaying that one can deposit selenium seeds onto an FTO surface to achieve films with smaller bang baps and even better film thickness, homogeneity, conformality, and overall morphology leading to competitive absorber layers produced via inexpensive electrochemical deposition techniques. A comparison of two different substrate suppliers/FTO characteristics to determine if the deposition or other specifications of the FTO film affect the resulting deposited Sb_2Se_3 film morphology. Further work is proposed to continue to explore seeding composition, temperatures, and procedural order to further optimize film morphology and performance.

2. Overall Introduction:

According to the Environmental Protection Agency's (EPA) current report, in the last year greenhouse gas emissions have increased by 5 percent in the U.S alone with the majority of these emissions due to fossil fuels.[1] The various greenhouse gases which contribute to climate change

include carbon dioxide (CO_2) , methane (CH_4), nitrous oxide (N_2O), and sulfur hexafluoride (SF_6) with CO_2 making up the majority of these emissions. In fact, in 2021, CO_2 emissions from fossil fuel combustion increased by 7% relative to the previous year[1] and in the hundred years between 1900 (280 ppmv) and 2000 (412.5 ppmv) we have seen the amount of CO_2 rise by 132.5 parts per million per volume (ppmv) which corresponds to 2.51 W/m^2 of radiative force on the environment.[2,3] This increase in greenhouse gases has begun noticeable changes to the sea level and global temperature primarily due to the burning of fossil fuels such as diesel and coal. The Intergovernmental Panel on Climate Change (IPCC) reported that between 1901 and 2018, the average global sea level rose by 15–25 cm (6–10 in), or 1–2 mm per year[1a] and the World Meteorological Organization (WMO) confirmed these claims adding that between 2013 and 2022 this rate of sea level rise has increased to an average of 4.62 mm per year.[1b] As environmental conditions worsen due to human activity, scientists and society alike have been searching for greener energy sources.

To have any chance of slowing or reversing this process all facets of science, industry, and the commercial market must make a switch to renewable, carbon neutral sources of energy. There are countless green energy options being explored in hopes of mitigating or even reversing these pollution issues. Two major fields of study are alternative fuels for energy storage and photovoltaic (PV) solar cells for energy harvesting. Each of which can provide at least a portion of the world's usable energy.

One promising alternative fuel is hydrogen, which is already being produced as a green fuel for vehicles and generators. The two main methods for producing hydrogen as a fuel are

methane/steam reforming and electrolysis. Steam reforming uses natural gas and lighter hydrocarbons along with steam in a reactor that converts the methane into carbon dioxide (CO_2) and hydrogen (H_2), while electrolysis uses a metallic anode/cathode pair to split H_2O into its hydrogen and oxygen gas components. The issue with both methods is the cost of the immense energy required to run these processes on a commercial scale and that methane reforming still contributes to emissions by producing CO_2 as a byproduct. Besides hydrogen, another renewable fuel could be produced from CO_2 using an electrochemical cell that can recapture and reform a CO_2 atmosphere into either CO, liquid formate, methanol, or longer chain alcohols for commodity fuel. By engineering an earth-abundant/iron-based catalyst to decrease the amount of energy required to produce these fuels, more cheaper fuel production options can be proliferated to automotive fueling stations and energy storage solutions leading to a cleaner energy sector overall!

Because electricity harvested via solar cells can replace the burning of fossil fuels as a form of energy production, improving the efficiency and cost of these and other carbon-neutral energy-harvesting devices has become very important in the efforts toward a cleaner atmosphere. Numerous different compositions have been explored for the several layers that make up a solar cell stack in hopes of finding an earth abundant, non-toxic, and efficient photovoltaic design. The layer that has the greatest potential for improvement is the absorber layer, which is the one which functionally absorbs the sunlight, and via an n-type (electron-rich) and a p-type (electron poor/hole rich) layer effectively converts the sun's energy into usable, storable electric energy. (The functional mechanism is discussed more in the solar cell introduction section)

While these thin absorber layer films have been produced a number of ways including reactive pulse laser deposition, spin-coating, spray pyrolysis, thermal evaporation, and physical and chemical vapor deposition, many of these are considered non-uniform and/or expensive. One method that may provide a solution to this issue is electrodeposition. This method has minimal waste generation, easy initial set up, is considered low cost, and because one chemical bath could potentially be used for several depositions, this method has amazing potential for industrial scalability.[4]

A material that has recently been a topic of interest among absorber layer researchers is antimony selenide (Sb_2Se_3) also known as antimonselite. Other materials that have been studied for this purpose include CdTe, $Cu(In,Ga)Se_2$ (CIGS), $Cu_2(Zn,Sn)S_4$ (CZTS). The issue with these options is that indium and tellurium are scarce, and Cadmium is toxic to humans.[5] The goal of the PV industry today is to employ light weight, non-toxic, durable, high efficiency, earth abundant, and inexpensive materials, and synthesis processes. This goal can be met by Sb_2Se_3 if the layer deposition process and composition can be tuned and optimized. The answer to this optimization may lie in tuning the pre-deposition and post-deposition surface treatments and annealing steps and the electrochemical deposition potential, temperature, and other deposition parameters. These are examined by this work in the quest for the inexpensive deposition of a competitively efficient Sb_2Se_3 absorber layer.

3. Catalysts for Facile Alternative Fuel Production:

3.1.0 Introduction to Catalysts for Facile Alternative Fuel Production:

Numerous research groups have worked on catalyst compositions and structures to make the carbon dioxide reduction reaction (CO_2RR) and hydrogen evolution reaction (HER) more facile and therefore cheaper, and more selective for a single product containing C-H bonds. Like all catalysts, CO_2RR and HER catalysts lower the activation energy for catalysis.[6] By engineering these catalytic molecules, specifically the secondary coordination sphere (SCS), and by understanding the fundamental proton-coupled electron transfer (PCET) chemistry needed, we can optimize their performance for fuel production. Other researchers have shown that incorporating positive charges into the SCS promotes anodic modulation of that cluster's reduction potential.[7]

It has been demonstrated that the CO_2 binding and reactivity of nanoparticle and heterogeneous catalysts are strongly affected by both delocalized and localized charge effects.[8] Many more publications have discussed this same phenomenon with regard to hydrogen selectivity and evolution.[9,10,11] These previous works report on the outcome of cyclic voltammetry (CV) experiments. During these experiments three electrodes (a working electrode (WE), reference electrode (RE) and a counter electrode (CE)) are employed to produce a plot which shows the anodic and cathodic or redox potentials that occur during the electrochemical reaction. These potentials are presented as V vs. SCE (saturated calomel electrode) which describe the type of reference electrode used during the CV experiment shown in figure 1.
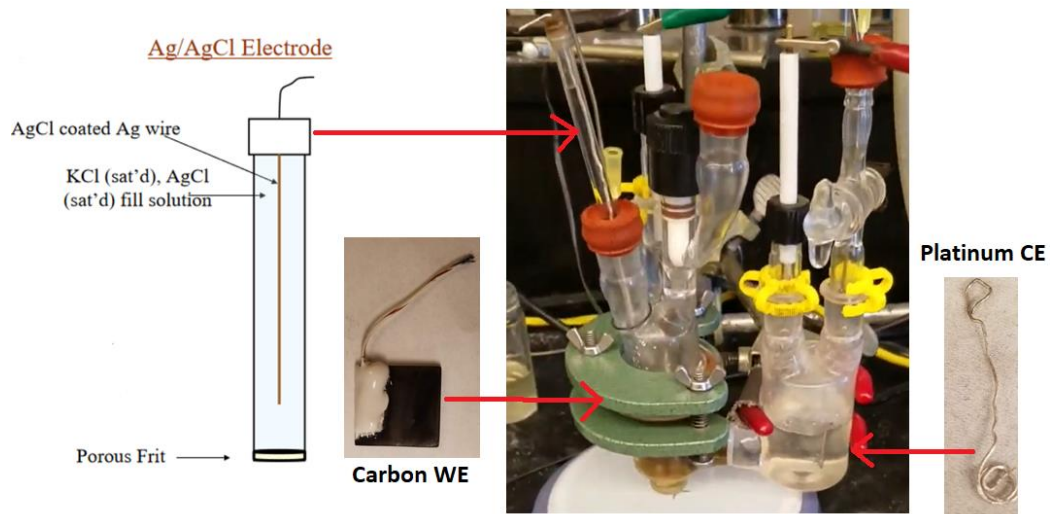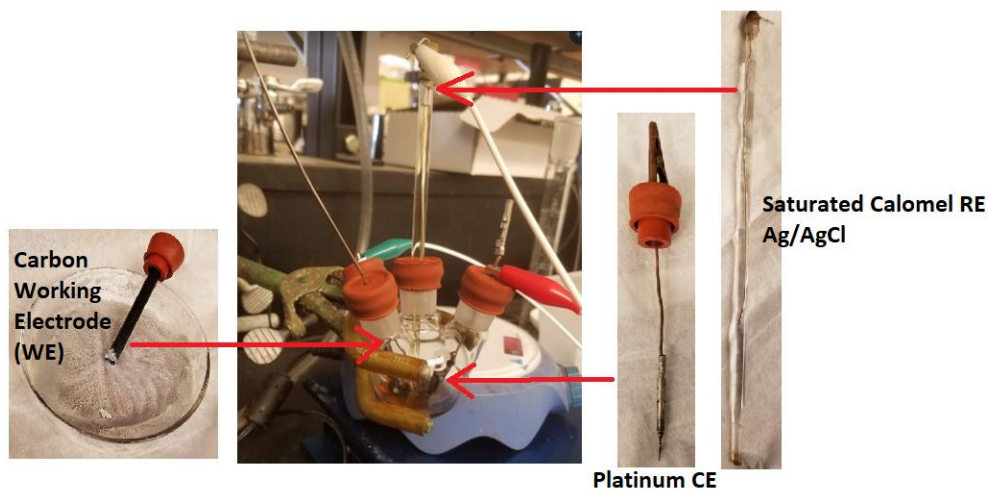
Figure 1: Top - The electrochemical setup for measuring the production of hydrogen in an acetonitrile, organic acid, and nitrogen environment. All electrodes are labeled and shown as a real photo image. as well as the components of the system. Bottom – The electrochemical setup for measuring the production of formate in a water and CO_2 environment. All electrodes are labeled. The reference electrode schematic in the bottom left image shows the RE and its internal components.[12]

When positively charged ions are included on a redox-active molecular scaffold, there is a measurable anodic shift of the $E_{1/2}$ values (defined as the potential that is half-way between the forward wave peak and the peak of the return wave in an electrochemical).[7,28,13] (See Figure 3) This work focuses on $[Fe_4N(CO)_{12}]$ and similar molecules which convert CO_2 to formate at a potential of -1.2 V vs. SCE. In unpublished spectroscopic studies using IR and Moesbauer spectroscopy, studies have shown that the cluster cores of $[Fe_4N(CO)_{10}(PTA)_2]^-$ and $[Fe_4N(CO)_{10}(^{Me}PTA)_2]^+$ are spectroscopically similar regardless of phosphine ligand charge (Figure 2).[12]

PTA[Fe$_4$N(CO)$_{10}$(PTA)$_2$]-   Fe$_4$N(CO)$_{10}$ (MePTA)$_2$]+
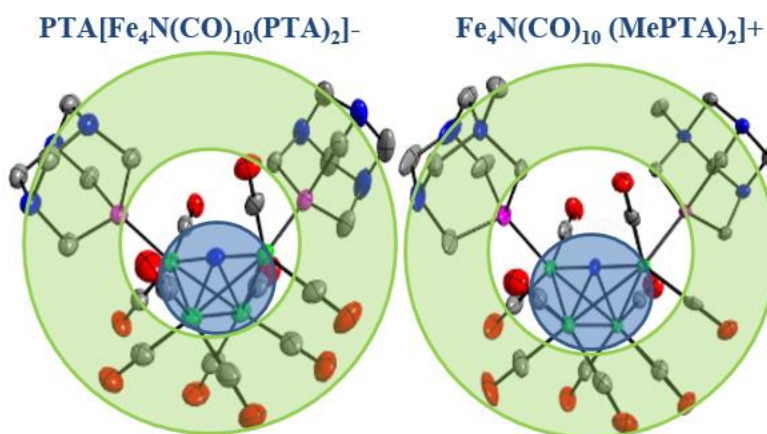
Figure 2: Definition of primary coordination sphere (blue circle) and secondary coordination sphere (SCS) (green circle) shown on two novel molecules, $[Fe_4N(CO)_{10}(PTA)_2]^-$ and

[Fe₄N(CO)₁₀(ᴹᵉPTA)₂]⁺. The primary coordination sphere is defined as the central metal atoms $[Fe_4N(CO)_{10}(^{Me}PTA)_2]^+$. *The primary coordination sphere is defined as the central metal atoms (green iron atoms in this case) and molecules that are attached directly to it, while the SCS consists of attached molecules which are hydrogen bonded to ligands in the primary coordination sphere and portions of a ligand backbone.*
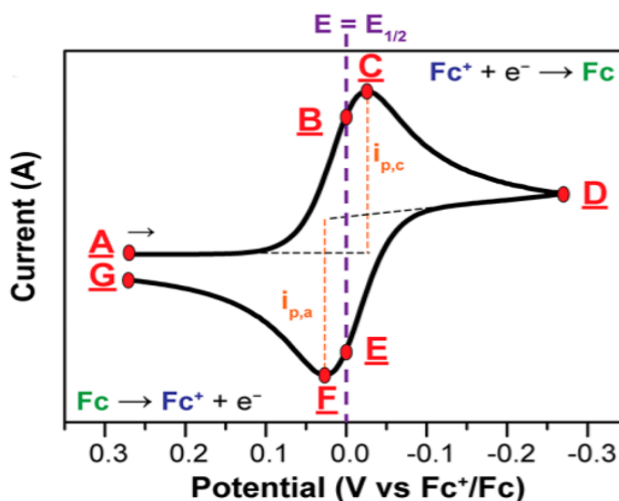
Figure 3: *Plot of common "duck curve" during a routine ferrocene calibration cyclic voltammetry experiment. By applying the range of potentials, we can see the reduction trace on the top moving to the left and the oxidation trace moving to the left. The $E_{1/2}$ is labeled by a purple dotted line. $I_{p,c}$ is the peak current which shows the locations of the two peaks which averaged results in the $E_{1/2}$ value.*

This dissertation describes an approach to CO_2RR and HER which uses earth abundant iron incorporated into carbonyl clusters that promote reduction of protons to form hydride intermediates. pKa or the acid dissociation constant is a commonly used number that describes the strength of an acid. A strong acid will have a pKa of less than zero and the pKa number increases the weaker the acid described. By varying the pKa of the source of protons employed, the hydride intermediates can react with protons to evolve either H_2 or with CO_2 to produce

formate. By synthesizing and testing the $Fe_4N(CO)_{12}$, $[Fe_4N(CO)_{10}(PTA)_2]^-$, $[Fe_4N(CO)_{10}(^{Me}PTA)_2]^+$, and other catalyst clusters, this dissertation works to show how these compositions can catalyze the production of hydrogen gas from an organic acid component and also formate from a carbon dioxide atmosphere.

In future studies, the formate formed also has the potential to be paired with a bioengineered e coli which, in theory, can enact a series of biological pathways giving the system the ability to form pyruvate, bioethanol, or even bio-ethylene (a bio-produced, biodegradable plastic)!

3.2.0 Project Description:

Recent work from Mayer et al has demonstrated that specifically, when the secondary coordination sphere (SCS) is positive, the reaction rates and catalytic activity increase dramatically via an anodic shift in observed $E_{1/2}$ values.[10] Although the precise mechanism responsible for this influence is not fully understood, values that have been measured and studied to elucidate this reaction include the $E_{1/2}$ potential and the cation charge[14], the Lewis acidity of the catalyst[15], and the IR absorption band energies.[16] Many of these past studies focused on the redox-inactive cations present and how they affect the electric field environment of the catalyst. The incorporation of these cations may also have some kinetic effect as seen in the experiments of Yang et al, where the reaction rates of C-H oxidation and N_2 evolution were significantly increased along with the enhancement of the cluster's linear free energy relationships.[11] Yang et al. demonstrated the importance of using many different techniques to probe the electronic structure beyond simply performing electrochemical experiments to achieve and develop a better understanding of the electronic effects of the redox-active metal ion.

Similarly, Hosseinzadeh et al.'s work with heme iron proteins and peroxidases showed that both the secondary sphere of the heme cofactor and the long-range protein structure are adjacent enough to affect the redox potential of the iron. Factors shown to affect the $E_{1/2}$ in this work include the net charge, the amount of hydrogen binding and π-π stacking, the amount of solvent exposure, and the hydrophobicity of the protein.[18] These publications and many like them show us that studying the electrochemical data alone is not enough to deconvolute the effects of these factors.

Fout et al provided an illustration of this relationship by incorporating small charges in the SCS at a far distance from the iron center and was able to tune $E_{1/2}$ for an Fe(II/III) couple over a 400 mV range.[19] Still other works have demonstrated that substituting annilinium (an organic compound C_6H_7N) on to Iron(tetraphenylporphyrinato) (TPP-FE) complexes modulated the $E_{1/2}$ and the rate of both oxygen reduction reactions (ORR) and carbon dioxide reduction reactions (CO_2RR).[19] In each example, it is not understood whether the changes in E½ stem from an electronic inductive effect at the metal center or from an electrostatic effect of the cations in the SCS, and it is further little understood which of these parameters lead to the observed large enhancement in electrocatalytic rates.

Other works (see *History and Theory* section) have shown that the $E_{1/2}$ value is not only affected by SCS effects, but also the charges incorporated at some distance from the redox-active metal center. This dissertation sets out to better understand this mechanism and charge effects. While increased catalytic activity has been observed, it is not fully understood whether the changes in $E_{1/2}$ are due to the electrostatic effect of the cations in the SCS or an electronic inductive effect at the

metal center. It is also not known how to tune these parameters to achieve the largest enhancement of the catalytic rates, but based on these works, it is probable that by installing charged groups onto the redox-active cluster so that the charge is some distance away from the iron core, we can potentially enhance substrate transport and modulate the catalyst thermodynamics and the $E_{1/2}$ value. A better understanding of these effects can lead to targeted catalyst design.

3.3.0 Project Objectives:

Specific Aim 1: Probe the effect of incorporating a positive charge in the secondary coordination sphere (SCS) molecular design of $Fe_4N(CO)_{12}$ and its ability to undergo hydrogen evolution reactions (HER) by electrochemically evaluating six catalysts with a variety of charged SCS groups.

Specific Aim 2: Probe the effect of incorporating a positive charge in the SCS molecular design of $Fe_4N(CO)_{12}$ and its ability to undergo carbon dioxide reduction reactions (CO_2RR) including reactions with formate as a sole product by electrochemically assessing several catalysts with a variety of charged SCS groups.

Specific Aim 3: Via collaboration with the Atsumi group [117,118] use a catalyst that demonstrated reliable performance in CO_2RR to produce formate as a sole product to construct an electrochemical environment containing CO_2, H_2O, organometallic catalyst, and modified E. coli bacteria to achieve facile and/or solar driven production of isobutanol or pyruvate bioplastics.[23]

Charge effects, whether delocalized or localized, have been shown to strongly affect CO_2 binding and reactivity in heterogeneous and nanoparticle catalysts.[21] This dissertation explores the

electronic structures of iron carbonyl clusters containing positively charged SCS functional groups that may accelerate CO_2 transport without enhancing H^+ transport in molecular systems. This work explores the effect that these positively charged groups exert on the electronic and thermodynamic properties of the redox-active catalyst core. In many instances the observed reactivity differences in synthetic molecular systems are attributed to effects of the SCS without regard to the possible thermodynamic changes of the catalyst core. This dissertation hopes to distinguish these two effects.

It is recognized that positively charged ions included within a redox-active molecular scaffold modulate an anodic shift in observed $E\frac{1}{2}$ values. The precise mechanism by which this influence occurs has been the subject of several studies where evidence for correlation of $E\frac{1}{2}$ with Lewis acidity,[22] cation charge, and IR absorption band energies has been presented under a variety of conditions. Electric field effects promoted by redox-inactive cations have also been explored. In addition to those thermodynamic manifestations of cation incorporation, kinetic manifestations have been observed in reactivity outcomes such as changes in linear free energy relationships for N_2 evolution and enhanced reaction rates in C-H oxidation.[23] This collective work illustrates the need to use multiple methods of probing electronic structure, rather than relying exclusively on electrochemistry as a signature of the electronic effects of the redox-active metal ion.

More specific to understanding SCS effects in molecular electrocatalysts, $E\frac{1}{2}$ is also altered by incorporation of charges at a distance from the redox-active metal center and those effects need to be better understood. Charged groups installed at a distance from catalyst active sites can enhance substrate transport, and they also modulate $E\frac{1}{2}$ and the catalyst thermodynamics.

Using a series of substitutions on $[Fe_4N(CO)_{12}]^-$, a series of clusters where SCS charges and cluster redox potential are varied are studied and presented. This combined electrochemical and spectroscopic approach probes both the overall effect of positive charges on reduction potential and the effects of the cations on the cluster core. It is determined that positive charges incorporated into the SCS promote an anodic shift of reduction potentials, and that measured shift in reduction potential can be attributed to an electrostatic effect which adds to the expected inductive effect.

3.4.0 History and Theory – Catalysts for Alternative Fuels:

3.4.1 The Butler Volmer Equation:

The Butler–Volmer equation is a widely used and cited fundamental kinetic relationship in electrochemistry. Also known as the Erdey-Grúz–Volmer equation, this equation describes how the voltage difference between the electrode and the bulk electrolyte effects the electrical current through an electrode for a unimolecular, single electron transfer (ET) occurring on a single electrode. Credit for this equation is attributed to English physical chemist, John Alfred Valentine Butler and German physical chemist, Max Volmer, who via study of the alteration of the fermi level of an electrode when in the presence of very small degrees of oxidation and reduction, were able to present a kinetic theory of the reason for the existence of the equilibrium potential first defined by Walther Nernst. This led to a theory describing the rates of heterogeneous electron transfer processes which is the form we use today. [23,24]

3.4.2 The History - 20s, 30s and Today:

Butler's original two publications, published in 1924, would later be cited as the birthplace of the Butler-Volmer (BV) equation. The papers explored the dissolution and plating of metals and how electron transfer occurs heterogeneously between the metal electrode and the solution phase of a redox couple. In these experiments, Butler assumed that the redox-active species was involved in a competitive adsorption to the electrode and introduced the concept of a "balance point" of particle electron transfer that exists at a higher energy between the oxidized and reduced states of the redox couple. Butler, with these works, described a dynamical or kinetic explanation concerning either metal immersed in solution with like metal ions, or an inert electrode in contact with a redox couple-containing solution.[25,26]

The problem with Butler's original explanation of this behavior is that he was only concerned with the oxidized and reduced states and did not consider the possibility of a polarization-dependent transition state between the two. This is where Volmer adds his namesake to the equation via his work with hydrogen evolution reactions (HER). In their 1930 paper, Erdey-Grúz and Volmer focused on cases of HER where the reduction of protons to hydrogen atoms is the rate determining step (RDS).[27,28] From this work they were able to add to Butler's original explanation and include mechanisms describing the observed polarization and overpotential data in the context of HER. They found that the RDS of proton reduction is dependent on both the anodic and cathodic directions of the reaction and that these rates must be equal if the system is in equilibrium. Since the reduction of protons is a one-electron, unimolecular step they did not have to describe the more complicated multistep-type process and did not explore descriptions for other types of electrochemical reactions.

In 1931 R.W. Gurney added to the conversation his own description of heterogenous electron transfer reactions through the lens of quantum mechanical explanation.[29] In his publication, Gurney concerned himself with irreversible electron transfer (ET) for HER in water by integrating the probability of transition between the two redox states. This led him to coin the term "transfer coefficient" which is defined as the relative scaling between the vibrational strength of the two oxidation states of the redox-active species.[30] Using this term and quantum mechanical first principles, Gurney accounted for the observed empirical Tafel slope and thermal dependance.

When Butler continued his work in 1932, he applied Gurney's explanation to a hydrogen oxidation reaction and worked to describe the adsorption of H(ads) from H_2 and concluded with a kinetic expression that included both the cathodic and anodic processes simultaneously as they are when in equilibrium. Therefore, the BV equations we use today have a sum of two exponential terms: one for each direction of current density in the redox reaction. In this publication, Butler also included the empirical transfer coefficient term introduced by Gurney a year before and was able to linearize his equation with respect to the equilibrium condition to the form of the equation used today.[31]

Today, you can find this version of the BV equation in countless papers, articles, and textbooks to describe the relationship between electrode and current density, however, throughout these formulations, there appears to be a lack of uniformity in the definitions and descriptions of variables and use cases. Over time and through the course of millions of references to these equations worldwide, the meaning of coefficients and variables such as the transfer coefficient,

overpotential, and exchange current density seem to be conflicting, or in some cases, a matter for debate. As the field of electrochemistry expands, the BV equation is now used in the description of both electroanalytical chemistry such as voltammetry, and in electrochemical energy conversion and storage such as in batteries and fuel cells without much uniformity in standards or kinetic theory. It is also evident that the descriptions provided by electrochemical textbooks [32-34] may be misapplied in research literature. Some portion of this confusion is likely due to the translation of the original BV equation to more complicated multistep electrochemical processes including the electrocatalytic reactions of oxygen or hydrogen. In the following sections, I will explore the publications and textbooks alike to give an overview of the commonly used forms of the BV equation, how it is related to the Arrhenius relationship, and how its validity is limited by use cases.

3.4.3 How is the Arrhenius Relationship Involved?

In the vast majority of reactions that occur in a solution phase the rate of the reaction will vary with temperature. The linear relationship between ln(k) and 1/T is by no means a new concept, in fact, it was first published by the Swedish physicist and physical chemist, Svante Arrhenius in 1889.[35] The equation he put forth is now known as the Arrhenius equation and takes the form below.

Equation 1:
$$k = Ae^{-\frac{EA}{RT}}$$

Where k is known as the rate constant, R and T are the universal gas constant and absolute temperature respectively, and E_A is defined as the activation energy in units of joules. The exponential on the right side of this equation describes the probability that applied thermal

energy will overcome the energy barrier of height E_A. The coefficient A describes the frequency of attempts to overcome the energy barrier and is often called the frequency factor.[33] This equation is commonly visualized as an Arrhenius plot illustrated in figure 4. The interpretation of these plots is such that the steeper the slope, the higher the activation energy.[36]
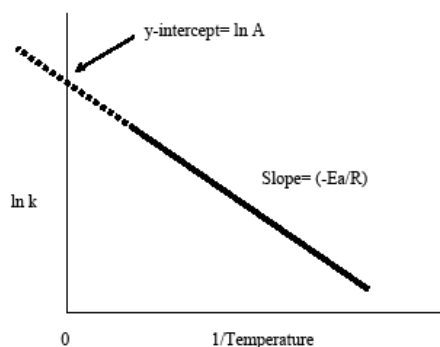
Figure 4: *An example of an Arrhenius plot where the y intercept is equal to the natural log of the frequency factor and the slope is equal to the negative activation energy over the gas constant.*

In electrochemistry, a simple unimolecular process like those discussed in the works of Butler and Volmer, a reaction coordinate plot illustrates the reaction's progress along a defined favorable path, this is the same as the path with the higher energy "balance point" between the redox states that Butler tried to define in his 1924 publication. These reaction coordinates define a surface made up of potential energies as a function of the progress of the reaction. In the simplest version, shown in figure 5, there are only two zones, the products and the reactants which are shown as the minima on the energy surface defined by their stability. Other levels and configurations exist such as chemical intermediates or other molecular states, but due to their instability they must lie at energies higher than the two minima illustrated here.

Figure 5 defines the stable low potential energy of a product, the even lower potential energy of the product, and the high potential energy that must be surmounted to get from one minimum to the other. One can think of the height of the central peak as the quantity of the activation energy to perform the reaction. They are sometimes referred to as E_{Af} for the forward reaction or E_{Ab} for the backward reaction.
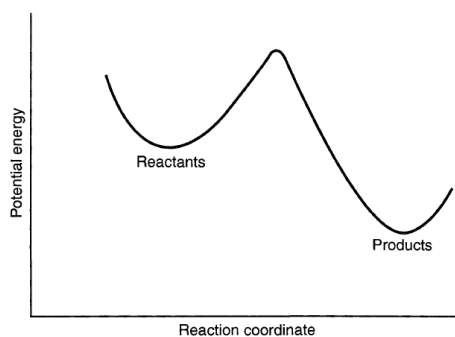
***Figure 5:** Simple representation of a reaction coordinate plot showing potential energy changes during a reaction coordinate reaction.*

Equation 2a:
$$k = A\, e^{\frac{-\Delta H^{\ddagger}}{RT}}$$

Equation 2b:
$$k = A'\, e^{\frac{-\Delta H^{\ddagger} - \Delta T S^{\ddagger}}{RT}}$$

Equation 2c:
$$k = A'\, e^{\frac{-\Delta G^{\ddagger}}{RT}}$$

Expanding the Arrhenius equation, we can define E_A as the standard internal energy in traversing from one of the minima to the peak of the surface also referred to as the transition state denoted by the double dagger symbol. The energy of this state can be defined in terms of the standard

entropy of activation ($\Delta S^{\ddagger}$), the standard enthalpy of activation ($\Delta H^{\ddagger}$), to the standard free energy of activation ($\Delta G^{\ddagger}$) as shown in the three equations above.[33]

Relating these descriptions back to electrochemistry, it stands to reason that the magnitude of the potential on an electrode sill strongly affects the kinetics of reactions occurring on the electrode surface. Erdey-Grúz, Volmer, and Gurney observed that the hydrogen of their reactions evolved rapidly at certain potentials, but not at all outside of that range. Since potentiostats allow for control over the interfacial potential difference as a means of controlling reactivity, it follows that having an equation that can predict the dependance of k_f (forward rate constant) and k_B (backward rate constant) on applied potential would be extremely useful.

The next step to understanding the variables and relationships at play in the BV equation, we will now briefly examine the below reaction which describes a sodium atom dissolved in mercury. If the atom is within the mercury, it has a low energy, but if the atom is moved away from this favorable position, its energy barrier rises.
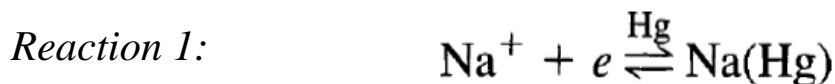
Reaction 1: $$Na^+ + e \underset{}{\overset{Hg}{\rightleftharpoons}} Na(Hg)$$

By applying the same reaction coordinate plot to this reaction, we can see the curves intersect at the transition state in between the two states described on each side of the above reaction equation. Here the height of the barrier to oxidation or reduction determines the reaction rate achieved for those states.

If the rates of oxidation and reduction are equal, the system is in equilibrium (figure 6a) and the potential can be written as $E_{eq.}$ If the potential is changed to a more positive potential, the energy of the reactant electron is lowered and the curve corresponding to the left side of the reaction

equation drops with respect to the right-side term depicted as the reduction barrier appearing raised and the oxidation barrier appearing lowered. This configuration allows the net anodic current to flow. (Figure 6b) Likewise, when the potential is set more negative than E_{eq}, the energy surfaces shift in the opposite direction and the reduction barrier appears lowered while the oxidation barrier appears raised allowing the net cathodic current to flow.
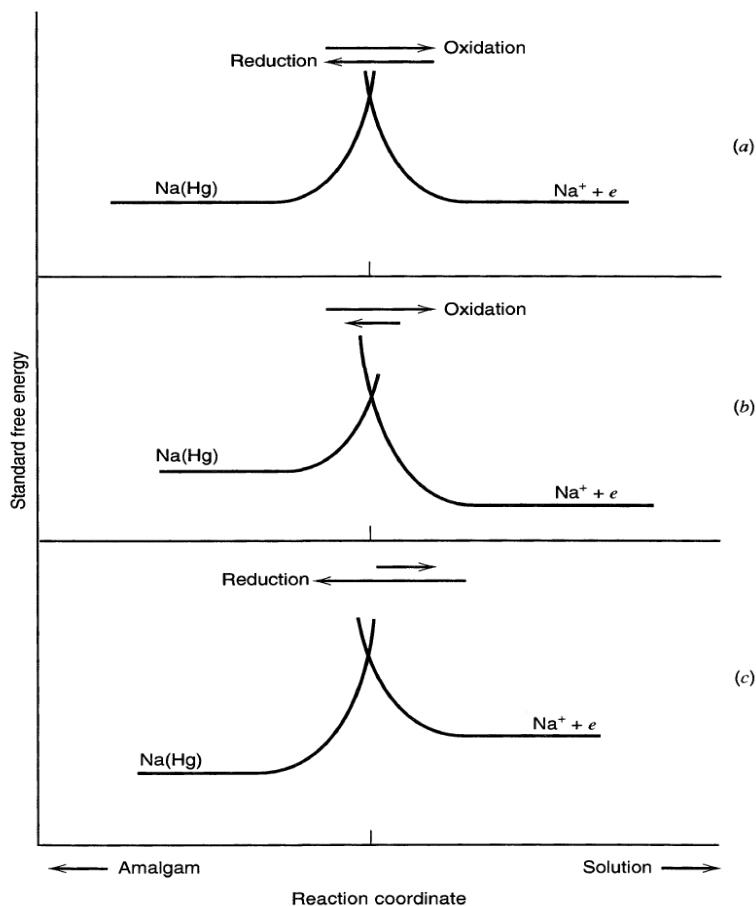

Figure 6: *Simple representation of standard free energy changes during a faradaic process, (a) At a potential corresponding to equilibrium, (b) At a more positive potential than the equilibrium value, (c) At a more negative potential than the equilibrium value.*[33]

In the electrochemical cell used for cyclic voltammetry (CV), the electrode reactions are heterogeneous in nature and the rate of charge transfer occurring at the electrochemical interface depends on several factors beyond just the potential such as adsorption of reactants, intermediates and products, and the structure of the double layer that forms at the electrode surface. A double layer is the two layers of charge that surround a submerged object such as the electrode. The first layer is referred to a surface charge and is made up of ions adsorbed onto the object, the second layer is composed of ions that are attracted to the electrode's surface by the coulomb force and acts as a screen to the first layer.[37]

In the simplest case of one-electron transfer (ET) reaction where species O and R engage in a one-electron transfer at the interface without being involved in any other chemical step (shown below). An expression relating the current to the electrode potential can be developed from absolute rate theory as applied to the electrochemical interface. For reactions at this interface the free energy barrier height is dependent on the potential drop across the interface.

Reaction 2:
$$O + e \underset{k_b}{\overset{k_f}{\rightleftarrows}} R$$

A shift in the electrode potential from 0 to a value E will cause the barrier for the oxidation $\Delta G^{\ddagger}$ to decrease by a fraction of the energy change denoted as α also known as the transfer coefficient (thanks Gurney!). The total energy change is equal to nFE where n is the number of electrons transferred, F is the Faraday constant and E is the applied potential. At the same time, the

potential shift from 0 to *E* will cause the barrier for reduction to increase by (1-α)*nFE. These

shifts are illustrated by figure 7.
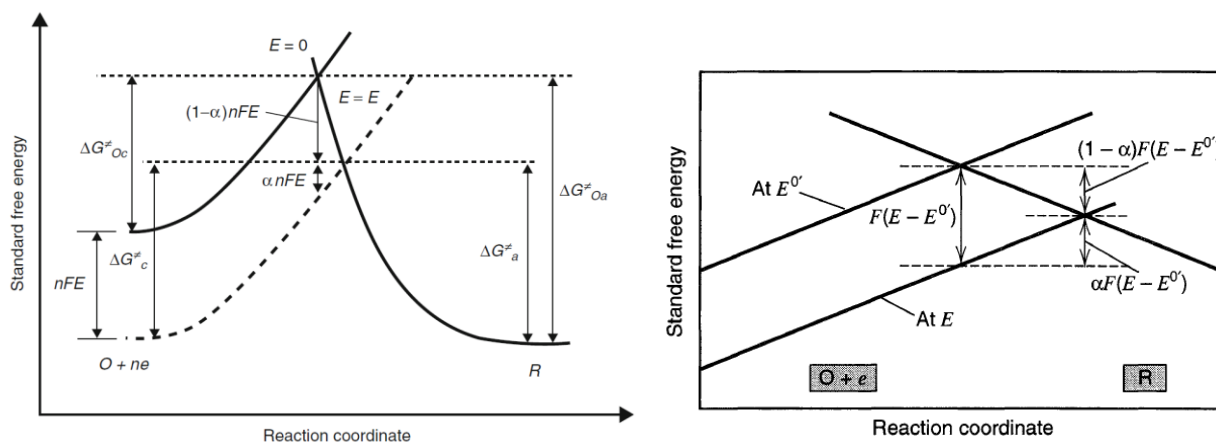
Figure 7: *Effects of a potential change on the standard free energies of activation versus*

coordinate curves for oxidation and reduction. The right image shows a magnified picture of the

boxed area in the left image. E = Ee and E < Ee (broken line parabola)

To put the relationships depicted in figure 7 in the form of an equation, we can note that at

potential *E*, we can now define $\Delta G_{0a}^{\ddagger}$ and $\Delta G_{0c}^{\ddagger}$ as the anodic and cathodic activation energies

respectively and $_\Delta G_{a}^{\ddagger}$, , $\Delta G_{c}^{\ddagger}$, are the barriers for oxidation and reduction respectively, leading to

the following pair of equations[33] :

Equation 3a: $$G_a^{\ddagger} = G_{0a}^{\ddagger} - (1 - \alpha)F(E - E^{0'})$$

Equation 3b: $$G_c^{\ddagger} = G_{0c}^{\ddagger} - \alpha F(E - E^{0'})$$

The *E* and *E₀'* values included above are terms defined originally by the Nernst equation shown

below where *E* denotes the reduction potential, *E₀'* is the standard potential, *R* is the universal

gas constant, T is temperature in kelvin, z represents the ion charge in moles of electrons, F is the

Faraday constant, and Q denotes the reaction quotient.[38]

Equation 4:
$$E = E^0 - \frac{RT}{zF} \ln Q$$

We can now once again assume that the previously defined rate constants k_f and k_b have an

Arrhenius form that can be expressed as:

Equation 5a:
$$k_f = A_f \exp(-\Delta G_c^{\ddagger} / RT)$$

Equation 5b:
$$k_b = A_b \exp(-\Delta G_a^{\ddagger} / RT)$$

Bringing the transfer coefficient into this relationship, we get the following set of equations:

Equation 6a:
$$k_f = A_f \exp(-\Delta G_c^{\ddagger} / RT) \exp[-\alpha f(E - E^{0'})]$$

Equation 6b:
$$k_b = A_b \exp(-\Delta G_{0a}^{\ddagger} / RT) \exp[(1 - \alpha) f(E - E^{0'})]$$

Where $f = F/RT$ and the first two factors in each of these expressions form a product that is

equal to the rate constant at $E = E^{\circ\prime}$ and independent of potential.[33] Which simplify further to:

Equation 7a:
$$k_f = k^0 \exp[-\alpha f (E - E^{0'})]$$

Equation 7b:
$$k_b = k^0 \exp[(1 - \alpha) f (E - E^{0'})]$$

When considering the BV equation used today in describing the electrochemical interface

reaction, we can switch to new rate constant symbols. Instead of forward and backward, we can

now use k_{red} (reduction rate constant) and k_{ox} (oxidation rate constant). Assuming there is an

arbitrary amount of oxidant and reductant in the solution we can achieve the following equation[36]:

Equation 8: $j = j_c + j_a = nFAk_{red}[O]_0 - nFAk_{ox}[R]_0$

Where the total current flowing, j, is the sum of the partial cathodic current (jc), and partial anodic current (ja), currents. A is the electrode area, F is the Faraday constant, n is the number of electrons transferred, and *[O]$_0$* and *[R]$_0$* are the surface concentrations of (O) oxidized reactant and (R) reduced reactant/species, respectively.

Equation 9a: $\frac{i}{i_0} = \exp(\alpha_a f\eta) - \exp(-\alpha_c f\eta)$

Equation 9b: $i = i_{0,ref}(\exp(\alpha_a f\eta)g_a - \exp(-\alpha_c f\eta_{ref})g_c)$

Equation 9c: $i = k_0 F(\exp(\alpha_a f(E - E_f^0))c_R - \exp(-\alpha_c f(E - E_f^0))c_O$

The Derivation of the Various Forms:

As mentioned by an earlier section, the expanding of the field of electrochemistry has led to an increase in creative uses of the original BV equation across numerous different applications. As the BV equation is applied to a vast variety of situations that Butler and Volmer could not have predicted, we can condense all the forms into three main versions: the engineering, the practical, and the electroanalytical BV equations shown below respectively.

In the following section, I will walk through a brief derivation of each of these three accepted forms of the BV equation, but before discussing derivations, it is important to thoroughly define the BV equation. We mentioned before that this equation is meant to describe a redox system at a

single electrode, but the BV equation embodies four phenomenological/strictly empirical statements:

1. Due to an electrochemical process being quasi-reversible, the current density at an individual electrode surface equals the sum of independent anodic and cathodic current densities.

2. The potential and concentration dependencies of each of the cathodic and anodic current density terms are separable.

3. Because the electrode polarization is proportional to the logarithm of current density, the potential dependence of both the cathodic and anodic current densities is known as a Tafel equation and is scaled by an empirical Tafel slope.

4. At zero net current density, the cathodic and anodic processes undergo a condition of dynamic equilibrium such that the polarization of the system is equal to the equilibrium potential due to the Nernst equation.[30]

The definition of a Tafel equation for constant concentrations of all species for cathodic current density is:

Equation 10: $$E - E^* = -A_c log_{10} \frac{-i_c}{i*_c}$$

while the Tafel equation for anodic current density is:

Equation 11 $$:E - E^* = -A_a log_{10} \frac{-i_a}{i*_a}$$

Here, E^* corresponds to an arbitrary reference value of electrode potential (not necessarily the formal reduction potential) which is defined with respect to a reference electrode. $I_c{}^*$ and $I_a{}^*$ are the reference current density magnitudes for cathodic and anodic reactions, respectively. The

coefficients A_a and A_c are always positive values and are known as Tafel slopes in units of volts. The source of these coefficients will be defined in a coming section on Tafel plots, but written in terms of transfer coefficients the Tafel slopes can be written as:

Equation 12:
$$a_m \equiv \frac{1}{f} \frac{\partial \, ln i_m}{\partial E}$$

$$\equiv \frac{1}{f} \frac{\partial \, ln 10}{A_m f}$$

Equation 13:
$$i = i_a + i_c$$

$$= i_a^* \exp\left(\alpha f (E - E^*)\right) g_a - i_c^* f (E - E^*)) g_c$$

To derive the engineering BV equation, we need to define a dependence on concentration for each current density. g_c and g_a will be the concentration dependence function for the cathodic and anodic current densities, respectively. When the concentration is equal to a chosen reference concentration g_c and g_a will be equal to 1, leading to the following empirical assumptions where i is current density.:

We can then consider the special case of equilibrium which describes when the net current density is equal to 0 and all concentrations are equal to the reference concentration which also means that $g_a = g_c = 1$. Also, at equilibrium the electrode potential is equal to a chosen reference potential leading to the following statement:

Equation 14:
$$i_a^* \exp(\alpha_a f (E_{eq,ref} - E^*)) = i_c^* \exp\left(-\alpha_c f (E_{eq,ref} - E^0)\right)$$

28

$$\equiv i_{0,ref}$$

By combining the last two equations, we achieve the following:

Equation 15:

$$i = i_{0,ref} \exp(-\alpha_a f(E_{eq,ref} - E^*)) \exp(\alpha_a f(E - E*))g_a$$

$$- i_{0,ref} \exp(\alpha_c f(E_{eq,ref} - E^*)) \exp(-\alpha_c f(E - E^*))gc$$

$$= i_{0,ref} (\exp(-\alpha_a f(E - E_{eq,ref})) g_a - \exp(-\alpha_c f(E - E_{eq,ref} - E^*))gc$$

This is almost the practical Butler Volmer equation, but polarization needs to be included. This may be one of the main sources for misuse of the BV equation. It may be easy to confuse the polarization term η_{ref} with the overpotential term (η) defined later as part of the engineering BV equation. η_{ref} is the polarization term and is defined as:

Equation 16: $\qquad\qquad\qquad \eta_{ref} \equiv E - E_{eq,ref}$

By including this term in the above description of the equilibrium case, we can derive the practical BV equation below![30]

Equation 17: $\quad i = i_{0,ref}(\exp(\alpha_a f\eta_{ref})g_a - \exp(-\alpha_c f\eta_{ref})g_c)$

Next, we can derive the engineering BV equation. For this form we simply need to set the current density to zero,

Equation 18: $\quad i_{0,ref} \exp(\alpha_a f \eta_{eq,ref}) g_a = i_{0,ref} \exp(-\alpha_c f \eta_{eq,ref}) g_c \equiv i_0$

include an exchange current density term (i_o),

Equation 19: $i = i_0 (\exp(\alpha_c f(\eta_{ref} - \eta_{eq,ref})) - \exp(-\alpha_c f(\eta_{ref} - \eta_{eq,ref})))$

and include an overpotential term.

This is a terrific opportunity to discuss the definition of overpotential. Overpotential (η) is in units of volts and describes the deviation from equilibrium potential due to electrode polarization. It is the difference between the instantaneous electrode-electrolyte potential difference and its equilibrium value as given by the Nernst equation and can be defined mathematically shown below.[30,36]

Equation 20: $\quad\quad \eta_{ref} - \eta_{eq,ref} = E - E_{eq} \equiv \eta$

Once we have overpotential defined and included we can then complete the derivation for the engineering BV equation shown below! This may look a lot like the practical BV equation form earlier, but it includes an important empirical assumption that the exchange current density is independent of the overpotential. This assumption can only be valid if there is no double layer phenomenon present. There is a technique to mitigate this double charge built into most modern potentiostats which involves a short pulse of 1 to 5 seconds of the target potential before the start of a cyclic voltammetry or constant potential electrolysis experiment, but this procedure may not completely guarantee that no double layer will form over the course of the experiment.

Therefore, this engineering BV equation should be avoided for any electroanalytical chemistry such as voltammetry and sensing.

Equation 21: $\qquad i = i_0(\exp(\alpha_a f\eta) - \exp(-\alpha_c f\eta))$

To derive the BV equation used for HER experiments we will need to begin with the equilibrium case once again as stated in the Nernst equation. Where g_{eq} is a general function of concentration dependence which also equals one with the concentration and reference concentration are equal. $f = F/RT$. [30-36]

Equation 22: $\qquad E_{eq} = E_{eq,ref} - \dfrac{1}{f} \ln g_{eq}$

Equation 23: $\qquad \eta_{eq,ref} = \left(E_{eq} - E_{eq,ref}\right) = -\dfrac{1}{f} \ln g_{eq}$

By rearranging the above equations and including the cathodic and anodic g terms we can arrive at the below equations where the α's are the transfer coefficents we are using to to constrain the g values. This relationship comes from the Tafel-like potential dependence that describes the special case of a well-mixed system with a reversible redox reaction where the cathodic and anodic contributions to the current densities are linearly seperable and the concentration at the electoactive surface is variable.

Equation 24: $\qquad E_{eq} = E_{eq,ref} - \dfrac{1}{f} \ln \left(\dfrac{g_a}{g_c}\right)^{\frac{1}{(\alpha_a + \alpha_c)}}$

Equation 25: $\qquad \left(\dfrac{g_a}{g_c}\right) = g_{eq}^{(\alpha_a + \alpha_c)}$

Then, redefining of g_a and g_c using the law of mass action we can achieve the below equations where C_o and C_r represent the concentrations of the oxidant and reductant in the system, respectively.

Equation 26:
$$g_a = \frac{c_R}{c_{R,ref}}$$

Equation 27:
$$g_c = \frac{c_o}{c_{o,ref}}$$

Then, if we include the transfer coefficients from Gurney's quantum mechanical derivation and set them equal to 1, we can achieve the following two equations:

Equation 28:
$$E_{eq} = E_f^0 - \frac{1}{f} \ln \frac{C_R}{C_o}$$

Equation 29:

$$i = i_{0,ref} \left(\exp\left(\alpha_a f \left(E - E_f^0 \right) \right) \frac{C_R}{C_{R,ref}} - \exp\left(-\alpha_c f \left(E - E_f^0 \right) \right) \frac{C_o}{C_{o,ref}} \right)$$

Then, by considering the special case where $C_{R,ref}$ equals $C_{O,ref}$ equals the reference concentration we can define:

Equation 30:

$$i = \frac{i_{0,ref}}{C_{ref}} \left(\exp\left(\alpha_a f \left(E - E_f^0 \right) \right) C_R - \exp\left(-\alpha_c f \left(E - E_f^0 \right) \right) C_o \right)$$

Finally, setting the exchange current density equal to the rate constant k_0 times Faraday's constant times the reference concentration we can simplify the previous equation to the

electroanalytical BV equation shown below! This is remarkably similar to the practical BV

equation that we first derived, but this version makes three important assumptions:

1.) The law of mass action is true.

2.) There exists a defined common reference concentration at which all the redox active

species are present.

3.) The equilibrium potential is a formal potential with respect to the concentration range of

interest. [30-36]

Equation 31:

$$i = k_0 F \left(\exp\left(\alpha_a f\left(E - E_f^0\right) \right) C_R - \exp\left(- \exp\left(\alpha_c f\left(E - E_f^0\right) \right) C_o \right. $$

As stated by the transition state theory of chemical kinetics, the free energies of activation

depend on the applied potential and the rate constants which depend on the free energies of

activation. These are the necessary relationships to derive the BV equation forms which

ultimately describe how the overall current across an electrode depends on the applied potential.

By switching our current term from i to j and putting F, R, and T back into the above equation

we can rewrite it as:

Equation 32: $j = j\{\exp\left(\frac{(1-\alpha)nF\eta}{RT}\right) - \exp\left(\frac{-\alpha nF\eta}{RT}\right)\}$

In the special case of achieving a plateau or S-shaped curve, (fully defined and discussed in a

coming section about the spreadsheet process) the below relation is true. Where j_c is the plateau

current density in units of mA cm^{-2}, *[cat]* is catalyst concentration in mol cm^{-3}, D is the diffusion

coefficient for the catalyst in cm^2 s^{-1}, and k_{obs} in units of s^{-1} is the observed rate that limits the

current at the plateau. [30-36]

Equation 33: $$jc = nF[cat]D^{\frac{1}{2}}x10^3$$

Subbing this plateau case relationship back into our final BV equation we obtain a slightly altered version of the BV equation for electroanalysis in which the dependence of both the anodic and cathodic peak potentials, E_{pa} and E_{pc}, on scan rate are considered accordingly to provide the assessment of the intercept and slope of the line for the calculation of α (the same transfer coefficient) and k_s (the rate constant).

Equation 34:

$$E_{pc} = -\frac{2.303RT}{2\alpha_c F}\log(v) + \left[E^{0'} - \frac{0.78RT}{\alpha_c F} + \frac{2.303RT}{\alpha_c F}\log(k_{s,c}\frac{\sqrt{RT}}{\sqrt{\alpha_c FD_c}})\right]$$

Equation 35:

$$E_{pa} = \frac{2.303RT}{2(1-\alpha_a)F}\log(v) + \left[E^{0'} + \frac{0.78RT}{\alpha_a F} - \frac{2.303RT}{(1-\alpha_a)F}\log(k_{s,a}\frac{\sqrt{RT}}{\sqrt{(1-\alpha_a)FD_a}})\right]$$

where Ep is the peak potential for the anodic (E_{pa}) and cathodic (E_{pc}) traces in V vs. SCE, $E^{0'}$ is the formal redox potential, R is the ideal gas constant (J K^{-1}mol^{-1}), T is temperature (K), F is Faraday's constant (C mol^{-1}), v is scan rate (V s^{-1}), D_c and D_a are the cathodic and anodic diffusion coefficients (cm^2 s^{-1}), and $k_{s,c}$ and $k_{s,a}$ are the heterogeneous rate constants (cm s^{-1}). The symmetry of the energy barrier to ET is described by α_c and α_a as described in an earlier section in the discussion of the energy surface plots. The relationship between $E_{1/2}$ and $E^{0'}$ is derived as ($E_{pc} + E_{pa}$)/2 from E_p's as defined in the above equations. Simplification can be achieved by considering the below equations[30-36]:

Equation 36: $$\alpha_c + \alpha_a = 1$$

Equation 37:
$$k_{s,c} = k_s e^{-\frac{\alpha_c F}{RT}(E-E0')}$$

Equation 38:
$$k_{s,a} = k_s e^{\frac{(1-\alpha_a)F}{RT}(E-E0')}$$

where, k_s is the heterogeneous rate constant (cm s^{-1}) standard rate constant rate constant at zero driving force and E is the applied potential. The above equation simplifies to the below equation at a point between E_{pc} and E_{pa} during the CV scan so that $E = E^{0'}$:

Equation 39:
$$k_{s,a} = k_{s,c} = k_s$$

This affords the final version below:

Equation 40:
$$E_{1/2} = E^{0'} + \frac{0.78RT}{2F}\left(\frac{\alpha_c - \alpha_a}{\alpha_c \alpha_a}\right)$$

With this definition specific to CV, the sum of α_c and α_a is equal to one for a one electron transfer event, and for a Nernstian wave, α_c and α_a are both equal to 0.5 such that the equation above yields $E_{1/2} = E0'$. For non-Nernstian waves with an asymmetric ET, the α's approach 0 and 1 and the measured $E_{1/2}$ gets further from $E^{0'}$. [30-36]

3.4.4 Limiting Conditions:

Throughout the derivations of the various forms of BV equations there are two limiting cases which I will list explicitly here. [33,39]

1.) There is a low overpotential region which is referred to as the polarization resistance region where $E = E_{eq}$ and the below is true:

Equation 41: $$|\eta| \ll \frac{kBT}{ne}$$

We can linearize the BV equation to the following form:

Equation 42: $I = I_0\left(\left(\frac{ne\eta}{k_BT}\right) + \frac{1-2\alpha}{2}\left(\frac{ne\eta}{k_BT}\right)^2 + \frac{(1-2\alpha-2\alpha^2)}{6}\left(\frac{(ne\eta)}{(k_BT))^3}\right) + \cdots\right)$

Where $\alpha = \frac{1}{2}$: Vanish

Under this condition we can make the following assumptions: R_{act} (> 0) is the constant resistance of the Faradaic reaction and the activation overpotential is positive at the anode and negative at the cathode if using a galvanic cell ($I > 0$):

Equation 43: $$I \sim I_0 \frac{ne\eta}{k_BT}$$

$$\eta \sim \frac{I}{R_{act}}, \quad R_{act} = \frac{k_BT}{neI_0}$$

At this limiting condition, the BV equation stated above takes the form:

Equation 44: $$j = j_0\left(\frac{zF}{RT}\right)\left(E - E_{eq}\right)$$

2.) The other limiting condition is a region of high overpotential. In this region the BV equation simplifies to the Tafel equation (discussed in section 2)

When $E \ll E_{eq}$ the equation is dominated by the first term:

Equation 45:
$$E - E_{eq} = \alpha_c - b_c \log j$$

When $(E \gg E_{eq})$ the equation is dominated by the second term:

Equation 46:
$$E - E_{eq} = a + b_a \log j$$

where *a* and *b* are Tafel equation constants (for a given reaction and temperature) The theoretical values of the Tafel equation constants are different for the cathodic and anodic processes. However, according to the Tafel slope as described in section 2, *b* can be defined as:

Equation 47:
$$b = \left(\frac{\partial E}{\partial \ln|I_F|}\right)_{c_i, T, p}$$

Where I_F is the faradaic current, expressed as $I_F = I_A + I_C$ where I_C and I_A are the cathodic and anodic partial currents, respectively.

3.4.5 Limitations and Validation:

As mentioned in section 1 regarding historical BV publications, the forefathers of these methods avoided complicated multistep reactions. In fact, one could group all electrochemical reactions into two main groups:

1.) The outer-sphere, one-electron transfer like that which occurs within the electrical double layer of a solution-phase

2.) The more complex processes where more than one electron may be transferred. These reactions often involve multiple steps, some of which can be chemical.[36]

As electrochemical reactions get more complicated, there are cases where the BV equation can no longer be used as a valid determination/characterization method. The reactions of interest to the scientific community involve organometallic clusters that undergo electrocatalysis in a series of consecutive steps. The slowest of these steps is known as the rate-determining step (RDS) while all other steps can be assumed to be in equilibrium. If the RDS happens to be the exchange of electron, then the reaction is said to be under electrochemical or activation control. This case includes reactions between organic molecules or those involving dissolution or gas evolution. Because the BV equations are written with the type 1 reactions and because it is empirical in nature, experimental verification is important for most modern uses of this equation. This verification can be done via a comparison of the current-voltage behavior with the ideal theoretical situation. Simulations of the ideal BV equation can be produced that solve the mass transport equation of the reaction while using the BV equation as a boundary condition at the electrode surface.[28,30] If one can deem the experimental data a good fit with theory, then the BV equation can be used to confidently determine the kinetic parameters of the system. While simulations have been published[28] and can be utilized for most electrochemical reaction situations, it is easy to misinterpret or overparameterized.

The experimental configuration contributes to our ability to control mass transport and draw conclusions about the electron transfer (ET) kinetics. Practices like choosing a uniform, planar electrode with a known geometry and surface area and striving for increased mass transport by optimizing volume and duration. This is important because if the rate of the reaction greatly exceeds the mass transport rate, then the response is purely thermodynamic, and no information can be gleaned about the heterogeneous kinetics from the current-potential behavior profile.

In a highly cited work by Matsuda and Ayabe[40] and in more recent publications[41,42], systems with a one-electron transfer were studied to find at what conditions does the BV equation loose its validity and must be replaced by a different model such as Nicholson, Shain, or Marcus Hush. Matsuda and Ayabe demonstrated a simple technique involving conventional CV using planar macroelectrodes under relatively quick scan rates under 1 Vs^{-1}. They identified a limit of reversibility using this experimental setup at a rate constant of 0.3 cm $s^{-1.}$ In any of these cases, as this limit is approached, the amount of uncertainty regarding the determined kinetic parameters increases leading to a regime of enhanced certainty in the range of $K_0 = 10^{-2}$ cm/s or slower.[40]

Textbooks[41,42] have presented simulations comparing the CV behavior of single electron transfer reactions and how these shapes depend on the values of the rate constant or transfer coefficients. Figure 5a for example, depicts a simulation of Fick's law comparing a variety of rate constants illustrating that when the rate constant reaches 10^{-2} s^{-1} or greater the curves become too similar to distinguish. This is likely due to these low-rate constant reactions

having sluggish ET, so slow compared to mass transport it leads to a current-sensitive quasi-reversible ET. Figures 7b and 7c show how the sensitivity of the shape of the CV trace depends on the transfer coefficient as a function of the rate constant. As K_0 approaches the "reversibility limit" it is not very affected by a change in α (transfer coefficient).
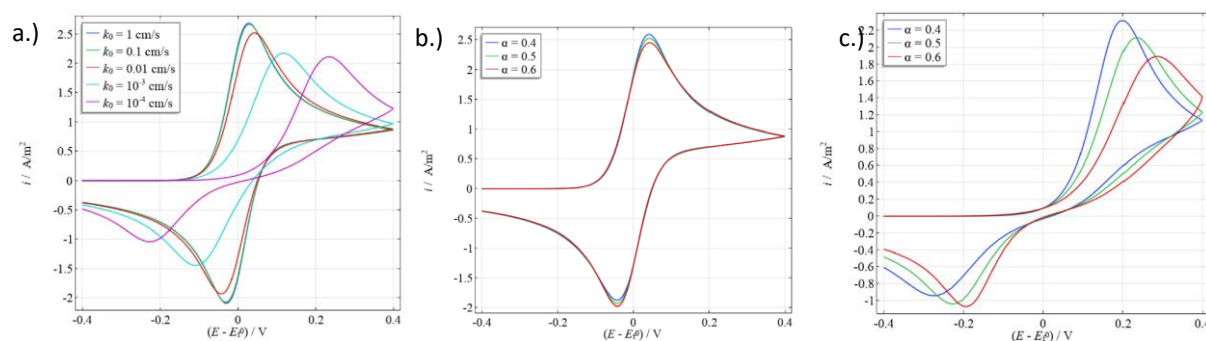

Figure 8: *Simulated Cyclic Voltammetry for a one-electron transfer reaction occurring at a macroelectrode in accordance with the electroanalytical BV equation. Concentration = 1mM, v =0.1 V s^{-1}, D=10^{-9} m^2 s^{-1}, T = 25 °C. a.) α =0.5 (transfer coefficient) for a range of K_0 (rate constants) b.) $K_0 = 10^{-2}$cm s^{-1} for a range of α values. c.) $k_0 =10^{-4}$ cm s^{-1} for a range of α values.*[40-42]

In fact, in figure 8b, as α increases only a slight elevation in the return peak and slight reduction of forward peak is observable. From these simulations, we can observe that the transfer coefficient naturally becomes more significant for reactions with slower kinetics. Figure 8c clearly shows the effect of the transfer coefficient. For $k_0 =10^{-4}$ cm s^{-1}, an increase in α makes the trace more irreversible as defined by the lowering of the peak current and a displacement of the wave further from the formal potential. At higher values of α, we see both the forward and return wave shift anodically with respect to their position at α = 0.5.

3.4.6 Deviating Cases:

Through our exploration of the history, derivation, and forms of the BV equation, it has become clear that it can be applied and validated for a wide range of single-electron transfer electrochemical situations. There are however some cases to which this equation does not apply. When the overpotential is very high for example, the reaction's transfer coefficients can be potential-dependent. Both the BV equation and the Tafel equation lose validity over a range of potentials where the solvent window or mass transport limitations become prohibitive.[30]

In cases utilizing nanoelectrodes, the thickness of the diffusion layer becomes too similar to the thickness of the electrochemical double layer. In this situation, the electron transfer step is affected by the charge on the electroactive species. This phenomenon can be partially described by "Frumkin effects" which is defined as the slowing of the rate of reaction due to the energetic or entropic effects caused by the adsorption of reactants and/or intermediates to the electrode.[43,44] These effects can either attenuate or enhance the applied current and are most notable in dilute/weakly supported electrolyte solutions and when the electrode is a 90 nanometers or smaller.[30] While nano-electrodes pose a problematic mass transport regime with altered mechanisms and rate determining steps compared to their micro-sized counterparts, a modified form of the BV equation can be derived to account for these changes. Also, because nano-electrodes have a larger potential range than micro-electrodes in which the current is limited kinetically by the electron transfer, reactions with higher overpotentials can be more easily performed and observed. Even with these rare exceptions to the BV equation, both the BV equation and the Tafel equation effectively predict the relation between the electrode overpotential and the electron transfer rate with no real limit no matter the distance between the

electrochemical interface and equilibrium which may not be completely consistent with our modern understanding of electron transfer, but through experimental validation, we can confirm if these predictions can be deemed valid for any given reaction.

3.4.7 Tafel Equations and Tafel Plot:

Julius Tafel, born in Switzerland in 1862 focused much of his work on organic redox reactions using the electrodes themselves as electrocatalysts. Though he began by studying these effects on peroxide and hydrazine, by 1896 his work was centered more around strychnine, pyrrolidine and caffeine with various metals serving as electrodes in these experiments.[45] In 1899 Tafel released a paper discussing how different common metals behaved differently with regard to electrolytic reductions and explaining the relationship between overpotential and current which showed a logarithmic dependence.[33,46,47]

Equation 48: $$i = a' e^{\frac{\eta}{b'}}$$

Equation 49: $$\eta = a \mp b \ln I$$

The above equations explain the observed dependence of current on potential under various circumstances. The current is limited either partially or entirely by the rate at which the electro-reactants are transported to the electrode surface. Hence, in cases where low current and efficient stirring mass transport are not rate determining factors, the current is instead controlled by interfacial dynamics.[33] *a* and *b* are defined as characterizing constants and *I* (*i*) refers to the current. The +/- is included to account for either the anodic or cathodic reaction type. Tafel was able to arrange the common metals he observed according to ability to perform catalysis

(disturbing effect) and found the following: Pt > Ag > Sn > Cu > Hg > Zn > Fe. From this and

later work Tafel uncovered that:

1.) Led and liquid mercury can be used as cathodes.

2.) Electrodes should undergo pretreatment before use in electrochemistry experiments.

3.) Platinum's high disturbing effect, reversibility, and inertness is an ideal counter electrode.

4.) Organic reduction and hydrogen evolution reactions (HER) are in competition for

   cathode potential.[48]

While Tafel was not the first to notice the logarithmic bond between overpotential and current,

he was the first to systematically test this and identify overpotential as the critical unit for

measurement to the harsh criticism of his colleagues and mentors.[45] By 1909 Tafel was a prolific

author publishing 40 papers on either electrochemistry or other organic chemistry topics. In 1910

he retired due to poor health, but still managed to publish over sixty review articles before taking

his own life in 1918. Though Tafel did not convert his equations to an overarching rate theory,

Tafel's legacy continues with Butler and Volmer completing this step in 1930.[45]

Derivation of the Tafel Equation and Plot

   As mentioned above Julius Tafel was interested in the logarithmic dependence of

   overpotential and current. Starting from the anodic/cathodic equations for current mentioned

   in the BV section redefined below[36]:

Equation 50: $$j = j_a = j_0 exp[\frac{(1-\alpha)nF\eta}{RT}]$$

Equation 51:
$$j = j_c = j_0 exp[\frac{\alpha nF\eta}{RT}]$$

One can define the Tafel slope logarithmic dependence of on j given by as shown below[36]:

Equation 52:
$$\eta = 2.303 \frac{RT}{(1-\alpha)nF} log j_0 + 2.303 \ X \ \frac{RT}{(1-\alpha)nF} log j_a$$

Equation 53:
$$\eta = 2.303 \frac{RT}{\alpha nF} log j_0 - 2.303 \frac{RT}{\alpha nF} log j_c$$

These equations can be simplified to this common equation where a and b are constants and j is current[36]:

Equation 54:
$$\eta = a + b \ log j$$

When this equation is converted to a graphical form, the *a* and *b* constants are depicted as the intercept and slope respectively as illustrated in figure 9 below[36]:
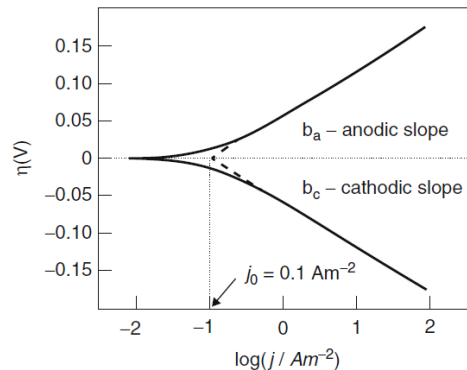

Figure 9: *Tafel Plot showing location of the exchange current density.*

When interpreting a Tafel plot like this, one can calculate the exchange current density (j_0) from the intercepts and extrapolation of the potential to the equilibrium potential as shown. The slope (b) is referred to as the Tafel slope which is positive for anodic reactions and negative for cathodic reactions. This slope can be used to calculate the symmetry factors for the prediction of the reaction mechanism of both simple and complex reactions.[33,36]

For most cases, this linear dependence occurs at overpotentials of 50–100 mV and the Tafel slope b value also indicates the quantity of electrons exchanged in the reaction. For example, when there is only one electron exchanged the charge transfer coefficient will be 0.5 and the theoretical Tafel slope at room temperature is +/-118 mV per decade. In this way, we can use Tafel plots to understand the mechanism of a reaction and indicate the identity of a rate-determining step of the overall reaction. [36]

Further interpretation of the log(i) vs. η Tafel plot involves understanding that there is an anodic branch with a slope equal to $(1-\alpha)F/(2.3RT)$ while the slope of the cathodic branch is $(-\alpha F)/(2.3RT)$ where α is again the transfer coefficient. Figure 9 below shows extrapolation to the intercept point of log(i_0). As the overpotential approaches 0 we see the plots deviate dramatically. This deviation is due to the prominence of back reactions that can no longer be considered negligible. The back reaction is defined as the anodic process when a net reduction is considered or as the cathodic process when a new oxidation is observed. From a plot such as the one shown in figure 9 both the transfer coefficient and the exchange current are easily accessible.
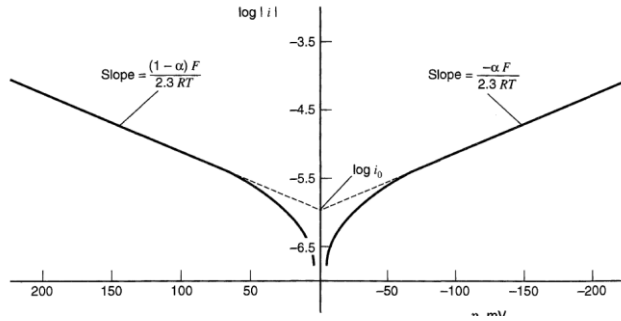
Figure 10: *Tafel Plot showing anodic and cathodic branches of the current-overpotential slopes and determination of the transfer coefficient and the exchange current density for the case of:*

Reaction 3: $O + e \leftrightarrow R$ *where a = 0.5, T = 298 K, and $j_0 = 10^{-6}$ A/cm^2.*[33]

Special Case of the Tafel Equation/Plot (Large Overpotential):

If the overpotential of the reaction is large in either the negative or positive direction, then some of the terms inside the bracket below become negligible.

At large negative overpotentials for example, $\exp(-\alpha/\eta) >> \exp[(1-\alpha)/\eta]$ and the above equation becomes:

Equation 55: $$i = i_0[e^{\alpha f\eta} - e^{(1-\alpha)f\eta}$$

Equation 56: $$i = i_0 e^{-\alpha f\eta}$$

Equation 57: $$\eta = \frac{RT}{\alpha F}\ln i_0 - \frac{RT}{\alpha T}\ln i$$

In this case, the classic Tafel equation no longer fits the behavior, but only regarding the intercept constant (*a*) which now becomes[49]:

Equation 58:
$$a = \frac{2.3RT}{\alpha F} \log i_0$$

While the slope, *b,* remains as it was defined earlier. Other than this alteration, we can assume

that the Tafel equation holds as long as the "back reaction" contributes less than 1% of the

current as defined below:

Equation 59:
$$\frac{e^{(1-\alpha)f\eta}}{e^{-\alpha f\eta}} = e^{f\eta} \leq 0.01$$

This implies that $|\eta| > 118$ mV at 25°C. The reason Tafel relationships cannot be observed for

such cases is because when the electrode kinetics are reasonably facile, the system will approach

a mass-transfer-limited current by the time such an extreme overpotential is established and the

Tafel relationship requires the absence of mass-transfer effects on the current. If, on the other

hand, the electrode kinetics are sluggish with significant activation overpotentials, good Tafel

relationships can be observed. This supports the fact that Tafel behavior is an indicator of totally

irreversible kinetics where no significant current flow occurs except at high overpotentials,

where the faradaic process is effectively unidirectional and, therefore, chemically irreversible.[33]

Limiting Cases:

Now that we have explored the origins of Tafel's equation and plot we can revisit the limiting

case discussed in the last section in reference to the BV equation. It is important to note that

these equations are limited to the region of high overpotential. In this region the BV equation

simplifies to the Tafel equation[33,39]:

When $E \ll E_{eq}$ the equation is dominated by the first term:

Equation 60: $$E - E_{eq} = a_c - b_c \, logj$$

When $(E \gg E_{eq})$ the equation is dominated by the second term:

Equation 61: $$E - E_{eq} = a + b_a \, logj$$

where *a* and *b* are Tafel equation constants (for a given reaction and temperature) The theoretical values of the Tafel equation constants are different for the cathodic and anodic processes. However, according to the Tafel slope as described in section 2, *b* can be defined as:

Equation 62: $$b = \left(\frac{\partial E}{\partial \ln |I_F|} \right)_{c_i, T, p}$$

Where I_F is the faradaic current, expressed as $I_F = I_A + I_C$ where I_C and I_A are the cathodic and anodic partial currents, respectively. [33,39]

3.4.8 Turn-over Frequency and the Modern Tafel - Style Plot:

In CV experiments and electrochemistry in general, the catalytic current usually results from the culmination of chemical reactions, steady-state linear diffusive transport, and electrode electron transfers as depicted in figure 11 below.
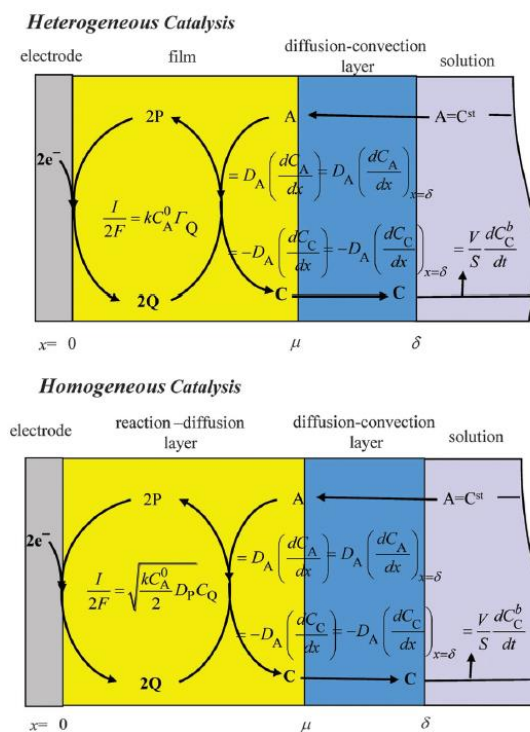
Figure 11: *Illustration of an electrochemical reaction showing the three mechanisms at play:*

Electrode electron transfer, chemical reactions, and steady-state linear diffusive transport in

both heterogeneous and homogeneous molecular catalysis of an electrochemical reaction. X to μ

represents the distance to the electrode surface, μ to δ is the film or reaction layer thickness, and

δ on is the diffusion layer thickness. $D_{subscript}$ represents the diffusion coefficients. $G_{subscript}$

represents the surface concentrations. $C_{subscript}$ is the volume concentrations. G^0_P and C^0_P are the

total surface and volume concentrations of the catalyst, respectively. S is the electrode surface

area, V represents the cell compartment volume, I is the current density, and k is the catalytic

second order rate constant.[50,51]

Based on these electron transfer interactions for both homogeneous and heterogeneous cases,

these reactions can be described by the following equation.[51,52]

Equation 63:
$$\frac{dC_C^b}{dt} = -\frac{SD_A}{V}\left(\frac{dC_c}{dx}\right)_{x=\delta} = \frac{IS}{2FV}$$

If the catalytic reaction is fast, then it can be described by either equation 64 or 65 below

Equation 64:
$$\frac{I}{2F} = kC_A^0\Gamma_Q$$

Equation 65:
$$\frac{I}{F} = \sqrt{(2kC_A^0 D_P)}\left(C_Q\right)_{x=0} i$$

for heterogenous and homogeneous cases, respectively.

By the classical definition turnover number (TON) is defined as "the ratio between the number of molecules transformed by the catalytic reaction and the number of catalyst molecules employed to achieve this transformation. This definition is depicted as the following equation and is rediscussed in different terms in a coming section.[51]

Equation 66:
$$TON = \frac{molC}{mol(P+Q)} = \frac{C_C^b * V}{\Gamma_P^0 * S} = kC_A^0\frac{\Gamma_Q}{\Gamma_P^0} * t$$

Which can be rewritten as turnover frequency (TOF) as shown in the equation below. TOF has units of hertz and can be defined as the number of electron transfers per second. Where Γ represents the surface concentrations, C is the bulk concentration, and k is a rate constant

Equation 67:
$$TOF = kC_A^0\frac{\Gamma_Q}{\Gamma_P^0}$$

50

When the reaction is both homogeneous and rapid, we can assume ''pure kinetic and steady-state conditions" close to the electrode surface resulting in the mutual compensation of catalytic reaction and catalyst diffusion[51]:

Equation 68:
$$Dp\frac{d^2C_Q}{dx^2} - 2kC_A^0C_Q = 0,$$

$$with\ (C_Q)_{x=\infty} = 0,\ \left(\frac{dC_Q}{dx}\right)_{x=\infty} = 0$$

This occurs within the reaction–diffusion layer shown in figure 11 where the Q-profile obtained by space integration of the above differential equation leads to the following boundary condition[51]:

Equation 69:
$$C_Q(x) = (C_Q)_{x=0}\exp\left(-\sqrt{\frac{2kC_A^0}{D_P}}x\right)$$

This boundary condition corresponds to the film thickness as defined by

Equation 70:
$$\mu = \sqrt{\frac{D_P}{2kC_A^0}}$$

If we then keep the above definition of TON as in the heterogeneous case, we can define the total amount of the catalyst per surface area in the reaction layer as shown below[51]:

Equation 71a:
$$\frac{1}{TOF} = \frac{\exp(-f\eta)}{TOF_0} + \frac{2\sqrt{kC_A^0}}{k_s^{het,cat}} \frac{\exp(-\frac{f\eta}{2})}{\sqrt{TOF_0}}$$

Equation 71b:
$$mol(P+Q)_\mu = S\sqrt{\frac{D_P}{2kC_A^0}}C_P^0$$

This leads to slightly altered definition for TON and TOF as defined below:

Equation 72:
$$TON = \frac{molC}{mol(P+Q)_\mu} = kC_A^0 \frac{(C_Q)_{x=0}}{C_P^0} * t$$

Equation 73:
$$TOF = kC_A^0 \frac{(C_Q)_{x=0}}{C_P^0}$$

From this equation, we can then ignore any molecules not present in the reaction and only count catalyst molecules that are present in the reaction layer. While any catalysts present outside the reaction layer zone may still participate as stock to avoid catalyst deactivation, but for the fast reactions that obey Nernst law we can only include the molecules involved which leads to the following definition for both the heterogeneous and homogeneous cases:

Equation 74:
$$TOF = \frac{kC_A^0}{1+\exp[f(E-E_{cat}^0)]}$$

Where f = F/RT and E^0_{cat} is the catalyst standard potential, i.e., the standard potential of the P/Q couple. This can be expanded to the heterogeneous case[51]:

Equation 75:
$$\frac{1}{TOF} = \frac{\exp{(-f\eta)}}{TOF_0} + \frac{2\sqrt{kC_A^0}}{k_S^{het,cat}} \frac{\exp{(-\frac{f\eta}{2})}}{\sqrt{TOF_0}} + \frac{\exp{[-f(E_{AC}^0 - E_{cat}^0)]}}{TOF_0}$$

and for the homogeneous case:

Equation 76:
$$\frac{1}{TOF} = \frac{\exp{(-f\eta)}}{TOF_0} + \frac{\sqrt{2D_P}}{k_S^{cat}} \frac{\exp{(-\frac{f\eta}{2})}}{\sqrt{TOF_0}} + \frac{\exp{[-f(E_{AC}^0 - E_{cat}^0)]}}{TOF_0}$$

With the following true for both cases[51]:

Equation 77:
$$TOF_0 = kC_A^0 \exp{[-f(E_{AC}^0 - E_{cat}^0)]}$$

It is evident from these definitions that there is a clear relationship between the TOF and the overpotential for each catalyst. We can use this relationship to achieve precise comparison between various catalysts. This conflicts with the old assumption that catalysts are characterized only by these two parameters independently without interaction. In the updated version of the Tafel-style plot which shows log(TOF) vs. overpotential we can define a region of best catalysis performance in the upper left-hand corner of the plot as shown in figure 12 below.

$$\frac{1}{TOF} = \frac{\exp(-f\eta)}{TOF_0} + \begin{cases} heterogeneous: \\ 2\sqrt{kC_A^0}/k_S^{het,cat} \\ homogeneous: \\ \sqrt{2D_P}/k_S^{cat} \end{cases} \frac{\exp\left(-\dfrac{f\eta}{2}\right)}{\sqrt{TOF_0}} + \frac{\exp\left[-f\left(E_{AC}^0 - E_{cat}^0\right)\right]}{TOF_0}$$
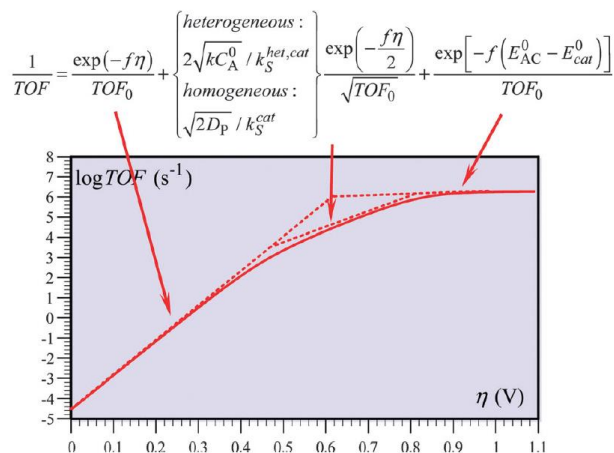

Figure 12: A single trace on a Tafel-style plot showing the turnover frequency vs. overpotential relationship and the link between the terms of the mathematical definition and the regions of the plot.

Figure 12 above shows three distinct zones: one with independence from η at large values of η, one with linear variation with an F/[RTln(10)] slope at small values of η, and the middle region, with a F/[2RTln(10)] slope linear variation that corresponds to the kinetic contribution of electron transfer to the catalyst. The middle segment will decrease in size as electron transfer speed increases until ultimately disappearing. Plots like these can help us visualize the characterization of the catalytic properties of organometallic molecules specifically by using the TOF_0 (the turnover frequency at an overpotential of zero). This Tafel-style plot differs from the classical Tafel plot as this modern version considers TOF which allows for the determination of the three distinct regions while the classic version is a linear approximation of the kinetically controlled relationship between the current, or current density, and the overpotential of an electrochemical reaction during electron transfer using the transfer coefficients described in an above section.[33,51]

More recent applications of these TOF-η plots, including the research presented in this dissertation, use slightly altered versions of the above equations shown below where i_{el} is the current during electrolysis, TOF_{max} is the maximum turnover frequency obtained from CVs, F is Faraday's constant ($F = 96500$ C mol^{-1}), A is the surface area of the glassy carbon working electrode ($A = \sim 1.77$ cm^2), D is the diffusion coefficient, $[C_0]$ is the concentration of the catalyst, E_{appl} is the applied potential during electrolysis, $E_{1/2}$ is the half-wave potential for the catalytic wave, $E^0 CO_2/HCO_2H$ is the standard reduction potential of the $CO_2/HCOOH$ couple in the chosen solvent and t is the electrolysis time.[53,54]

Equation 78: $$i_{cat} = n_{cat} FA[C_0]\sqrt{Dk_{CO_2}[CO_2]}$$

Equation 79: $$\frac{i_{cat}}{i_P} = 4.484\sqrt{\frac{RT}{F}} * \sqrt{TOF_{max}} * v^{-1/2} *$$

Equation 80:

$$E_S^0(CO_2/HCOOH, A\,H) = E_{aq}^0(CO_2/HCOOH) - \frac{RT}{2F}\left(\frac{K_{h,CO_2,aq\to g}}{K_{h,CO_2,s\to g}}\right) -$$

$$\frac{\left(2\Delta G_{t,H^+,S\to aq}^0 - \Delta G_{t,HCOOH,S\to aq}^0\right)}{2F}$$

Equation 81: $$TOF = \frac{TOF_{max}}{1+\exp\left[\left(\frac{F}{RT}\right)(E_{CO_2/HCO_2H}^0 - E_{\frac{1}{2}} - \eta)\right]}$$

3.4.9 Faradaic Efficiency:

Michael Faraday has a prolific legacy spanning countless fields including the discovery of diamagnetism, electromagnetic induction, and electrolysis. In addition to discovering new compounds of chlorine and carbon, he also succeeded in producing novel glass and alloy compositions, liquefying several gasses, and inventing the version of the Bunsen burner that we still use today![55,58] More relevant to electrochemistry is his work in the 1830s developing the laws of electrolysis and widely used terminology such as ion, electrodes, anodes, and cathodes.[59-63] Two main laws resulted from this work:

1.) The mass of the elements deposited at an electrode is directly proportional to the amount of charge present. See equation below; where m is mass, Q is the charge, and Z is the constant of proportionality also known as the electro-chemical equivalent.

Equation 82:
$$\frac{m}{Q} = Z$$

2.) When the same amount of electric current is passed through different electrolytes/elements connected in series, the mass of the substance liberated/deposited at the electrodes is directly proportional to their chemical equivalent/equivalent weight (E) which is equal to the molar mass (M) divided by the valence (v) as shown below.

Equation 83:
$$E = \frac{Molar\ mass}{Valence}$$

3.4.10 Definition and Derivation:

Along with his laws of electrolysis, another useful calculation that came out of Faraday's work is that of faradaic efficiency which describes how efficiently the electrons or charge is transferred in an electrochemical system. The faraday is a unit for charge equal to 1 coulomb per volt and Faraday's constant (F) is equal to 96,485 coulombs per mol and correlates charge with moles of matter and electrons. The equation for Faradaic Efficiency (FE) is shown below where n is number of moles of electrons transferred during the reaction, Q is the amount of charge in coulombs passed and F is the faraday's constant[53]:

Equation 84: $$FE = n/\left(\frac{Q}{2F}\right)$$

 When understanding the derivation of the equation for faradaic efficiency, it helps to start with Gibbs free energy (ΔG) which is equal to the total change in enthalpy of the process (ΔH) minus temperature (T) times the total change in entropy (ΔS) of the process:

Equation 85: $$\Delta G^0 = \Delta H^0 - T * \Delta S^0$$

In the case of water electrolysis, a common situation observed by Faraday, the change in enthalpy is equal to 285.8 kJ/mole and the heat that must be added is equal to the change in the standard entropy is 48.7 kJ/mole which is multiplied by the standard temperature (T = 298 K) a table of the entropy, enthalpy and free energy values involved in the water-splitting reaction at standard temperature and pressure is shown below[64]:

Table 1: **Entropy, enthalpy and free energy values involved in the water-splitting reaction at standard temperature and pressure**

	kJ/mole	Volts
Standard Gibbs free energy, ΔG^0	237	1.23
Standard enthalpy, ΔH^0	286	1.48
Standard entropy term, $T \times \Delta S^0$	48.7	0.25

To calculate the standard voltages that correspond to the change in the Gibbs free energy for this reaction, one can use the following equation:

Equation 86: $$\Delta G^0 = -n * F * E^0$$

where n is the number of electrons called for in the half reactions per mole of water (or other substrate solution) split ($n = 2$ for H_2O), F is Faraday's constant ($F = 96{,}500$ coulombs mole^{-1}) and E_0 is the standard potential in volts. In the water example at standard conditions, the voltage is negative while the Gibb's free energy is positive which means that the reaction is not spontaneous.[64]

To perform the splitting of an H_2O molecule into its gaseous components it requires a minimum of 1.23 V as shown in the table above. When this reaction occurs in a closed system such as an electrolyzer the water/substrate would theoretically cool due to the change in entropy. In a real situation, heat is supplied by the surrounding environment which keeps the solution from cooling. This means that in an electrolyzer, there will be heat flowing into the system promoting the reaction, but in the fuel cell version of the system, the recombination of gaseous elements (or

other fuels) produces heat which flows into the surroundings. Therefore, the efficiency of a simple electrolyzer can be described by the below version of the FE equation[64]

Equation 87:

$$Electrolyzer\ Efficiency = (100\%\ x\ Operating\ Voltage)\ /\ G^0$$

As the electrolyzer becomes more complex, such as in the case of electrochemical reduction of CO_2 to CO, one can use a theoretical charge value and the amount of product detected via gas chromatography (GC) or NMR (nuclear magnetic resonance) spectroscopy. For gaseous products such as hydrogen, one can calculate the FE of their production by converting the area of the detection peak by subtracting by the y-intercept and dividing by the slope of a known calibration curve generated by making known volumes of hydrogen injections. This calibration curve is then compared to the amount of solution, substrate, and catalysts present to determine the value of z (the number of electrons transferred for H_2 production) and n (the of moles of H_2 created as determined by the GC analysis) in the equations below where Q is the charge passed during the bulk electrolysis and F is the Faraday constant.[53,65]

Equation 88:

$$Faradaic\ Efficiency(\%) = \frac{Q_{Experimental}}{Q_{Theoretical}} * 100 = \frac{z * n * F}{Q} * 100$$

Similarly, the amount of liquid fuel produced via an electrolyzer and therefore the efficiency with which it is produced is by integrating the peak area of product in the NMR spectrograph as compared to a known standard. This peak area is multiplied by the calibration slope like that

used with GC analysis and the concentration of product produced is determined and converted to moles easily using the molar mass of the product and amount of solution used in the reaction. The number of electrons in each successful production of a product molecule by dividing the total charge passed by the Faraday constant. When we divide the number of moles of product by the number of moles of electrons transferred and multiply that by 100%, we can achieve the percent Faradaic efficiency of fuel production. This is a rearrangement of the above equations.

Equation 89:

$$\frac{\left(\frac{\left(\frac{Q}{F}\right)}{n}\right)}{z} \times 100\% \quad \Longrightarrow \quad \frac{Q}{(z*n*F)} \times \frac{1}{100\%} \quad \Longrightarrow \quad \left[\frac{(z*n*F)}{Q}\right] \times 100\%$$

3.4.11 Limitation when Faradaic Loss Occurs:

Whether the electrolyzer is an electrolytic or galvanic cell they are still subject to faradaic losses when the electrons in the system participate in undesired side reactions. These losses can be characterized by the production of heat or chemical byproducts. In Faraday's water splitting experiment described above, some electrons are diverted into the production of hydrogen peroxide instead of gaseous O_2 and H_2. Those diverted electrons (the amount of which will vary depending on the electrochemical cell setup) cannot be counted in the Faradaic efficiency and must be considered faradaic loss. Similarly, the O_2 and H_2 can recombine before leaving the bulk solution which will affect the resulting Faradaic efficiency. In cases where a proton exchange membrane is employed, some electrons derived at the anode may cross the membrane and reach

the cathode without participating in the working-side reaction. This is comparable to the self-discharge issue that occurs in lithium-ion batteries decreasing battery life.[65,66]

Faradaic loss can be calculated by subtracting the total product detected analytically from the theoretical yield predicted. This type of faradaic loss only makes up a portion of energy losses that occur in these electrochemical systems. Overpotential is also considered a form of energetic loss as defined as the difference between the theoretical and actual electrode voltages needed to drive the reaction at the desired rate. As we have seen with rechargeable lithium-ion batteries, the battery is only capable of providing a voltage that is less than that which charged it. In this case, we can consider the overall energy efficiency as the product of Faradaic efficiency and voltage efficiency.[33,65-67]

3.4.12 Faraday-Efficiency Effect:

In a previous section above, the recombination of O_2 and H_2 during a water-spitting reaction was mentioned. This type of slowing of the reaction and therefore decrease in the FE can be described as the Faraday-efficiency effect. This effect is defined as the possibility of misinterpretation of the data from electrochemical experiments via the failure to consider a total possible Faraday efficiency of less than 100 percent. It was only in recent decades that the excess heat produced in these types of systems was not assumed negligible. The experiments of Pons Fleishmann and Bose showed that this excess heat is in fact being produced and is measurable which directly contradicts the old adage that "The Faraday efficiency is assumed to be unity."[67,68]

Using the below equation, we can calculate the amount of excess heat produced during an electrolysis reaction while ignoring the Faradaic efficiency.

Equation 90:

$$Apparent\ Excess\ Heat\ (\%) = 100\ x\ \frac{Eout - \int(V - 1.481)I\ dt}{\int(V - 1.481)I\ dt}$$

Where E_{out} is measured energy output, V is experimental applied potential, I is applied current, and t is time. This equation can serve as a check of the determined FE value. Due to the singularity occurring near the voltage of electrolysis (in this case 1.481 V), one can determine a small but favorable error in determining the actual FE which will lead to an incorrect calculation of the excess heat ratio of near infinity when accurately this value should be zero.[67,69]

3.4.13 Rate Constants:

To effectively define rate constants, it is best to begin with the following general reaction equation:

Reaction 4: $$aA + bB \rightarrow cC + dD$$

This general reaction equation is often described by the rate law below:

Equation 91: $$rate = k[A]^m[B]^n$$

Where k is known as the rate or proportionality constant. Rate laws, like the one above, are mathematical representations of the relationship between the concentrations of the reagents and

the reaction rate. These can be expressed differentially to describe the change in reactant and

product concentrations over time or as an integration which describes how the actual

concentrations of these components change with time. The value of k can be used to characterize

the reaction itself as well as the reaction conditions. For example, each reaction has a

characteristic rate constant for a given set of conditions (temperature, type of solvent, pressure,

etc.) Other conditions that affect the rate constant value are the concentration of reagents A and B

and the m and n values which are derived from the experimental measure of how the reactant

concentrations change with time. These exponents are referred to as the reaction orders which is

defined as the degree to which the rate of the reaction depends on the concentration of each

individual reactant. Though the rate constant is dependent on these conditions, it will not change

with reaction coordinate as the reaction progresses. It is important to note that k is in units of s^{-1}

as a necessity to ensure that the rate is in units of concentration per unit time (M/s). That being

said, the units of k do depend on the rate law for that particular reaction.[69]

In the case of the hydrolysis of t-butyl bromide shown as a reaction equation below:

Reaction 5:

$$(CH_3)_3CBr_{(soln)} + H_2O_{(soln)} \rightarrow (CH_3)_3COH_{(soln)} + HBr_{(soln)}$$
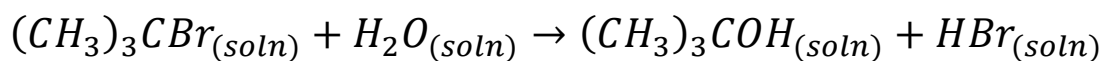
The rate is this reaction is directly proportional to the concentration of the $(CH_3)_3CBr$ but is

unaffected by the concentration of water present. So, as determined experimentally the m value

would be 1 while the n value is 0 as illustrated below:

Equation 92: $\qquad rate = \dfrac{\Delta[A]}{\Delta t} = k[A]^m[B]^n$

Equation 93:

$$rate = -\frac{\Delta[(CH_3)_3CBr]}{\Delta t} = k[(CH_3)_3CBr]^m[H_2O]^n$$

Equation 94:

$$rate = k[(CH_3)_3CBr]^1[H_2O]^0 = k[(CH_3)_3CBr]$$

As a comparison to the reaction and rate equations described above, we can consider a similar reaction involving methyl bromide (CH_3Br) below. This reaction differs from the previous one in that while this reaction also has a reaction order of 1, the value of k is about 10^6 times less that the t-butyl bromide equation which translates to the methyl bromide occurring approximately one billion times slower than the than t-butyl bromide version of the reaction.[69]

Equation 95: $$rate = -\frac{\Delta[CH_3Br]}{\Delta t} = k'[CH_3Br]$$

Equation 96: $$rate = k''[CH_3Br][OH^-]$$

To interpret these rate laws, it helps to think of k as a measure of the kinetic ability of the redox couple. For example, the larger the value of k, the shorter time is required for the reaction to complete and systems with a small rate constant will appear sluggish. The fastest published reactions are those with very simple electron transfers that have k value of 1 to 10 cm/s.[33] One such type of reaction is the reductions and oxidations of aromatic hydrocarbons. These include reactions involving catalysts with substituted pyrenes, anthracenes and perylenes.[71-72] These fast

reactions do not involve any other process than the electron transfer and resolution and have no notable molecular form alterations.

When the reaction is more complicated, such as those involving electron transfer and molecular rearrangement, it is usually very sluggish. This is reported true for the reduction of molecular oxygen to water or hydrogen peroxide and for the reduction of protons to molecular hydrogen as in hydrogen evolution reactions (HER).[33,73-75] Systems like these often involve multistep mechanisms which slow the rate of the reaction. There have even been reports of k values less than 10^9 cm/s which means the kinetic reactivity is within a range of ten orders of magnitude.[33,76,77]

In the previous section, it was discussed that the rate law including the rate constant and reaction orders are determined experimentally, but what does that look like in an electrochemical electrolyzer? The Berben lab, of the University of California, Davis, and many other groups begin by using the BV equation explained in section 1. The electron transfer rate constant is assessed using the following approach in which the dependence of both the anodic and cathodic peak potentials, E_{pa} and E_{pc}, on scan rate is considered according to the following equations. E_{pa} and E_{pc} are determined from the highest-most point on the forward wave and the lowest point on the return wave of the cyclic voltammogram of the reaction. The α and ks values are determined from the intercept and slope of a plot of peak potential vs. log of scan rate. This data is collected by running the CV experiment at several scan rates and measuring the anodic and cathodic peaks.
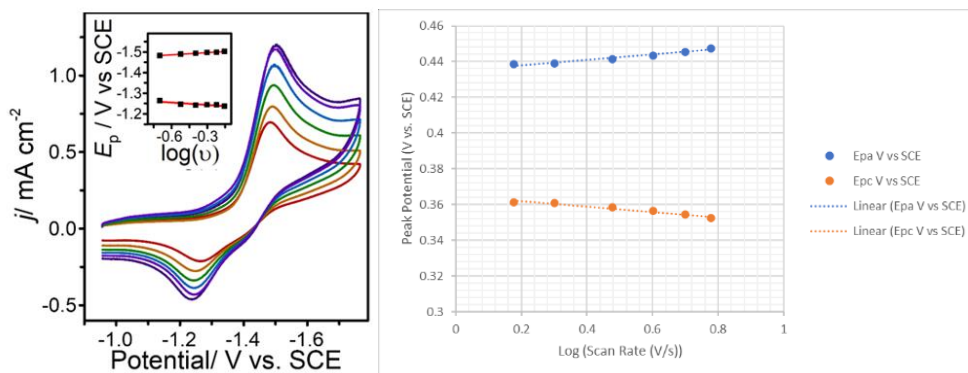
Figure 13: *On left, the results of a cyclic voltammetry experiment collected in 0.1 M Bu₄NBF₄*

MeCN under N₂ with GC at 3 mM of [Fe₄N(CO)₁₀(ᴹᵉPTA)₂] at scan rate from 0.3 – 0.8 V s⁻¹:

Inset best fit lines with equations y = 0.1145x – 1.2188 and y = -0.1012x -1.8581.On right, a

larger representation of the inset showing the transformation of the data so that the y intercept

and slope are equal to the transfer coefficient (α) and rate constant (kₛ) respectively.

The values of peak potential (E_{pc}/E_{pa}), transfer coefficient ($α_c$ /$α_a$), scan rate (ν), formal redox

potential ($E^{0'}$), ideal gas constant [R], temperature (T), Faraday's constant (F), and the estimated

heterogeneous rate constant from the BV plot in figure 10 were plugged into the BV equation

below to determine a theoretical estimate of the diffusion coefficient (D_c /D_a) which will be

described further in a coming section:

Equation 97:

$$E_{pc} = -\frac{2.303RT}{2\alpha_c F}\log(\nu) + [E^{0'} - \frac{0.78RT}{\alpha_c F} + \frac{2.303RT}{\alpha_c F}\log(k_{s,c}\frac{\sqrt{RT}}{\sqrt{\alpha_c F D_c}})]$$

Equation 98:

$$E_{pa} = \frac{2.303RT}{2(1-\alpha_a)F} \log(v) + [E^{0'} + \frac{0.78RT}{\alpha_a F} - \frac{2.303RT}{(1-\alpha_a)F} \log(k_{s,a} \frac{\sqrt{RT}}{\sqrt{(1-\alpha_a)FD_a}})]$$

The transfer coefficients (α_c and α_a) describe the symmetry of the energy barrier to electron

transfer (ET). The relationship between $E_{1/2}$ and $E^{0'}$ is derived as $(E_{pc} + E_{pa})/2$ from E_p's as

defined in the equations above and simplified via the series of equations below.

defined in the equations above and simplified via the series of equations below.

Equation 99: $\qquad\qquad\qquad \alpha_c + \alpha_a = 1$

Equation 100: $\qquad\qquad\qquad k_{s,c} = k_s e^{-\frac{\alpha_c F}{RT}(E-E0')}$

Equation 101: $\qquad\qquad\qquad k_{s,a} = k_s e^{\frac{(1-\alpha_a)F}{RT}(E-E0')}$

where, k_s is the heterogeneous rate constant (cm s^{-1}). This is the standard rate constant at zero

driving force and E is the applied potential. The above equation simplifies to the below equation

at a point between E_{pc} and E_{pa} during the CV scan so that $E = E^{0'}$:

Equation 102: $\qquad\qquad\qquad k_{s,a} = k_{s,c} = k_s$

This affords the final version below:

Equation 103: $\qquad\qquad E_{1/2} = E^{0'} + \frac{0.78RT}{2F} (\frac{\alpha_c - \alpha_a}{\alpha_c \alpha_a})$

With this definition based on the specific CV, the sum of α_c and α_a is equal to 1 for a single

electron transfer event, and for a Nernstian wave α_c and α_a are 0.5 such that equation 1 yields $E_{1/2}$

$= E^{0'}$. If the CV trace is non-Nernstian with an asymmetric ET, the transfer coefficients approach

0 and 1 and the measured $E_{1/2}$ gets further from $E^{0'}$.

There is more than one type of rate constant that can be determined in a multistep catalytic reaction. For example, the rate determining rate constant (k_{cat}). We can determine this value from the plateau in the catalytic current in a plot of linear sweep voltammograms (LSV) that are shown to be in a scan rate independent regime. If a plateau current can be reached during the CV experiment, then the catalytic current scales with the square root of the observed rate constant according to equation below:

Equation 104: $$jc = nF[cat]D^{\frac{1}{2}} kobs^{\frac{1}{2}} \; x \; 10^3$$

where, j_c is the plateau current density in units of mA cm^{-2}, *[cat]* is catalyst concentration in mol cm^{-3}, D is the diffusion coefficient for the catalyst in cm^2 s^{-1}, and k_{obs} in units of s^{-1} is the observed rate that limits the current at the plateau. The rate determining constant k_{cat} in units of M^{-1} s^{-1} is then determined according to equation below:

Equation 105: $$k_{obs} = [\text{H}^+]k_{cat}$$

where, [H$^+$] is the concentration in units of M of organic acid in MeCN (*i.e.,* butanoic acid or 2-methylphenol).

The plateau current must be extracted from the catalytic LSV plot which cannot be done accurately without a standard linear background subtraction/correction. This removes the capacitive current in the system. The resulting background-subtracted-LSV is then normalized to $j = 0$ at potentials 300 mV more positive than the catalytic current at $E_{cat/2}$. A representative example of linear background subtraction is shown in figure 14 below.
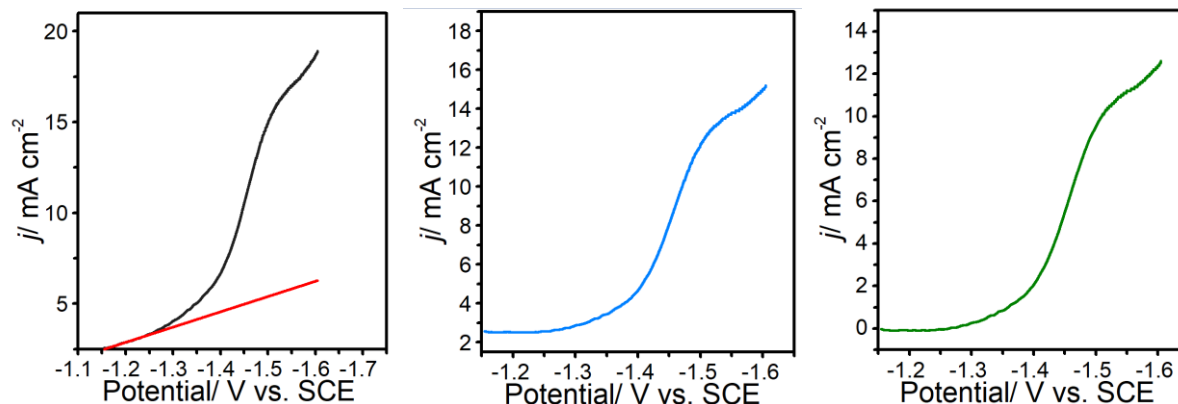
Figure 14: *On left, the black line is raw experimental CV forward wave while the red line is the*

background to be subtracted. In the center, the normalized background current LSV. On Right,

the resulting LSV where j = 0.

Each LSV is compared to the ideal S-shaped catalytic current which is produced using the

canonical function for an S-shaped waveform according to equation below:

Equation 106:
$$j = \frac{j_c}{1 + e^{F/RT(E - E_{cat/2})}}$$

where, j is current density in mA cm^{-2}, E is scanning potential in V vs SCE, $E_{cat/2}$ is the catalytic

halfwave potential in V vs SCE, and all other variables have been defined previously.

For cases when the kinetics of electron transfer influences the S-shaped waveform, the catalytic

halfwave potential shifts towards a negative potential relative to $E^{0'}$ when $k_s / (D^{1/2} k_{obs}^{1/2}) < 1$ as

described by the mechanism according to the equation below:

Equation 107:
$$E_{cat/2} = E^{0'} + \frac{RT}{\alpha F} \ln \ln \frac{k_s}{(Dk_{obs})^{\frac{1}{2}}}$$

With a *kobs* value from the BV or peak potential vs. log of scan rate method described above. This equation provides an estimate of the diffusion coefficient.

3.4.14 Diffusion Coefficient:

There are a few different useful methods for theoretically determining the diffusion coefficient. One is via the BV equation shown in the previous section and another is the Randles–Ševčík (RS) equation, two versions of which are shown below:

Equation 108: $$j_P = 446.3nFC \left(\frac{nFD}{RT}\right)^{\left(\frac{1}{2}\right)} \nu^{\frac{1}{2}}$$

Equation 109: $$i_P = 0.4463 \left(\frac{F^3}{RT}\right)^{\frac{1}{2}} n^{\frac{3}{2}} AD_o^{\frac{1}{2}} C_o^* \nu^{\frac{1}{2}}$$

Where i_p/j_p denotes the peak current in amps, n is the number of electrons transferred in the redox, A represents the electrode area in cm^2, F is the Faraday constant in C mol^{-1}, D represents the diffusion coefficient in cm^2/s, C is the catalyst concentration in mol/cm^3, ν denotes the scan rate in V/s, R is the Gas constant in J K^{-1} mol^{-1}, and T is the temperature in K. The RS equation expresses the effect of scan rate on the current of the peak potential, shown in figure 13. In simple reversible redox events such as that of the ferrocene/ferrocenium couple, we observe that the concentration, scan rate, and diffusional properties of the catalytic species affects the peak current.[33,78]

As scan rate increases, *Ip* also increases. The amount of current passing through the electrode is limited by the species' ability to diffuse to the electrode surface which is influenced by the catalyst and substrate concentration gradient near the electrode. When we change the voltage, the

concentration at the surface of the electrode is affected based on the Nernst equation introduced in an earlier section. The higher the scan rate, the faster the voltage sweep and the larger the concentration gradient at the electrode which results in a higher current.

In the same way the BV equation was used in conjunction with the peak potential vs. log of scan rate in the previous section, we can use a linear plot of i_p vs. $v^{1/2}$ and the known experimental variables to determine another estimate of the diffusion coefficient for the organometallic molecules present in the system. Then the slope of the i_p vs. $v^{1/2}$ plot can provide information about if the reaction is reversible, if there is a molecular structural change involved in the reaction process, and the stoichiometry of the of the redox reaction.[33,63,79]

Determination via DOSY:

To check the validity of the diffusivity constant estimations of the BV and RS methods and therefore the accuracy of the determined rate constants, there is terrific value in our ability to measure it using nuclear magnetic resonance (NMR). Diffusion ordered spectroscopy (DOSY) is a type of proton NMR that works via a series of spin echo spectra measured at different pulse gradient strengths to produce and analyze the various signal decays to separate the NMR signals of different species based on their respective diffusion coefficients.[80,81] The diffusion coefficient of a molecule is dependent on the hydrodynamic radius of that molecule.[82]

For accurate acquisition of the diffusion coefficient from DOSY the optimization of several parameters is required. These parameters include the solvent (mixture), which is related to viscosity, the pulse sequence/type of DOSY experiment, the range of gradients, the diffusion

delay, the number of gradients, the diffusion gradient pulse length, the dynamic range of the displayed diffusion coefficients, and the fitting routine used for the diffusion dimensions.

Figure 15 below depicts a basic DOSY pulse sequence based on spin echo which is described as the refocusing of spin magnetization by a pulse of resonant electromagnetic radiation.[83-85] The first encoding gradient pulse works to create a "corkscrew" pattern of magnetization directions then the second pulse returns and realigns the magnetization direction back to where it started. During the relaxation time between pulses, molecules in the sample diffuse which leads to a mixing of magnetization directions so that the direction of magnetization does not quite reach the direction at which it started pre-first-pulse. By varying the gradient strengths instead of the relaxation time, we can create a series of spectra where the signals decay as a function of the applied gradient power.[68,86] The longer, more powerful applied gradients will create a tighter corkscrew effect which means that there is a greater chance that the diffusion will be evident during the relaxation time.
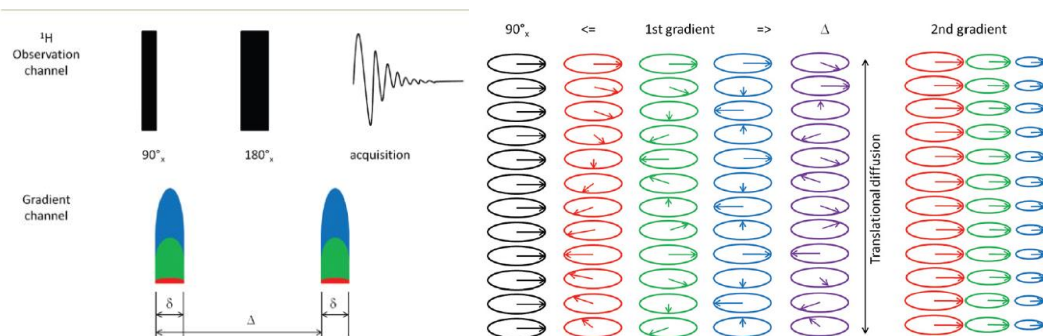
Figure 15: *On left, illustration of a simple DOSY pulse sequence showing the first proton pulse aligning the magnetization to the x-direction where δ represents the diffusion gradient pulse length and Δ denotes the relaxation time between the first and second pulse. On the right, a color-match depiction of the first gradient pulse creating the corkscrew effect followed by a second pulse which inverts the magnetization vector in the x–y plane undoing the first pulse's effect. The colors illustrate the strengths of the applied gradient pulses: red = 2%, green = 50%, and blue = 95%. The greater the strength the tighter the corkscrew effect and the easier it is to observe changes in the signal due to diffusion.[83]*

The higher the diffusion coefficient, the faster the molecule diffuses, and the more mixing will occur during the time between pulses and the less magnetization will be recovered post-second-pulse. Because the degree of mixing during the time between pulses depends on how fast the molecules can mix or diffuse in the NMR sample tube; small, easily diffusible molecules will mix rapidly, and the amount of magnetization recovered after the second pulse will diminish as a function of pulse gradient strength faster than it would with larger, slower diffusing molecules. Theoretically, the slowest diffusing molecule should lose equal to or greater than 95% of its initial signal at the highest pulse strength.

The analysis of DOSY magnetization results can be performed using the below equation.

Equation 110: $$\frac{I}{I_0} = e^{-Dg^2\delta^2\sigma^2g^2\Delta'}$$

Where *I* is current, *D* denotes the translational diffusion coefficient; *g* the gyromagnetic ratios of the studied nuclei; δ the pulse field gradient (PFG) duration, and σ represents the gradient shape factor. The diffusion delay shown as Δ', is the same as the Δ time described previously, but corrected based on the specific pulse sequence and gradient shape.[93,96] For accuracy we should also consider the shape of the molecules as this will affect the hydrodynamic radius of the molecule according to the Stokes–Einstein equation shown below:

Equation 111: $$D = \frac{k_B T}{6\pi\eta r_H}$$

Where *D* equals the diffusion coefficient ($m^2\ s^{-1}$); k_B represents the Boltzman's constant *T* is the temperature, η denotes the viscosity of the solution, and r_H is the hydrodynamic radius of the solute. Because magnetization signal is only lost in the z-direction and not in the x-y plane, it is able to measure translational diffusion coefficients which is exactly the value required to check the estimates from the BV and RS methods previously described.

3.4.15 Determining Values from the S-Shaped Plateau Curve:

To accurately utilize the equation below, two conditions must be true, one, that the CV trace is S-shaped so that the kinetic parameter and excess factor are balanced meaning that pure kinetic conditions are met, and substrate consumption is negligible, and two, that the current vs. potential curve is not affected by changes in scan rate.[90]

Equation 112: $$i_p = FSC_P^0\sqrt{D}\sqrt{k_e C_A^0}$$

Where I_p is the plateau current, S is the electrode surface area, $C^0{}_P$ and $C^0{}_A$ denote bulk

concentration of the catalyst and substrate respectively, D is the diffusion coefficient based on

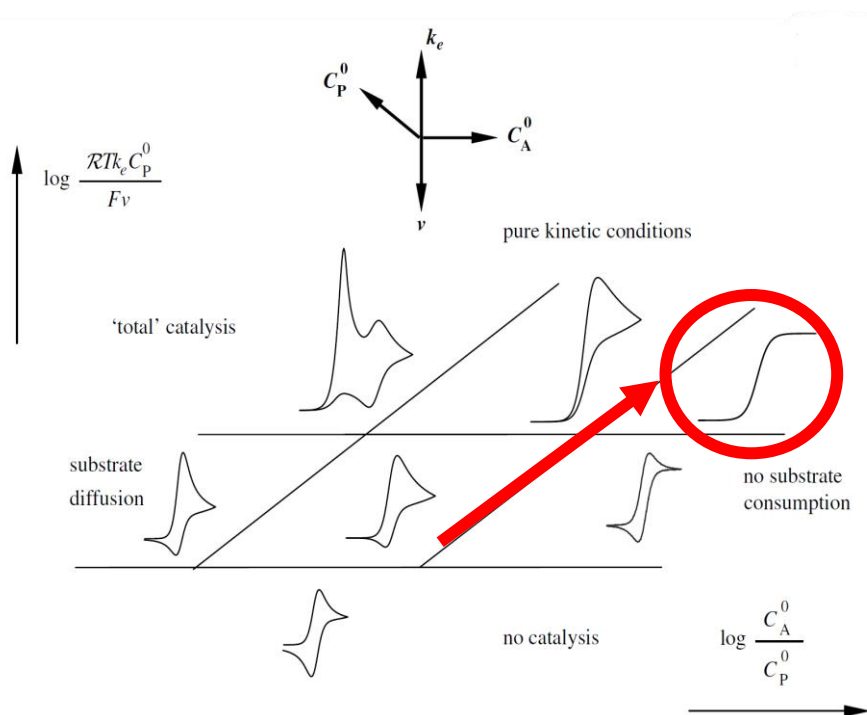results of DOSY NMR, and k_e is the rate constant of forward homogeneous electron transfer.[90]

Figure 16: *Homogeneous catalysis electrochemical reactions. Kinetic zone diagram in*

the case where the homogeneous electron transfer step is rate limiting[90]

To achieve the S-shape curve with CV it requires a balance of acid/substrate concentration and

scan rate. One can tune this relationship through several consecutive CV experiments moving

from the original peak shape to the target plateau shape. This curve is then overlaid with a

theoretical S-Shape curve based on the equation defined above to check for fit. This ideal curve

is based on the partial cathodic current (j_c) determined based on the below equations introduced

in a previous section, and the range of potentials scanned during the CV experiment.

*Equation 113:* $$j = j_c + j_a = nFAk_{red}[O]_o - nFAk_{ox}[R]_o$$

Equation 114: $$j_C = nF[cat]D^{\frac{1}{2}} k^{\frac{1}{2}}_{obs} \; x \; 10^3$$

Once an appropriate fit is achieved, many known values are entered into the spreadsheet including the $E_{cat/2}$ and $E_{1/2}$ values found from the peak shaped catalyst only (no substrate present) CV trace, the diffusion coefficient from BV or RS and DOSY NMR, the catalyst concentration, and either the thermodynamic potential ($E_{H/H2}$) or pka values found from literature for the acids used as substrate in the system. The observed rate constant value achieved from the slope of the peak potential vs. log (scan rate) plot described in an earlier section for the rate constant of the catalytic reaction is then converted to a normalized rate constant (k) by dividing by the electrode surface area. These values are then compared to the rate constant of forward homogeneous electron transfer found based on the S-shaped plot plateau current and the equation shown above. The coordinate lists for the ideal S-shaped curve and the corrected CV data are truncated to save space.

Dataset 1: Parameters Required to Achieve S-Shaped Curve for ($Fe_4N(CO)_{12}$) Sample

Known Values	
Ecat/2 V vs SCE	
	-1.701
D cm2/s DOSY	D cm2/s CV
1.06E-05	1.06E-05
kobs 1/s	k (1/s)
26	2.83E+03
[Cat]	
0.0000003	
E1/2 for cat.	
-1.6345	
EH/H2 butyric	
-0.981	
EH/H2 o-cresol	
-1.26	
SR=8 V/s	
Acid Concentration= 0.64 mM	

Calculated Values		
	norm kobs	
jc	1/s	F/RT
2.450233	2.826086957	38.94337

Fitted S-shaped Curve
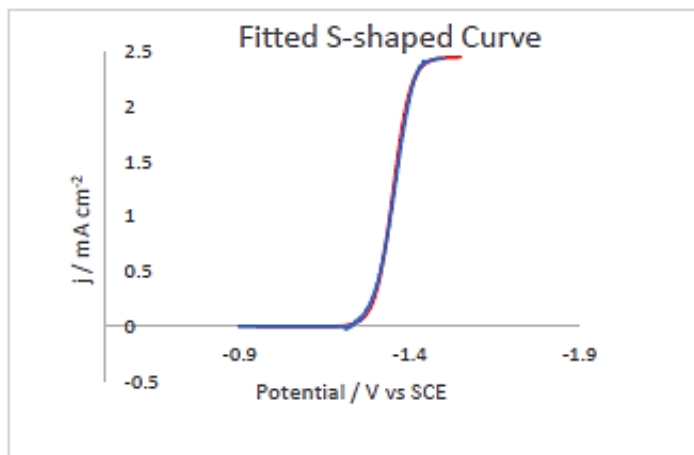
Dataset 2: Background Correction of the S-Shaped Curve Data

Current (A) vs. Potential (V vs. SCE) for (Fe$_4$N(CO)$_{12}$) Sample

Ideal S-Shaped Curve			Corrected CV Data	
Scanning Potential	Current Density		Potential (V vs. SCE)	Current (mA/cm^2)
-1.3	-0.95	4.04705E-07	-1.20647	0.00E+00
-1.31	-0.96	5.97403E-07	-1.20747	0.00E+00
-1.32	-0.97	8.81853E-07	-1.21047	-2.21E-02
-1.33	-0.98	1.30174E-06	-1.21147	-7.36E-03
-1.34	-0.99	1.92156E-06	-1.21247	-1.51E-02
-1.35	-1	2.8365E-06	-1.21347	-1.13E-02
-1.36	-1.01	4.18708E-06	-1.21447	-1.17E-02
-1.37	-1.02	6.18073E-06	-1.21547	4.67E-03
-1.38	-1.03	9.12364E-06	-1.21647	-1.99E-02
-1.39	-1.04	1.34678E-05	-1.21747	2.12E-03

3.4.16 Conversion from Plateau Values to Final Tafel-Style Plot:

The tafel-syle plots are constructed as discussed in previous sections with overpotential (η) as the independent variable beyond the thermodynamic potential driving electrocatalysis defined below. TOF is calculated from k_e determined from S-shaped waveforms and [H$^+$] = 1 mM for each cluster-acid pair according to the experimental conditions used. The thermodynamic potential ($E^0_{HA/H2}$) from literature was discussed earlier is plugged into the equations below along with the formal redox potential ($E^{0'}$) which is approximately equal to the E$_{1/2}$ determined from the CV trace to achieve a value for overpotential. When we plug all the values in the TOF

equation below; *kcat*, $E_{cat/2}$ from the CV trace, concentration of substrate, *F/RT*, overpotential, and the thermodynamic potential, a TOF can be achieved. Then, by plugging in a range of overpotentials a TOF can be achieved for each one. This is called the normalized TOF (TOF$_{norm}$) and appears as a column in the spreadsheet in the *Results and Discussion* section below. The Tafel-style plot presented is then a plot of log(TOF$_{norm}$) vs. overpotential which allows for the standard Tafel-like plot currently used in literature to compare the performance of novel and commercially available organometallic catalyst clusters!

Equation 114: $$\eta_{ref} \equiv E - E_{eq,ref}$$

Equation 115: $$\eta = E^0_{\left(\frac{HA}{H2}\right)} - E^{0\prime}$$

Equation 116: $$TOF = \frac{k_{cat}[H^+]}{1 + e^{\frac{(F/RT(E^0_{\frac{HA}{H2}} - E_{\frac{cat}{2}} - \eta)}{}}}$$

3.5.0   Materials and Methods:

3.5.1 Physical Measurements:

Quantitative measurement of H$_2$ was performed on a Varian 3800 GC equipped with a TCD detector and a Carboxen 1010 PLOT fused silica column (30 m $\times$ 0.53 mm)(Supelco) using dinitrogen (99.999%, Praxair) as the carrier gas. H$_2$ concentration was determined using a previously prepared working curve. Infrared spectra were recorded in a sealed liquid cell (SPECAC) on a Bruker Alpha Infrared spectrometer. 13C NMR spectra were collected on an 800 MHz Bruker Avance III spectrometers equipped with a cryoprobe. 1H, 13C, 11B, and 31P NMR spectra were recorded at ambient temperature using a Bruker 400 MHz TopSpin spectrometer or a Bruker 600 MHz TopSpin spectrometer. Chemical shifts were referenced to

the residual solvent peaks. 31P NMR spectra were referenced using an external H_3PO_4 standard (chemical shift of H_3PO_4 = 0 ppm). Infrared spectra were recorded in dry and degassed acetonitrile in a sealed liquid cell (SPECAC) on a Bruker Alpha infrared spectrometer.[91-93]

3.5.2 Preparation of Compounds:

All manipulations were conducted using standard Schlenk or glovebox techniques under a dinitrogen atmosphere. Unless otherwise noted, solvents were deoxygenated and dried by thorough sparging with dinitrogen (Praxair, 99.998%) gas followed by passage through an activated alumina column. The $[Fe_4N(CO)_{12}]^-$ compound was synthesized according to literature preparation.[94] All other reagents were followed by passage through an activated alumina column. Deuterated solvents were purchased from Cambridge Isotopes Laboratories, Inc. and were degassed before use. Compounds $[Fe_4N(CO)_{10}(MePTA)_2]$ OTf (3-OTf), $[Fe_4N(CO)_8(MePTA)_4](OTf)_3$ (4-OTf$_3$), and $[H- Fe_4N(CO)_{12}]$ were prepared following previously reported methods[91], where MePTA$^+$ is 1-methyl-1-azonia-3,5-diaza-7-phosphaadamantane. All other reagents were purchased from commercial vendors and used without further purification[91-93]

The $[Fe_4N(CO)_{11}(NO^+)]$ was prepared using a modified version of a published procedure[91,93, 94], and further characterization was obtained. $[Na(diglyme)_2][Fe_4N(CO)_{12}]$ (100 mg, 0.104 mmol) was dissolved in 5 mL of dry degassed dichloromethane in a 25 mL Schlenk tube under a N_2 atmosphere. The reaction mixture was cooled at −78 °C in a dry ice−acetone bath for 30 minutes. After it was cooled, the dichloromethane solution was cannula transferred to another 25 mL Schlenk tube having NOBF$_4$ (12.2 mg, 0.104 mmol) in a −78 °C dry ice−acetone bath. The

reaction mixture was stirred rapidly for another 1 hour in a $-78\ °C$ cold bath. Then, it was warmed to room temperature and stirred for another 30 minutes. Dichloromethane was removed in vacuo to afford a black powder. Then, 50 mL of dry degassed hexane was added to the black powder and stirred for 2 hours. A black crystalline powder (34.8 mg, 58% yield) was obtained from a concentrated hexane solution held at $-16\ °C$ for $2-3$ days. IR νCO(Hex): 2093 (vw), 2053 (vs), 2035 (s), 2027 (s), 2018 (w), 2004 (w), 1981 (vw); νNO 1789 (s) cm^{-1}. IR νCO(THF): 2094 (vw), 2053 (vs), 2034 (s), 2024 (sh), 2016 (b), νNO 1777 (s) cm^{-1}. IR νCO(MeCN): 2063 (s), 2007 (vs), 2000 (w), 1991 (s), 1964 (w); νNO 1745 (s) cm^{-1}. Combustion analysis calculated for $C_{11}Fe_4N_2O_{12}$: C, 22.96; N, 4.87. Found: C, 22.96; N, 5.08[91-93]

3.5.3 Electrochemical Measurements:

CV data were recorded under a dinitrogen atmosphere (Praxair, 99.998%) using a CH Instruments Electrochemical Analyzer Model 620D or 1100, a glassy carbon working electrode (CH Instruments, nominal surface area of 0.0707 cm^2), a platinum wire auxiliary electrode, and an Ag/AgNO$_3$ nonaqueous reference electrode with a Vycor tip. Reported potentials are all referenced to the SCE couple and were determined using ferrocene as an external standard where $E_{1/2}$ ferrocene/ferrocenium is +0.400 V vs SCE in acetonitrile. CVs were collected with 100% IR compensation. The effect of adding 5% H$_2$O to the acetonitrile referencing solution on the ferrocene/ferrocenium couple is minimal (18 mV). This was purified by dissolving in ethyl acetate and washing with Milli-Q water followed by recrystallization of Bu$_4$NBF$_4$ from boiling anhydrous ethanol and dried under vacuum at 70 °C for 48 hours before use. Nonaqueous electrolyte solutions were stored over 3 Å molecular sieves which had been activated by heating under vacuum at 200 °C for at least 72 hours.[91-93]

Controlled potential electrolysis (CPE) experiments were performed in a custom designed gastight glass cell under one atm of static dinitrogen (Praxair, 99.998%) or 13CO_2 (Cambridge Isotopes, 99.8% chemical purity, 99.9% isotopically pure 13C) as needed. Solutions were sparged with the gas of interest prior to the commencement of the experiment. The counter electrode compartment was separated from the working electrode compartment by a glass frit of medium porosity. In a typical experiment, 25 mL of electrolyte solution was used in the working electrode compartment and 25 mL of electrolyte was used in the counter electrode compartment. The working electrode was a glassy carbon plate (Tokai Carbon) with the nominal surface area immersed in solution of 8 cm^2. The auxiliary electrode was a coiled Pt wire (BASi). CO_2 was obtained from dry ice and transferred to experiments via cannula. Gas measurements were performed using a gas-tight syringe (Vici) to inject 100 μL gas samples into a Varian 3800 gas chromatogram equipped with a thermal conductivity detector. Gas samples were extracted from a sparged, septum-capped side arm on the working electrode compartment.

In between CPE experiments, the cell and working electrodes were sonicated in 5% v/v nitric acid for 10 min, rinsed with water, sonicated in MeOH for 10 minutes, rinsed, and sonicated in water for 10 min. [91-93]

3.5.4 IR-SEC Analysis:

Infrared spectra were recorded on a Bruker Alpha Infrared spectrometer (2 cm^{-1} resolution). Infrared spectroelectrochemical (IR-SEC) measurements were performed using a gas-tight, optically transparent thin-layer solution IR cell fabricated by Prof. Hartl at the University of Reading, Reading, U.K.[95] The IR-SEC cell contained a masked Au-minigrid working electrode

(32 wires/cm), a Pt-gauze auxiliary electrode, and an Ag-wire pseudo-reference electrode and had CaF_2 windows. In each experiment, electrochemical reduction of the species of interest was monitored by IR spectroscopy for a period of 5−9 minutes. Diffusion and mixing of the redox products, generated at the working and auxiliary electrodes in the IR cell, was reasonably suppressed within the total experimental time (no more than 9 min for one complete measurement). Degassed and air-free samples were loaded directly into the IR-SEC cell using a Luer-lock syringe.[91-94]

3.6.0   Results:

3.6.1 Spreadsheets - Description of Spreadsheet, Equations Utilized, Raw Data Input:

3.6.2 Butler Volmer Calculations:

The spreadsheet below is a tool to use the BV equation. By plugging in the peak potential values from CVs of different scan rates to plot the peak potential vs. log(scan rate) to calculate the intercept and slope which are the transfer coefficient (α) and rate constant (k_s) respectively. Once these are determined the below equation is used to estimate the diffusion coefficients.

Equation 117:

$$E_{pc} = -\frac{2.303RT}{2\alpha_c F}\log(v) + \left[E^{0'} - \frac{0.78RT}{\alpha_c F} + \frac{2.303RT}{\alpha_c F}\log\left(k_{s,c}\frac{\sqrt{RT}}{\sqrt{\alpha_c FD_c}}\right)\right]$$

Equation 118:

$$E_{pa} = \frac{2.303RT}{2(1-\alpha_a)F}\log(v) + \left[E^{0'} + \frac{0.78RT}{\alpha_a F} - \frac{2.303RT}{(1-\alpha_a)F}\log\left(k_{s,a}\frac{\sqrt{RT}}{\sqrt{(1-\alpha_a)FD_a}}\right)\right]$$

Dataset 3: Various Potentials (V vs. SCE) vs. Scan Rate for a ($Fe_4N(CO)_{12}$) Sample

Scan rate V/s	log Scan rate	Epa	Epc	Epa V vs SCE	Epc V vs SCE	E1/2	Correction
0.1	-1	0.461	0.403	0.429	0.371	0.432	-0.032
0.25	-0.602059991	0.464	0.405	0.4295	0.3705	0.4345	-0.0345
0.5	-0.301029996	0.459	0.404	0.4275	0.3725	0.4315	-0.0315
0.75	-0.124938737	0.461	0.404	0.4285	0.3715	0.4325	-0.0325
1	0	0.461	0.404	0.4285	0.3715	0.4325	-0.0325
1.5	0.176091259	0.472	0.395	0.4385	0.3615	0.4335	-0.0335
2	0.301029996	0.473	0.395	0.439	0.361	0.434	-0.034
3	0.477121255	0.475	0.392	0.4415	0.3585	0.4335	-0.0335
4	0.602059991	0.478	0.391	0.4435	0.3565	0.4345	-0.0345
5	0.698970004	0.48	0.389	0.4455	0.3545	0.4345	-0.0345
6	0.77815125	0.482	0.387	0.4475	0.3525	0.4345	-0.0345
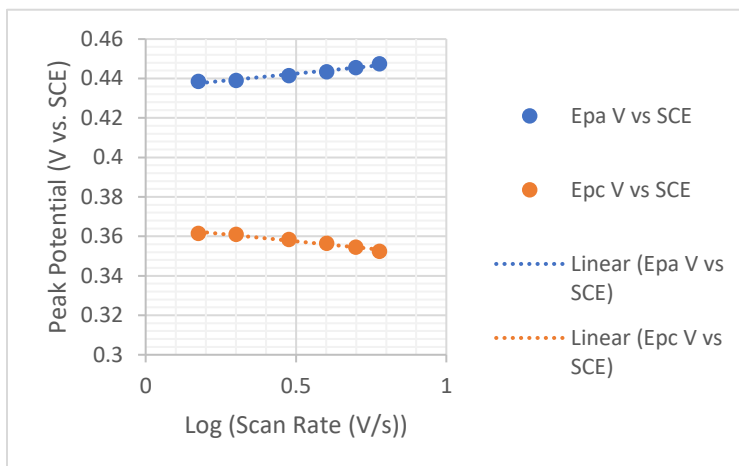
logks C	logks A
-0.078882008	0.140239272

ks C Rate	ks A Rate
0.833907715	1.381144989

3.6.3 Randles–Ševčík Calculations:

The spreadsheet below is a tool to use the RS equation. By plugging in the peak potential values from CVs of different scan rates to plot the peak current vs. scan rate squared to ensure that this relationship is linear and therefore the RS equation below can be used to determine another estimate of the diffusion coefficient to compare to the analytical value from DOSY NMR.
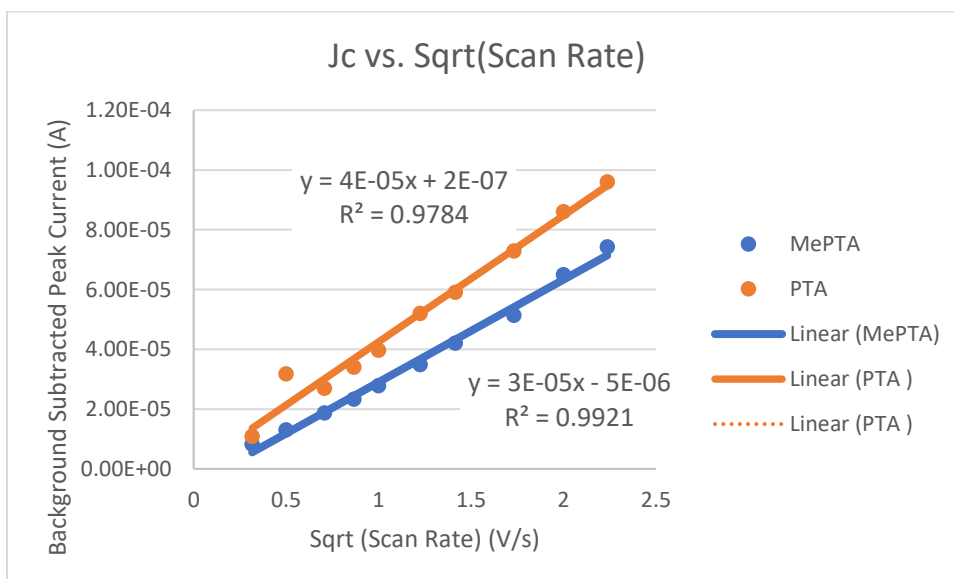
Equation 119: $$j_P = 446.3nFC\left(\frac{nFD}{RT}\right)^{\left(\frac{1}{2}\right)} v^{\frac{1}{2}}$$

Equation 120: $$i_P = 0.4463\left(\frac{F^3}{RT}\right)^{\frac{1}{2}} n^{\frac{3}{2}}AD_o^{\frac{1}{2}} C_o^* v^{\frac{1}{2}}$$

Dataset 4: Peak Current (A) vs. Scan Rate for [Fe4N(CO)10(PTA)2]⁻ and [Fe4N(CO)10(MePTA)2]⁺ Samples

MePTA				
R	sqrt(SR)	J (A)	Jb (A)	Jc (A)
0.1	0.316228	1.09E-05	2.64E-06	8.23E-06
0.25	0.5	1.68E-05	3.77E-06	1.31E-05
0.5	0.707107	2.48E-05	6.05E-06	1.87E-05
0.75	0.866025	3.04E-05	7.18E-06	2.33E-05
1	1	3.67E-05	8.88E-06	2.78E-05
1.5	1.224745	4.72E-05	1.23E-05	3.49E-05
2	1.414214	5.65E-05	1.45E-05	4.20E-05
3	1.732051	7.07E-05	1.94E-05	5.14E-05
4	2	9.00E-05	2.51E-05	6.50E-05

PTA				
SR	**sqrt(SR)**	**J (A)**	**Jb (A)**	**Jc (A)**
0.1	0.316228	1.82E-05	7.32E-06	1.08E-05
0.25	0.5	3.33E-05	1.54E-06	3.18E-05
0.5	0.707107	4.66E-05	1.96E-05	2.70E-05
0.75	0.866025	5.84E-05	2.43E-05	3.40E-05
1	1	7.30E-05	3.33E-05	3.97E-05
1.5	1.224745	8.86E-05	3.66E-05	5.20E-05
2	1.414214	1.06E-04	4.70E-05	5.91E-05
3	1.732051	1.34E-04	6.07E-05	7.29E-05
4	2	1.60E-04	7.40E-05	8.60E-05

Jc vs. Sqrt(Scan Rate)

$y = 4E{-}05x + 2E{-}07$
$R^2 = 0.9784$

$y = 3E{-}05x - 5E{-}06$
$R^2 = 0.9921$

X-axis: Sqrt (Scan Rate) (V/s)
Y-axis: Background Subtracted Peak Current (A)

Legend: MePTA, PTA, Linear (MePTA), Linear (PTA), Linear (PTA)

3.6.4 Faradaic Efficiency Calculations:

The spreadsheet below is a tool to use the FE equation. The first tables and plot are a record of the calibration process during which mixtures of known volumes of nitrogen and hydrogen gas are injected into the gas chromatograph (GC). The slope and intercept are used in the calculations of moles of product hydrogen achieved in the constant potential electrolysis (CPE) experiment. The actual calculation of FE% then includes the volume of the headspace, the volume of the sample injection, the concentration of substrate and catalyst, and the area of the peak reported by the GC to achieve a value for the amount of moles of H_2 produced (n), the number of electrons transferred for H_2 production (z) is known to be 2, based on the reaction cycle shown in figure 17 below and the total charge passed (Q) is known from the output of the CPE experiment, the spreadsheets also include the Faraday constant (F). Once all this data is entered, the Faradaic efficiency can be calculated. Also, the turnover number (TON) can be calculated by dividing the mmols of H_2 in the total headspace volume by the mmols of catalyst in the system. This value is synonymous with the catalytic rate constant (k_{cat}) and is defined as the maximum number of chemical conversions of substrate molecules per second that a single active site will execute for a given catalyst concentration. The TON divided by the duration of the active site interaction is the turnover frequency (TOF).[96,97]

Equation 121:

$$Faradaic\ Efficiency(\%) = \frac{Q_{Experimental}}{Q_{Theoretical}} * 100 = \frac{z*n*F}{Q} * 100$$

Equation 122:
$$TON = \frac{n_{product}}{n_{cat}}$$

Equation 123:
$$TOF = \frac{TON}{t}$$

Dataset 5: Calibration Measurements for More Accurate Measurement of Hydrogen Production:
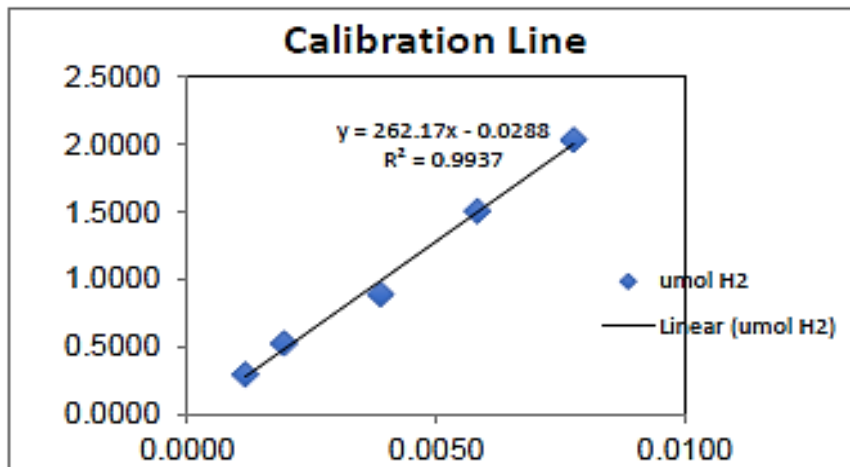
%H2	0.00047438
volume H2(ml)	0.05
volume N2(ml)	105.4

%H2	0.00028463
volume H2(ml)	0.03
volume N2(ml)	105.4

%H2	0.00142315
volume H2(ml)	0.15
volume N2(ml)	105.4

%H2	0.00094877
volume H2(ml)	0.1
volume N2(ml)	105.4

Slope:	262.172071
y-intercept:	-0.0288114

Dataset 6: CPE Chamber and Gas Sample Parameters for the Calculation of HER

Efficiency

	injection #1	injection #2	injection #3
vol. sample injected(uL):	100	100	100
peak value(mV*s):	89.74	91.21	76.5
umol H2(sample):	0.342404173	0.348011178	0.291902989
mmol H2 (total headspace):	0.126689544	0.128764136	0.108004106
mmol Fe4N cluster	0.2	0.2	0.2
Vol. headspace (ul):	37000	37000	37000
	injection #1	injection #2	injection #3
Headspace (mL)	62	62	62
solvent added (mL)	25	25	25
Net headspace (uL)	37000	37000	37000
Charge passed (C)	25.446	25.446	25.446
Faradaic efficiency	96.08	97.65	81.91
TON	0.63	0.64	0.54
TOF per hour	1.15	1.17	0.98

$$[Fe_4NL_{12}]^{n+1} \xrightarrow{e^-} \boxed{[Fe_4NL_{12}]^{n}} \xrightarrow{e^-} [Fe_4NL_{12}]^{n-1}$$

H₂ ↖ H⁺

H⁺

$[H\text{-}Fe_4NL_{12}]^{n}$
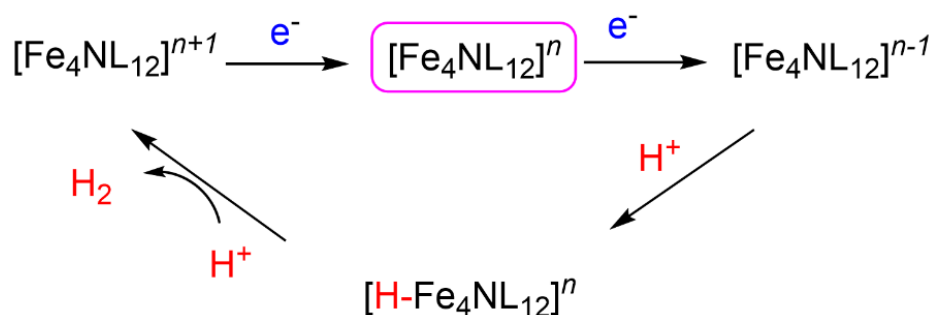
Figure 17: *Proposed HER mechanism for all organometallic clusters evaluated. Pink represents the start of the catalytic cycle. n is -1 for all catalysts assessed. n is followed by -1 or +1 depending on the cluster charge*

3.6.5 Locating the Scan Rate Independent Regime:

It is important to only use scan rates from the scan rate independent regime to achieve an S-shaped plateau curve as only under these conditions can we use the equation, described in a coming section, to achieve the overall rate constant of the full catalytic reaction shown in figure 18 and to achieve a normalized TOF and overpotential for the system. Finding the scan rate independent regime is fairly simple. Several CVs are performed at several scan rates.

These forward waves are then normalized based on the procedure described in an earlier section. Finally, these normalized curves are overlaid to reveal a region where no matter what scan rate is employed, the curves are directly on top of one another. The data list is truncated below to save space. Figure 19 shows the final product for publication.
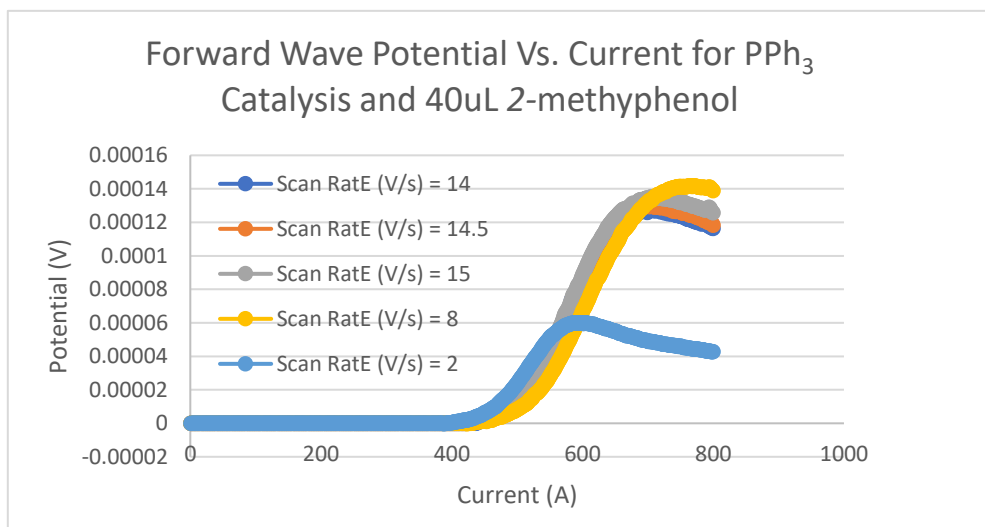
Figure 18: Overlay of many scan rates to locate the area of overlap and therefore the scan rate independent regime that corresponds to the S-Shaped curve in CV/LSV (linear sweep voltammetry).

Dataset 7: Calculation of TOF Based of the pairing of 2-methylphenly and

$[Fe_4N(CO)_{10}(PTA)_2]^-$ and butanoic acid and $[Fe_4N(CO)_{10}(MePTA)_2]^+$

TOFmax	TOFnorm	F/RT
150000	16304.35	38.94336875
EH/H2		
-0.981		Overpotential
		0.442
Ecat/2		
-1.423		

TOFmax	TOFnorm	
1100	1760	
EH/H2		Overpotential
-1.26		0.32
Ecat/2		
-1.58		

η	TOFnorm	logToFnorm
0	0.000545514	-3.26319403
0.1	0.0267975	-1.57190572
0.2	1.316282027	0.11934895
0.3	64.41009766	1.80895396
0.4	2658.615136	3.42465547
0.5	14761.95098	4.16914376
0.6	16269.74241	4.21138068
0.7	16303.6419	4.21228463
0.8	16304.33346	4.21230305
0.9	16304.34753	4.21230342
1	16304.34782	4.21230343
1.1	16304.34783	4.21230343
1.2	16304.34783	4.21230343
1.3	16304.34783	4.21230343
1.4	16304.34783	4.21230343
1.5	16304.34783	4.21230343

η	TOFnorm	logToFnorm
0	0.006813749	-2.166613863
0.1	0.334652634	-0.475405752
0.2	16.29023618	1.211927381
0.3	553.6327174	2.743221747
0.4	1685.246386	3.226663405
0.5	1758.412183	3.245120684
0.6	1759.967648	3.245504685
0.7	1759.999341	3.245512505
0.8	1759.999987	3.245512665
0.9	1760	3.245512668
1	1760	3.245512668
1.1	1760	3.245512668
1.2	1760	3.245512668
1.3	1760	3.245512668
1.4	1760	3.245512668
1.5	1760	3.245512668
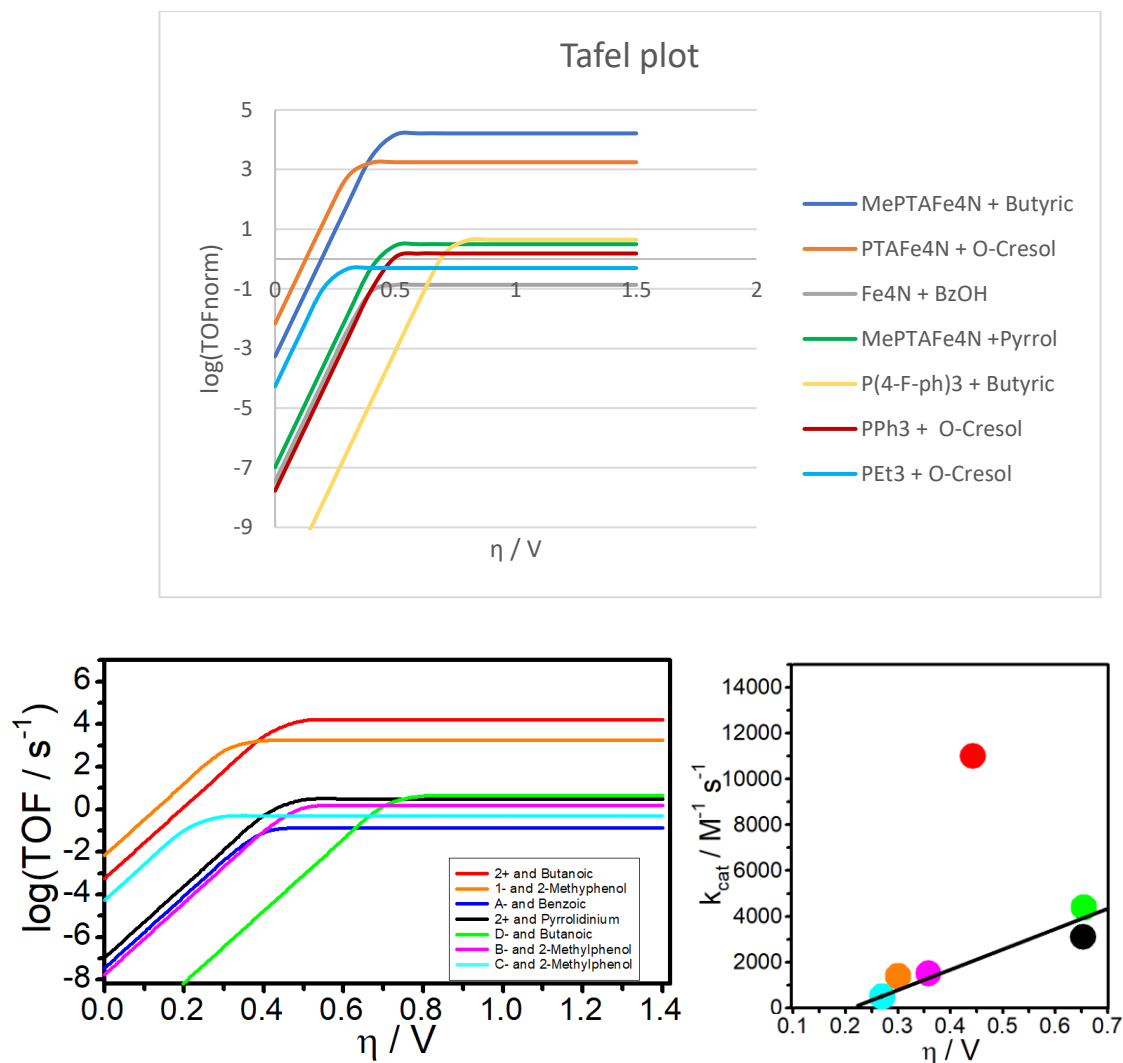
Figure 19: *Images for publication. Left - Plot of kcat vs. ($E^0_{HA/H2} - E_{1/2}$) for all clusters tested for hydrogen evolution reaction (HER) using uncharged organic acids (with anionic conjugate base). Right - Plot of kcat vs. ($E^0_{HA/H2} - E_{1/2}$) for all clusters evaluated for HER using cationic organic acids (with neutral conjugate base.)*

3.6.6 Discussion of Results:

The electrochemical, spectroscopic and reactivity properties of six clusters are probed in this work, and include Na[Fe$_4$N(CO)$_{10}$(PTA)$_2$] (Na-**1**), [Fe$_4$N(CO)$_{10}$(^{Me}PTA)$_2$]I (**2**-I), [Fe$_4$N(CO)$_{12}$]$^-$

(**A**⁻), [Fe₄N(CO)₁₁(PPh₃)]⁻ (**B**⁻),[1] [Fe₄N(CO)₁₁(PEt₃)]⁻ (**C**⁻), and [Fe₄N(CO)₁₁(P(*p*-F-ph)₃)]⁻ (**D**⁻)

which have all been previously reported ((PTA = 1,3,5-triaza-7-phosphadamantane, $^{Me}PTA^+$ = *N*-

methyl-1,3,5-triaza-7-phosphadamantanium, Chart 1).

Chart 1. Clusters and atom numbering scheme used in this work.
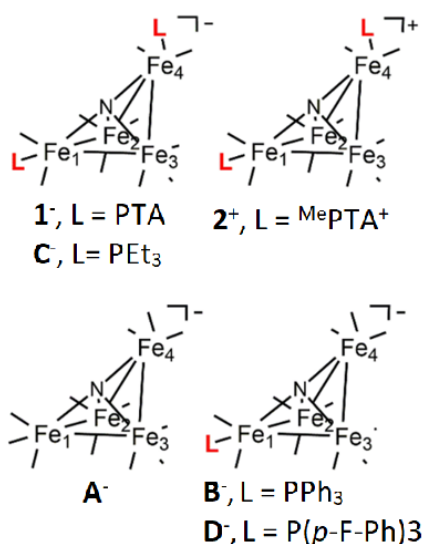
Electrochemical measurements using cyclic voltammetry (CV) were performed on 0.1 M

Bu₄NBF₄ MeCN solutions of 1 mM **1**⁻ and **2**⁺ (Figure 20a). The CV of **2**⁺ is a quasi-reversible

wave with a peak-to-peak separation of 94 mV during a 0.1 V s⁻¹ scan and peak current ratio

(j_{pc}/j_{pa}) of 1.9. The peak current scales linearly with the square root of the scan rate which

suggests a diffusion-controlled electron transfer (ET) at the electrode with a diffusion coefficient

(*D*) of 9.2 × 10⁻⁶ cm² s⁻¹ (Figure 20b) For **2**⁺ the halfwave potential ($E_{1/2}$) was determined to be -

1.42 V vs SCE. The $E_{1/2}$ for **1**$^{1-/2-}$ was not determined easily from the CV due to the large

apparent peak-to-peak separation, ΔE_p, between E_{pa} and E_{pc} (350 mV). The non-Nernstian

waveform generated by **1⁻** during CV suggests either sluggish ET or an electrochemical process

in which ET and a chemical step are related under a single CV wave. [29]
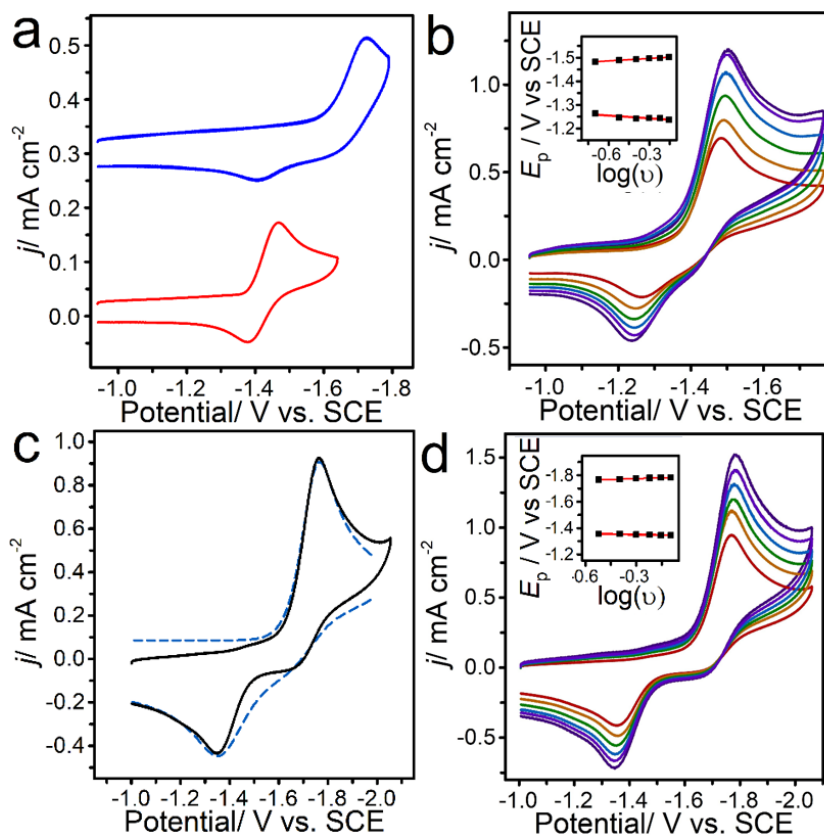
Figure 20: *CVs collected in 0.1 M Bu₄NBF₄ MeCN under N₂ with GC. (a) 1 mM of **1⁻** (blue,*

*offset by 0.3 mA cm⁻²) and 1 mM of **2⁺** (red); at 0.1 V s⁻¹. (b) 3.5 mM of **2⁺** at 0.2 – 0.7 V s⁻¹:*

*Inset best fit lines with equations y = 0.0408x – 1.2308 and y = -0.0353x -1.5073. (c) 3 mM of **1⁻***

*at 0.2 V s⁻¹ (back) and digital simulation (blue dotted). (d) 3 mM of **1⁻** at 0.3 – 0.8 V s⁻¹: Inset*

best fit lines with equations y = 0.1145x – 1.2188 and y = -0.1012x -1.8581.

To accurately interpret the origin of non-Nernstian behavior in the CV wave for **1**$^-$, we first used infrared-spectroelectrochemistry (IR-SEC) as a probe for changes in the distinct v_{CO} vibrational frequencies of **1**$^-$. This experiment probes the chemical reversibility of the ET event over longer times scales.[98] A 1 mM solution of **1**$^-$ was electrolyzed at -1.6 V over a period of time. The shift of Infrared spectroelectrochemistry (IR-SEC) absorption bands to lower energy is consistent with greater metal to ligand back bonding into π^* orbitals of the CO ligands. The re-oxidation of **1**$^{2-}$ to **1**$^-$ at -2.1 V led to its conversion into **1**$^-$. The less than quantitative conversion of **1**$^{2-}$ to **1**$^-$ likely arises from slow decomposition that occurs by applying a positive potential for a prolonged time. The spectral data for **1**$^+$ supports a proposal based on CV that the **1**$^{1-/2-}$ couple is non-Nernstian because of a slow ET rate and asymmetric barrier for ET, and that reduction of **1**$^-$ into **1**$^{2-}$ is not associated with a chemical step.[99,100]

Having determined that **1**$^{-/2-}$ is chemically reversible over longer times scales via the spectral and CV curve shape data, it is likely that the large peak-to-peak separation of the **1**$^{-/2-}$ couple results from a large Marcus reorganization energy[101], For an electrochemically reversible cluster, this separation between peaks is likely linked to the migration of the phosphine around the cluster surface of 1- upon reduction since it is well-established that CO and phosphine ligands on carbonyl cluster surfaces are fluxional.[102]

IR-SEC was required to prove that the 1$^-$/2$^-$ charge couple of the **1**$^-$ cluster is chemically reversible for each catalyst evaluated. This successful determination of this reversibility would prove that the large peak-to-peak separation observed for the 1$^-$/2$^-$ couple results from a large reorganization energy. Based on published results, in instances where kinetic factors strongly influence the ET,

the relationship between the $E_{1/2}$ and the formal potential ($E^{0'}$) can be calculated by $E_{1/2}$= (Epa +

Epc)/2 and is dependent on the symmetry of the electron transfer barrier in the Butler-Volmer (BV)

model for ET. According to the BV model, the dependence of the cathodic and anodic peak

potentials (E_{pc} and E_{pa} respectively) on scan rate is as defined in the equations below:

Equation 124:

$$E_{pc} = -\frac{2.303RT}{2\alpha_c F}\log(v) + [E^{0'} - \frac{0.78RT}{\alpha_c F} + \frac{2.303RT}{\alpha_c F}\log(k_{s,c}\frac{\sqrt{RT}}{\sqrt{\alpha_c FD_c}})]$$

By using the BV equation above and the subsequent equations shown in the theory section, it

was determined that $E^{0'}(1^-/2^-)$ = -1.58 V and based on the CV results it was calculated that $E_{1/2}$ (1$^-$

/2$^-$) = -1.56 V (Figure 20c). The difference in $E^{0'}$ for the 1$^-$/2$^-$ and 2$^+$/0 couple is about 190 mV

which is consistent with the hypothesis that due to contributions of the local electric field applied

by the positively charge ligand, the MePTA$^+$ promotes an anodic shift in redox potentials.[10] In

previously reported cases of transition metal complexes with intercalated group 1 and 2 cations

and trimethylammonium substituents in the SCS, similar electrostatic effects were observed.[103]

Once we determined an $E^{0'}$ for **1**$^{1-/2-}$ and **2**$^{+/0}$ we could then use the BV approach to establish an

electron transfer (ET) rate constant (k_{sc}). The kinetically slower ET for reduction of **1**$^-$ into **1**$^{2-}$ is

reflected in k_{sc} = (1.2 ± 1.4) × 10^{-3} cm s^{-1} while the reduction of **2**$^+$ into **2** is faster, k_{sc} = (5.9 ±

1.5) × 10^{-3} cm s^{-1}, and similar to that reported previously for reduction of **A**$^-$ (k_{sc} = 5 × 10^{-3} cm s$^-$

^{1}).[103]

The preceding results indicate that the reduction potential for **2**$^+$, which has two positively charged

MePTA$^+$ functional groups in the SCS is 190 mV more anodic than that of **1**$^-$ which has analogous

SCS functional groups sans the positive charges. Previously published spectroscopic studies from

Berben et al. discuss that some of this anodic shift may be caused by an electrostatic effect and therefore the cluster core in 2^+ should be more electron rich than expected based on a simple scaling relationship such as reduction potential. In the same publications, that scaling relationship demonstrated a linear correlation over a structurally similar series of four iron carbonyl clusters.[10, 92,104]

In cases where ET is strongly influenced by kinetic factors the relationship between formal potential ($E^{0'}$) and the $E_{1/2}$, calculated from $E_{1/2} = (E_{pa} + E_{pc})/2$, is dependent on the symmetry of the ET barrier in the Butler-Volmer model for ET. Using this theory, we determined that $E^{0'}(1^{-/2-})$ = -1.58 V, and based on the CV results it was calculated that $E_{1/2}(1^{-/2-})$ = -1.56 V. The difference in $E^{0'}$ for the $1^{-/2-}$ and $2^{+/0}$ couple, about 190 mV, is consistent with the hypothesis that $^{Me}PTA^+$ promotes an anodic shift in redox potentials due to contributions of the local electric field applied by the positively charge ligand.[92] Similarly, electrostatic effects have been previously reported in transition metal complexes with intercalated group 1 and 2 cations and trimethylammonium substituents in the SCS.[105] Having established an $E^{0'}$ for $1^{1-/2-}$ and $2^{+/0}$, we also assessed the ET rate constant (k_{sc}) using the Butler−Volmer approach in which the dependence of both the anodic and cathodic peak potentials, E_{pa} and E_{pc}, respectively, on scan rate (Figure 20 b-d). The kinetically slower ET for reduction of 1^- into 1^{2-} is reflected in $k_{sc} = (1.2 \pm 1.4) \times 10^{-3}$ cm s^{-1}. Reduction of 2^+ into 2 is faster, $k_{sc} = (5.9 \pm 1.5) \times 10^{-3}$ cm s^{-1}, and similar to that reported previously for reduction of A^- ($k_{sc} = 5 \times 10^{-3}$ cm s^{-1}).[104]

The preceding results indicate that the reduction potential for 2^+, which has two positively charged $^{Me}PTA^+$ functional groups in the SCS, is 190 mV more anodic than that of 1^- which has analogous

SCS functional groups absent the positive charges. According to a previously published spectroscopic study, some of this anodic shift is caused by an electrostatic effect and therefore the cluster core in 2^+ should be more electron rich than expected based on a simple scaling relationship such as hydricity vs. reduction potential. That scaling relationship has previously been demonstrated to show a linear correlation over a structurally similar series of four iron carbonyl clusters.[91,92] Unfortunately, our attempts in this work to measure the hydricity of intermediates including (H-**1**)$^-$ and (H-**2**)$^+$ were unsuccessful, despite our prior successes using IR-SEC to obtain hydricity values for clusters including (H-**A**)$^-$ and (H-**B**)$^-$. Instead, characterization of the rate of PT (k_{PT}) and the observed rate for hydrogen evolution from **1**$^-$ and **2**$^+$ (k_{obs}) was possible and those results are described in the foregoing paragraphs.

Monoprotic organic acids were used to probe H$_2$ evolution with **1**$^-$ and **2**$^+$ so that reaction conditions such as [H$^+$] and pK_a in MeCN solution could be carefully controlled. Addition of *2*-methyphenol (C$_7$H$_8$O) (pK_a = 27.5, $E^0_{HA/H2}$ = -1.26 V vs SCE)[107] to a solution of 1 mM of **1**$^-$ resulted in the loss of the return oxidative wave assigned to the oxidation of **1**$^{2-}$ and a current increase at j_{pc} that scales linearly with [H$^+$] (Figure 21a). The current at j_{pc} produced by the reaction between *2*-methyphenol and the GC electrode is negligible compared to the current produced when **1**$^-$ is also present in solution (Figure 21a).
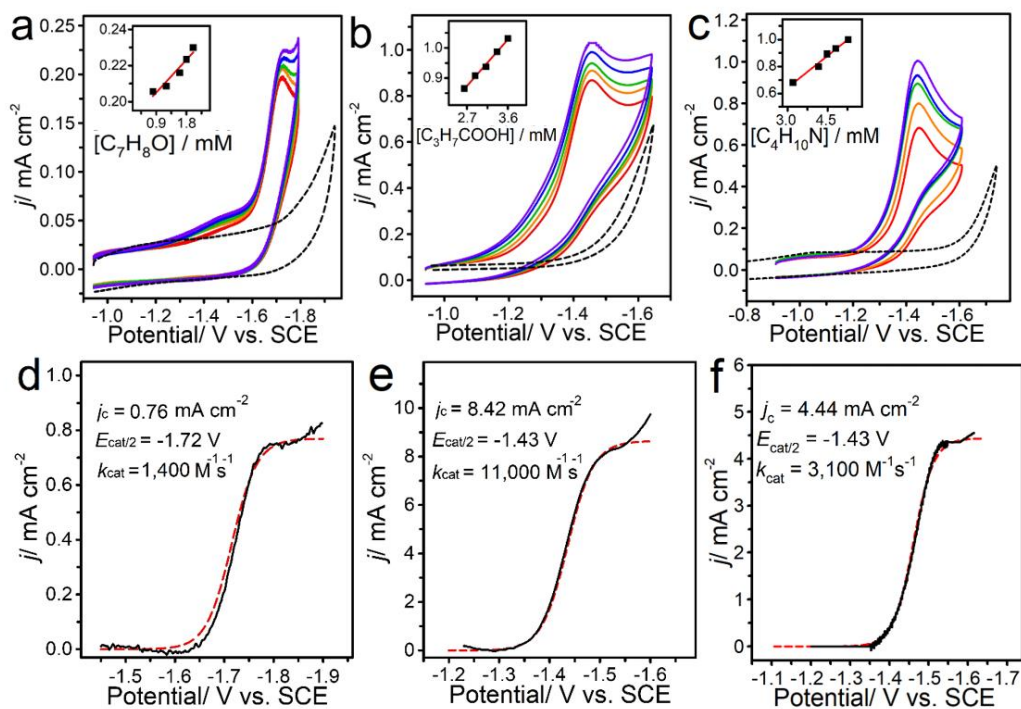
Figure 21. *CVs and LSVs collected in 0.1 M Bu₄NBF₄ MeCN under N₂ with GC. (a) 0.3 mM of 1⁻ with 0.66 – 3.2 mM 2-methyphenol at 0.1 V s⁻¹ (color) and 2-methyphenol acid blank (dotted). (b) 0.3 mM of 2⁺ with 4.2 – 5.6 mM butanoic acid at 0.1 V s⁻¹ (color) and butanoic acid blank (dotted) (c) 0.3 mM of 2⁺ with 4.16 – 5.6 mM pyrrolidinium at 0.1 V s⁻¹ (color) and pyrrolidinium acid blank (dotted). (d) 0.3 mM of 1⁻ with 9.2 mM 2-methyphenol at 8 V s⁻¹ (black), best-fit to canonical S-shaped wave (red dotted). (e) 0.3 mM of 2⁺ with 6.2 mM butanoic acid at 50 V s⁻¹ (black), best-fit to the canonical S-shaped wave (red dotted). (f) 0.3 mM of 2⁺ with 6.2 mM pyrrolidinium acid at 50 V s⁻¹ (black), best-fit to canonical S-shaped wave (red dotted)*

In a similar experiment involving 1 mM solution of 2^+, the $2^{+/0}$ couple became irreversible when [2-methyphenol] = 1.5 – 8 mM. The peak height is very near equal to the current produced by the $2^{+/0}$ couple and is independent of [2-methyphenol, and that waveform suggests that an EC-type mechanism occurs in which ET to afford **2** is followed by a slow PT event that yields (H-**2**)⁺.[105]

A catalytic reaction to afford H_2 is not mediated by 2^+ using *2*-methyphenol as substrate and we hypothesize that this is the case because the thermodynamic potential (η') for that reaction is only 160 mV compared with 320 mV for reaction of 1^- with *2*-methyphenol. To promote a catalytic reaction with 2^+ we introduced butanoic acid (C_3H_7COOH)($pK_a = 22.7$, $E^0_{HA/H2} = -0.98$ V vs SCE) and pyrrolidinium ($C_4H_{10}N$)($pK_a = 19.2$, $E^0_{HA/H2} = -0.77$ V vs SCE) the substrate which has η' for hydrogen evolution of 440 mV and 650 mV, respectivly.[106] CV's recorded of solutions containing 2^+ and butanoic acid, and separately, 2^+ and pyrrolidinium both generate a catalytic current that scales linearly with $[H^+]$ (Figure 21b-c). This trend in catalytic current resulting from >300 mV of potential for H_2 evolution is observed for all organometallic clusters in this study. Controlled potential electrolysis (CPE) performed of each acid and cluster combination confirms that the catalytic current near $E_{cat/2}$ productively evolves hydrogen The faradaic efficiency results of testing the following 6 catalysis are shown in table 2 below: $Na[Fe_4N(CO)_{10}(PTA)_2]$ (Na-**1**), $[Fe_4N(CO)_{10}(^{Me}PTA)_2]I$ (**2**-I), $[Fe_4N(CO)_{12}]^-$ (**A**$^-$), $[Fe_4N(CO)_{11}(PPh_3)]^-$ (**B**$^-$), $[Fe_4N(CO)_{11}(PEt_3)]^-$ (**C**-), and $[Fe_4N(CO)_{11}(P(4-F-ph)_3)]^-$ (D-) (PTA = 1,3,5-triaza-7-phosphadamantane, $^{Me}PTA^+$ = *N*-methyl-1,3,5-triaza-7-phosphadamantanium, (Chart 1)

Table 2: **Controlled potential electrolysis of 0.5 mM organometallic cluster and 20 mM organic acid in 0.1 M Bu$_4$NBF$_4$ MeCN under N$_2$ for 600 s.**

	Acid	Potential / V vs SCE	Charge / C	FE% H$_2$
1$^-$	2-methyphenol	-1.7	**1.0362**	96%
Blank	2-methyphenol	-1.7	**3.2269**	**52%**
2$^+$	butanoic	-1.4	**4.4415**	97%
2$^+$	butanoic	-1.4	**9.2375**	99%
Blank	butanoic	-1.4	**5.1021**	**51%**

Cyclic voltammetry (CV) was performed on 0.1 M Bu$_4$NBF$_4$ MeCN solutions of 1 mM **1**$^-$ and **2**$^+$ to obtain electrochemical measurements. The CV of **2**$^+$ results in a quasi-reversible wave with a peak current ratio (j_{pc}/j_{pa}) of 1.9 and a peak-to-peak separation of 94 mV.

Because we observe that the peak current scales linearly with the square root of the scan rate we can assume a diffusion-controlled electron transfer (ET) at the electrode. Diffusion ordered spectroscopy nuclear magnetic resonance (DOSY NMR) experiments corroborate with the below calculation to determine that this diffusion-controlled ET had a diffusion coefficient (*D*) of 9.15 × 10^{-6} cm^2 s^{-1}.

Equation 125:
$$E_{1/2} = E^{0\prime} + \frac{0.78RT}{2F}\left(\frac{\alpha_c - \alpha_a}{\alpha_c \alpha_a}\right)$$

Equation 126:
$$j_P = 446.3nFC\left(\frac{nFD}{RT}\right)^{\frac{1}{2}} v^{1/2}$$

Using the above equations, (The Randles-Sevcik method) the diffusion coefficient was determined in MeCN. The Randles-Sevcik equation above describes the relationship between current and scan rate for a diffusion-based redox event. Here, j$_p$ is the peak current density (mA cm^{-2}), n is the number of electrons transferred, v is the scan rate (V/s), C is the concentration (mol cm^{-3}), and F, R, and T are Faraday's constant (C mol^{-1}), the ideal gas constant (J K^{-1} mol^{-1}), and temperature (K) respectively. Using the slope of the best fit line of j$_{pc}$ versus $v^{1/2}$ affords a diffusion coefficient for **2**$^+$.

The halfwave potential (E$_{½}$) for **2**$^+$ was determined to be -1.42 V vs SCE. There was some difficulty determining the E$_{½}$ for the **1**$^{1-/2-}$ couple because it shows a large apparent peak-to-peak separation, ΔE$_p$, between E$_{pa}$ and E$_{pc}$ (ca. 350 mV) making it non-Nernstian in nature. A non-

Nernstian waveform suggests that either **1**⁻ exhibits slow ET or a different electrochemical process which combines ET with a related chemical step in a single CV wave.[107]

To probe H_2 evolution with **1**⁻ and **2**⁺, monoprotic organic acids were used to carefully control reaction conditions such as $[H^+]$ and pK_a in MeCN solution. 2-methyphenol ($CH_3C_6H_4(OH)$) (pK_a = 27.5, $E^0_{HA/H2}$ = -1.26 V vs SCE) [108] was added to a solution of 1 mM of **1**⁻ resulting in the loss of the return wave peak that indicated the oxidation of **1**$^{2-.}$ There was also an increase in the peak current (j_{pc}) that scales linearly with $[H^+]$ (Figure 21). We can define the current at j_{pc} produced by between 2-methyphenol and the GC electrode as negligible when compared to the current produced when **1**⁻ is also present in solution (Figure 21). When controlled potential electrolysis (CPE) was performed at -1.7 V vs SCE with 0.5 mM **1**⁻ and 20 mM 2-methyphenol, H_2 evolution was confirmed in the form of measurable hydrogen gas content in the head space of the electrochemical cell with a 96% Faradaic efficiency (FE).

When a similar experiment was performed with a 1 mM solution of **2**⁺, the **2**$^{+/0}$ couple became irreversible when [2-methyphenol] = 1.5 – 8 mM. The resulting peak current height is nearly equal that of the **2**$^{+/0}$ couple and is independent of [2-methyphenol].
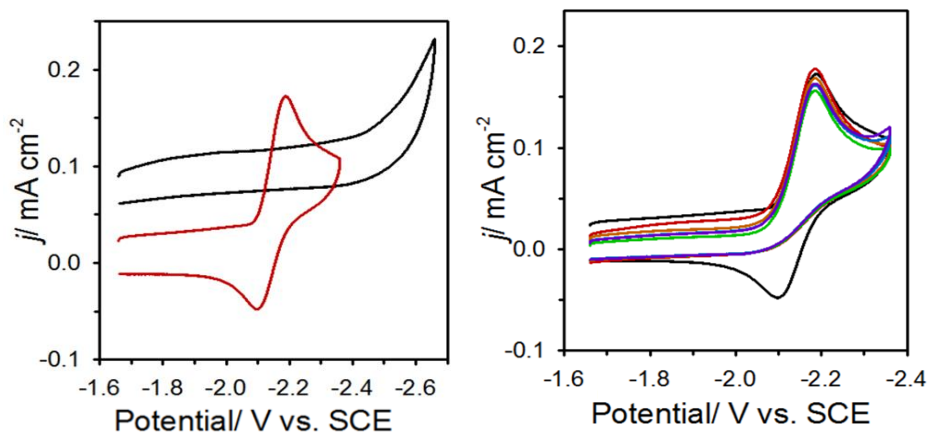
Figure 22: *CVs collected in 0.1 M Bu$_4$NBF$_4$ MeCN under N$_2$ at 100 mV s^{-1} with GC. (Left) 1 mM of 2$^+$ (red), and 8 mM 2-methyphenol (black). (Right) plot of peak current versus [2-methyphenol] from CVs collected in 1 mM of 2$^+$.*

Scheme 2: Two proposed HER mechanisms for 1$^-$, 2$^+$, A$^-$, B$^-$, C$^-$, D$^-$. Pink represents the start of the catalytic cycle. n is -1 or +1 based on the organometallic cluster. x = -1 or +1 depending on the organometallic cluster.
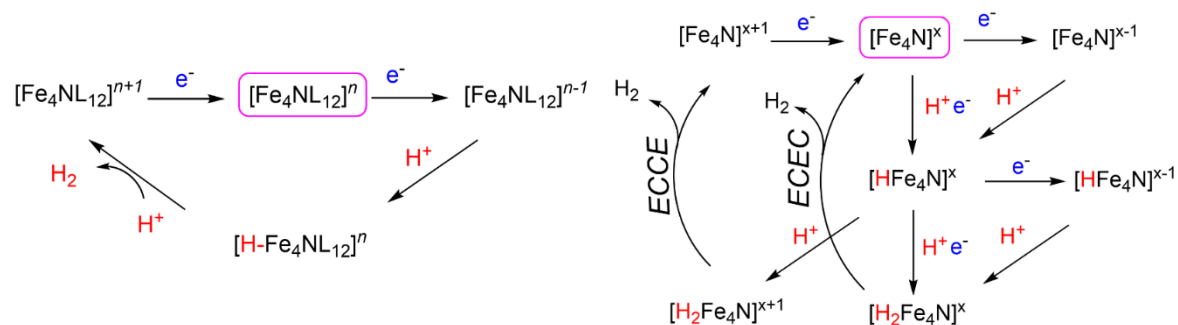
In consideration of the data achieved above, it is likely that the series of organometallic clusters studies (i.e., **1$^-$**, **2$^+$, B$^-$, C$^-$**, and **D$^-$**) achieve H$_2$ evolution via the proton coupled electron transfer initiated step shown in scheme 2. This reaction begins with the generation of a cluster hydride, and is followed by the subsequent ET and PT steps which can occur in any order as we are unable to

determine if the overall mechanism is EECC or ECEC (where the E step denotes an electrochemical and the C denotes a chemical step) as shown and discussed in 2020 paper from Wang and Johnson including scheme 2.[103]
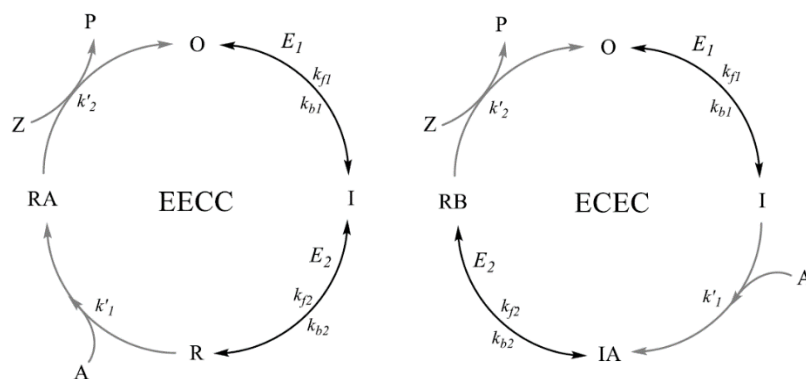
Scheme 3: Definition of the EECC and ECEC reaction cycle where E represents an electrical step and C represents a chemical step.[103]

In scheme 3 from Wang and Johnson et al, O represents an oxidized state; I represents a one-electron reduced state, and R, a two-electron reduced state. A and Z are two co-substrates involved with the chemical steps, while P is the product. RA refers to a two-electron reduced substrate-bound intermediate state. While in the ECEC mechanism, IA and RB refer to the one-electron and two-electron reduced substrate-bound intermediate states, respectively.[103]

The waveform shown in figure 22 suggests that this reaction must operate via an EC-type mechanism. The evidence shown indicates that the mechanism at work begins with ET to afford the intermediate **2** followed by a slow proton transfer (PT) which then yields $(H-2)^{+}$.[109]

To achieve the H_2 product observed in the CPE experiments, there must be a catalytic reaction which is not mediated by 2^+. By using *2*-methyphenol for both reactions, we can understand how the thermodynamic overpotential (η) helps us describe which mechanism is at work. The reason for the observed difference in reactivity between 2^+ and 1^- when reacted with *2*-methyphenol as the substrate is due to the difference in the thermodynamic driving force or overpotential for hydrogen evolution. When *2*-methyphenol is used as the substrate in a reaction with 1^- the overpotential (η) for the reaction is 320 mV while the same experiment with 2^+ yields an overpotential that is much lower at 160 mV according to reactions 2-4 below:

Reaction 6: $\textbf{HA} + \textbf{e}^- \rightleftharpoons \textbf{½ H}_2 + \textbf{A}^-$ $\textbf{\textit{E}}^0{}_{\textbf{HA/H2}}$

Reaction 7: $\textbf{Cat} + \textbf{e}^- \rightleftharpoons \textbf{Cat}^-$ $\textbf{\textit{E}}^{0\prime}$ ($\approx \textbf{\textit{E}}_{1/2}$ **for** 2^+ **and A**$^-$)

Reaction 8: $\textbf{HA} + \textbf{Cat}^- \rightleftharpoons \textbf{½ H}_2 + \textbf{Cat}$ $\eta = \textbf{\textit{E}}^0{}_{\textbf{HA/H2}} - \textbf{\textit{E}}^{0\prime}$
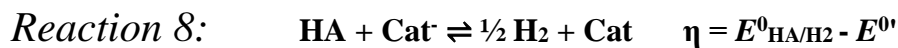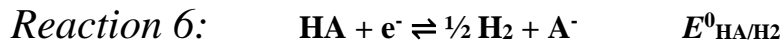
Here, HA/A$^-$ refers to an organic acid and its conjugate base and Cat/Cat$^-$ are the Fe-clusters in the oxidized and reduced forms. To achieve a more catalytic reaction with 2^+ we introduced a stronger acid. By using butanoic acid ($C_4H_8O_2$)(pK_a = 22.7, $E^0{}_{HA/H2}$ = -0.98 V vs SCE) which has η for hydrogen evolution of 440 mV[35] as the substrate in a reaction with 2^+ we were able to obtain CVs that show a catalytic current that scales linearly with $[H^+]$, and CPE experiments performed at -1.4 V vs SCE with 0.5 mM 2^+ and 20 mM butanoic acid confirm the evolution of H_2 with 98% FE.

In an attempt to probe the kinetic and mechanistic factors of reactions between 1^- or 2^+ and organic acids in MeCN, CV experiments were performed under catalytic conditions where substrate is incorporated in excess and therefore is not depleted during the CV scan so that a steady-state current, or S-shaped CV wave can be reached. By increasing acid content and scan rate, the S-

shaped curve could be reached. This CV trace shape represents a regime in which the kinetic parameter λ_e and the excess factor γ are tuned so that two assumptions become true:

1.) The kinetic parameter is large enough (large rate constant and/or small scan rate) for pure kinetic conditions to be met.

2.) The excess factor is large enough for the consumption of the substrate to be negligible.

Equation 127:
$$\lambda_e = \left(\frac{RT}{F}\right)\left(\frac{k_e C_P^0}{v}\right)$$

Equation 128:
$$\gamma = C_A^0/C_P^0$$

Where C^0_P and C^0_A are the bulk concentrations of the mediator and substrate, respectively and once in this regime, the rate constant k_e can be derived from measurement of the plateau current via this equation:

Equation 129:
$$i_p = FSC_P^0\sqrt{D}\sqrt{k_e C_A^0}$$

Once an S-shaped or plateau forward wave is achieved it can then be compared to the theoretical ideal plateau curve and from this comparison catalytic rate can be determined using the equations described below.[103,110]

Equation 130:
$$jc = nF[cat]D^{\frac{1}{2}} kobs^{\frac{1}{2}} \, x \, 10^3$$

Here, j_c is the plateau current density in units of mA cm^{-2}, [cat] is catalyst concentration in mol cm^{-3}, D is the diffusion coefficient for the catalyst in cm^2 s^{-1}, and kobs in units of s^{-1} is the observed rate that limits the current at the plateau. The rate determining constant k_{cat} in units of M^{-1} s^{-1} was determined according to the equation below.

$k_{obs} = [H+]k_{cat}$ where, [H+] is the concentration in units of M of organic acid in MeCN (i.e., butanoic acid or 2-methylphenol).

Equation 131
$$j = \frac{j_c}{1+e^{\frac{F}{RT}\left(E-E_{\frac{cat}{2}}\right)}}$$

Where, j is current density in mA cm^{-2}, j_c is current density in mA cm^{-2}, E is scanning potential in V vs SCE, $E_{cat/2}$ is the catalytic halfwave potential, and all other variables have been defined previously.

Since a steady-state regime is required to make the comparison to the ideal behavior, we performed linear sweep voltammograms (LSV's) at sufficiently large ratios of [substrate]/[catalyst] and higher scan rates until CV peak currents were observed to be scan rate independent. Figure 23 shows that as scan rate increases the current moves from being scan rate dependent at low scan rates to scan rate independent at the higher scan rates.[109] To ensure an accurate measure of j_c, each LSV plot was corrected for any capacitive current via linear background subtraction and compared to a model of the ideal s-shape/steady state conditions. Once the LSV plots were background corrected they were then normalized to $j = 0$ at potentials 300 mV more positive compared to the catalytic current at $E_{cat/2}$.
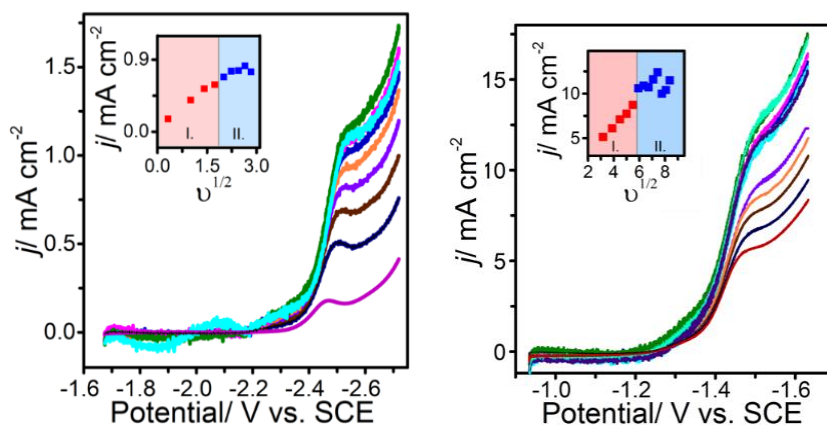
Figure 23: *Scan rate independent forward wave LSVs for **1**⁻ Na[Fe₄N(CO)₁₀(PTA)₂] (Left) and*

2⁺ *[Fe₄N(CO)₁₀(MePTA)₂] (Right). Inset shows the two distinct scan rate regimes the scan rate*

dependent regime (red) and the scan rate independent regime (blue)

Both clusters **1**⁻ and **2**⁺ appear to have limited current production at the plateau pointing to a rate

determining step (RDS) in the catalytic mechanism. The observed catalytic rate is related to the

bimolecular rate and the concentration of substrate by $k_{obs} = k_{cat}[H^+]$ where k_{cat} refers to the rate

limiting bimolecular rate constant in $M^{-1} s^{-1}$. The k_{cat} for **1**⁻ and **2**⁺ differ by one order of magnitude

and are $1.4 \times 10^3 M^{-1} s^{-1}$ and $1.1 \times 10^4 M^{-1} s^{-1}$, respectively. We can investigate more about the

mechanism for catalysis by inspecting the relationship between $E_{cat/2}$ (the potential read at half of

the limiting plateau current) and $E_{1/2}$ (defined above)[103]

For **2**⁺, $E_{cat/2} \approx E_{1/2}$ at -1.43 V and this is consistent with either an ECCE or ECEC mechanism

where ET is sufficiently fast as not to be influenced by the kinetics components of ET.[111] In

contrast, $E_{cat/2} = $ -1.72 V for **1**⁻ and this is 160 mV more negative than $E_{1/2}$ and 140 mV more

negative than $E^{0'}$: this suggests that sluggish ET associated with reduction of **1⁻** is driving $E_{cat/2}$ towards more cathodic potential as predicted by the non-Nernstian relationship between $E_{cat/2}$ and $E_{1/2}$. The plateau in the catalytic current in LSVs which was shown to be in a scan rate independent regime (figure 23) was used to determine the rate determining rate constant k_{cat}.

A common plot used to compare and contrast the performance of various catalysts is the Tafel-style plot.[14] This graphic representation relates the turnover frequency (TOF) and the overpotential (η) for H_2 evolution (Figure 24, left). The data used in this plot was determined using the k_{cat} and $E_{cat/2}$ extracted from the S-shaped LSV as well as the standard reduction potential for the catalytic reduction of Brønsted acid in MeCN. Based on the design of these Tafel-style plots, an ideal catalyst would appear in the upper-left in the low η, high TOF region. With this in mind, we can see that the Fe-clusters with a double substitution as is the case for **1⁻**, **2⁺**, and **C⁻** perform better than the parent cluster **A⁻** and the single-substituted Fe-clusters of **B⁻** and **D⁻.** The apparent improvement in the performance (TOF vs η) may be explained by the phosphine ligand's ability to inductively donate an electron into the metal-bonded framework of the cluster effectively changing the hydricity of the metal-cluster hydride. We can again observe this inductive effect in the performance of **B⁻** and **D⁻** as they fall in the low overpotential regime since **D⁻** contains the much less donating (p-F-Ph)₃ ligand. Another aspect to consider is the steric effect. For example, the clusters **1⁻**, **2⁺**, and **C⁻** have similar shape and size and appear to modulate the availability of catalytically active sites in these organometallic clusters as a function of cone angle, but more information about bond lengths and angles will be needed to complete this analysis. (Stated in the proposed work section).
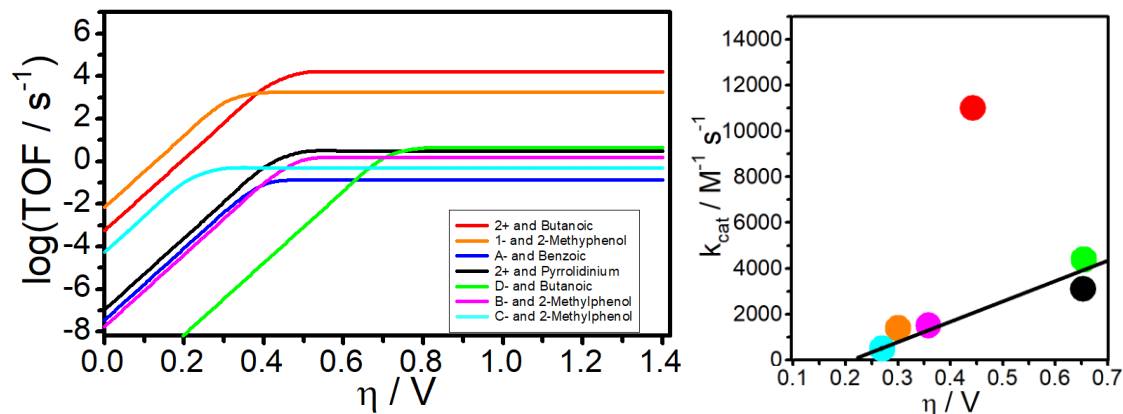
Figure 24: *(Left)Tafel-style analysis of **A⁻** with Benzoic acid (blue), **2⁺** with butanoic acid (red) 2+ with pyrrolidinium (black), **1⁻** (orange), **B⁻** (pink), and **C⁻**(cyan) with 2-methylphenol, and **D-** with butanoic (green). TOF calculated as $k_{cat}[H^+]$ where $[H^+] = 1$ mM. TOF-η for **A⁻** was determined from foot-of-the-wave analysis of CV data using the FOWA method described in literature.[103] (Right) Linear free energy plot of k_{cat} versus to ($E^0_{HA/H2} − E_{1/2}$) demonstrating the electrostatic effect in **2⁺** in relationship to **1⁻**, **B⁻**, **C⁻**, and **D⁻**.*

To reiterate the naming mechanism of the synthesized and tested clusters they are as follows: Na[Fe₄N(CO)₁₀(PTA)₂] (Na-**1**), [Fe₄N(CO)₁₀(MePTA)₂]I (**2-I**), [Fe₄N(CO)₁₂]⁻ (**A-**), [Fe₄N(CO)₁₁(PPh₃)]⁻ (**B-**), [Fe₄N(CO)₁₁(PEt₃)]⁻ (**C-**), and [Fe₄N(CO)₁₁(P(4-F-ph)₃)]⁻ (**D-**) (PTA = 1,3,5-triaza-7-phosphadamantane, MePTA₊ = N-methyl-1,3,5-triaza-7-phosphadamantanium

The mechanism responsible for the observed enhancement in the TOF of the **2⁺** cluster is likely that the MePTA ligand stabilizes the transition state during proton transfer. **2⁺** interacts with the negative charge that builds up on the carboxylate (**A⁻**) during proton transfer. This data supports the potential dual function of the positive charges in the SCS:

(1) By lowering over potential via inductively shifting the redox potentials.

(2) By enhancing rate via stabilizing charge-separated intermediates.

To assess the latter point, pyrrolidinium ($C_4H_{10}N$) (pKa = 19.24 in MeCN) was used as it does not have a negatively charged conjugate base ($H_2A^+ \square\square HA + H^+$). When this substrate was incorporated, a lower TOF was achieved which begins to deconvolute the thermodynamic and kinetic effects from having positive charges in the SCS.

One very interesting finding is that the TOF- η relationship is drastically affected by the proton source. When the negatively charged acid, butanoic acid was used as the conjugate base, 2^+ performed better than all other clusters tested. This is likely due to the stabilization of charge-separated intermediates during the reaction's transition state (Scheme 3). Stabilization of this kind had been commonly observed in CO_2RR in examples which Lewis acids are introduced as cocatalysts[15] or the SCS is functionalized with a positive charge[14] in order to improve TOF. Based on these examples from literature, the improved performance of 2^+ is likely the response of negative charge buildup on the carboxylate during the rate determining proton transfer step being stabilized by the MePTA$^+$ ligand**.** Therefore, we can claim that if the improvement in performance were due to an electrostatic interaction between the MePTA$^+$ and the butanoic acid then if the protons were from a neutrally charged Brønsted acid such as pyrrolidinium used as the substrate then this electrostatic effect would be quenched. This is observed when the catalyst 2^+ is used in the presence of pyrrolidinium it only performed slightly better than 1^- and B^- and much worse than it did with butanoic acid as the substrate. (Figure 24 left). We can observe in consideration of this series of organometallic clusters that the linear free energy relationship between k_{cat} and ($E^0_{HA/H2}$

– $E_{1/2}$) has no electrostatic contribution from the ligands in the SCS (Figure 24, right). This observation supports that this series of catalysts exhibits a breaking of the scaling relationship achieved by 2^+ via a leveraging of the electrostatic effect.
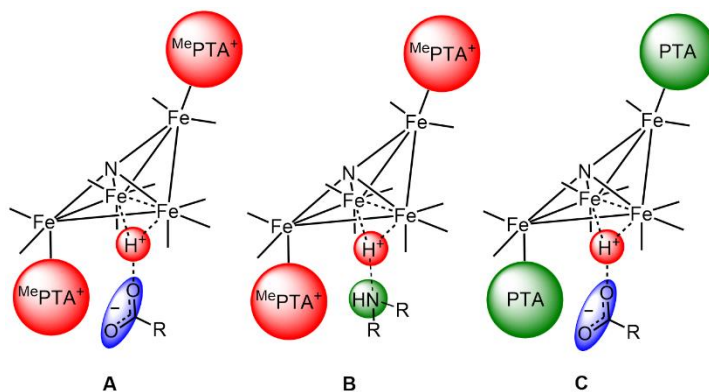
Scheme 3. (A) Stabilization of charge-separated intermediates in the transition state structures of 2^+, (B) No stabilization of the intermediates in the transition state structures of 2^+. (C) No stabilization of charge transition state structures of 1^-. Red denotes positive charge, blue denotes negative charge, and green denotes neutral charge. Red and blue combination in proxy is electrostatically stabilized.

3.7.0   Conclusions:

Until these preliminary findings, it was unclear how the addition of positively charged SCS ligands improve catalysis. In a number of previous studies, it was debated if these ligands favorably change the thermodynamics or kinetics of the reaction or both. By employing the series of substitutions on $[Fe_4N(CO)_{12}]^-$ discussed in these preliminary results, a series of clusters with modified SCS environments were synthesized and electrochemically studied for HER. Our careful control of the chemical structure and pKa of the substrates as a proton source we were able to begin to deconvolute the kinetic from the thermodynamic components of these reactions regarding

electrocatalytic rates. The data achieved thus far supports a 3-fold action of the positive charges in the SCS:

(1) They lower the thermodynamic redox potential of the catalyst.

(2) Via inductive effects, they preserve the inner sphere electronics of the metal(s) in the structure of the catalyst.

(3) They enhance the rate of the catalysis by stabilizing charge-separated intermediates.

The third function elucidated by these preliminary findings is the function that most directly "breaks" the linear free energy relationship *i.e.,* the scaling relationship and leads to such dramatic catalytic performance and rate improvement.

Considering the data described above, it is likely that this series of organometallic clusters (*i.e.,* 1^-, 2^+, B^-, C^-, and D^-) are catalysts for H_2 evolution via a mechanism initiated by PCET step (Scheme 2). Following the generation of cluster hydride, the subsequent ET and PT steps could occur one or the other first and we cannot determine whether the overall mechanism is *ECCE* or *ECEC*. To further probe the kinetic and mechanistic details of reactions between 1^- or 2^+ and organic acids in MeCN, we performed CV experiments under catalytic conditions where excess substrate is included and is therefore not depleted during the CV scan so that a steady-state current, or S-shaped CV wave, is reached and from which the catalytic rate can be determined.[106, 112] To reach the steady-state regime, we performed linear sweep voltammograms (LSV's) at sufficiently large ratios of [substrate]/[catalyst] and high scan rate until LSV's with scan rate independent current were observed.[113] The LSVs were corrected for capacitive current by linear background

subtraction and simulations were performed using the conical function for the S-shaped electrocatalytic response to fit the electrocatalytic waves (Figure 21d-f)[114]

For both 1^- and 2^+, the current produced at the plateau is limited by the rate determining step (RDS) in the catalytic mechanism such that $k_{obs} = k_{cat}[H^+]$ where k_{cat} is the rate limiting bimolecular rate constant in $M^{-1} s^{-1}$. The k_{cat} for 1^- and 2^+ differ by 1 order of magnitude and are $1.4 \times 10^3 M^{-1} s^{-1}$ and $1.1 \times 10^4 M^{-1} s^{-1}$, respectively. More can be learned about the catalytic mechanism from the relationships between the catalytic halfwave potential or $E_{cat/2}$ (the potential read at half of the limiting plateau current) and $E_{1/2}$. For 1^-, $E_{cat/2} = $ -1.72 V and this is 160 mV more negative than $E_{1/2}$ and 140 mV more negative than $E^{0'}$: this ET associated with reduction of 1^- is driving $E_{cat/2}$ towards more cathodic potential as predicted by the non-Nernstian relationship between $E_{cat/2}$, $E_{1/2}$, α, and k_s. In the case of 2^+, $E_{cat/2}$ is -1.43 V ($\approx$10 mV more negative than $E_{1/2}$), and this difference does not elicit conclusive evidence regarding a kinetic influence of ET. Although not conclusive, this observation of 2^+ is conducive to a Nernstian-type *ECCE* or *ECEC* mechanisms which has an $E_{cat/2}$ equal (or at more positive potentials) to $E_{1/2}$ where a ±3 mV of accuracy is expected in carefully calibrated experiments.

The catalytic Tafel plot relating the turnover frequency (TOF) and the overpotential (η) for H_2 evolution can be used to benchmark the performance of these organometallic clusters (Figure 24, left). These plots were constructed using the k_{cat} and $E_{cat/2}$ extracted from the S-shaped LSV and the standard reduction potential for the catalytic reduction of Brønsted acid in MeCN as detailed previously. An ideal catalyst would have a low η and high TOF, which would fall on the upper-left-hand side of a catalytic Tafel plot. In this regard, the twice substituted Fe-clusters of 1^-, 2^+,

and **C⁻** outperform the Fe-parent cluster **A⁻** and the once substituted Fe-clusters of **B⁻** and **D⁻**. This may suggest enhancement in TOF-η because of the inductive electron donation of phosphine ligands into the metal-bonded framework, and the influence on hydricity of the metal-cluster-hydride. The inductive effect is again observed in the low overpotential regime for **B⁻** and **D⁻** where **D⁻** contains the less donating (*p*-F-ph)₃ ligand. The steric effect would certainly play a role in the TOF-η relationship and in our study **1⁻**, **2⁺**, and **C⁻** appear to demonstrate this point as a function of cone angle. More data around this would be required to conclude the effect steric affect, however, when these competing phenomena are taken together it is inductive effect which plays a more dominating role in determining TOF-η.

Interestingly, the TOF-η of **2⁺** is drastically swayed by the proton source. For example, experiments performed with butanoic acid whose conjugate base is negatively charged (*i.e.,* butanoate), **2⁺** is the best performer. It is likely that the enhancement TOF-η is the result of stabilization of charge-separated intermediates in the transition state (Scheme 3). This phenomenon is traditionally observed in CO_2RR electrocatalysts whereby the enhancement in TOF is leveraged by introducing Lewis acids as cocatalysts or by functionalizing the secondary coordination sphere with positive charge. In the case of **2⁺**, the buildup of negative charge on the carboxylate during the rate determining PT step is stabilized by $^{Me}PTA^+$. It follows that if an electrostatic interaction between $^{Me}PTA^+$ and butanoate were occurring then this effect would be quenched by introducing protons from a Brønsted acid whose conjugate base does not have charge. Indeed, TOF-η of **2⁺** with pyrrolidinium demonstrates a catalytic performance which is only slightly better compared to **1⁻** and **B⁻** (Figure 24 left). As a result, the linear free energy relationship between k_{cat} and ($E^0_{HA/H2} - E_{1/2}$) is observed in this series of organometallic clusters that have no

electrostatic contribution from the ligands in the secondary coordination sphere (Figure 24, right). The assessment performed concludes that the linear free energy relationship across this series catalyst also demonstrates a breaking of the scaling relationship for **2**⁺ by virtue of the electrostatic effect.

3.8.0   *Proposed Future Work:*

Specific Aim 1- Catalysts for HER: Much of this dissertation has been done towards the goal of testing six organometallic catalysts, but only very initial testing has been performed on the 3 phosphine substituted clusters denoted as **B⁻, C⁻,** and **D⁻** in chart 1. The next step toward finishing this aim is to continue to synthesize enough of these catalysts for use in cyclic voltammetry (CV) experiments with a variety of substrate (acids) with a range of pKa values to determine the optimal substrate for each catalyst for improved performance and enhanced reaction rate. Next these clusters will all also need to be evaluated using pyrrolidinium as a neutral acid substrate as a method of defining the SCS's ability to stabilize charge-separated intermediates via ion-pairing. Constant potential electrolysis (CPE) will be required to elucidate the TOF and Faradaic efficiency of the electrochemical environment at producing hydrogen gas as the major product of the catalytic reaction. Infrared spectroelectrochemistry (IR-SEC) to support the reversibility of the redox reaction will require more trials. These experiments are necessary to accurately interpret the origin of non-Nernstian behavior in the CV wave for **1⁻** (chart 1), as they can be used as a probe for changes in the distinct vibrational frequencies of these catalysts. IR-SEC probes the chemical reversibility of the electron transfer event over time scales longer than that of CV.[10] IR-SEC should also provide information about if there is strong metal to ligand back bonding into the π* orbitals of the CO ligands. If **1⁻** is non-Nernstian because of a hypothesized

slow ET rate and asymmetric barrier for ET, then IR-SEC would elucidate that [109,115] Combining IR-SEC analysis with x-ray crystallography can be integral in uncovering the bond lengths and cone angles of the synthesized catalysts and subsequently how large a role the steric effect of these SCS ligands plan in the TOF-η relationship for the catalysts which defines their performance and efficiency. This data is necessary to uncover if the improved catalytic performance of these substituted clusters is dependent on the cone angle and therefore the availability of the catalytically active sites on these organometallic clusters. Figure 25 below depicts the results of two of the clusters composed of the iron inner coordination sphere and a commercially available ligand. (**C-** and **B-** in chart 1) This figure shows the very preliminary results of these clusters with *2*-methyphenol acid. This experiment was only performed once and, in the future, would require repeat experiments and with the full gamut of acids described above.

PPh3 and O-Cresol (*2*-methyphenol): **PEt3 and O-Cresol (*2*-methyphenol):**
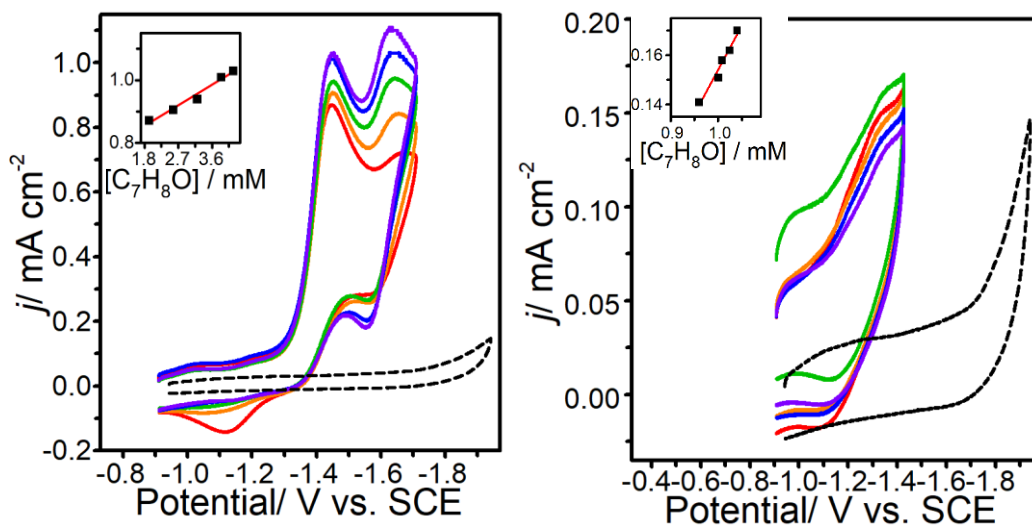
Figure 25: *CVs and LSVs collected in 0.1 M Bu₄NBF₄ MeCN under N₂ with GC. Left- 0.3 mM of*

B⁻ with 0.66 – 3.2 mM 2-methyphenol at 0.1 V s⁻¹ (color) and 2-methyphenol acid blank (dotted).

Left- 0.3 mM of C⁻ with 0.66 – 3.2 mM 2-methyphenol at 0.1 V s⁻¹ (color) and 2-methyphenol acid

blank (dotted)

Specific Aim 2 - Catalysts for CO₂RR: The long-term goal of the foreseeable research is to

enhance the rate of formate production relative to HER. This involves exploring ways to tune the

catalyst's selectivity for CO₂RR instead of HER.[109,116] This may involve further tuning of the

molecular design of the catalyst by synthesizing and testing different phosphine ligands on the

Fe-organometallic cluster or it may be more focused on tuning the parameters of the

electrochemical set up such as the working potential, the atmosphere composition and pressure,

the solvent, or the substrate employed in the system. Both possibilities should be probed for

improved CO₂RR selectivity. Beyond optimizing selectivity, the efficiency of formate

production will also need to be defined for each catalyst/environment combination therefore

similar CV, constant potential electrolysis (CPE), nuclear magnetic resonance (NMR), and IR-SEC will need to be employed as in the HER aim discussed above. The desired deliverable of *Aim 2* is to identify which factors of the molecular structure and environment affect the rate and selectivity of the catalysts to produce formate. In the same way the preliminary results point to three discrete actions that the SCS charge perform to improve HER efficiency, I hope to uncover the same definition for the CO_2RR selectivity and rate increase by determining variables such as the half wave potential ($E_{1/2}$), plateau current density (j_c) the diffusion coefficient (D) , observed reaction rate (k_{obs}), Faradaic efficiency (FE), turn over frequency (TOF), and overpotential. With variables such as these, I will be able to catalog a series of clusters in terms of their formate production performance and report on the mechanisms involved in this behavior.

Specific **Aim 3- Bio-Electrochemical Hybrid System: (Collaboration with Atsumi Lab)**

$Fe_4N(CO)_{12}$ has been identified as a reliable and efficient CO_2RR catalyst and should be uses it in series of long duration CPE experiments where the Fe-cluster will be in solution with water under a CO_2 atmosphere to selectively produce formate from the CO_2 of the atmosphere. Also, in the electrochemical cell setup, a type of modified E. coli bacteria can be employed. This work has been done in the Atsumi lab.[117,118] This bacterium has been altered to require formate and CO_2 (in addition to the default carbon source, glucose) for growth via essential amino acids (glycine and serine) production in minimal media.

Because E coli cannot naturally use formate, two pathways needed to be altered beforehand. A plasmid was employed to overexpress exogenous genes that enable E coli to use formate via the formate assimilation pathway to make methylene THF which is an intermediate on the way to

the essential amino acids. Then, through overexpression and reversal (towards glycine instead of away from glycine) of the second pathway, the glycine cleavage system (GCS) on a plasmid system, this E coli can use CO_2 to a great enough extent to achieve growth. By using these two pathways (the reverse GCS and the formate assimilation pathway) CO_2 is combined with the methylene THF produced by formate to produce glycine, glycine is then combined with another equivalent of the methylene THF from formate to produce serine and then serine can produce pyruvate which is known as the central metabolite due to its ability to be converted into a wide variety of useful products.

Continuing from my collaboration with the Atsumi lab, future work would be to demonstrate that this E coli is able to grow in a minimal media environment with formate, CO_2, and glucose which in turn means that the bacteria is efficiently assimilating CO_2 and formate into its central metabolism (i.e., pyruvate). Once this has been successfully achieved, several pathways can be engineered downstream towards the production of desired products. One proposed method is to direct metabolism towards a previously demonstrated product such as isobutanol.[118] If E coli can be successfully proven to primarily use formate and CO_2 as its main carbon sources, then it represents an exciting mechanism for renewable biological production using the C1 carbon sources that have previously been restricted to slow-growing photoautotrophic organisms. By using an organometallic catalyst in a constant potential electrolysis (CPE) cell setup to convert CO_2 to formate, we are cutting down from two carbon feedstocks to one and also providing an environment for the genetically modified E coli to grow by capturing the formate produced during electrolysis and producing a useful biproduct such as isobutanol or pyruvate.[117,118] If this work were to be continued a lab would want to create a closed system which has water,

electricity, CO_2, E.coli, and catalyst as the inputs and a useful fuel such as isobutanol or pyruvate as the sole product.
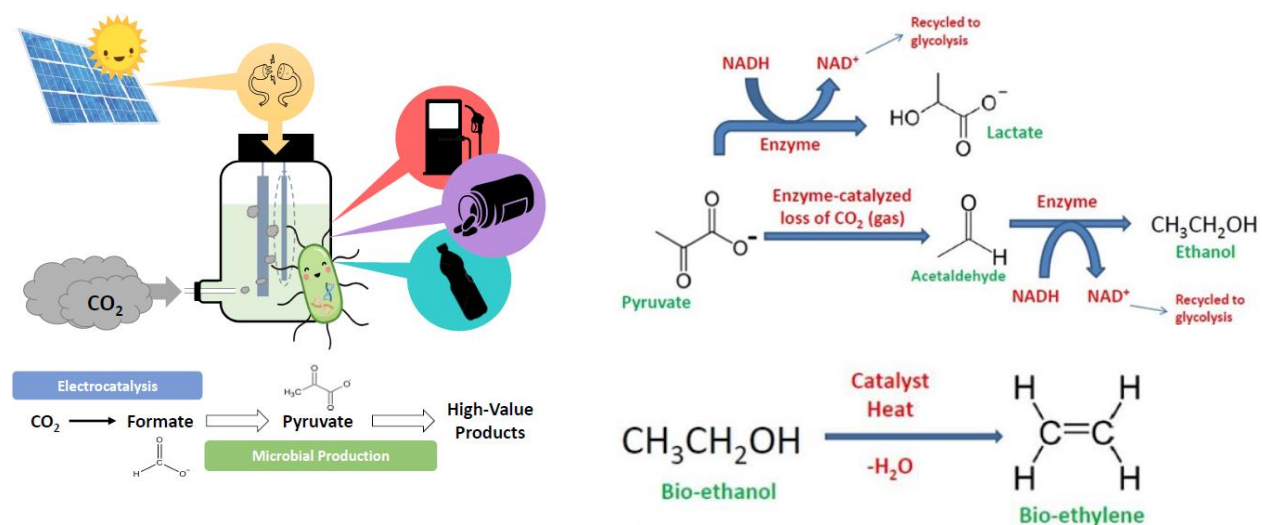

Figure 26: *A schematic showing the possible application of e. coli and carbon dioxide and formate to produce pyruvate which can then be transformed to bioethanol and even bio-ethylene via the chemical pathway shown on the right-hand side.*[117,118]

4. Electrodeposition of Absorber Layers

4.1.0 Introduction:

While the progress made in catalysing the production of alternative fuels is extremely important in the quest for a cleaner energy source and environment, this dissertation also focuses on the solar cell/PV approach to solving these problems. As mentioned in the initial introduction, some materials studied for this purpose include CdTe, $Cu(In,Ga)Se_2$ (CIGS), $Cu_2(Zn,Sn)S_4$ (CZTS), and recently Sb_2Se_3. The goal of the PV industry today is to employ light weight, non-toxic, durable, high efficiency, abundant, and inexpensive materials, and synthesis processes. One method that has been explored to achieve these goals is to synthesize the PV layer as a thin film via

electrochemical deposition to achieve a much lower-cost process compared to the chemical vapor deposition (CVD), physical vapor deposition (PVD), and close space sublimation (CSS) which was the process responsible for the Sb_2Se_3 absorber layer with the highest efficiency recorded. The hope of this study is to prove that using a reusable (to an extent) electrochemical bath for the deposition of these layers can be competitive with other Sb_2Se_3 films produced by more expensive means. If successful, the synthesized films should be light weight and display competitive efficiency, lower defect populations, and a dense conformal film.

PV cells require a layered architecture to convert solar photon energy into usable electricity. Common builds can have many layers such as a window layer, absorber layer, back mirror layer, back surface field, contact layers, and in some cases, an anti-reflection coating layer.[119] The functionality of a PV device depends on an n-type (electron-rich) and a p-type (electron poor/hole rich) layer. The electrons move from n-type to p-type creating a depletion zone in-between. As the electrons move across this zone, the former p-type layer becomes negatively charged while the n-type side of the depletion zone now contains positively charged ions. The interaction of these oppositely charged ions (seen in figure 27) creates an internal electric field which prevents further motion of electrons and holes. Incoming solar photons then strike the, now electron rich, p-type side of the depletion zone (also known as the absorber layer), ejecting electrons, and leaving holes. This causes the electric field which then moves electrons to the n-side and holes to the p-side which can easily occur through a metallic contact creating the flow of electricity to be harvested.[119,120]
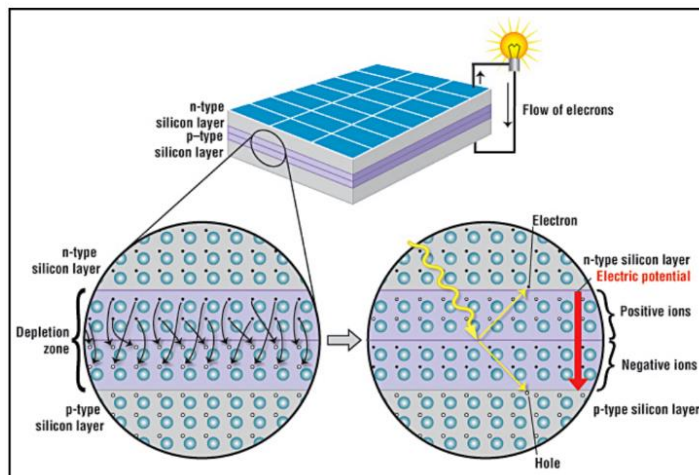
Figure 27: *Schematic representation of a solar cell, illustrating the n-type and p-type layers, with an expanded view of the depletion zone at the junction between the n-type and p-type layers.*[120]

To better understand the target composition (Sb_2Se_3) it helps to understand the precursor metals. In the study performed for this work, the following precursors were used in the electrochemical bath setup: SeO_2 and $K(SbO)C_4H_4O_6$, but to understand the structure of Sb_2Se_3 it is of interest to compare the structures of both antimony and selenium metal and observe how they, in essence, fit together to produce the Sb_2Se_3 structure. Figure 28 below shows how similar the three crystal structures are. Even though selenium metal is a hexagonal structure and antimony takes a rhombohedral structure, it is visibly evident how these two structures together can produce the orthorhombic structure of antimony selenide.[121-125]
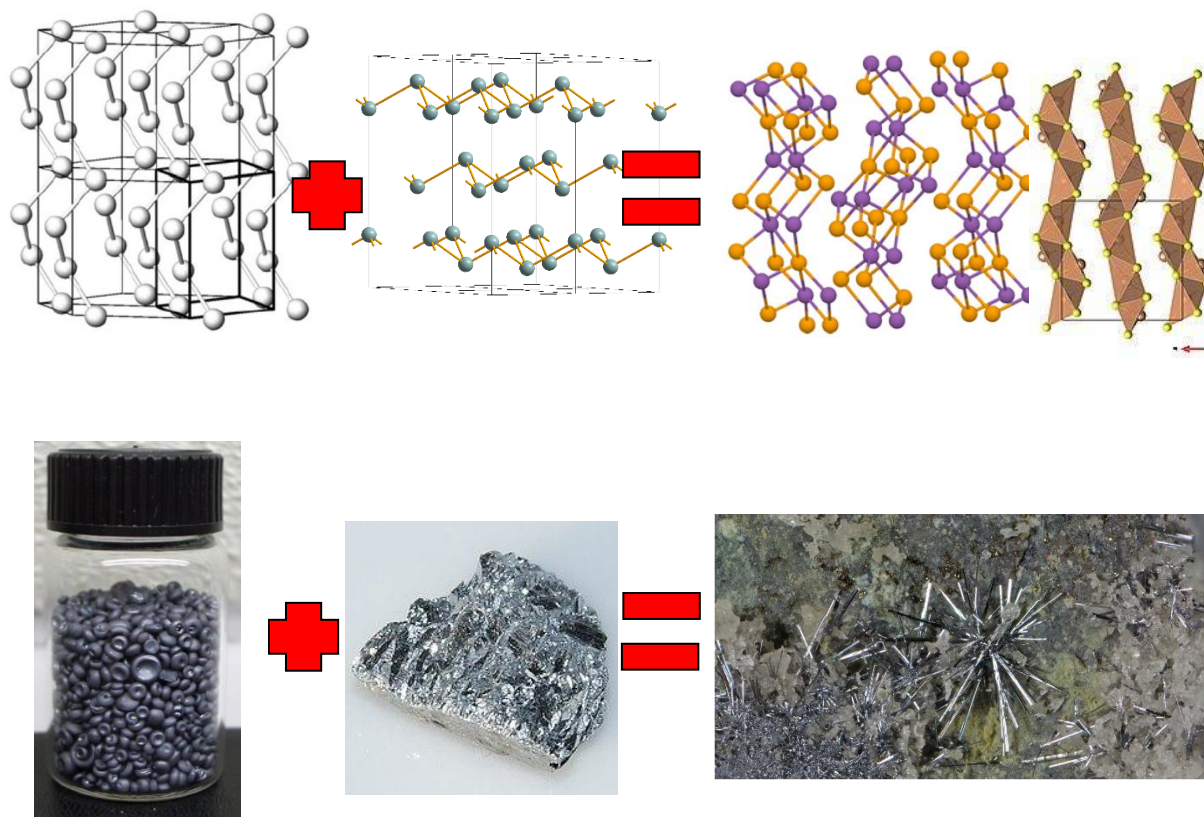
Figure 28: *Top from left to right – hexagonal crystal structure of selenium metal, the rhombohedral crystal structure for antimony metal, and two different visualizations of the orthorhombic antimony selenide crystal structure. Bottom from left to right – selenium, antimony, and Sb_2Se_3 metals as they can be found either commercially or in nature.*[121-125]

It is also important to understand how Sb_2Se_3 is structured from an atomic level. Sb_2Se_3 is a Stibnite structured that crystallized into an orthorhombic Pnma space group where two Sb_2Se_3 sheets in the $(0,0,1)$ direction match with two inequivalent Sb^{3+} sites. The Sb^{3+} is bonded to 5 Se^{2-} atoms to form $SbSe_5$ square pyramids (see figure 28 top right). The pyramids share corners with two equivalent $SbSe_6$ octahedra, edges with three equivalent $SbSe_6$ octahedra, and other edges with four equivalent $SbSe_5$ square pyramids. The corner-sharing octahedral occurs at a tilt angle of $5°$. There

is a range of Sb–Se bond distances in this structure ranging from 2.62–3.04 Å. The second Sb^{3+} site is bonded to six Se^{2-} atoms to form distorted $SbSe_6$ octahedra that share corners with two equivalent $SbSe_5$ square pyramids, edges with four equivalent $SbSe_6$ octahedra, and the remaining edges with three equivalent $SbSe_5$ square pyramids. As far as the Sb-Se bond distances, there is also a range this time from 2.71–3.25 Å. These relations show that three inequivalent Se^{2-} sites are present. In the first Se^{2-} site, Se^{2-} is bonded to 5 Sb^{3+} atoms to form distorted edge-sharing $SeSb_5$ square pyramids. In the second Se^{2-} site, Se^{2-} is bonded in a 3-coordinate geometry to three Sb^{3+} atoms. In the third Se^{2-} site, Se^{2-} is bonded in a 3-coordinate geometry to three equivalent Sb^{3+} atoms.[124,125]

The paragraph above very briefly describes the mechanism responsible for the function of a solar cell, but to take a deeper dive into how these PV devices function, it is imperative to discuss bandgaps. Fundamentally an energy band gap simply refers to the minimum energy the outermost electrons require to jump from the parent atom's orbital which leaves a hole. The electrons that are excited by this minimum energy or greater can then take part in the conduction of electricity for a wide variety of semiconductor devices including solar cells. The band gap distance for a semiconductor is in between the non-existent gap of conductors and the very wide bandgap of insulators. The most common solar cells on the market today are silicon which has a well-known band gap of 1.11 eV (electron-volts)[126]. To have a band gap this size means that the photons which strike the silicon absorber layer must have an energy greater than 1.11 eV to exceed the energy barrier required to knock an electron off of the silicon atom to become conductive electricity. In comparison, a CdTe absorber layer which is currently a research priority for many universities has a band gap of 1.44 eV which means they require even more energetic photons to produce

harvestable energy. In a later section of this dissertation, I discuss methods for determining a bandgap length and what the experimental and theoretical band gaps for Sb_2Se_3 are. Spoiler alert: it's better than CdTe.

Overpowering/overheating a solar cell can cause stability issues, solutions for which are being fiercely studied by every producer of solar cells whether they be organic, dye sensitized, perovskites etc. If the photon energy is much more that that needed to create an electron–hole pair then the excess energy is released as heat and since solar cells are already meant to sit in direct sunlight, extra heat is not helpful for increased efficiency. An increase in temperature results in higher kinetic energy for the electrons so they require less energy to break away from their parent atom, however this is not as optimistic as it sounds as the energy converted is only what corresponds to the energy of the bandgap and all excess photon energy ends up wasted as heat within the solar cell. It is estimated that a common silicon solar panel will lose about 1.1% of power output efficiency for every one-degree increase.[126] The exact solar spectrum energy at which solar cells operate can be calculated using the Shockley-Queisser equation. The Shockley-Queisser limit is also referred to as the radiative efficiency limit, or the Shockley Queisser efficiency limit and is defined as the maximum theoretical efficiency a solar cell can achieve using only a single p-n junction to collect power from the cell where the only loss mechanism accounted for is radiative recombination in the solar cell. To reiterate the use of this efficiency limit, one can consider that a material with a bandgap of 1.1 eV should have a SQ efficiency of 30%.[126a]

Originating from astrophysical measurements of a perfect 6000K black-body spectrum and then refined to use the more accurate global solar spectra, this limit is considered one of the most

fundamental values to characterize PV performance. Once solar cell technology evolved to include a back surface mirror the limit was adjusted to a maximum solar conversion efficiency to 33.16% for a single-junction solar cell with a bandgap of 1.34 eV.[126b] This means that of the 1000 W/m^2 the sun shines onto the solar cell, only 33.7% is capable of being converted into electricity.(~ 337 W/m^2). While the best commercially available QS limit is 32%, an energy conversion efficiency *that* high is practically unheard of, mostly due to losses such as reflection off the front of the cell, light blockage from the thin wires on the cell surface, and light scattering off grain boundaries, defects, and other inhomogeneities. The highest conceivable efficiencies would be for a theoretical multi-junction solar cell with an infinite number of layers, the corresponding limit would be 68.7% for normal sunlight or 86.8% using concentrated sunlight [126c,d]

Regardless of the deposition/growth method of the absorber layer, one factor that has been proven to play a major role in the device performance is layer thickness. Mascaro et al., via performing a wide variety of electrodeposition experiments with a range of independent parameters found that film thickness is a variable that can be tuned for better performance. When films are on the thin side, especially if it is thinner that the range of electron absorption depths, their series resistance and defect count may be low which leads to favorable charge collection but will lose photocurrent and therefore energy via excessive light transmission. However, when the film becomes too thick, series resistance, bulk defects, and carrier recombination increases, and the charge collection efficiency decreases along with overall performance and efficiency.[127] The task of electrochemical deposition then becomes to deposit an absorber layer that is thick enough to absorb the photons as the correct excitation depth, but not so thick as to cause high defect count and series resistance. The film must also me thick enough to detect with the x-ray collisions of XRD (X-Ray Diffraction)

analysis that is, not so thin that the x-ray beam overshoots and goes through without any interaction with the film.
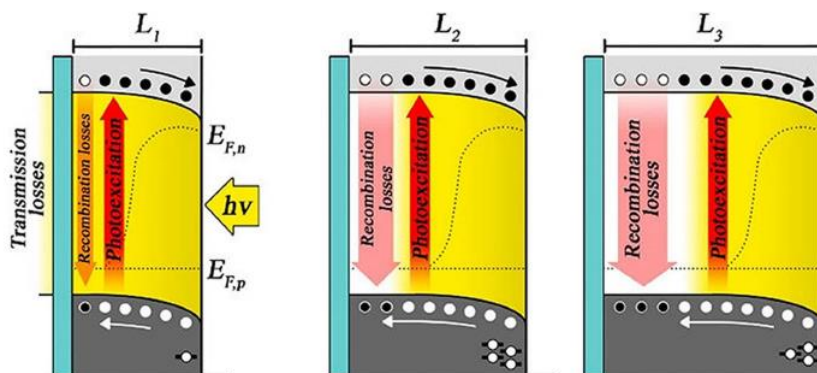

Figure 29*: Schematic diagram of the films thickness (where L3>L2>L1). This schematic depicts how thickness effects the transmission and recombination losses, and charge accumulation. "hv" represents the incident light, $E_{F,n}$ and $E_{F,p}$ refer to the quasi-Fermi level for photogenerated electrons (black full circles) and holes (white empty circles), respectively.*[127]

As with the alternative fuel project discussed in the first half of this dissertation, a 3-electrode system is used in this research as well. However, instead of using the potential to reduce and oxidize the components of the bath to produce target products such as hydrogen gas or liquid formate, the electrochemistry is providing a potential to plate contents of the bath onto the solid substrate surface. A schematic of this process and photographs from the lab bench are shown in figure 30 below. The reference electrode (Ag/AgCl) and the counter electrode (platinum) are of the same type as in the catalysis experiments the difference is that in the redox catalysis the working electrode was a piece of polished glassy carbon, but in the absorber layer deposition, the working electrode is a piece of fluorine-doped tin oxide (FTO) coated soda-lime glass. FTO is a very common material used in many photoelectric applications due to its ability to transmit incoming light. It has low surface resistivity, scratch and abrasion resistance, high optical

transmittance, thermal stability up to high temperatures, and is inert to a wide range of chemicals.[128,129]

Electrochemical deposition is a phenomenon during which a metallic ion can become a solid metal and deposit on the cathode surface if enough electric current passes through the electrolyte solution. In addition to the aforementioned precursors, sodium sulphate (Na_2SO_4) was used as the acidic metallic salt solution electrolyte which form by dissolving a metallic salt in water. This process results in a deposited film because the available ions in the bath, due to replenishment process, are going to deposit at the negatively charged cathode or in this case the FTO. In general, electrochemical deposition utilizes two electrochemical baths while in our case the three electrodes share one bath with the reference electrode vessel containing a silver chloride solution. Historically, grain size and general morphology has been controlled to mere nanometres by tuning the bath composition, pH, temperature, and current density. Diverse nanostructures such as nanorods, nanowires, nanotubes, nanosheets, dendritic nanostructures, and composite nanostructures all have been fabricated by electrochemical synthesis.[130,131]
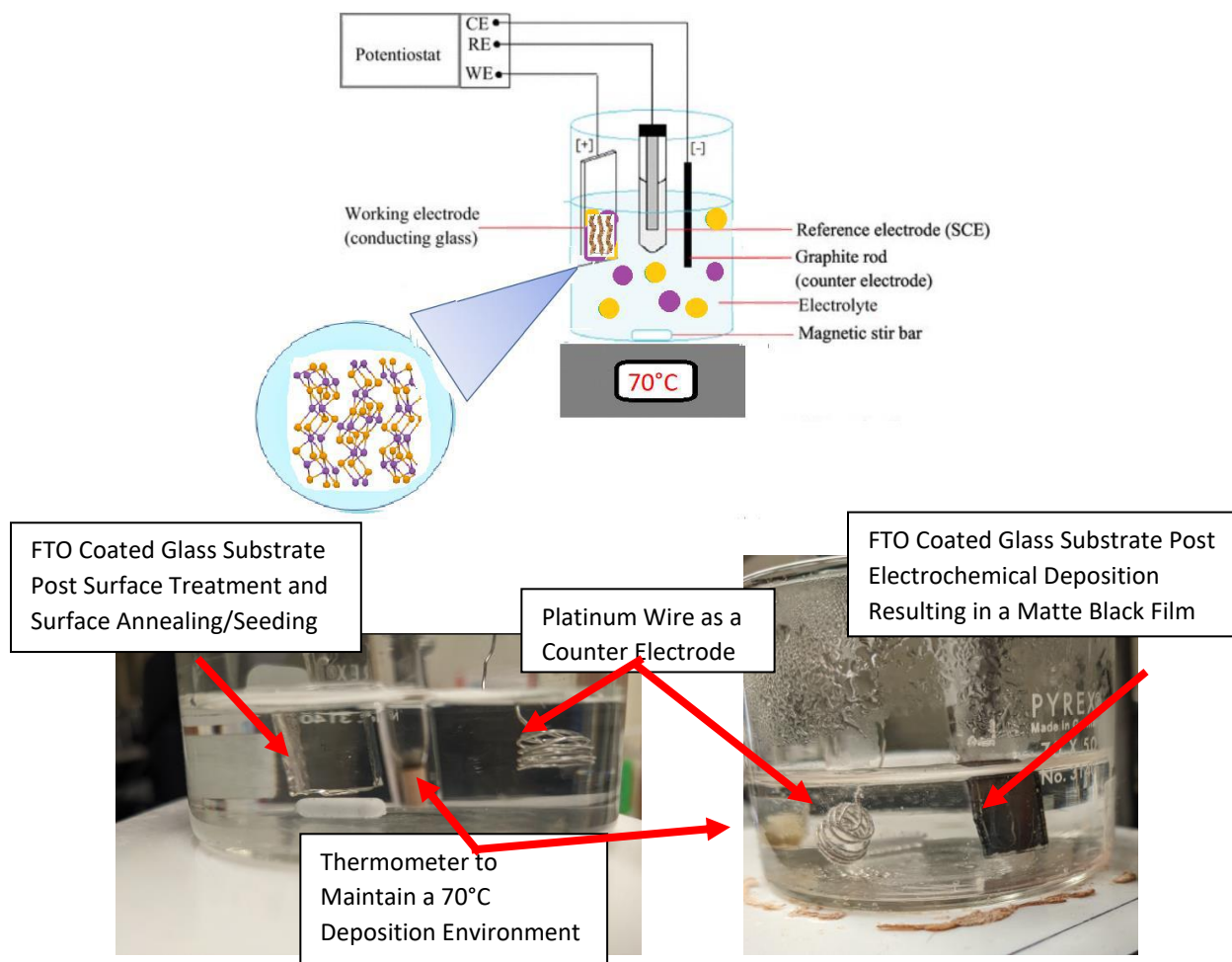
Figure 30: *Top – Schematic of a three-electrode setup for electrochemical deposition of Sb₂Se₃.*

The hot plate shown below the beaker is showing 70°C which is the temperature used during many

of the depositions performed in this dissertation. The film shown on the FTO working electrode is

the crystal structure of the target material (Sb₂Se₃). The magnified circle is a larger image of the

Sb₂Se₃ crystal structure.[132] *Bottom Right– photograph of the system before potential is applied.*

Bottom Left - Photograph of the system after potential has been applied. The dark film has

appeared on the FTO side of the glass substrate.

As seen in the photo, after the potential have been applied, only one side of the glass substrate accumulated the film. That is the electrically active FTO side while the other side is simply bare soda-lime glass. By utilizing this setup, this dissertation explores the deposition (nucleation and growth) of Sb_2Se_3 on fluorine doped tin oxide (FTO) coated glass while tuning deposition and treatment parameters such as FTO supplier/surface morphology, deposition temperature, the presence of a chemical pre-deposition treatment, the use of a post-deposition annealing treatment, and the use of a pre-deposition thermal/seeding treatment.

As will be discussed in the literature review in the *History and Theory* section, many works have performed selenization in a tube furnace after the electrochemical deposition to improve the morphology, crystallinity, and selenium content of the deposited film. However, little or no work has been done wherein the annealing step occurs before the electrochemical deposition. This dissertation also explored if a pre-deposition anneal at 300°C in an inert argon atmosphere in the presence of pristine selenium.

This work then analyzes the micro/nanoparticle films resulting from these various depositions via characterization and performance analysis using scanning electron microscopy (SEM), energy-dispersive X-ray spectroscopy (EDS), X-ray diffraction (XRD), surface photovoltage (SPV) measurements, ultraviolet–visible (UV-Vis) spectroscopy, and photoelectrochemical (PEC) measurements. The data achieved here will hopefully lead to further study of this promising method for the cheaper robust deposition process of not just the absorber layer, but all PV device layers.

4.2.0 Project Description:

As described in previous sections the main goal of this work is to:

1) Display that a film of competitive performance can be grown via electrochemical deposition.

2) Show how changing various parameters before, during, and after the deposition affects the thickness, band gap, performance, and composition of the film.

The inspiration for this work stems from a paper from Lee et al. in which electrochemical depositions of Sb_2Se_3 onto molybdenum were performed with a few interesting post-deposition treatments including a combination of annealing steps in a rapid thermal annealing (RTA) system at 300 °C for one hour first in the presence of antimony-rich precursors followed by an identical annealing treatment in the presence of solid selenium to attempt to not only grow/recrystallize a thick uniform Sb_2Se_3 film, but to synthesize one with the optimal orientation for photon absorption of [001]. This orientation is favorable because it has been observed that when aligned in this way, the orthorhombic structure of Sb_2Se_3 tends to form stronger covalent bonds than in other or mixed orientations.[133] Also, the orthorhombic structure is a stack of one-dimensional parallel ribbons weakly bonded to each other via van der Waals forces leaving Sb_2Se_3 free of dangling bonds between the layers. Coincidentally, the lack of dangling bonds leads to low potential differences and minimal recombination loss at grain boundaries.[134-136] Lee et al. saw that the use of these two post-depositions anneals suppressed antimony dissolution into

the liquid selenium which occurs due to the tendency of antimony to form polycrystalline structures. As a result, successful Sb_2Se_3 films were achieved with the [001] orientation.[4]

Another group that broke ground on the electrochemical deposition of Sb_2Se_3 on FTO was Mascaro and Costa et al.[127,139,140] who tested the effects of interesting pre-treatments of the FTO substrate itself including immersing the substrate in a $KMnO_4$ (potassium permanganate) solution followed immediately by a one-hour hydrophilization soak in 708°C solution of water, H_2O_2 (hydrogen peroxide) and NH_4OH (ammonium hydroxide). The $KMnO_4$ treatment was never fully rationalized in the publications of the Mascaro lab, but referencing other works the $KMnO_4$ surface treatment is extremely similar to that utilized on the photovoltaic (PV) hole transfer layers (HTL) and graphene oxide (GO) optoelectrical layers by Kashif et al. and Yang et al. [137,138] This work showed that with this treatment the GO was able to perform at the lowest bandgap observed and attributed this enhancement to the exfoliated surface, high crystallinity, and well-formed *sp2*-hybridized carbon that led to strong bonding.[137]

Yang et al studied how $KMnO_4$ treatments affect the hole transfer layer (HTL) of perovskite PV layers. It was found that $KMnO_4$ acts as a dual functional dopant achieving high efficiency film when compared to other perovskite solar cells (PSCs). The treatment led to an increase in charge carrier extracting ability and a decrease in charge recombination.[138] The success of these works revolves around the concept that $KMnO_4$ is a strong oxidizer and exfoliate which improves the overall conductivity of the substrate surface by improving the bonding to the GO (or similar substrate such as FTO) due to the enhanced activity of the oxygenated functional groups.

Costa/Mascaro et al. also experimented with a post deposition annealing step during which, like

Lee et al., the films were annealed at several temperature for a variety of durations in a tube furnace in the presence of a crucible of pristine selenium powder. It was found that the optimal parameters for this post deposition anneal is 300° C for 3 hours as this resulted in the highest photocurrent.[127,139,140]

The highest performance Sb_2Se_3 film recorded using electrochemical deposition was by Lee et al. at 1.8% efficiency, but Costa/Mascaro et al. was able to improve this efficiency in 2018 by including a 5% FeO_2 concentration in the electrochemical bath solution. The best of the produced films were deposited at -0.6 volts at room temperature until the film reached a total charge of 600 mC and a film thickness between 300 and 400 nm. Then these samples received a thermal treatment at 300 °C for 3 hours. With these methods and a dual pre-deposition surface treatment of immersing in a solution of 0.5 mol L−1 $KMnO_4$ and a hydrophilization step of submersion in a $H_2O/H_2O_2/NH_4OH$ solution at 70 °C. The optimization of these steps afforded a power-conversion efficiency of 5.6%.[139] That being said, the highest performance of an Sb_2Se_3 absorber film by any growth method was 9.2% efficient and was achieved by Li et al. via close space sublimation.

One obvious result that these high-achieving films have in common is their morphology they both had relatively tall, thick needle-like structures. These morphologies are favorable for an absorber layer as the deep valleys between the needles provide a high surface area for increased photon absorption. Similarly, optically the film should appear black as the best absorber should not reflect any light.

The method that Li et al. used to produce this world record performing Sb_2Se_3 is CSS (close space sublimation).[141] Li et al. proposed a growth process to grow a nanorod array with high absorbance ability. CSS can be described as four stages: surface absorption, film growth, splitting, and the nanorod array growth stage. During the first step, Sb_2Se_3 possesses a 1D crystal structure and is comprised of $(Sb_4Se_6)n$ ribbons. The calculated results showed that the antimony and selenium atoms are spilt from the Sb_4Se_6 and scattered/deposited on the Mo surface. The resulting ribboned structure of Sb_4Se_6 then collapses so long as the Sb_4Se_6 unit runs parallel to the Mo (110) surface. Once the surface absorption is complete the next three steps (film growth, splitting, and nanorod growth) consist of growing the Sb_2Se_3 nanorods as the Sb_2Se_3 vapor continuously evaporates from a solid Sb_2Se_3 source. Because the generated lateral stress begins to exceed the strength of the van der Waals bonds between the $(Sb_4Se_6)_n$ ribbons, the transition from thin film type growth to nanorod growth occurs. Then the nanorods elongate and the array densifies with splitting between rods becoming deeper. Li et al. postulates that this is due to the higher growth rate in the ribbon direction due to stronger covalent Sb–Se bonds internally in the ribbon. Li et al. understood that the rough surface of a thicker nanorod absorber enhances the light harvesting and thus reduces the optical reflection.[142] Also, the [001] preferential orientation of the nanorods can facilitate long-range carrier transport along $(Sb_4Se_6)_n$ ribbons and will therefore guarantee the carrier extraction will increase as will short circuit current density.[143]
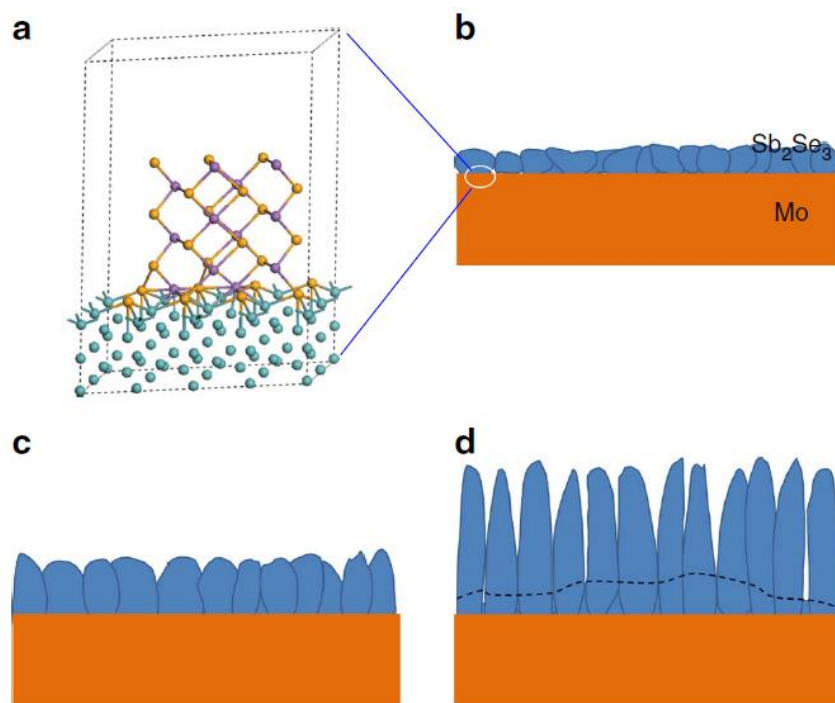
Figure 31: *Growth model of the Sb$_2$Se$_3$ nanorod arrays on Mo substrate performed by Li et al.* ***a***
depicts an atomistic model of Sb$_4$Se$_6$ unit on the (110) plane of Mo. ***b–d*** *show schematics of the*
Sb$_2$Se$_3$ at different growth stages with ***b*** *showing the thin film growth,* ***c*** *the split, and* ***d*** *the*
nanorod array growth (top part(blue) exhibits nanorod array morphology and the bottom
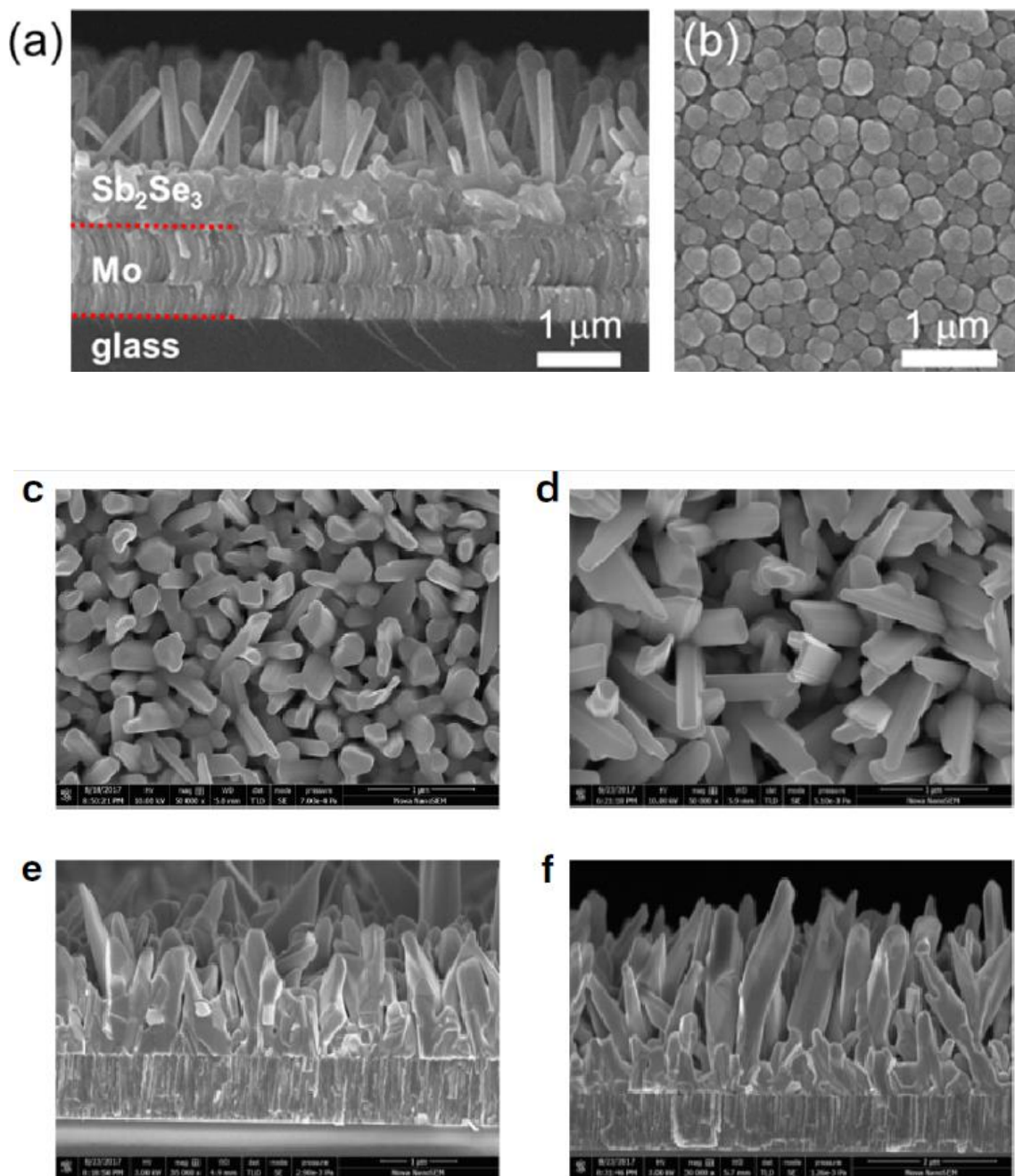*(orange) is a compact layer)*

Figure 32: *Morphologies of best performing Sb₂Se₃ absorber layers.* ***a and b*** *show edge on and top-down SEM images respectively of fabricated by an electrodeposition process and that have a substrate structure made of fully inorganic materials created by Lee et al. This device had a cell size of 0.072 cm² exhibited an efficiency of 1.8% with a Jsc (Short Circuit Current) of 14.9*

mA/cm^2, Voc of 0.365 V, and fill factor (FF) of 33.1% under one sun conditions (AM. 1.5 G, 100 mW/cm^2) .[4] c-f SEM images of films produced by Li et al. using not electrochemical deposition, but instead close space sublimation (CSS) The interface engineering with TiO$_2$ of this cell led to an independently verified record power-conversion efficiency of 9.2% for the Sb$_2$Se$_3$ solar cells (ZnO:Al/ZnO/CdS/TiO2/Sb$_2$Se$_3$ nanorod arrays/MoSe$_2$/Mo) with an absorber thickness over 1000 nm while maintaining a high fill factor of 70.3%. The values of external quantum efficiency (EQE) are higher than 85% in a wide spectral range from 550 to 900 nm, approximating the values of well-developed CdS/Cu(In,Ga)Se$_2$ thin film solar cells.[141]

Standing on the shoulders of giants like Lee, Costa, Mascaro, and Li, I strove to expand on this work and attempt to achieve homogenous, conformal, Sb$_2$Se$_3$ morphologies by first tuning temperature, pre-deposition treatments, and annealing temperature/environment and then, instead of only performing a post-deposition anneal, it is annealed before the electrochemical deposition in an environment of not a precursor, but pristine antimony or selenium powder or a combination of the two. The idea here is once the process can be optimized, the pre-deposition step could lead to the deposition of either selenium and/or antimony seeds which will act as a nucleation site for growth during electrochemical bath deposition. This growth from the pre-deposited seed will hopefully show the same nanorod/needle morphology of the [001] orientation without the need for vacuum deposition of CSS.

Specific Aim 1: Identify a reliable method to deposit the target film composition (Sb$_2$Se$_3$) including precursors/electrolyte solution, optimal pH, and deposition parameters such as temperature, stirring speed (rotations per minute) and applied current. Characterize the resulting

films with optimal microscopy, scanning electron microscopy (SEM), energy-dispersive X-ray spectroscopy (EDS), X-ray diffraction (XRD), surface photovoltage (SPV) measurements, ultraviolet–visible (UV-Vis) spectroscopy, and photoelectrochemical (PEC) measurements.

Specific Aim 2: Probe the effects of treatments and deposition parameters specifically various deposition temperatures, pre-deposition chemical surface treatment, and post-deposition selenium rich annealing treatment. Characterize the performance and band gap and determine if this process creates a more conformal morphology with a Sb_2Se_3 composition via optimal microscopy, scanning electron microscopy (SEM), energy-dispersive X-ray spectroscopy (EDS), X-ray diffraction (XRD), surface photovoltage (SPV) measurements, ultraviolet–visible (UV-Vis) spectroscopy, and photoelectrochemical (PEC) measurements.

Specific Aim 3: Probe the effects of a pre-deposition selenium seeding heat treatment. Characterize the morphology and composition after the seeds are initially deposited and then again after the electrochemical deposition. Determine how the morphology of the FTO as deposited on the glass by the supplier affects the resulting Sb_2Se_3 film morphology. The performance and band gap will be analyzed to determine if this process creates a more conformal morphology with a Sb_2Se_3 composition via optimal microscopy, scanning electron microscopy (SEM), energy-dispersive X-ray spectroscopy (EDS), X-ray diffraction (XRD), and ultraviolet–visible (UV-Vis) spectroscopy for thorough surface characterization.

4.3.0 History and Theory:

Perhaps the first use of electrodeposition to produce a deposited coating for use in PVs was in 1988 by Gobet and Tannenberger who first attempted this process with silicon dissolved in a

nano-porous solvent. [144] Since then, this process for deposition has been attempted and reinvented for many different materials with the first electrochemical deposition of Sb_2Se_3 attempted in 1999 by Torane et al. who concluded that the resulting coating layer was heavily dependent on the deposition potential and electrolytic bath concentration. [145] Sb_2Se_3 has been reported in literature as a p-type semiconductor with a band gap of 1.075 eV to 1.21 eV. [146] As mentioned above, the world record performance of a PV with an Sb_2Se_3 absorber layer was achieved by Li et al in 2019 via CSS, but a great many materials have been studied as an option for the solar absorber layer and therefore, it helps to review the best performance of a purely electrochemically deposited absorber materials throughout scientific history.

4.3.1 Metal Oxides:

In the 2011 paper by Cao et al. synthesized three types of Cu_2O/ZnO p-n heterojunctions via electrochemical deposition (ECD). This process consisted of using a two-electrode electrochemical system to perform galvanostatic cathodic deposition of the ZnO film. During this process, conductive glass slides coated with 350 nm of fluorine-doped tin oxide coated glass (FTO glass) served as the cathode while 1 cm^2 zinc sheets served as the anode. A 0.05-0.5M zinc nitrate solution was used as the electrolyte in this system. The experimental parameters were a deposition temperature of 70°C, at an applied current density of 0.35 mA/cm^2 for 60 min. This method afforded ZnO nanorods by immersing the synthesized nanotubes into an 0.125 M KOH alkaline solution at 80°C for 2 hours to selectively dissolve the (001)-face. Once this process was complete, the growth of the full Cu_2O/ZnO heterostructure could begin. This process involves using the nanorods on FTO glass as a cathode for ECD of a Cu_2O film using a 0.4 M $CuSO_4$ and 5M lactic acid solution as electrolyte at a pH of 12 via the addition of NaOH. This second ECD

operated at 0.35mA/cm^2 for 30-150 minutes. Finally, gold contacts were cool sputtered on

through plastic masks.[147]
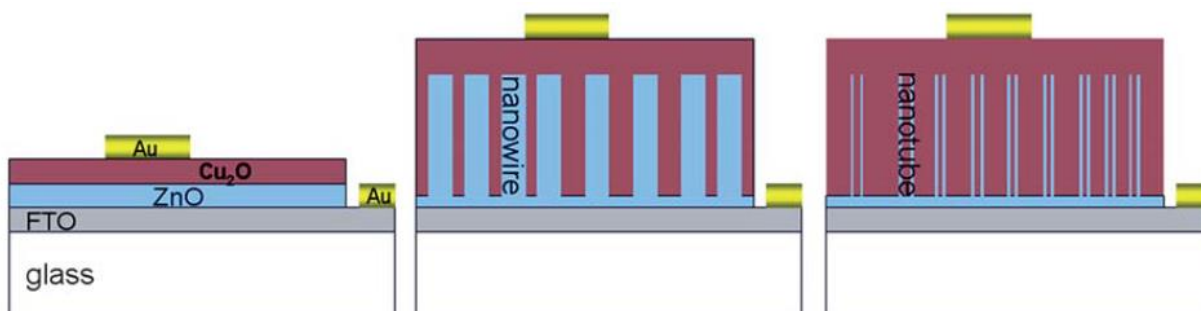
Figure 33: Cao et al. produced three different heterostructure architectures via low-cost ECD each composed of n-type zinc oxide (ZnO) film, nanowires or nanotubes covered with a p-type cuprous oxide (Cu$_2$O) thin film. [147]

The resulting SEM images showed a morphological dependance on zinc nitrate concentration

in the electrolyte solution appearing as a dense sheet at 0.5M, but an array of quasialigned

nanorods at 0.05M.
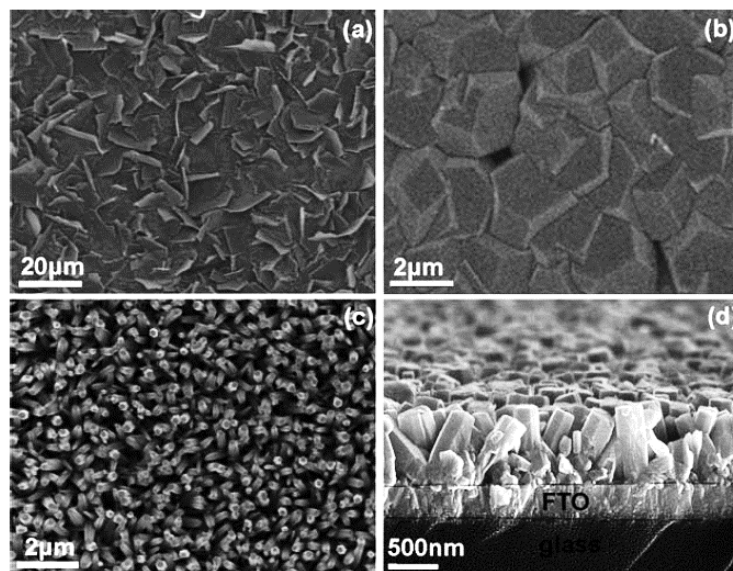
Figure 34: *SEM images of the surface morphology of the Cao et al. (a) ZnO film (Zn(NO₃)₂,*

0.5 M, 0.3 mA/cm₂, (b) Cu₂O film (CuSO₄, 0.4 M, 0.35 mA/cm²), (c) ZnO nanowire

(Zn(NO₃)₂, 0.05 M, 0.3 mA/cm²), and (d) cross section SEM image of (c).[147]

Cao et al.'s ability to produce nanotubes stems from a property of ZnO to react with both acidic

and basic ions to produce soluble salts. This reactivity can occur with any amphoteric oxide. The

potassium hydroxide chemical etching process described above effectively removed material

from the (001)-face hollowing out nanorods into nanotubes. The effect of this process in the

formation of heterostructure was that compared to planar Cu_2O/ZnO film solar cells, the

nanowire arrays were able to achieve 6.5 times the efficiency and 4.5 times the short-circuit

current. This correlates to a maximum short circuit current density reachable for all three

architectures, however, the formation of the nanotubes decreased the open-circuit voltage and

conversion efficiency. This improvement is likely due to the high quality of single crystals, but

the etching that was required for nanotube creation caused short circuiting between the Cu_3O and

glass substrate which negatively affected the efficiency of the solar cell. Cao et al. showed that ECD and etching are effective methods for solar cell growth and synthesis, but more research was needed to see the fruits of these findings. [147]

Ten years after Cao's work on electrochemically deposited oxides for active PV layers, Sherman et al. used a similar, but electroless, technique to deposit SnO_2 which was referred to in publications as a liquid phase deposition.[148] The process consists of synthesizing SnO_2 flower-like particles by using a solution of water, ethanol, $SnCl_4 \cdot 5H_2O$, NaOH, and $Na_3C_6H_5O_7 \cdot 2H_2O$ and subjecting this solution to a 24-hour hydrothermal treatment at 200°C before drying to afford the particles. A second type of particles (spherical) was also synthesized for comparison following a 2002 procedure[149] involving a commercial suspension of amorphous to weakly crystalline SnO_2 nanoparticles which was diluted with acetic acid, nitric acid, NaOH, and water. This also underwent hydrothermal treatment and finally dried. These particles were then made into a paste by resuspending the premade particles in ethanol, PEG (polyethylene glycol), and PEO (polyethylene oxide) producing a polymeric paste which could then be spread onto an FTO substrate and sintered at 450°C for 45 min in air. The layers produced this way were soaked in N_3 dye used in (cis-diisothiocyanato-bis(2,2′ -bipyridyl-4,4′ -dicarboxylic acid) ruthenium(II)) in ethanol and employed as ~1 cm²-area photoanodes in dye-sensitized solar cells (DSSCs).

When the nanoparticles were compared on the fully assembled DSSCs the spherical version performed with an average short-circuit current six times larger with a five times greater conversion frequency than the current produced by flower-like particle DSSCs, but the flower morphology particle cells have a greater open circuit voltage by 31%. However, even after the

addition of a compact SnO_2 blocking layer on the FTO, a TiO_2 surface coating, and a $(NH_4)_2TiF_6$ treatment, Sherman et al.[148] could only achieve an efficiency of 1.72% which is drastically lower than that achieved by 2014, 2015, and 2020 DSSCs attempts using other deposition methods with conversion efficiencies of 5-7%. [150,151,152] This inferior performance compared to previously published cells containing organic electrolyte may be due to the effects of water (which has been considered a contaminant in DSSCs)[152], the dye-TiO_2 binding, and other side reactions with I_3^- ions, ligand substitutions, and the with ruthenium(II) base dye complexes.[148] While the Cao et al. electroless liquid deposition led to a better understanding of the types of synthesis and processing used for DSSC anodes and other solar cell layers, there are still many improvements to be made as we probe the photocurrent harvesting mechanism and the sources of conversion efficiency loss.

4.3.2 Metal Sulfides:

In 2008 and 2009 many sulfides were being explored for solar cell absorber layer applications. The main two sulfides of interest are tin sulfide and cadmium sulfide. Mathews et al. was a main contributor to the field at the time. Their involved using cyclic voltammetry (CV) to determine that the deposition of the SnS film on FTO occurred between -1 and -0.8 Vs Mathews et al. found that the films that were deposited during a -0.95V and 1V pulse had an orthorhombic crystal structure with similar grain size and lattice parameters as those of chemically deposited films. They achieved a SnS film with a 1.3 eV bandgap and when paired with a CdS heterojunction, a short circuit current density 0.72 mA/cm$_2$, an open circuit voltage110 mV, and a fill factor of 0.32.[153]

Mathews et al.[154,155] used two common reagents, Sn(II) salts and $Na_2S_2O_3$ in a three-electrode system as described previously. The deposition is the result of the following chemical reaction which is also similar to general sulfide semiconductor deposition. [153,156]

Reaction 9: $\quad S_2O_3{}^{2-} + 2H^+ \rightarrow S + H_2SO_3$

Reaction 10: $\quad Sn^{2+} + S + 2e^- \rightarrow SnS$
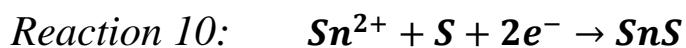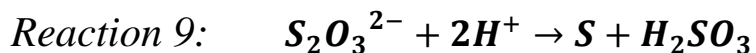
First, the elemental sulfur is released from $S_2O_3{}^{-2}$ in the solution and then the Sn and S are reduced at the cathode to form SnS. The deposition bath contains solutions of $SnCl_2$ and solutions containing $SnCl_2$ and Na_2SO_3. In the figure below two experiments are compared. The solution that contains Na_2SO_3 demonstrated a current increase from a potential -0.6 V with a cathodic peak at –0.9 V. In this range of potentials, it is likely that tin and sulfur are co-depositing. The anodic peak that is observed in the reverse scan is due to weakly bonded SnS and the dissolution of tin. On the other hand, the experiment with $SnCl_2$ only showed a cathodic current equal to zero until the maximum potential of -0.51 V at which point it the current increases to a cathodic peak of -0.6 V which corresponds to the reduction of Sn^{2+} to Sn. On the return scan crosses the forward trace at -0.53 V and leads to a well-defined anodic peak at -0.34 V which is a result of the dissolution of the tin layer that was formed during the cathodic scan.[153,156]
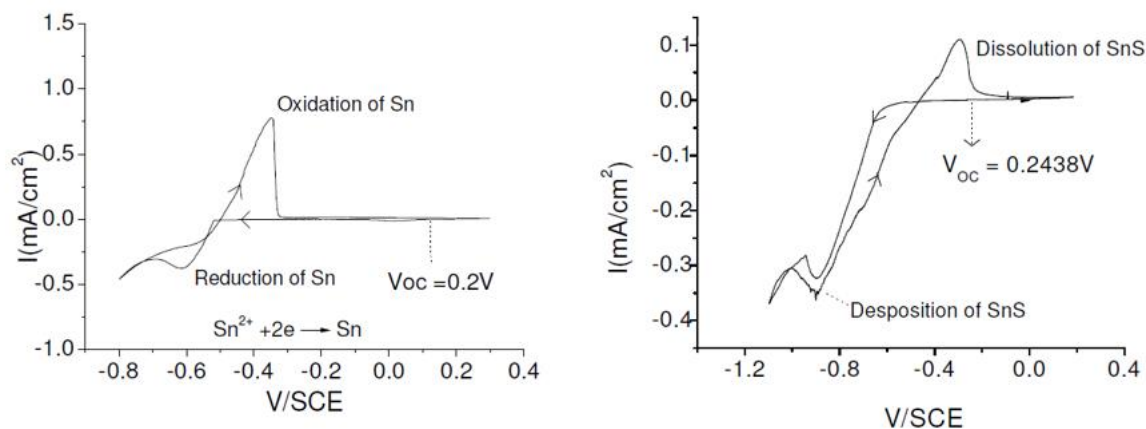
Figure 35: *Cyclic voltammograms from Mathews et al. Left - 1.5 mM SnCl₂ solution; Right - 1.5 mM SnCl₂ solution and 8 mM Na₂S₂O₃ solution; pH 2.5 to 3. The bath temperature was 45°C in both cases.* [153]

The figure below compares the current-voltage characteristics of the SnS/CdS heterojunctions prepared using pulse-electrodeposition of SnS versus that of chemical deposition. The pulse deposited (ECD) SnS had a *Voc* = 110 mV, *Jsc* = 0.72 mA/cm², and FF 0.32, while the chemically deposited cell showed *Voc* = 370 mV, *Jsc* = 1.23 mA/cm², and FF 0.44 which means that the chemically deposited film performs better but is still not competitive when compared to other deposition methods such as spray pyrolysis.

SnS thin films deposited using pulse electrodeposition, at potentials *V_on* of -0.95 V and *V_off* of +0.1 V show orthorhombic crystal structure with lattice parameters: *a:* 0.4328 nm; *b:* 1.1158 nm; *c*: 0.3984 nm. In these films, the zinc blende phase, SnS (ZB), which while possible to obtain from chemical deposition, was not observed. The optical band gap of electrodeposited SnS(OR) film was recorded as 1.33 eV, which is comparable with 1.23-1.33 eV reported previously by pulsed electrodeposition.[153] The chemically deposited orthorhombic films show a bandgap of

1.12 eV, while the SnS (ZB) show a higher band gap of 1.7 eV. The electrical conductivity of the film is 5 x 10-7 Ω^{-1} cm^{-1}, comparable with that of chemically deposited SnS(OR) film. The film was integrated as an absorber in photovoltaic structure: SnO2:F/CdS/SnS/graphite, showing *Voc* = 110 mV, and *Jsc* = 0.75 mA/cm2. These values are inferior to those reported in cells using SnS films obtained by electrodeposition, spray pyrolysis or by chemical deposition.[156,157]
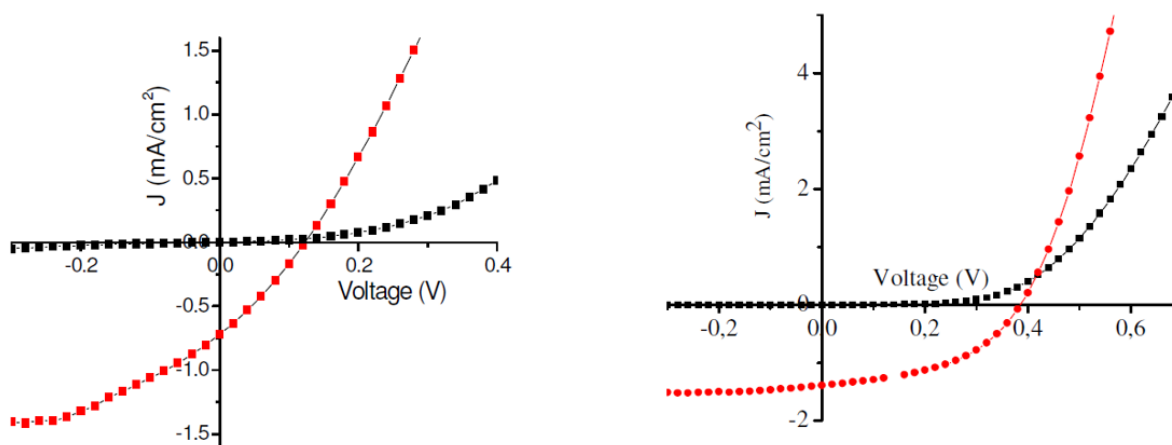
Figure 36: Current vs. Potential (J-V) plots showing characteristics of CdS and SnS photovoltaic structures. Left – SnS deposited via electrodeposition. Right – SnS deposited by chemical deposition.[153]

While Mathews et al. was focusing on SnS, several other groups were exploring CdS. Xi et al. for example worked to produce hybrid films composed of dense CdS nanorod arrays completely by electrochemical deposition and interpenetrating polybithiophene. The nanorods self-assembled on gold-coated glass substrates after a potential was applied to an electrolytic solution of cadmium sulfate and potassium thiocyanate. Once the nanorods had grown, the conjugated polymer polybithiophene was deposited into the nanorod arrays via in situ

electrochemical polymerization resulting in an interdigitated nanohybrid film. The film structure appears as dense packing of the polymer in the nanorod arrays with a filling ratio estimated to be 76%. Xi et al.[157] used Raman spectroscopy to confirm that there is measurable charge transfer between the polymer and CdS nanorods which is indicative of a high fill ratio and contact at the polymer-CdS interface. In the completed device build, these films achieved an open-circuit voltage of 0.84 V, a short-circuit current of 0.52 mA/cm^2, and an overall power conversion efficiency of 0.38%. In the figure below, CdS nanorods grew in a vertically aligned array. The dimensions of the nanorods were tunable by experimental conditions and were 20 to 40 nm across, and 100-300 nm high. From the top, the rod appears to take the wurtzite crystal structure with a hexagonal shape. These nanorods are aligned to the [001] direction with an average rod to rod spacing of about 20 nm at an estimated density of 4 x 10^{10} nanorods for each square centimeter which leaves about 75% open space in the structure that can be filled by polymer. [157]
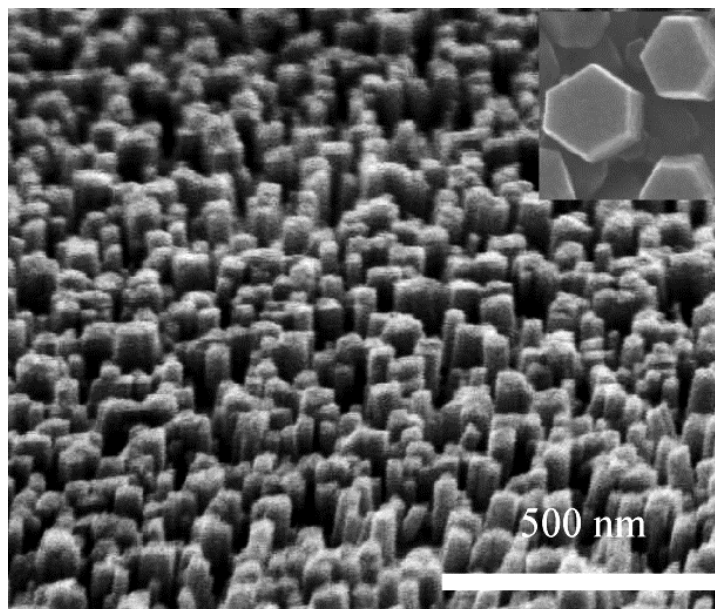
Figure 37: SEM image of a CdS nanorod array (side view). The inset is an enlarged top view of the nanorods. [157]

The resulting short-circuit current and fill factor of the nanohybrid solar cells were relatively low. This was discussed by Xi et al. as most likely due to electropolymerized polybithiophene generally having carrier mobilities orders of magnitude lower than regioregular poly(3-hexylthiophene). Electropolymerizing nevertheless improved the filling ratio by strengthening the interaction at the inorganic-polymer interface. This nanohybrid architecture demonstrated improved *Voc* and the process used by Xi et al. demonstrates a solution-based fabrication process which can be compatible with the kind of ambient environment low-cost roll-to-roll manufacturing that fuel the solar cell industry today. Xi et al. believed that the electro-polymerization process could be optimized by using monomers to yield polymers with small bandgap and high structural regularity. If one could master this process, they could intensely increase the power conversion efficiency of CdS and other compositions of absorber layers.[157]

As an extension of Xi et al.'s nanorod work, Penner and Hu et al. also tried to deposit CdS on

gold-coated glass. The Penner lab focused on electrochemical and chemical methods to deposit

CdS. The process that was published includes two steps: the electrochemical deposition of

cadmium, and the annealing of Cd in a H_2S atmosphere in order to convert Cd into CdS. This

process resulted in CdS nanocrystals and nanowires on highly oriented pyrolytic graphite

(HOPG).[158-161] It is widely accepted that electrochemical deposition methods are favorable

because it can achieve good monodispersity with a range of particle diameters. The diameter of

CdS nanocrystals is completely dependent on the diameter of the Cd precursor nanoparticles

which, like most electrochemically deposited metal precursors, have a very narrow size

distribution.[158]

The actual cadmium was deposited by potentiostatic electrochemical deposition at -0.80 V vs.

SCE for 10–15 min. Post-deposition, the obtained cadmium films were then heated in H_2S

atmosphere at 280–300°C for 30 min to convert Cd into CdS.[160,161] The image below shows two

solar cell builds that Penner et al. compared. On the left the schematic shows the pre-anneal build

with the Cd deposit only, while the image on the right shows the build after the H_2S annealing

environment. SEM of the two surfaces can be seen in figure 39.[161]
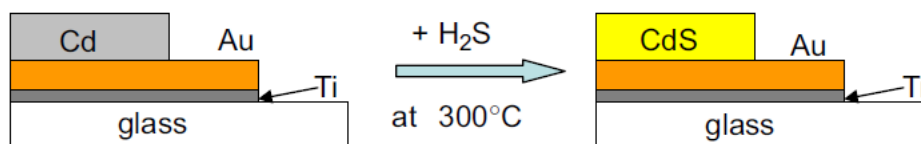
Figure 38: *Cross-section of glass/Ti/Au/Cd structure(a)before and(b) after the H_2S annealing*

process. [161]

The result of this 2-step deposition was a successful 90 nm thick electrochemical/chemical (E/C) deposited CdS on a 40 nm thick conductive gold film, which was adhered to glass surface by an intermediate 10 nm titanium layer. The crystalline phase was also hexagonal wurtzite just like Mathews et al., but with a (002) crystalline phase. Penner et al. completed the build by drop casting poly3-octylthiophene (P$_3$OT) on top of the CdS film, and the Au/CdS/ P$_3$OT/Au heterojunctions generated VOC of 880 mV and a low JSC of 0.06 mA/cm^2 when the cell is illuminated from Au/CdS side. Penner et al. explained that the possible reasons for the low JSC value are the large P$_3$OT film thickness and/or its low charge carrier mobility.
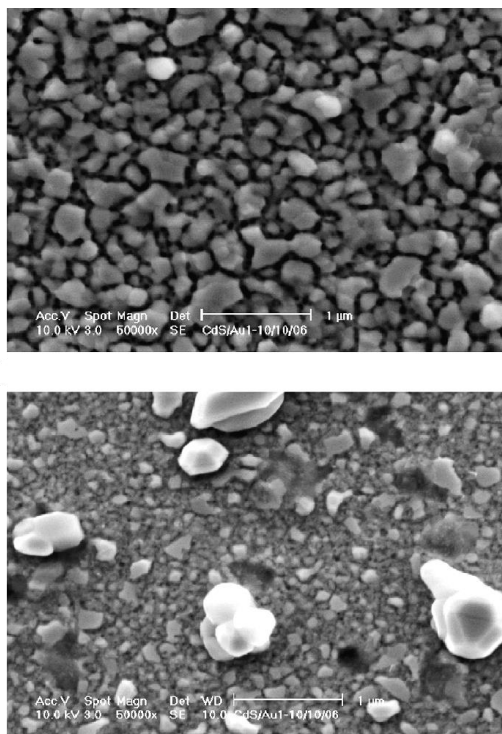
Figure 39: *Cross-section of glass/Ti/Au/Cd structure(a)before and(b) after the H$_2$S annealing process*

A full 10 years after Xi, Mathews, and Penner, Ichimura et al. also turned to sulfides as a potential solution to better absorber layers. Ichimura and Ji were interested in pyrite (FeS_2) and if it can be deposited via electrochemical deposition as a functional absorber layer.[163] They attempted this by first depositing ZnO using galvanostatic electrochemical deposition (ECD) on the indium tin oxide coated glass substrate. Then FeS_xO_y was then deposited on top of the ZnO. The film material is denoted as FeS_xO_y because the iron sulfide films deposited by ECD contain a significant amount of oxygen. The ECD consists of a 3-step pulse of potential and a DC bias. When tartaric acid was added as a complexing agent or chelating agent (a chemical compound which can bind with metal ions through multiple coordination bonds to form stable, water-soluble complexes), the FeS_xO_y could not deposit onto the ZnO layer. In the solutions without tartaric acid, the heterojunctions that showed rectifying electrical properties were able to be fabricated. Rectifying properties refer to those where a new signal is created with a single polarity. This happens when an alternating current waveform becomes a direct current waveform. Ichimura and Ji observed that the ZnO on the substrate may be dissolved during the FeS_xO_y deposition which can form a mixed interface layer and cause deterioration of the diode properties. The amount of ZnO that dissolves is dependent on the deposition potential form and on the ion distribution at the substrate surface. When the deposition occurs via galvanostatic ECD no ZnO dissolution was observed, but during pulse ECD ZnO dissolved. In the case of galvanostatic ECD, a concentration of thiosulfate ions released from the Fe^{2+} ion complex forms which does not occur during the pulse ECD reaction. The best performance achieved in this study was a short circuit potential (Jsc) of -10.6 μA cm^{-2}, an open-circuit voltage (Voc) of -3 mV, a fill factor (FF) of 0.25 and the conversion efficiency (η) of $8.0 \times 10-6\%$. Although the

efficiency was very low, this was the first time a p–n heterojunction photovoltaic cell based on

FeS_2 was dstrated.[163]

4.3.3 Metal Selenides:

As we move down the chalcogenides group on the periodic table, the next compounds in line are

selenides. One selenide that has been getting increased attention for PV applications is known as

CZTSe ($Cu_2ZnSnSe_4$). In 2014, Yao et al. utilized electrochemical deposition to produce a

copper/tin/zinc (Cu/Sn/Zn) stack. Yao, like Costa/Mascaro, employed post-deposition

selenization steps, but in this case, Yao et al. used a tin source during this low pressure anneal at

530°C. To probe the effect of the tin source on the morphology and performance of the absorber

CZTSe layer, three different selenization steps were compared. This treatment was of interest

because during previous selenization steps, tin is generally lost in exchange for the incoming

selenium. So, by introducing a source of tin during the anneal, one can achieve a copper-poor

and zinc-rich CZTSe absorber layer with Cu/Sn, Zn/Sn, Cu/(Zn + Sn), and Zn/(Cu + Zn + Sn).

Yao et al. realized these layer combinations had the following metallic element ratios

respectively: 1.86, 1.24, 0.83, and 0.3. The setup of the annealing chamber is shown below.[164]
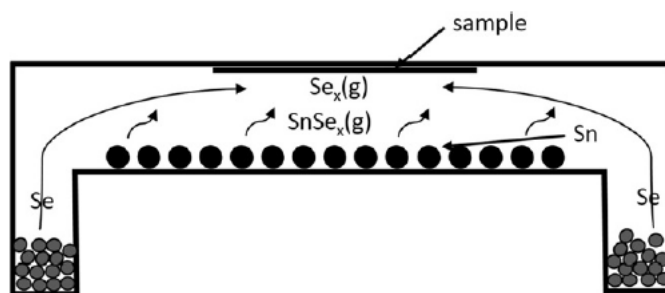
Figure 40: *The schematic diagram of the reaction from a tin source with selenium.*[164]

To produce a stoichiometric CZTSe thin film, $SnSe_x$ is required which can be achieved by reacting the tin source with selenium. Yao et al fabricated a CZTSe solar cell with a Mo/CZTSe/CdS/i-ZnO/Al-ZnO/Ni-Al structure with an active area of 0.358 cm^2. The resulting SEM from these layers show that the CZTSe thin films were selenized without a tin source, but samples that were treated with a tin source had larger grain sizes with small grains forming only at the surface. With a thickness of 1.5 microns, no additional tin film appeared granular and loose while samples with a tin source show an increase in crystallinity and tightly organized large grains. The tin-rich samples also did not have spaces or pinholes between the film and the molybdenum back contact layer. Moreover, increasing the annealing temperature from 400°C to 530°C the surface morphology continues to improve with a compact surface and large grains. The reasoning for these outcomes stems from the relationship of the partial pressure of the $SnSe_x$ and the decomposition of the CZTSe thin films. In the Yao et al experiments, the selenium gas pressure was kept low and without the $SnSe_x$ supply the CZTSe thin films decompose rapidly which yields internal crystallization and therefore poor surface morphology. With the tin source present at 400°C, the partial pressure of SnSe partially inhibits the internal decomposition of CZTSe and produces structures with a good internal morphology, but poor external morphologies. When the higher temperature is used along with the tin source, the partial pressure of SnSex is enough to inhibit both the surface and internal decompositions of the CZTSe thin films which greatly improved the quality of the surface and microstructure of the films.[164]
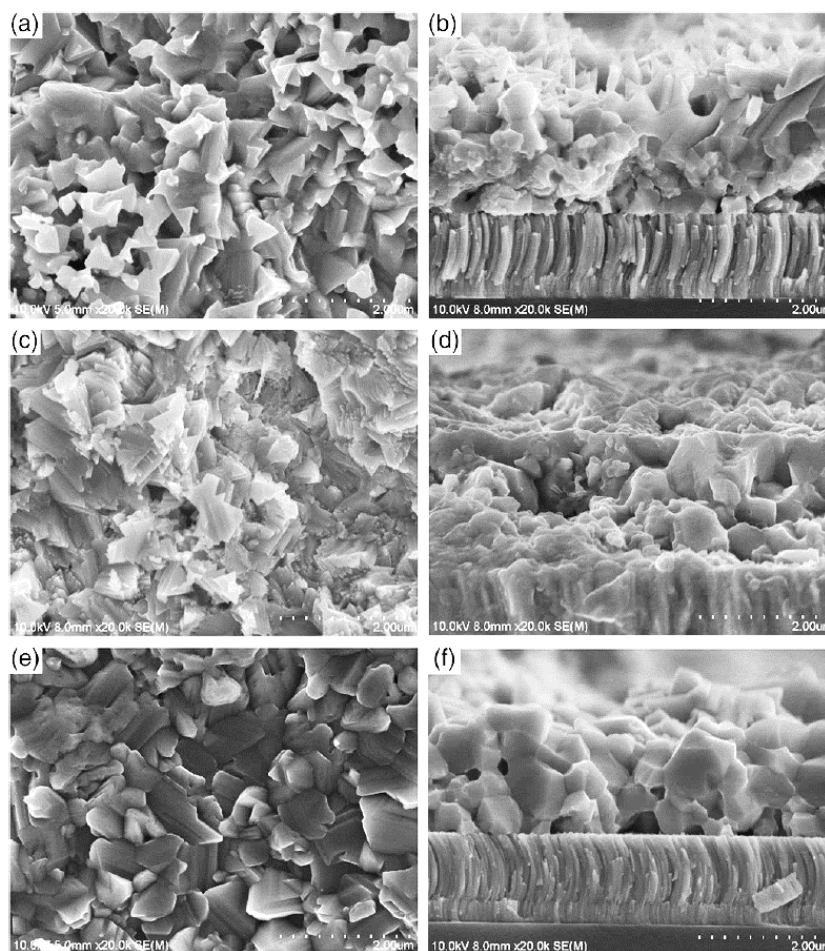
Figure 41: *Surface and cross-section SEM images of CZTSe thin films prepared by the various selenization conditions. (a-b) Without a tin source, (c-d) with a tin source at a temperature of 400°C, and (e-f) with a tin source at 530°C.*[164]

The film samples tended to align to a (112) orientation in which the tin selenide content was high. Because no Mo-Se phase was observed which means that the selenium pressure was too low, so when the temperature was increased a very thin $MoSe_2$ layer could be seen at the interface between Mo and the CZTSe. The best of the stacks produced contained a CZTSe absorber layer deposited via Yao et al.'s low-cost electrodeposition process in a Cu/Sn/Zn stack

layer followed by selenization at a low pressure. This solar cell device achieved an efficiency of 4.81%.[164]

Another group to try their luck at producing CZTSe films was Jeon et al.[165] They also employed electrodeposition to fabricate a highly efficient copper–zinc–tin–selenide ($Cu_2ZnSnSe_4$; CZTSe). To do this, CZT serves as metallic precursor film with a copper-rich and zinc-poor composition. This CZT was deposited directly in a single aqueous bath containing Cu, Zn, and Sn cations ($CuSO_4 \cdot 5H_2O$, $ZnSO_4 \cdot 7H_2O$, $SnCl_2$, and trisodium citrate as complexing agent.[165-167] A constant current density of 1.18 mA/cm^2 was then applied via the three-electrode system and the CZT film was successfully deposited onto molybdenum-coated soda lime glass substrates. This initial film was then converted into a CZTSe film via a post-deposition anneal in a two-zone tube furnace under a selenium atmosphere which Jeon et al. experimented with by evaluating a range of annealing temperature between 400°C to 600 °C. There was a post-annealing step added as well during which the samples were soaked in an aqueous KCN solution (potassium cyanide) for 2 minutes to remove possible any Cu_xSe-based secondary phases.[167] After this rinsing, a 70 nm CdS buffer layer was deposited via chemical bath deposition, i-ZnO/AZO layers via RF (radio frequency) sputtering, and a Ni/Al contact grid via thermal evaporation to complete the device stack. The image below shows the molybdenum and CZT film layers.
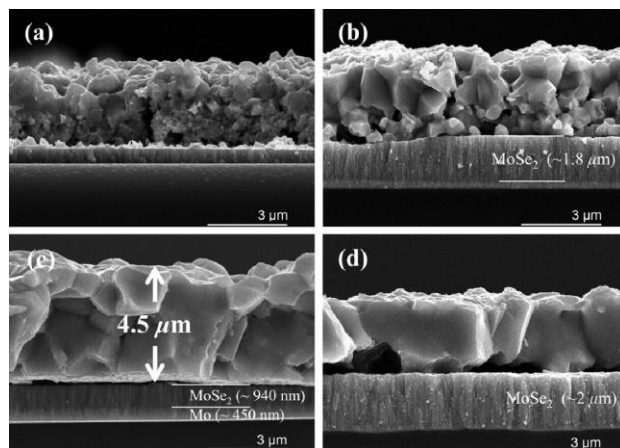
Figure 42: *Cross-sectional SEM images of the CZTSe thin films annealed at (a) 400°C, (b) 500°C, (c) 550°C, and (d) 580 °C.*

Jeon et al found that the crystallization of CZTSe begins at 400°C and is completed at 500°C, while crystal growth can continue at higher temperatures. Worried the enhanced crystallinity would lead to worsened physical properties, the thin films were annealed at 550°C which allowed for some of the lab's most efficient layers with up to 8.0% active efficiency making it one of the highest efficiencies for CZTSe thin-film solar cells prepared via electrodeposition. Jeon et al. proposed that future work of interest would be to attempt to improve efficiency by also optimizing film thickness, antireflection coating, $MoSe_2$ formation, and p–n junction properties. The main takeaway from the work of Jeon et al. is that the crystallinity and microstructure as a whole can be improved by increasing the selenization temperature. However, this means that physical instability will occur in the form of deformation of the glass substrate (occurs at 600°C). Therefore using 550°C should be an optimal temperature and indeed led to Jeon et al.'s best device with a bandgap of 1.02 eV, and an efficiency of 8.0%, one of the highest efficiencies reported for electrodeposited CZTSe thin film solar cells.[164]

I would be remised if I didn't at least mention the work being done on $CuInSe_2$ (CIS). One notable example of this is the 2020 paper by Mandati et al.[168] They used a two-electrode pulse electrodeposition to produce a pure CIS absorber layer without using additives or complexing agents. They produced a Cu/In stack on both flexible and glass substrates via this economic pulse electrodeposition method and then selenized it with a two-zone tubular furnace.

To perform pulse electrodeposition (PED) to deposit the Cu/In precursor stack one must begin with the deposition of copper which comes from a solution containing $CuCl_2$, hydrochloric acid (for pH adjustment to 1), and LiCl (as an electrolyte). During the deposition this became $InCl_3$ + LiCl electrolyte. The two electrodes were comprised of molybdenum foil and Mo on glass as working electrodes with graphite as the anode. The reason a 2-electrode system was preferred over the 3-electrode version is because a two-electrode system is commonly used for large area deposition. The copper was deposited at a voltage of -1.5 V for 17 minutes which was immediately followed by the deposition of indium at -2.0 V for 20 minutes. Both the depositions were performed using PED with a at room temperature. The depositions with the same pulse conditions were performed both on Mo foil and Mo/glass substrates. The Cu/In stack was deposited before it was further selenized. The tube furnace contained a selenium source in one zone that kept a temperature range of 230–260 °C while the electrodeposited precursor was located in a different zone. Selenization was performed for 30 minutes at 550 °C in an inert argon atmosphere with a tube pressure of 2 mbar.[168]
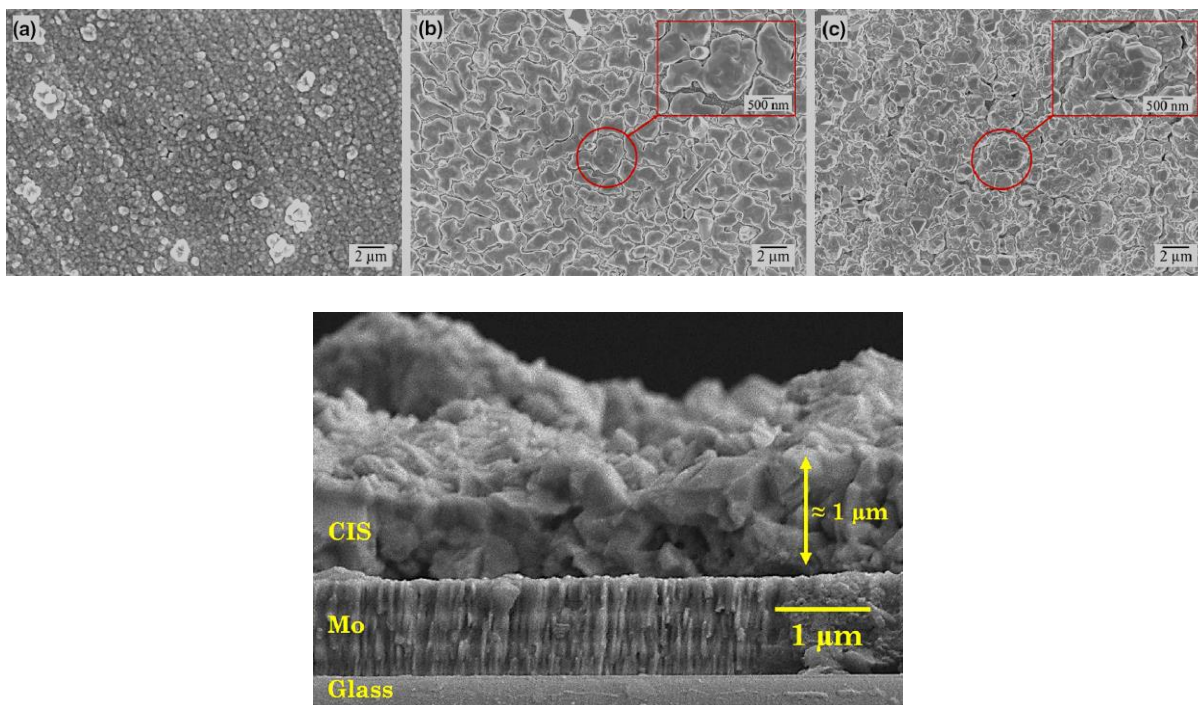
Figure 43: *Top - Surface morphology of pulse electrodeposited (a) Cu layer, (b) Cu/In stack and (c) selenized CIS absorber. Insets show the high magnification images of corresponding red circular area in (b) and (c). Bottom - Cross-sectional morphology of pulse electrodeposited selenized CIS absorber.*[168]

The resulting films from Mandati et al. were polycrystalline, one micron thick with a 0.9 Cu:In ratio (copper poor) and a tetragonal chalcopyrite phase. The full device stack was capable of a power conversion efficiency of 5.2%. Mandati believes that this technique can be further improved, perhaps by the addition of gallium, to obtain low-cost CIS and $CuInSe_2$.[168]

All of these absorber layers have led us to antimony selenide which as mentioned in earlier sections has low toxicity, low cost, and high earth abundance. This light absorbing material behaves as a V2-VI3 semiconductor and has an orthorhombic structure consisting of 1D ribbons

bonded by van der Waals forces. Because Sb_2Se_3 grows as a low complexity single crystalline phase, it maintains relatively good stability. Complete with an impressive bandgap of 1.0-1.2 eV and a low grain growth temperature Sb_2Se_3 appears to be an extremely promising functional film for PVs.[169,170,171]
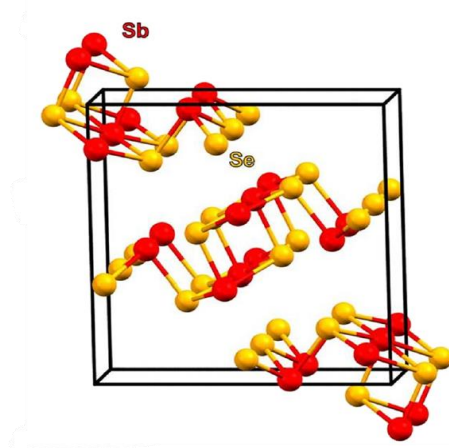
Figure 44: *The crystal structure of Sb₂Se₃ created using Mercury 3.9 (Copyright CCDC 2001-2016) and the CIF files from Inorganic Crystal Structure Database.*[172,173]

To better understand how to choose electrodeposition parameters, I would like to touch on the use of cyclic voltammetry (CV) as a tool to choose the operating potential depending on the desired product. Costa/Mascaro et al. used this method very purposely in 2017 before the experiments discussed in earlier sections. CV voltammograms are essentially a map to the reactions involved in electrochemistry with the bottom trace trough being the reduction potential and the top trace peak being the oxidation reaction. In the case of Costa et al., figure 45-left shows the electrochemical behavior of the 1.0 mM H_2SeO_3 (from hydrolyzed SeO_2) while figure 45-right shows 1 mM SbO^+ from hydrolyzed $KSbOC_4H_4O_6$ solutions. Figure 46 shows the

equimolar mixture with equal parts selenium and antimony precursor on Pt (geometric area of

0.1 cm^2) and FTO (geometric area of 0.8 cm^2).

The resulting voltammograms show the electrochemical behavior of the platinum or FTO in

supporting electrolyte only in black. The platinum substrate saw adsorption and desorption at

potentials between 0 and -0.25 volts and the formation and reduction of PtOx at potentials 0.5

and 0.36 volts, respectively. Figure 45-left shows the production of H_2SeO_3 with three cathodic

peaks and two anodic peaks evident. The peak at 0.16 and 0.01 V are indicative of the reduction

of Se^{4+} to Se^0 by underpotential deposition (UPD) (see reactions below). The peaks at ~-0.5 volts

can be associated with the reduction of Se^0 to Se^{2-} via two electrons[174] (or of Se^{4+} to Se^{2-} via six

electrons)[175] (see reactions below)

Reaction 11:
$$H_2SeO_{3(aq)} + 4H^+_{(aq)} + 4e^- \leftrightarrows Se_{(s,\ adatoms)} + 3H_2O_{(l)}$$

Reaction 12:
$$H_2SeO_{3(aq)} + 4H^+_{(aq)} + 4e^- \leftrightarrows Se_{(s,\ bulk)} + 3H_2O_{(l)}$$

Reaction 13:
$$Se_{(s,bulk)} + 2H^+_{(aq)} + 2e^- \leftrightarrows H_2Se_{(aq,g)}$$
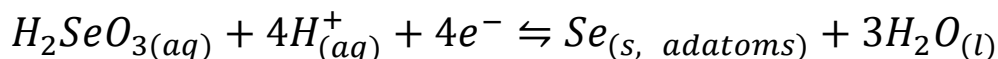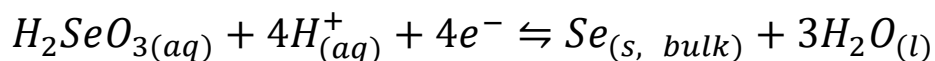
Reaction 14:
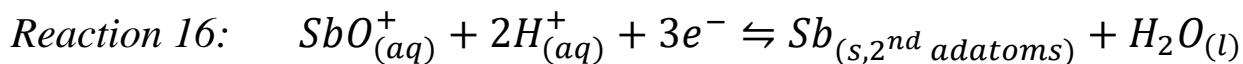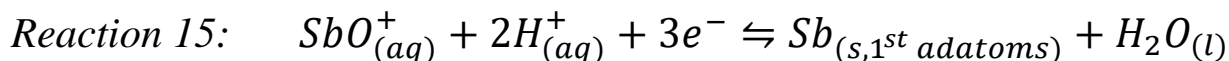$$H_2SeO_{3(aq)} + 6H^+_{(aq)} + 6e^- \leftrightarrows H_2Se_{(aq,g)} + 3H_2O_{(l)}$$
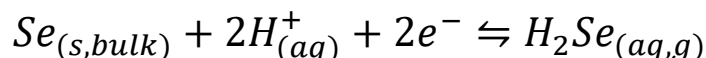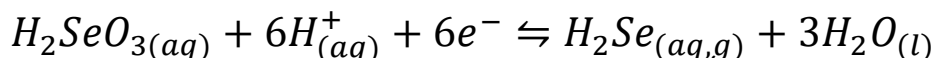
These voltammograms were run at a variety of inversion potentials using a platinum substrate

(Figure 45 – Left), namely -0.05, -0.20, -0.40 and -0.80 V and the results were compared to those

of the FTO substrate, shown in figure 46b. Jung et al.[176] found that the Sb^{3+} is reduced to Sb^0 on

Pt there are two underpotential deposition (UPD) peaks and one large deposition peak. These peaks can be described by the equations below:

Reaction 15: $\quad SbO_{(aq)}^{+} + 2H_{(aq)}^{+} + 3e^{-} \leftrightharpoons Sb_{(s, 1^{st}\ adatoms)} + H_2O_{(l)}$

Reaction 16: $\quad SbO_{(aq)}^{+} + 2H_{(aq)}^{+} + 3e^{-} \leftrightharpoons Sb_{(s, 2^{nd}\ adatoms)} + H_2O_{(l)}$

Reaction 17: $\quad SbO_{(aq)}^{+} + 2H_{(aq)}^{+} + 3e^{-} \leftrightharpoons Sb_{(s, bulk)} + H_2O_{(l)}$
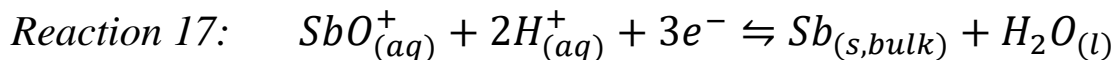
Observing the green line voltammogram shown on Figure 46a, we can observe a peak occurring at the same potential of the Se and Sb 1st adatom UPDs, meaning that in this region, the antimony and selenium adatoms can react in the solid state to form Sb_2Se_3 which was also observed by Chen et al. on a gold surface.[140,177] Finally, shown by the black curve in figure 46b, the reaction occurring at the FTO electrode. Unlike the reaction at the platinum surface, no hydrogen adsorption or desorption process is observed. When the reverse scan is observed, an anodic peak can be observed which indicates the re-oxidation of FTO (*) and the blue trace peak shows the H_2SeO_3 electrochemical behavior, as expected, there are no peaks related to the deposition/dissolution of selenium adatoms. From plots like those in figures 45 and 46, Costa et al. determined that the ideal potential to apply during the electrochemical deposition is -0.6 volts. In this region of the voltammogram, the growth is controlled by activation instead of diffusion which allows for better composition control.[140] In this work, Costa et al. performed a post-deposition thermal treatment to elucidate how this affects the optoelectronic quality and photoactivity toward hydrogen gas generation (from water splitting) of electrodeposited Sb_2Se_3 thin films.
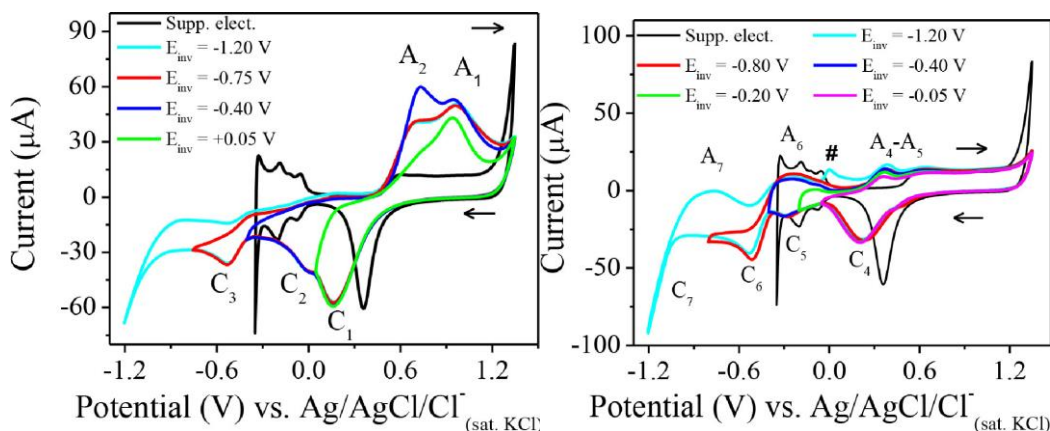
Figure 45: *Left - Cyclic voltammograms on Pt with different inversion potentials (E_{inv}) at a scan rate of 50 mVs^{-1}, for the solution constituted of 1.0 mM $H_2 SeO_3$ in 0.5 M Na_2SO_4/H_2SO_4 at pH 2. The black line voltammogram shows the electrochemical profile of Pt in the supporting electrolyte. Right - Cyclic voltammog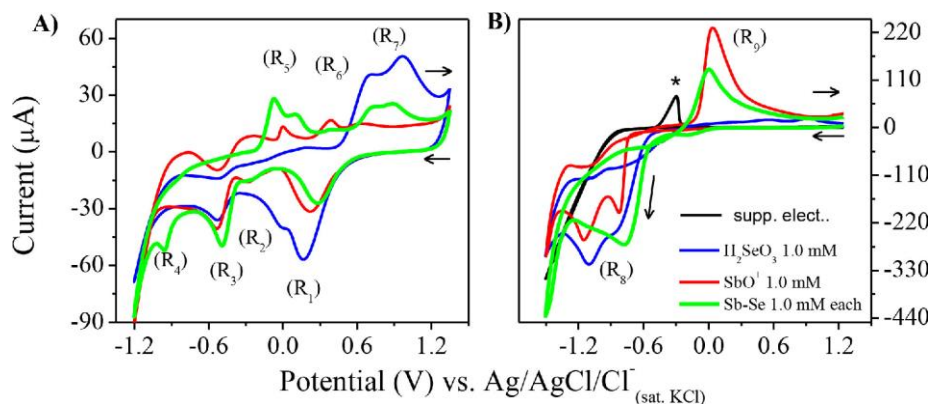rams on Pt with different inversion potentials (E_{inv}) at a scan rate of 50 mVs^{-1}, for the solution containing 1.0 mM SbO^+ in 0.5 M Na_2SO_4/H_2SO_4 at pH 2. The black line voltammogram shows the electrochemical profile of Pt in the supporting electrolyte.*[140]

Figure 46: *Cyclic voltammograms on A) Pt or B) FTO at a scan rate of 50 mVs^{-1}, and for the solutions containing 1.0 mM H$_2$SeO$_3$ (blue line), 1.0 mM SbO$^+$ (red line), and their equimolar mixture (green line) in 0.5 M Na$_2$SO$_4$/H$_2$SO$_4$ at pH 2.*[140]

Following this work, the Costa et al. team then went on to experiment with including an iron dopant and were able to achieve decent device stability and a certified efficiency of 5.6%. These Sb$_2$Se$_3$ films were obtained by co-electrodeposition under potentiostatic conditions with a bath content of 2.5 mmol/L of K(SbO)C$_4$H$_4$O, 2.0 mmol/L of SeO$_2$, 0.5mol/L of Na$_2$SO$_4$, and FeSO$_4$ compositions ranging from 0.125 to 1.25 mmol/L or 5%- 50% of the dopant relative to the antimony content of the bath. 600 millicoulombs of total charge was found to be the maximum to keep the film between 300 and 400 nm in thickness.[139, 140] After the electrochemical deposition is complete the film was then annealed at 300 °C for 3 hours in an inert tube furnace with selenium powder in order to recrystallize the low crystallinity films that result from electrochemical deposition and also add selenium to the film composition.
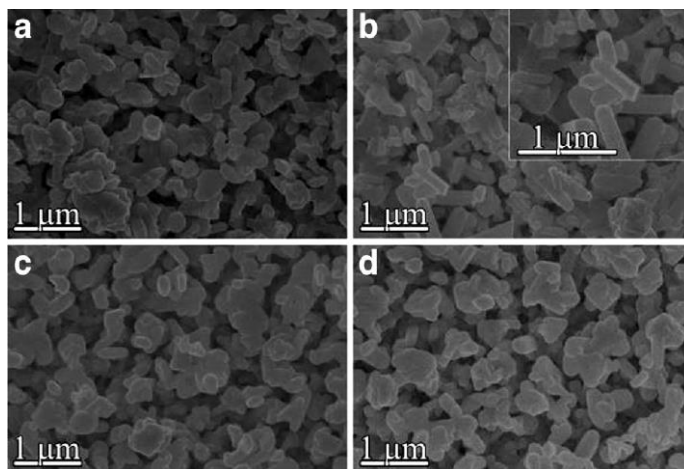
Figure 47: *Surface FE-SEM micrographs of thin films with 50kx of magnification. a non-doped film and those obtained from electrolytic bath with b 5%, c 20%, and d 50% of Fe ions (relative to Sb content in the bath)*[139]

Iron as a dopant was found to affect the band gap and the morphology very little, but the resulting electronic properties and photoactivity were measurably improved. The film obtained from a deposition bath composed of 5% of iron which had about the same photocurrent as undoped samples, but showed a carrier density that was three orders of magnitude higher than that of an undoped sample. Such a significant improvement in photocurrent may have a higher fill-factor and efficiency.[139]

Because the innovation this dissertation offers is depositing seeds to incite the growth of the film via nucleation and growth, it made sense to end this history section with a study by Shi et al.[178] In this work, a nitric acid bath containing Sb^{3+} and SeO_2 species was used to deposit a film on indium doped tin oxide (ITO) via chronoamperometry (CA) technique. Shi et al. proposed that the deposition occurred via a large overvoltage through 3D nucleation and growth mechanism

followed by diffusion limited growth. Like my own results, Shi et al. confirmed that orthorhombic Sb_2Se_3 particles with their size between 90 and 125 nm were obtained, and EDS showed that the atomic ratio for antimony and selenium was approximately 2:2.63, a good match to the expected stoichiometry.[178]
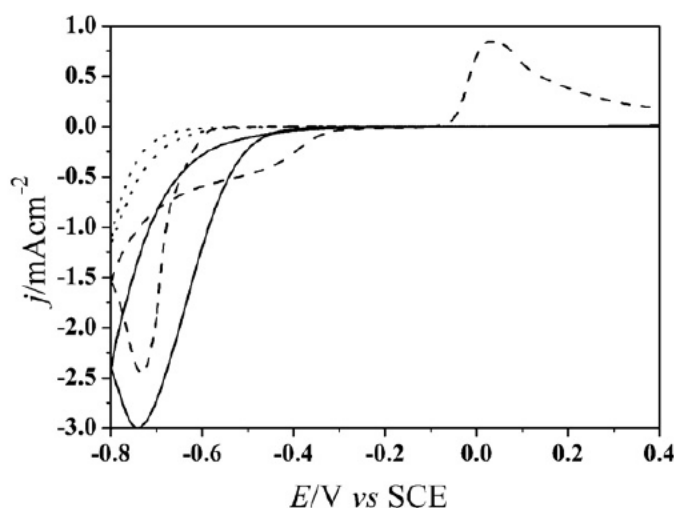

Figure 48: Cyclic voltammograms for n-Si electrode recorded by Shi et al. in different solutions: 0.1 M HNO₃ (dotted line); 4 mM Sb³⁺ + 0.1 M HNO₃ (dashed line); 2 mM SeO₂+ 0.1 M HNO₃ (solid line).[178]

This voltammogram showed that the onset current occurred at potential −0.42 V. This cathodic current, when compared to the background electrolyte only containing SeO_2 or Sb^{3+}, could be attributed to the reduction of Se (IV) because the reduction of Sb^{3+} occurred at more negative potential, but more likely due to the influence of Sb (III). This influence becomes evident in figure 49 that there is a cathodic current peak shift positively to −0.58 V compared to that of SeO_2 and the current intensity also increased.
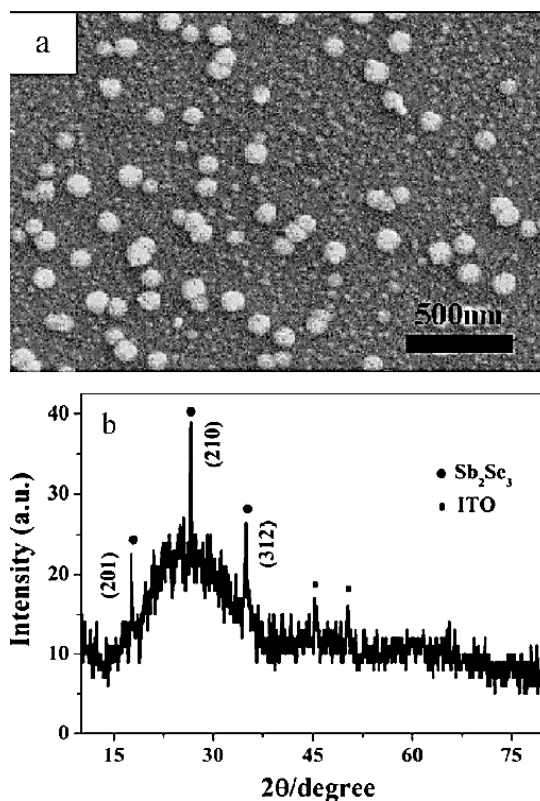
Figure 49: *SEM image (a) and XRD pattern (b) for Sb$_2$Se$_3$ electrochemically deposited onto ITO at E = −0.54 V.[178]*

Figure 49a shows the morphology of deposits produced at E = −0.54 V. Uniform particles can be seen with diameter at about 90–125 nm. The look of these particles and their pitch are quite different from morphologies I achieved. (In results section below). What I find most shocking about this 2012 study from Shi et al. is the large distance between these particles. The work cited, made no mention of the duration of the electrochemical deposition, but from what we learned from more recent papers from Costa/Mascara and from what I have observed myself it is likely that too low a temperature and too low a duration was used to deposit these seeds. By increasing either of these parameters, the density and coverage of seeds should become much greater.

The EDS spectrum that was achieved by Shi et al. showed that the element ratio for Sb:Se of 2:

2.65 which is very close to the 2:3 stoichiometric goal for which they were striving. The XRD

showed that a favorable orientation of (210) was achieved, but according to other later works the

most favored film orientation is (001). Shi et al. was comparing his orientation to the standard

diffraction pattern for naturally occurring Sb_2Se_3. It would be a few years before the optimal

orientation for solar cell absorber applications would be discovered.

Shi et al found that the potential used for fabrication of Sb_2Se_3 (E = −0.54 V) compound was not

sufficient to reduce antimony which means that Se particles formed in the over potential region

following the following equation:

Reaction 18: $$H_2SeO_3 + 4e^- + 4H^+ \rightarrow Se + 3H_2O$$

At the time of particle formation, the strong interaction between Se particles and soluble Sb (III)

species was such that, the deposition of Sb^{3+} occurred on the surface of Se particles.

Reaction 19: $$3Se + 2Sb^{3+} + 6e^- \rightarrow Sb_2Se_3$$

Shi et al. went further and attempted to grow a bulk Sb_2Se_3 film on his electrochemically

deposited seeds, which inspired the work that I am striving for now which is to selenize the

surface of the FTO in an inert tube furnace, leaving seeds which we can then electrochemically

deposit a film layer on.

A valuable result that came out of the work of Shi et al. was the equation for progressive

nucleation. This equation came from the lab's interest in understanding the nucleation and

growth kinetics of antimony in the electrodeposition process. They recorded current – time

transients for deposition of antimony onto the ITO substrate at the constant potential $E = -0.60$ V. This interpretation led to the curve shown in figure 50 showing the deposition transients plotted in a dimensionless form via normalizing two variables "j" and "t" with respect to the maximum current "j_{max}" and the corresponding time "t_{max}" at which point the maximum current was observed.[178,179] These data transformations shown in figure 50 follow the equation shown below to obtain the theoretical plots for progressive and instantaneous nucleation growth mechanism were calculated according to following equations: [178,180,181]

Equation 132: $\quad \dfrac{i^2}{i_{max}^2} = 1.9542 \left[\dfrac{t_{max}}{t}\right] \left[1 - \exp\left(-1.2564 \dfrac{t}{t_{max}}\right)\right]^2$

For Instantaneous Nucleation:

Equation 133: $\quad \dfrac{i^2}{i_{max}^2} = 1.2254 \left[\dfrac{t_{max}}{t}\right] \left[1 - \exp\left(-2.3367 \dfrac{t}{t_{max}}\right)\right]^2$
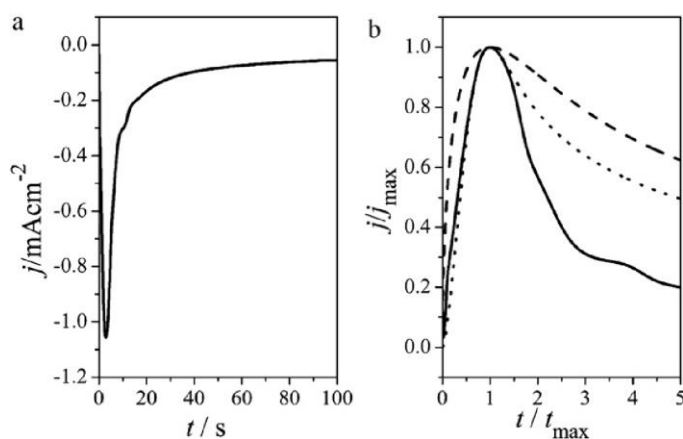
***Figure 50:** Current–time transient for selenium deposition onto ITO substrate at E = −0.68 V. (b) normalized current transient plotted in dimensionless form (solid line), the theoretical curve for instantaneous (dotted line) and progressive (solid line) nucleation.[178]*

Figure 50b depicts the calculated plots and a dimensionless form of the experimental plot of antimony reduction. This agreed with theoretical curves for instantaneous nucleation and growth mechanism, except for after the maximum peak value. After this point, the deposition slowed and deviated from the instantaneous process model. Shi et al. put forth that this deviation may be due to partial kinetic control of the growth.[178, 182]

4.3.4 Compositional Analysis with X-Ray Diffraction:

X-ray powder diffraction (XRD) was discovered in 1912 by German Physicist, Max von Laue, when he noticed that crystalline substances' lattice planes can act as three-dimensional diffraction gratings for x-ray wavelengths.[99] This technique operates on the phenomenon that x-rays can interfere constructively only when Bragg's Law is satisfied. Bragg's Law ($n\lambda = 2d \sin \theta$ where λ is the wavelength of the x-ray, d is the spacing of the crystal layers, θ is the incident angle, and n is an integer) is a law that relates the wavelength of electromagnetic radiation to the diffraction angle and the lattice spacing in a crystalline sample.[200] During XRD, a cathode ray tube generates x-rays by heating a filament to produce electrons which are then filtered to produce monochromatic radiation. A collimator then concentrates the beam and directs it toward the sample, bombarding the target material with electrons which produce x-rays that are then deflected and collected. The sample is scanned at a range of 2θ angles so that nearly all possible diffraction directions are achieved due to the random orientation of the powder or thin film sample. These diffracted X-rays are then detected, processed, and counted. The diffraction peaks are then converted to d-spacings (the distance between successive, parallel planes of atoms) to allow determination of the sample's composition as each material has a characteristic set of d-

spacings. In this way, databases are used to compare and assign the 2θ angles and d-spacings to known literature values.[98]

4.3.5 Compositional Analysis with Energy Dispersive Spectroscopy:

Energy Dispersive X-Ray Analysis (EDX), also known as Energy Dispersive Spectroscopy (EDS) is a technique commonly performed at the same time as SEM to achieve information about the sample composition. During SEM, electrons are used to produce images with varying contrast/grayscales denoting differences in atomic numbers of the sample's materials. An EDX detector is often paired with an EDX detector with which X-rays can also be used as a signal to ascertain chemical information. Because every atom contains a characteristic number of electrons at unique energy levels positioned in shells with different, discrete energies, an electron beam can be used to hit the inner shell of an atom to knock off an electron from the shell. This interaction leaves a positively charged electron hole on the atom so that when the electron is displaced, it attracts another electron from an outer shell to fill the vacancy. Whenever an electron falls from a high energy level to a lower energy level, the difference in energy is released. In this case, the energy released is in the form of an x-ray with a unique signal dependent on the element present and the transition executed. EDX generated x-rays occur in two steps: 1. The electron is knocked off the atom leaving a hole behind, and 2. The hole is filled by a new electron from a higher energy shell releasing a characteristic x-ray. Once those x-rays have been emitted, they can be detected by a silicon drift detector which uses software to interpret the x-ray signal in the form of elemental mapping or line scans which aim to identify each element that exists in the sample. [197] The signals generated and detected can be used for both qualitative and quantitative analysis including enabling users to identify both the type of elements as well as their percentage in the sample. However, because the x-rays used in EDS

analysis occur at a depth of 2 microns, EDS cannot always be considered a quantitatively accurate measurement. The *Practical Electron Microscopy Database*[196] has published that EDS can have a wide range of inaccuracies with typical accuracies. Low tolerances of ~2% can be achieved if standards composed of compositions similar to that of the sample are used to calibrate the EDS system, but without such standards, the common tolerance is around 10% with an accuracy of less than 50% for especially rough samples.[196] Due to these expected inaccuracies, EDS is often used only as a comparison to other compositional data such as XRD or for rough compositional comparisons between two similar samples or between two locations on the same sample.

4.3.6 Absorber Band Gap Determination from UV-Vis:

To determine the band gap of the deposited film, two methods were employed. One method was Kubelka Munk (KM) ultraviolet and visible (UV-Vis) measurements. The results from diffuse reflectance UV-Vis spectroscopy are presented in KM intensity vs. wavelength. Diffuse reflection was the chosen method for characterization of these Sb_2Se_3 films because the diffuse reflectance UV was developed specifically for materials in a neat state such as papers and powders, or in this case, thin films.[183] Since even pristine materials are still prone to internal inhomogeneities which cause changes in the propagation of light as it is scattered by any defects or inhomogeneities.

To describe this phenomenon theoretically, a model was developed by Paul Kubelka and Franz Munk in 1931 as a method for categorizing and modelling the appearance of films of paint. The model was meant to answer the question, "How does the color of a substrate change by the application of a coat of paint of specified composition and thickness, and especially the thickness

of paint needed to obscure the substrate".[184-188] Since then, the model has been used in many studies mostly for simple, but semi-infinite samples with one single parameter accounting for all the present geometric peculiarities and inhomogeneities. In the below equation, the scattering coefficient is *s* and R∞ is the diffuse reflectance:

Equation 134: $\quad R_\infty = 1 + \dfrac{k}{s} - \sqrt{\left(\dfrac{k}{s}\right)\left(2 + \dfrac{k}{s}\right)}$

Here, k represents the absorption coefficient of the sample (k = 4π (κ/λ)); where λ is the wavelength). This relatively simple form is easily solved for k/s yielding the familiar K-M transform[183]:

Equation 135: $\qquad\qquad \dfrac{k}{s} = \dfrac{(1-R_\infty)^{\wedge}2}{2R_\infty}$

This transform is proportional to the absorption coefficient and therefore is also proportional to the concentration. The term for scattering coefficient (s) is a semi-empirical parameter that was added to this model to account for the scattering process that takes place internally. The dominant contributors to the scattering coefficient are the refractive index of the sample and particle size whereas the wavelength and the absorption coefficient contribute very little and are described only as one constant term. This term is where this model can deviate from the experimental results as the scattering coefficient is gradually affected by wavelength.[183] The above equation for k/s describes the absorbance transformation as seen in transmission spectroscopy. Because it is relatively simple, this equation has been adapted to describe the diffuse reflectance transform in the standard UV-Vis software of commercial spectrometers like the one used in this dissertation.[183]

To transform the KM vs. wavelength data to a plot with which we can measure bandgap (KM vs. Energy in electronvolts), the wavelength must be converted to an energy in electron volts via

employing the below equation (E = energy, h = Planck's constant, c = speed of light, and λ = achieved wavelength) to determine the energy at the location of the highest slope of the plot.

Equation 136:
$$E = \frac{hc}{\lambda}$$

To achieve the bandgap, this equation can be adapted to 1240/ λ (in nm) = E (in eV). The bandgap is approximately equal to the wavelength that aligns with the steepest slope of the largest reflectance peak. This slope can be seen in the results section below.

4.3.7 Surface Photovoltage Measurements (SPV):

Surface photovoltage or SPV can be defined as the change in potential at the surface of a functional layer due to illumination. SPV measurements are useful in determining the minority carrier diffusion length in semiconductors. This means that it can be used to determine the distance a charged particle can diffuse. Because minority carriers are the key determinant of p-n junction behavior, measuring SPV can provide much information about the potential PV performance. SPV is a popular method since it is contactless and non-destructive. In this dissertation the absorber film on FTO coated glass is placed on a ground electrode with a kelvin probe hovering a small distance above it. A monochromator lamp illuminates the surface, scanning through a range of wavelengths to vary the absorption depth of the photons. If the carrier generation occurs very deep in the sample, then there will be very few minority carriers able to reach the surface of the film and the measured photovoltage will be very low.[188-190]
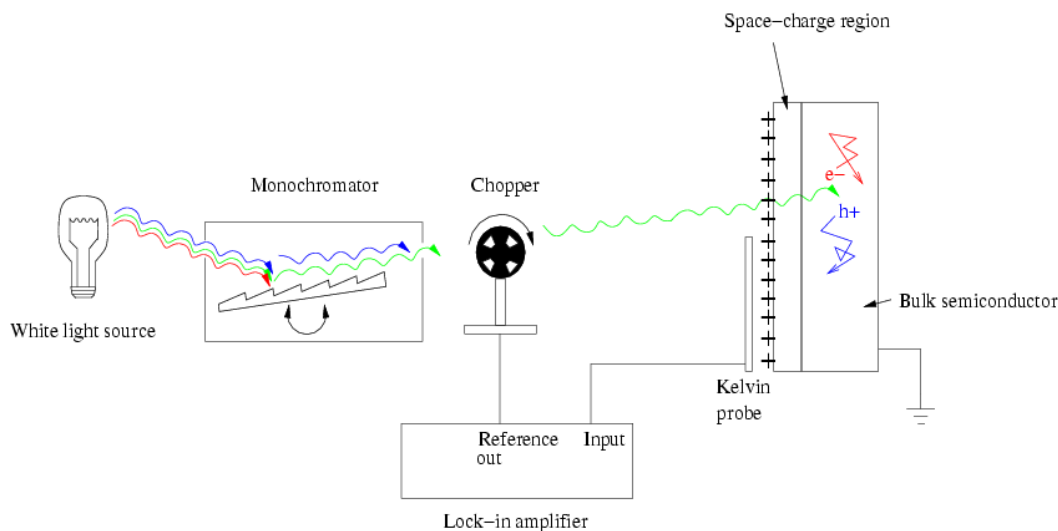
Figure 51: *Schematic of a typical SPV apparatus.*[188,189]

By monitoring the potential of the semiconductor surface while electron-hole pairs are generated

via a light source, we can achieve an SPV response for a variety of wavelengths of light. Often, a

built-in electric field is present due to defects located in the depletion region or space charge

region that is observed at the semiconductor surface. The electric field effectively reduces the

carrier density which appears on the band diagram as band bending away from the Fermi level.

This band bending is the source of the measurable surface potential. The energy of the incoming

photons creates electron-hole pairs within the bulk of the semiconductor that will then diffuse

through the semiconductor to reach the surface space charge region. Because photogenerated

minority carriers have a shorter diffusion length than the numerous majority carriers, the change

in surface potential upon illumination is therefore a measure of the ability of minority carriers to

reach the surface, aka, the minority carrier diffusion length.[188-190]

Another way to approach SPV analysis is to consider that the SPV signal is a direct result of each

time photogenerated charge carriers are separated in space. The signal is dependent on the

phenomenon of the photogeneration of mobile charge carriers, the recombination of charge carriers, and the transport and relaxation of space charges which are all the result of the absorption of light. The most useful of the data to be extracted from SPV measurements is the contact potential difference or CPD between the sample and the reference electrodes. SPV can be defined as its negative light-induced change ($-\Delta$CPD).[191]

As the electric potentials are measured between the two electrodes, one coated with a photoactive material (in this case, Sb_2Se_3), and one acting as a reference electrode. Both electrodes must be metallic but can be either be metals or transparent conductive metal oxides. Choosing the most favorable metal as the electrodes is dependent on the work function, W, which described the lowest energy that is required to remove an electron from the metal to the surrounding vacuum. There is a work function for the bare sample (W_s) and one for the reference electrode (W_{ref}). Figure 52 depicts how the sample and RE are connected electrically. The electrons can be observed flowing from the electrode with the lower of the two work functions to that of the higher work function. At the time of current flowing, the fermi energy of the sample and reference, ($E_{F,s}$ and $E_{F,ref}$ respectively) will continue to change until an equilibrium fermi energy is reached for both electrodes. Since the work functions remain constant, the difference between the two work functions is related to the electrostatic potential and is known as the CPD between both electrodes and can be described by the following equation[191]:

Equation 137: $$q * CPD \equiv W_{ref} - W_s$$

The adsorption of molecules or the deposition of photoactive material can affect the work function of the sample film. The figure 53 shows a situation where W_s is independent of the deposited photoactive material in the dark.
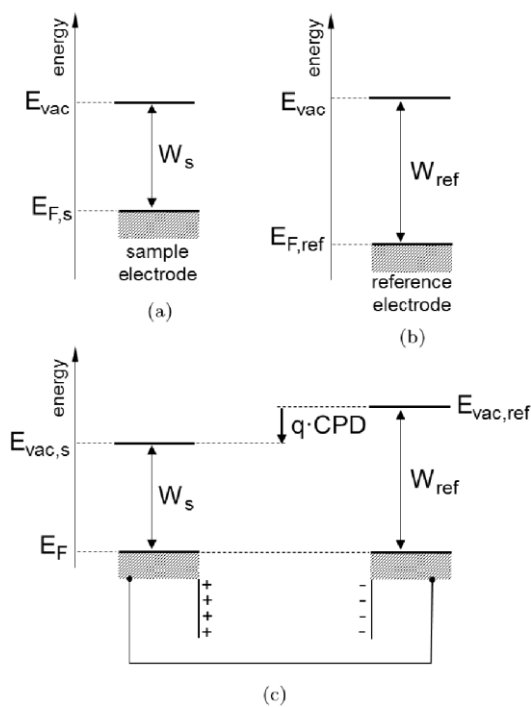

Figure 52: *a) Energies of isolated bare sample and (b) reference electrodes and (c) of electrically connected bare sample and reference electrodes. E_{vac}, $E_{F,s}$, $E_{F,ref}$, E_F, Ws, Wref and CPD denote the vacuum energy, the Fermi energies of the isolated sample and reference electrodes and of the connected electrodes, the work functions of the sample and reference electrodes and the CPD, respectively.*[191]
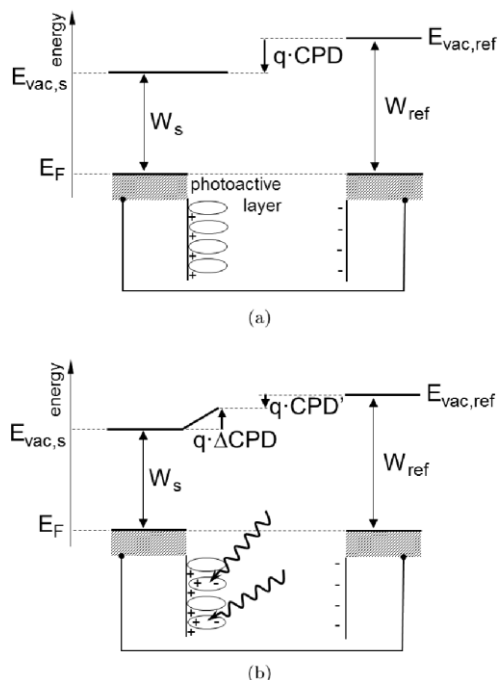
Figure 53: *Schematic diagram of energies for a sample electrode coated with a photoactive layer and connected with a reference electrode in (a) the dark and (b) under illumination. ΔCPD denotes the change of the CPD due to the separation of photogenerated charge carriers in space.*[191]

The results of collecting ΔCPD in the dark are only useful when compared to that of the sample under illumination. In this state, the photogenerated charge carriers are spatially separated meaning that the photogenerated electrons and holes move toward the region of the photoactive layer where the sample electrode and the external surface interface. An electrostatic potential arises in this region where photogenerated charge carriers are separated in space. By illuminating the surface, we are changing the work function of the sample electrode via separating the electrostatic potential between negative and positive charge carriers in the photoactive layer. The SPV is then defined as the difference between the work functions of the sample electrode under

illumination ($W_{s,ill}$) and in the dark ($W_{s,dark}$). In the following equation q is the elementary charge

an electron (1.602 x 10^{-19} coulombs).[191]:

Equation 138: $$q * SPV \equiv W_{s,ill} - W_{s,dark}$$

Therefore, if the work functions of the reference electrode in the dark ($W_{ref,dark}$) and under

illumination ($W_{ref,ill}$) are equal, then the SPV corresponds to the negative light-induced change of

the CPD:

Equation 139: $$SPV = -\Delta CPD$$

One can also use the change in the dipole at the surface of the sample to describe the

charge carriers separated in space. In figure 53 the ΔCPD is shown for an instance where the

separation of photogenerated electrons and holes occur at the interface between the external

surface and the sample electrode or when it is occurring at the interface with the sample

electrode and the external surface.[191]
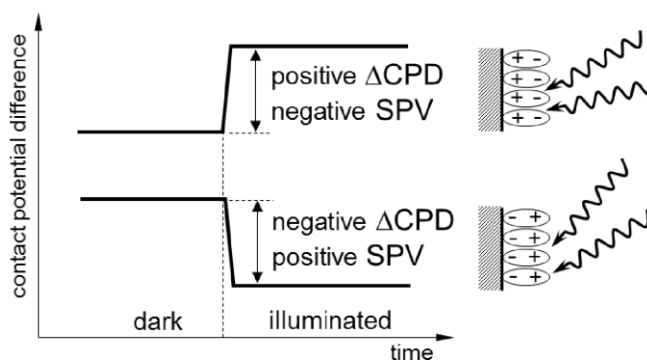
Figure 54: *Schematic change of the contact potential of sample electrodes coated*

with a photoactive layer resulting in separation of photogenerated electrons and holes

toward interface with the sample electrode and the external surface, respectively (negative

ΔCPD and positive SPV) or toward the external surface and interface with the sample electrode,

respectively (positive ΔCPD and negative SPV).[191]

From these fundamental models the SPV measurement can provide results in CPD vs. time and, by proxy, CPD vs. energy. The wavenumber of incident light is observed to change linearly versus time, so since the starting wavenumbers and ending wavenumbers are known at the time of experimental setup as well as the duration of the scan. The final step is to convert x-axis from time to wavenumbers and then convert wavenumbers to photon energy (in eV) via the photon energy equation in the UV-Vis section.

SPV analysis is a wide-spreading technique for useful semiconductor characterization especially in the photoactive field of solar cells. Determining the minority carrier diffusion length is required to characterize the performance of many other devices such as photo-conducting detectors and bipolar transistors. If one can be certain of the ratio of the diffusion length to the device dimensions, then one can determine the gain. SPV serves as a convenient method of measuring the density of impurity-derived recombination centers that limit device performance. In industry, SPV is performed as a test of material quality and performance.[189-192]

4.3.8 Photoelectrochemical Analysis (Chopped Light):

A final performance test known as a photoelectrochemical (PEC) linear sweep voltammetry (LSV) was performed. The chopped light experiments were performed using a three-electrode system described previously. The electrolyte used for PEC analysis is methylviologen (MV) and the film on FTO sample underwent a linear sweep through a range of potentials in darkness to achieve the orange background curve shown in figure 65 in the *Results and Discussion* section. During this experiment, a one-sun illumination lamp was directed at the film surface for 5 seconds on, 5 seconds off alternating. (Schematic shown in figure 55). A potentiostat was used to record the

change in current density as potential and lighting conditions are changed. The performance of the deposited films determined in this dissertation was too low to be competitive with the performance of other published absorber layers (on the order of microamps instead of mA), but the PEC/chopped light plots in a future section do show a positive current at more positive potentials including a positive current above the dark current background. This is the signature curvature of a p-type semiconductor as expected for an Sb_2Se_3 absorber layer.
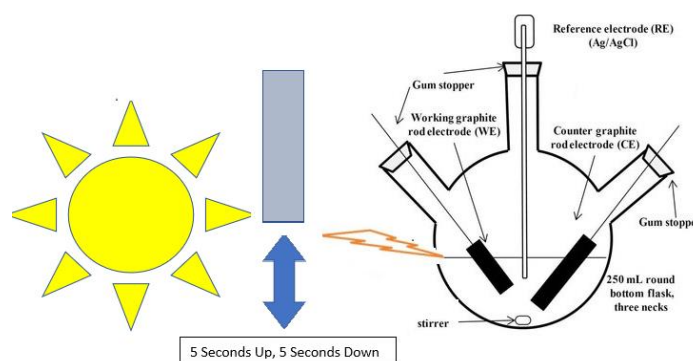
Figure 55: PEC LSV chopped light experimental setup depicting the three-electrode setup, the 1-sun illumination light source and the handheld shutter shown as a grey rectangle. This shutter blocks the light and transmits the light each for 5 seconds at a time producing the wave-like shape shown in the LSV plots in the "Results and Discussion" section below

4.4.0 Materials and Methods:

All chemicals were of analytical grade and used directly without further purification. The following reagents were used: Na_2SO_4 (Sigma-Aldrich, >99.9 %), H_2SO_4 (Sigma-Aldrich, 98%), FTO coated glass (3 x 3" x 2.2 mm, R: 12-14 ohm/sq) (MTI Corporation), FTO coated glass (50 mm × 50 mm × 2.2 mm, R: ~7 Ω/sq) (Sigma-Aldrich), Selenium(IV) oxide, SeO_2 99.8%, trace

metal basis (Thermo Scientific™), Potassium antimony(III) tartrate hydrate $K(SbO)C_4H_4O_6$ x 0.5, Greater Than or Equal to 99% (Millipore Sigma), Potassium Permanganate, Crystal, High Purity Laboratory Grade (Carolina Biological), LABCHEM Chemical Ammonium Hydroxide 1.0N (Grainger Industrial Supply), Hydrogen Peroxide, 30%, Reagent Grade (Carolina Biological), Isopropyl Alcohol 99.9% - ACS Reagent Grade (Alliance Chemical), Acetone, Semiconductor Grade, 99.5% (Thermo Scientific™) (Fisher Scientific), Spectrum Chemical Dehydrated Alcohol, 200 Proof, Biotech Grade (Cole-Parmer), Acros Organics AC419271000 Selenium, powder, <325 mesh 99.7% (Cole-Parmer). Water was purified to 18 MΩcm resistivity using a Nano-pure system. All substrates cleaved for edge-on SEM imaging were cut via a Vari/Cut VC-50 diamond blade. (LECO Corporation Michigan)

4.4.1 Treatment of FTO Substrates:

FTO was cleaned ultrasonically with the following solvents in-order for 5 min in each solvent: deionized water, ethanol, acetone, and isopropanol. The samples that received a $KMnO_4$ treatment were then immersed in a solution of 0.5 mol L^{-1} (0.9 g) $KMnO_4$ in deionized water for 1 h and washed with deionized water and 30% H_2O_2. Then, the FTO was hydrophilized for 1 h at 70°C in a solution of $H_2O/H_2O_2/NH_4OH$, in a ratio of 5:1:1 (10mL/2mL/2mL), respectively. Finally, it was rinsed with deionized water and dried in an air gas stream.

4.4.2 Depositing/synthesizing and Characterizing of Sb₂Se₃:

Electrochemical experiments were carried out using a potentiostat/galvanostat (Autolab PGSTAT 302 N, Metrohm-Eco Chemie). Cyclic Voltammetry (CV) was used to evaluate the electrochemical process of each element. A three-electrode configuration electrochemical cell was

used with fluorine-doped tin oxide (FTO, 12-14 ohm/sq, MTI corporation) coated glass working electrode (geometric area of 1 cm^2), a Pt wire counter electrode and a Ag/AgCl/Cl$^-$ (sat. KCl) reference electrode. A solution of 2 mM/L SeO$_2$ (0.055 g), 2.5 mM/L K(SbO)C$_4$H$_4$O$_6$ (0.203 g), and 0.5 M/L Na$_2$SO$_4$ (17.755 g) was prepared, and the pH adjusted to 2 by adding 0.01 M H$_2$SO$_4$ dropwise. This solution is then used as the substrate solution in the three-electrode system.

The deposition occurs by applying a potential via chronoamperometry for a set duration (see table 3). CV and LSV (linear sweep voltammetry) were carried out using a potentiostat/galvanostat (Autolab PGSTAT 302 N, Metrohm-Eco Chemie). The films are then analysed via a Bruker AXS X-ray diffractometer, a Thermo Fisher Quattro S Environmental SEM/EDS system, an Oriel Cornerstone 130 1/8 m Monochromator, a Kiethley Multimeter (2700), an E-Chem-Gamry Interface 1010E Poteniostat/Galvanostat/2RA, an Olympus BX51 Optical Microscope, and a UV-Vis -Thermoscientific-Evolution 220 UV-Visible Spectrometer.

4.4.3 Thermal Selenium Seeding Annealing/Treatment Process:

For the samples that underwent an annealing treatment: Once the film has been deposited on the FTO coated glass, rinsed with 18 MΩcm deionized water, and dried under a stream of air, it was annealed at 300°C for 3 hours in a Thermo Electron Corporation Lindberg BLUE M tube furnace under a constant flow of Argon in the presence of a crucible containing 0.2g of Se powder, or Sb Powder, or a combination of the two. Samples that underwent the pre-deposition seeding/annealing process was treat the same way but before electrochemical deposition instead of afterward.

4.5.0 Results and Discussion:

4.5.1 Cyclic Voltammetry Experiments:

Prior to performing the deposition of Sb_2Se_3, first a series of experimental cyclic voltammetry

(CV) experiments were performed to probe the reduction and oxidation potentials of each of the

precursors separately in solution. By comparing the CV plots of three different electrolyte

solutions: one containing the selenium precursor (SeO_2) only, one containing the antimony

precursor ($K(SbO)C_4H_4O_6$) only, and one with both precursors present, we can see how the two

precursor curves appear to add up to form the combined precursor solution curve. The combined

solution (with both precursors) as shown in figure 56 (blue trace), appears to be a combination of

the peaks shown for each of the single precursor solution traces.
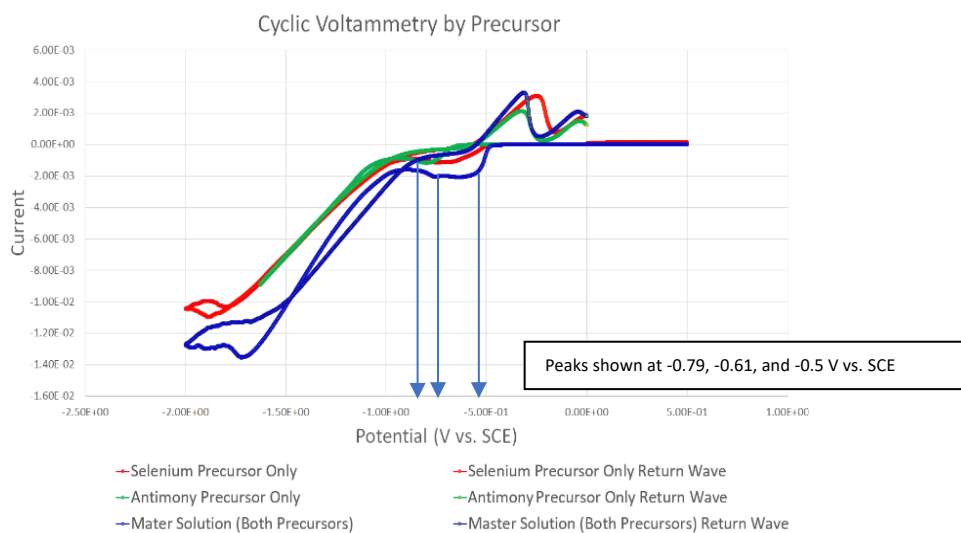
Figure 56: Cyclic voltammetry of separate precursor solutions using a three-electrode system including a platinum counter electrode, FTO glass working electrode, and a saturated calomel reference electrode (SCE). The red curve shows the CV results from a 2 mmol/L concentration of SeO_2 and 0.5 M/L concentration of Na_2SO_4 solution in deionized water. The blue curve shows the CV results from a solution with 2.5mM/L $K(SbO)C_4H_4O_6$ and 0.5 M/L concentration of Na_2SO_4

solution in deionized water. Finally, the blue line shows CV results from the combined solution used for all Sb_2Se_3 depositions consisting of 2 mmol/L concentration of SeO_2, and 2.5mM/L $K(SbO)C_4H_4O_6$ 0.5 M/L concentration of Na_2SO_4 solution in deionized water. The three main overlapping peaks as indicated by the combined traces are at -0.79, -0.61, and -0.5 V vs. SCE.

These results allowed for the determination of useful redox potentials for Sb_2Se_3 deposition. The peaks of note (labelled in figure 56) show that three potentials of interest include -0.79, -0.61, and -0.5 V vs. SCE. This informed the potentials used for deposition trials.

4.5.2 Compositional Analysis:

To ensure that the film deposited is, in fact, the target composition (Sb_2Se_3), EDS and XRD was employed. These were then compared to accepted results achieved in literature. Figure 57 shows the achieved XRD spectrum of film 6. All peaks in the XRD spectrum are identified as either FTO or Sb_2Se_3.

While EDS was used to confer the composition determined by XRD via weight and atomic percent ratios and elemental maps, this was mostly a qualitative analysis. Because the x-rays used in EDS analysis occur at a depth of 2 microns, EDS cannot be considered a quantitatively accurate measurement. The *Practical Electron Microscopy Database*[196] has published that EDS can have a wide range of uncertainty when it comes to reported atomic and weight percentages with typical accuracies reported with an approximate 10% error and an accuracy of less than 50% for especially rough samples. While these high compositional uncertainties can be mitigated by using standards composed of compositions similar to that of the sample to achieve low tolerances of ~2% of the measured value, these standards were not utilized in this

dissertation. Therefore, any EDS data reported is used only for determining the presence or absence of an element for comparison to the XRD results.
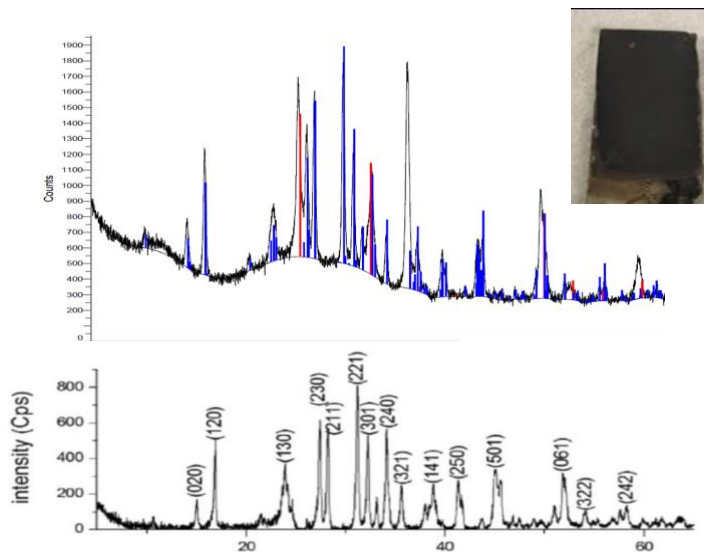

Figure 57: *Image in upper right showing an optical photo of film 6. The top image shows an XRD spectrum achieved from film 6 while the bottom image is a comparison XRD spectrum of pristine Sb_2Se_3 nanorod film from Ko et al.[193] The blue coloring of peaks in the top image represents peaks that match the spectrum of Sb_2Se_3 (also known as (antimonselite) while the red peaks match those of the tin oxide representative of the FTO coating on the substrate.*
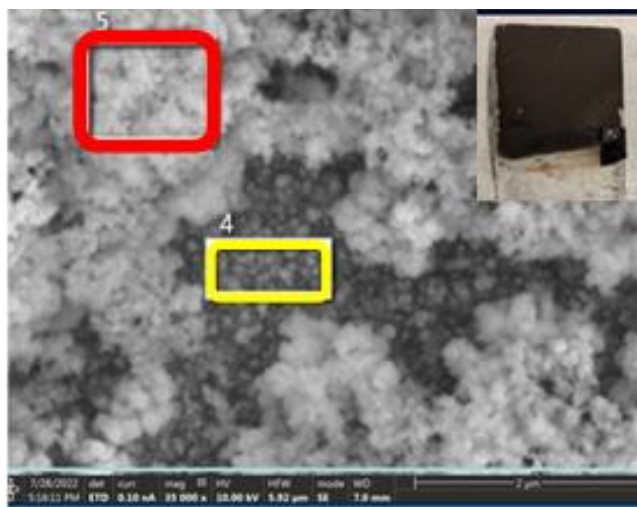
Figure 58: *Image on upper right showing an optical photo of film 9. An SEM image achieved from film 9 showing the lighter colored deposited film and the darker colored FTO beneath it.*

4.5.3 Deposition Temperature Comparison:

A parameter other than voltage and duration that affects the morphology and therefore performance of the absorber layer film is the temperature of deposition. Figure 59 shows the morphological and compositional differences between two films (8 and 9) that underwent the same conditions except for the deposition temperature differing. Refer to figure 58 for film 9 which was deposited at 25°C. We can compare this data to that shown in figure 59 of film 8 which was deposited at 70 °C. The morphology shows a denser film with much better coverage of the FTO surface when deposited at a higher temperature. This is because the added thermal energy enhances the kinetics of the electrochemical reaction making it easier to overcome the energy barrier of the surface energy of the of the FTO surface producing more nucleation sites. This allows for easier deposition of more homogeneous/denser films. The EDS map shown in figure 60c shows the success of the deposition to deposit antimony and selenium in the same locations on the surface.
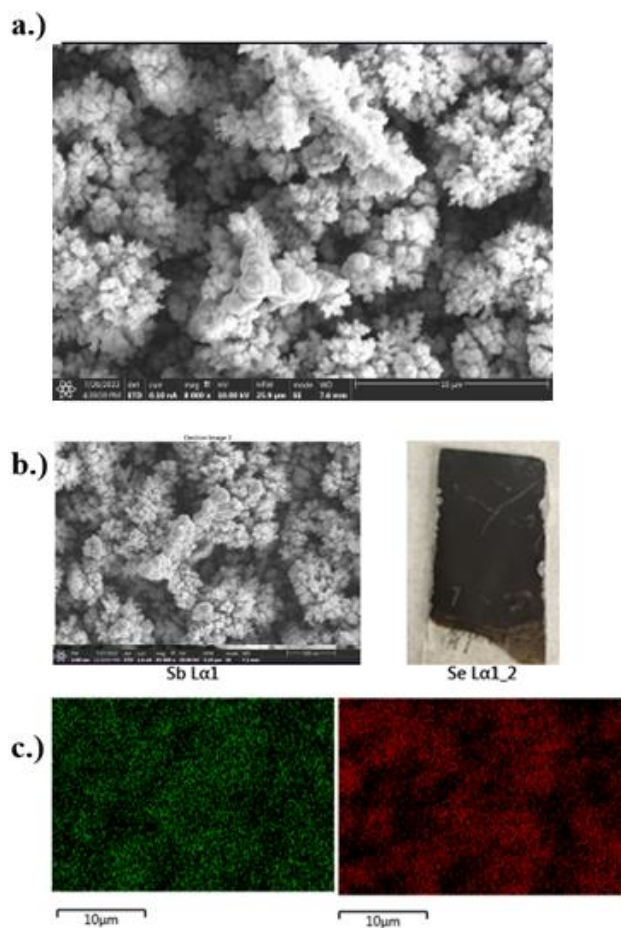
*Figure 59: Figure **a** shows the SEM micrograph of the surface of film 8. Figure **b** represents a similar morphology image with the optical image of the film. Figure **c** shows the corresponding EDS map of the location of antimony in green and selenium in red.*
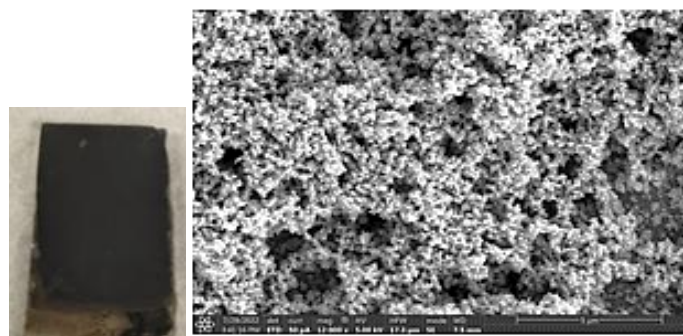

Figure 60: On left: an optical image of film 6. On left, an SEM micrograph showing the surface morphologies of this film.

4.5.4 KMnO$_4$ Treatment Analysis:

Costa et al. proposed a KMnO$_4$ surface treatment to improve deposition on the FTO coated glass.[139]

Employing this strong oxidizing solution treatment prior to the hydrophilization step affects the morphology as seen in figure 61 and 62. The improvement in the nanostructures and film density after performing this pre-treatment on the FTO is comparable to past literature in which a similar KMnO$_4$ surface treatment was utilized on the photovoltaic (PV) hole transfer layers (HTL) and graphene oxide (GO) optoelectrical layers.[137,138] The success of these works revolves around the concept that KMnO$_4$ is a strong oxidizer and exfoliate which improves the overall conductivity of the substrate surface by improving the bonding to the GO (or similar substrate such as FTO) as the oxygenated functional groups are more active.
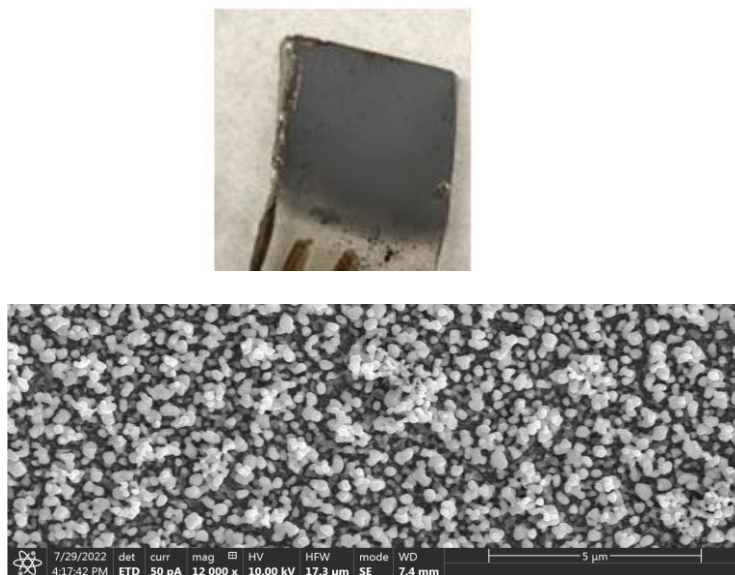

Figure 61: From top to bottom: an optical image of film 6, an SEM image of the surface morphologies of this film.

4.5.5 Anneal Treatment Comparison:

The final parameter probed for effects on Sb_2Se_3 absorber layers is the presence of a post deposition annealing treatment. As shown is figure 62 and 63, the presence of a 3-hour tube furnace anneal at 400 °C in an argon atmosphere with pure selenium powder present drastically affects the morphology and composition. In one example (Figure 62), the globular shapes become melded together to cover the surface much more completely and homogeneously. In the other example (Figure 63), the nanoparticles change shape producing larger, more globular shapes rather than the previous round flat shapes resulting in a single particle type instead of the non-homogeneous morphology of the pre-annealed sample.
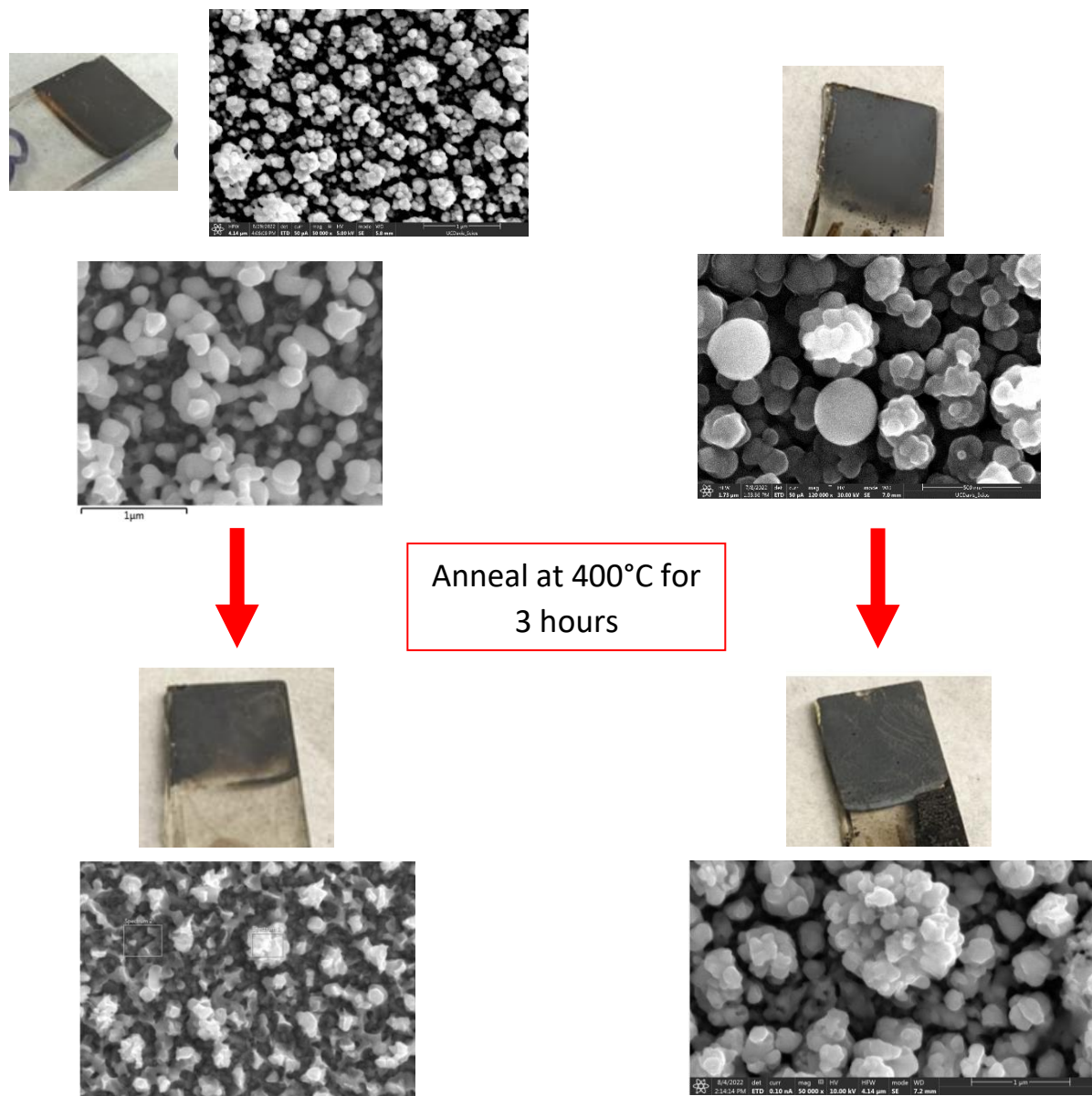
Anneal at 400°C for 3 hours

Figure 62 (Left): *The set of figures above the red arrow shows the optical image and SEM micrograph of film 2. The set of figures below the red arrow shows the optical image and SEM micrograph of the post-annealed film (2 – PA).*

Figure 63 (Right): *The set of figures above the red arrow shows the optical image and SEM micrograph of film 3. The set of figures below the red arrow shows the optical image and SEM micrograph of the post-annealed film (3 – PA).*

4.5.6 Experimental Bandgap Determination:

The bandgap as determined via UV-Vis measurements was then compared to similar SPV (surface photovoltage) measurements as described in the *History and Theory* section. The output SPV plots were background corrected and converted to eV in a similar manner by converting the potential achieved vs. time plot to a photovoltage vs. energy plot as shown in figure 64.

In the KM and SPV plots shown in figure 64, the red dotted lines indicate the energy in eV corresponding to the determined band gap of the film tested. For film 8 (top of figure 64) the UV-Vis measured the band gap while the SPV tests determined the bandgap to be 1.2 eV. For the post-annealed film 3 – PA the UV-Vis bandgap result is 1.15 eV while the SPV plots determined the bandgap to be 1.2 eV. These are both successfully in the accepted bandgap range of Sb_2Se_3 in literature: 1.075 eV to 1.21 eV.[146] Based on these experiments; the annealing treatment does not seem to affect the bandgap in any significant way. All the experimental data including the determined bandgap range determined using the described UV-Vis and SPV experiments can be found in table 3 in the *Experimental Results Table and Energy Diagram* section.
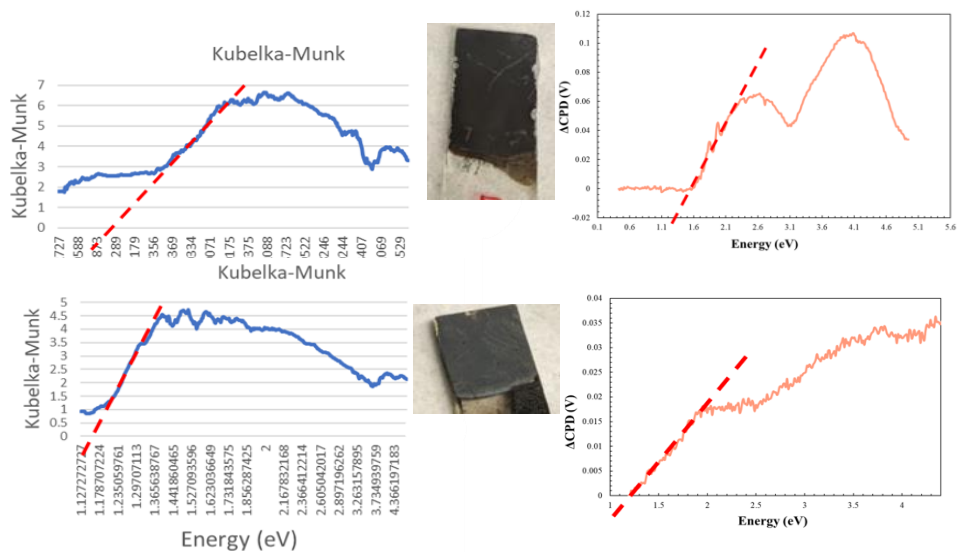
Figure 64: *Converted UV-Vis and SPV plots to determine the band gap of the deposited films. The top row shows the data for film 8 while the bottom row corresponds to film 3 – PA. The left side plots are the results of the Kubelka Munk UV-Vis measurements while the right side is the SPV results. The red dotted line follows the slope of interest (steepest area of the curve) and indicates the bandgap energy on the x-axis. As you can see the annealing treatment did not seem to affect the bandgap in a significant way.*
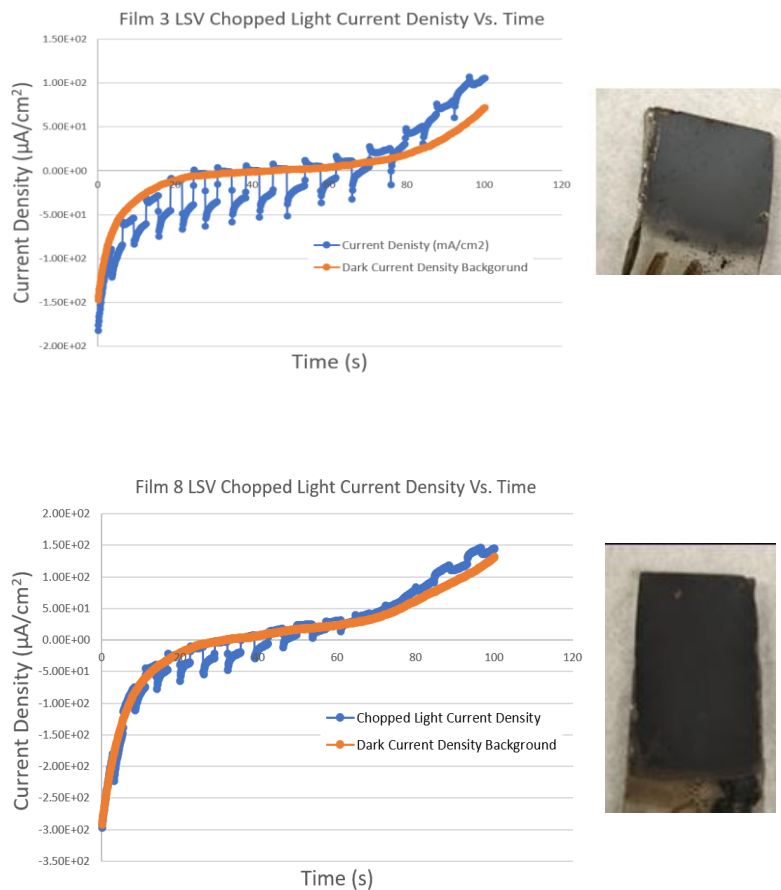
Figure 65: *Results of photoelectrochemical linear sweep voltammetry with one sun illumination chopped light. The orange curve represents the dark background while the blue curve shows the current density vs. applied voltage with shutter open for 5 seconds on, 5 seconds off alternating. The top image is film 7 and the bottom one is for film 8. (Discussed further in the "History and Theory" section)*
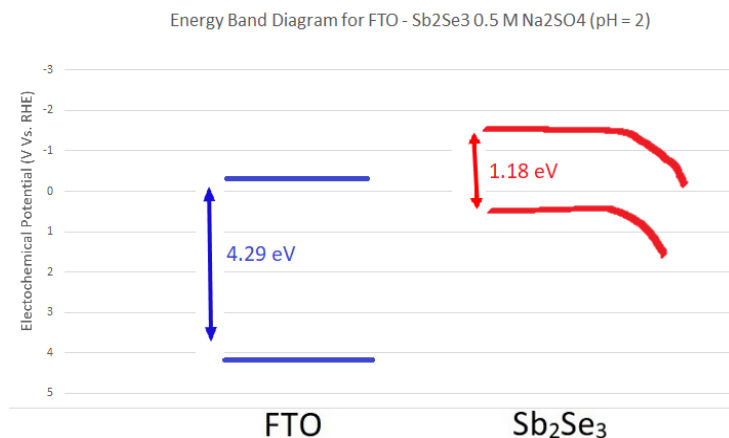
Figure 66: *Energy band diagram showing the conduction band, valence band, band gap of the working electrode coating (FTO), and the achieved target deposition material (Sb_2Se_3). Sb_2Se_3 was determined to be a p-type semiconductor as expected from literature, so the diagram includes band bending towards positive energies.*

4.5.7 Pre-Deposition Selenium Seeding Treatment Analysis by FTO Supplier:

Thus far, this work has explored many of the parameters that are tuneable in an electrochemical deposition of a PV absorber layer. CV experiments revealed the redox potentials of interest between the depositions using each of the precursor solutions and the combined solution. It is shown that Sb_2Se_3 can be successfully deposited via electrochemical means. The surface treatments, deposition temperatures, deposition duration, bath compositions, and post-deposition selenization steps were attempted, tuned, and discussed by my predecessors while my goal in this dissertation was to combine the most useful parameters and processes to optimize Sb_2Se_3 film growth via electrochemical deposition.

Following the thread of the work performed previously, a new possible process step revealed itself. In all electrochemical deposition literature reviewed for this dissertation, the only selenization or

annealing step was only present after the deposition has already been performed. This led to a curiosity about what would happen if this step occurred before the deposition. Would adding the same post-deposition annealing treatment to before the deposition improve the conformal quality of the film? Would the solid selenium in the tube furnace during the 300 °C 3-hour anneal deposit seeds onto the FTO surface and if so, how will the presence of seeds affect the film morphology?

This investigation began with performing the anneal on FTO coated soda lime glass from two separate substrate suppliers. Figure 67 below shows a picture of the annealing/seeding procedure setup while figures 68 and 69 show the differences between the SEM/EDS of the substrate surface of two different substrate suppliers after undergoing the KMnO$_4$ treatment for one hour (causing an amber color) followed by the H$_2$O/H$_2$O$_2$/NH$_4$OH hydrophilization step. "Supplier A" corresponds to FTO coated glass from MTI Corporation with the following specifications: 3 x 3" x 2.2 mm, R: 12-14 ohm/sq while supplier B refers to FTO glass form Sigma-Aldrich (50 mm × 50 mm × 2.2 mm, R: ~7 Ω/sq).
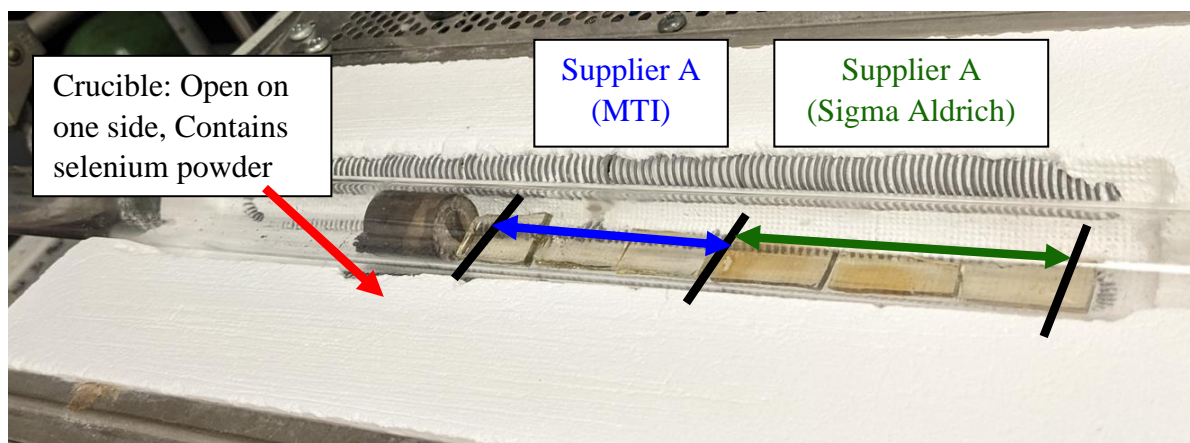

Figure 67: *Picture of tube furnace setup which was run at 300°C for 3 hours under a positive pressure flow of argon.*
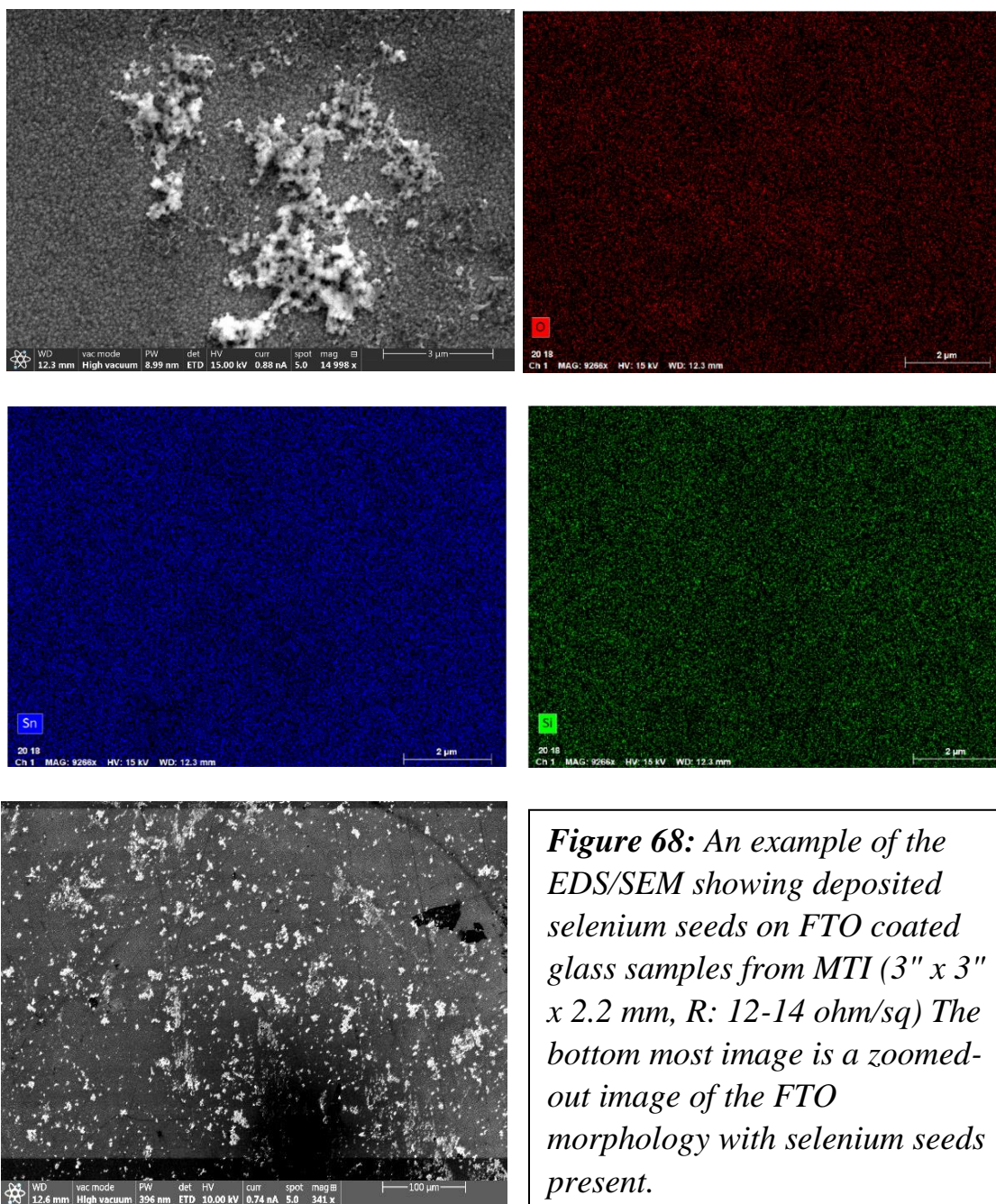
Figure 68: *An example of the EDS/SEM showing deposited selenium seeds on FTO coated glass samples from MTI (3" x 3" x 2.2 mm, R: 12-14 ohm/sq) The bottom most image is a zoomed-out image of the FTO morphology with selenium seeds present.*
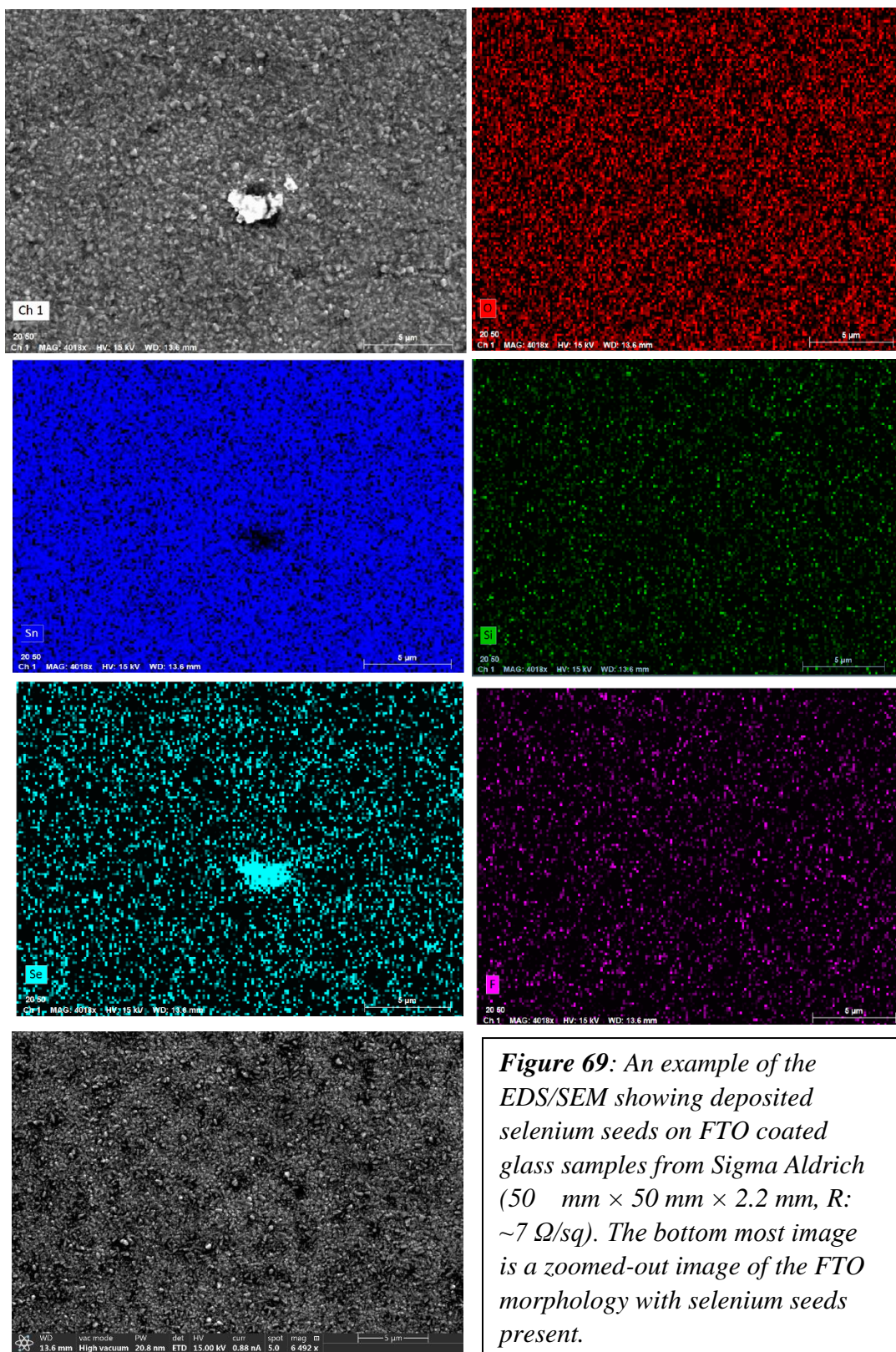
Figure 69*: An example of the EDS/SEM showing deposited selenium seeds on FTO coated glass samples from Sigma Aldrich (50   mm × 50 mm × 2.2 mm, R: ~7 Ω/sq). The bottom most image is a zoomed-out image of the FTO morphology with selenium seeds present.*

With the SEM/EDS evidence that seeds had been deposited seen above, the samples that underwent electrochemical bath deposition using the potential, temperature, and duration which was found to be optimal in the earlier parameter experiments. The films were then deposited on the seeds and further analyzed by UV-Vis measurements and further SEM and EDS including edge-on images after cutting samples in half via a diamond saw. Two of the UV-Vis results are shown below in figure 70. While the UV-Vis plot has a similar shape as those of the unseeded samples, the bandgap determined from these plots were less than those for the film deposited with no seeds. The band gap range found for all the seeded films regardless of the supplier is the 0.95 – 1.15 eV.
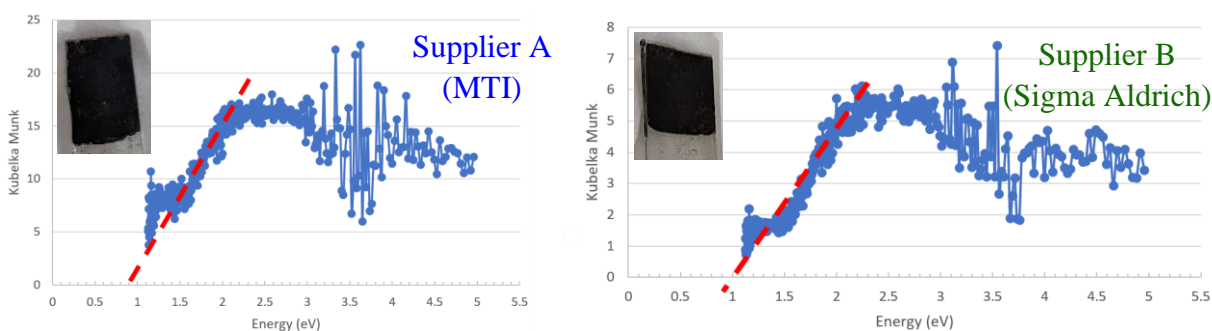

Figure 70: Results of UV-Vis analysis for bandgap determination for MTI substrates on the left (film 14S) and Sigma Aldrich on the right (film 16S). See the data table below for more information about the corresponding parameters used.

Two distinct morphologies were observed determined by the supplier. As seen in figures 68 and 69, the FTO layer on the substrate looks more globular with sphere-like particles for the MTI samples and more angular/prismatic features for supplier B. This indicates that each supplier used a different deposition method when depositing the FTO layer. As shown below, the morphology of the underlying FTO film has a profound effect on the resulting Sb_2Se_3 film

morphology. Figures 71 and 73 below capture the morphological differences between the two supplier substrates and therefore the two distinct types of deposited films.
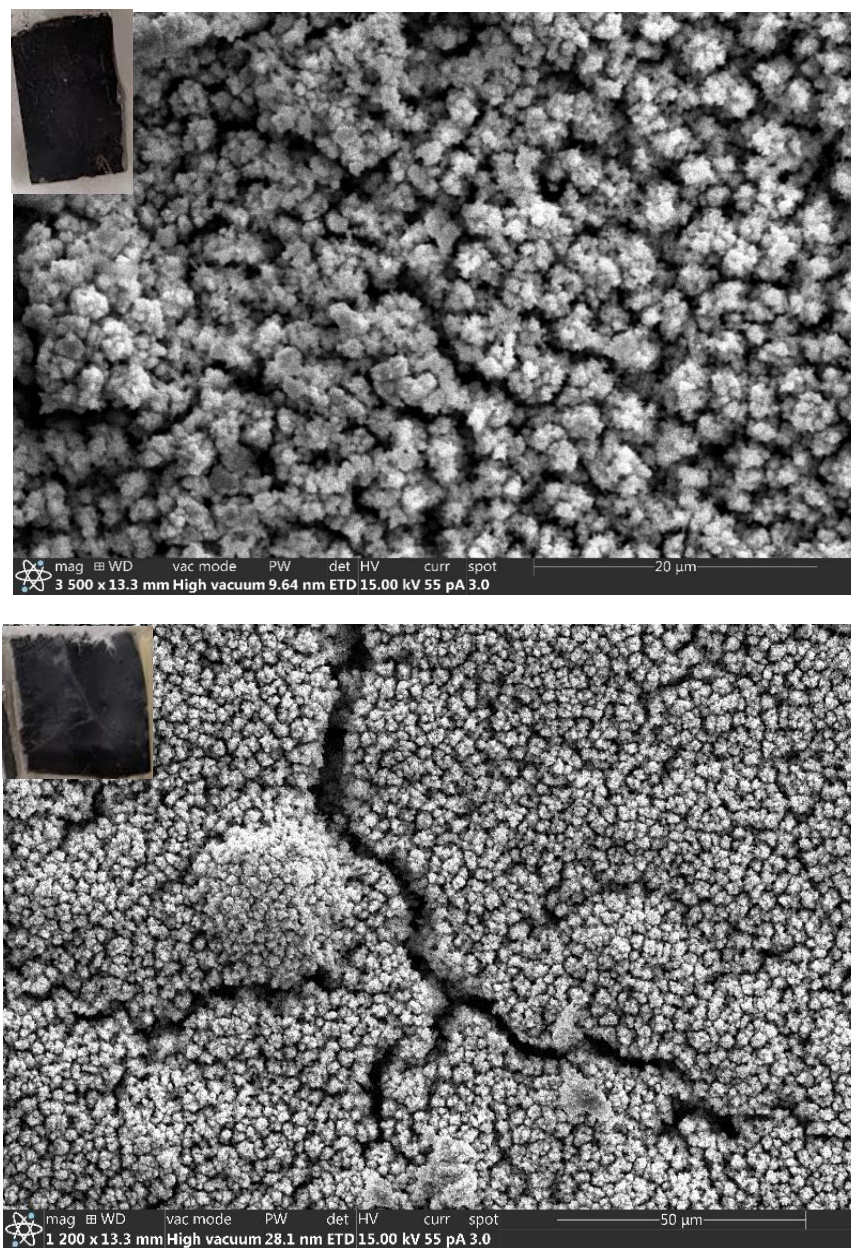

Figure 71: SEM micrographs showing morphologies of electrochemically deposited Sb$_2$Se$_3$ on pre-deposited selenium seeds on MTI-produced FTO coated glass. Top: Film 14S, Bottom: Film 15S. (Naked-eye photo included)

Figure 72*: SEM micrograph and EDS map and of electrochemically deposited Sb₂Se₃ on pre-deposited selenium seeds on Sigma Aldrich-produced FTO coated glass. Film 16S (Naked-eye photo included). This map shows the clean boundary (shown in red) between the FTO on glass (tin, silicon, and oxygen) and the film (antimony and selenium). The carbon map was included to show a bit of carbon tape for compositional contrast.*
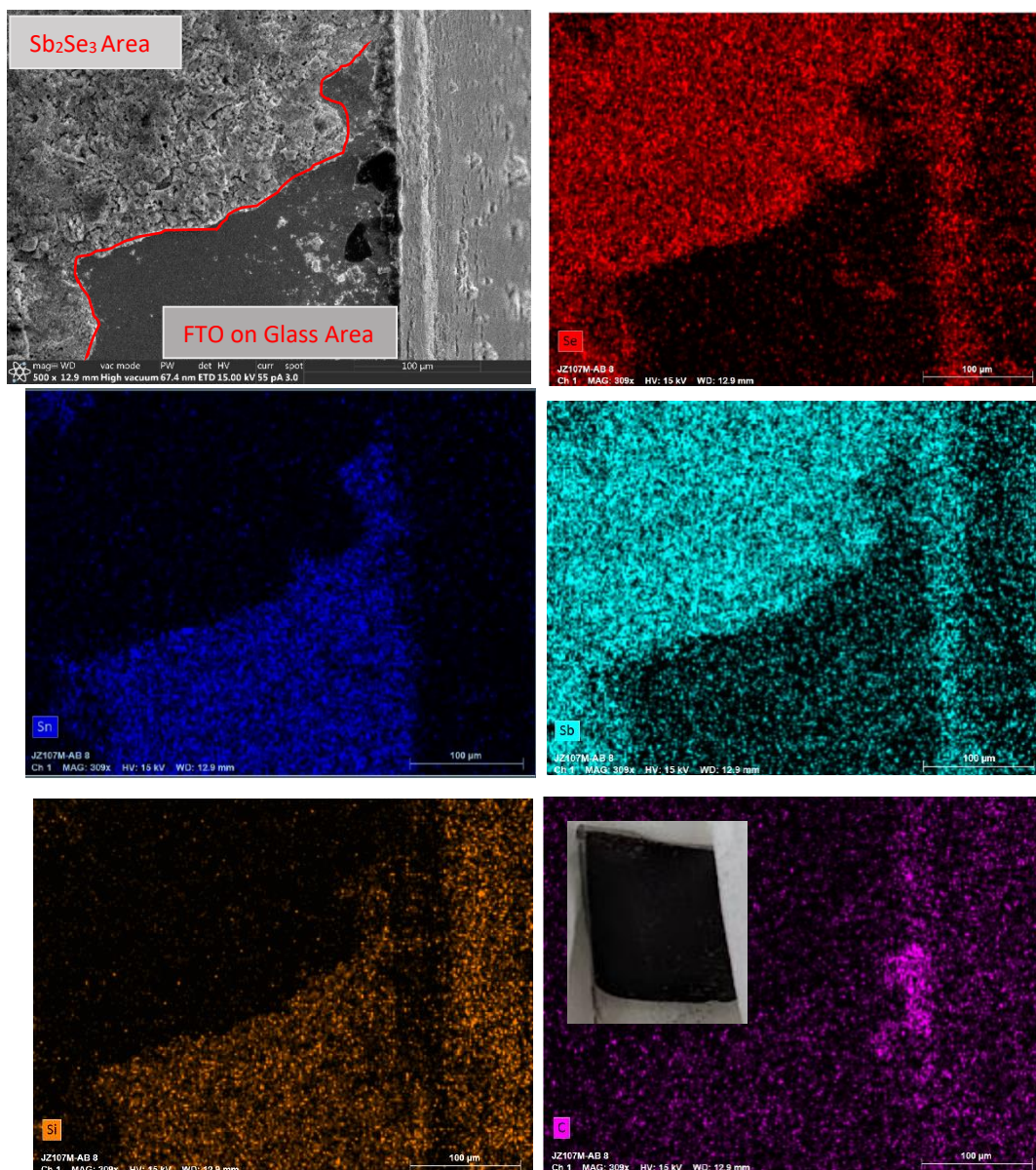
Figure 73: *SEM micrographs of electrochemically deposited Sb$_2$Se$_3$ on pre-deposited selenium*

seeds on Sigma Aldrich-produced FTO coated glass. Film 17S (Naked-eye photo included)

Figure 74: Edge-on SEM micrograph of electrochemically deposited Sb$_2$Se$_3$ on pre-deposited selenium seeds on MTI-produced FTO coated glass. Film 16S (Naked-eye photo included).

Figure 75: *Edge-on SEM micrograph of electrochemically deposited Sb₂Se₃ on pre-deposited selenium seeds on MTI-produced FTO coated glass. Film 16S (Naked-eye photo included). The inset shows a magnification of the morphology shown in the red-circled area.*
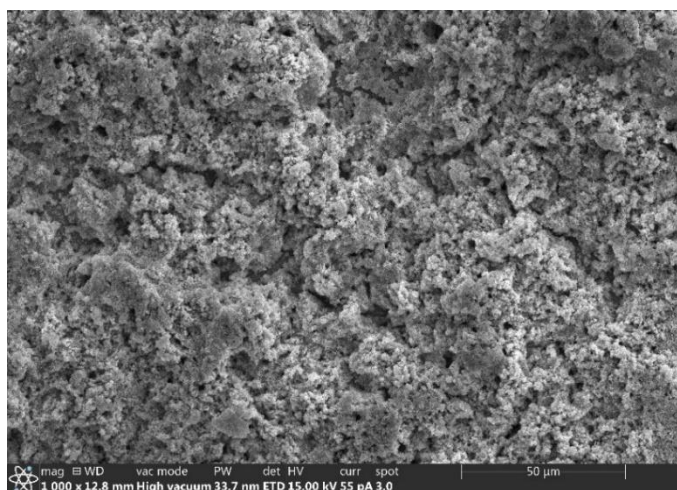
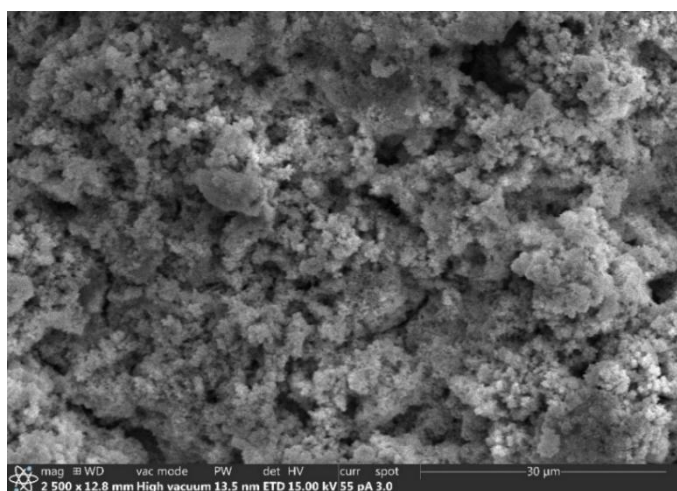*Figure 76: Edge-on SEM micrograph of electrochemically deposited Sb$_2$Se$_3$ on pre-deposited selenium seeds on Sigma Aldrich-produced FTO coated glass. Film 17S (Naked-eye photo included).*
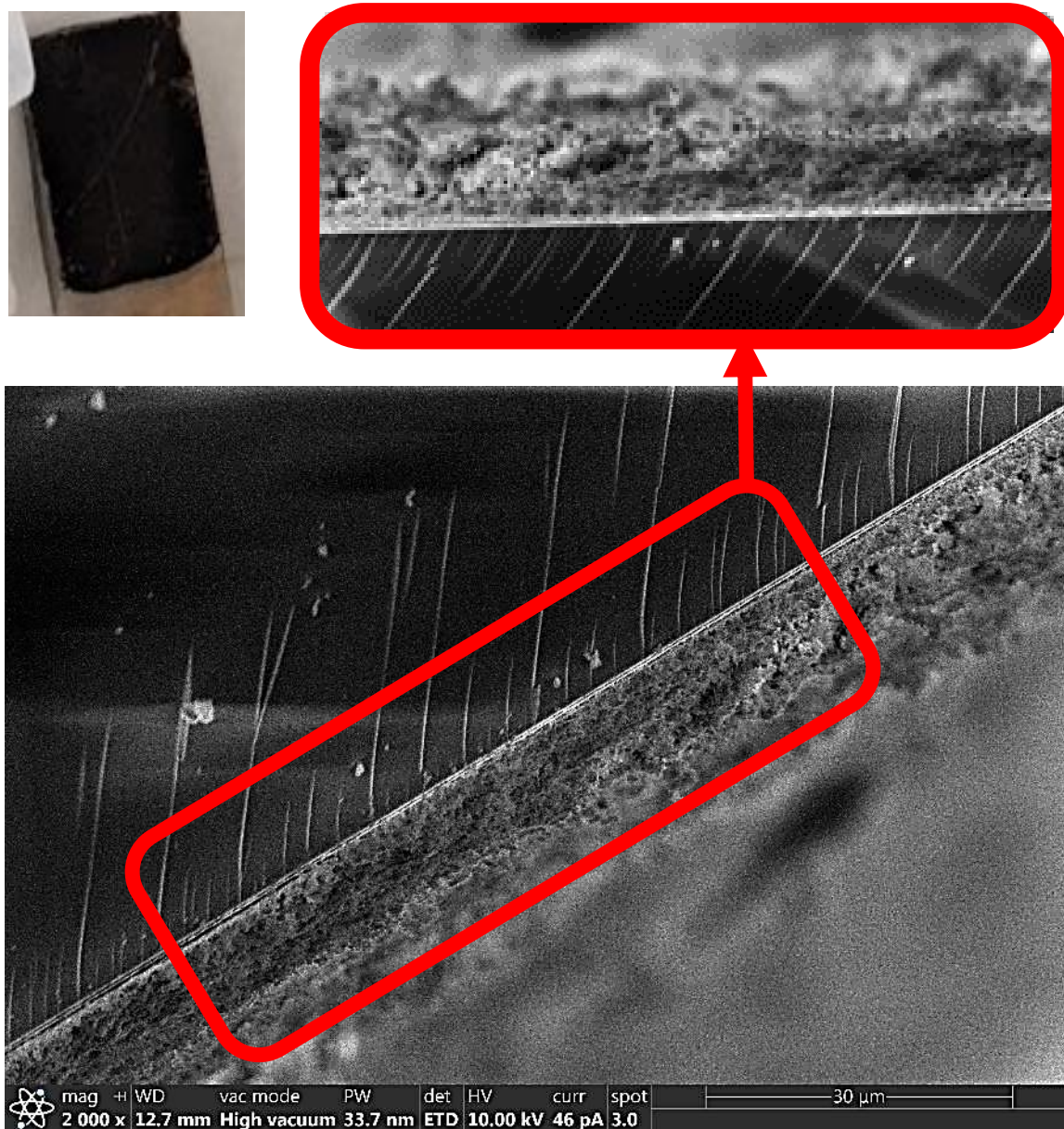
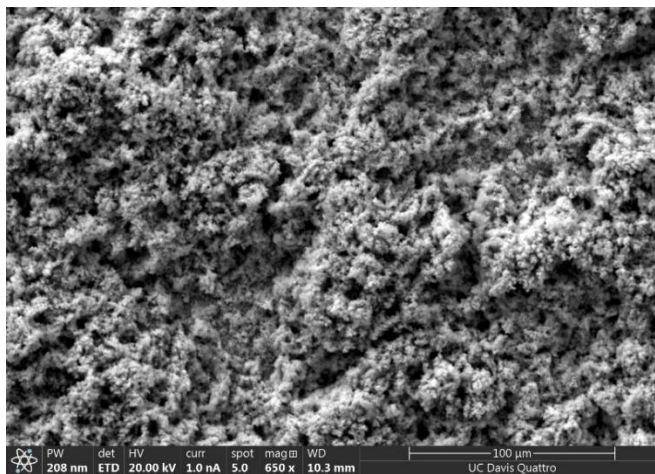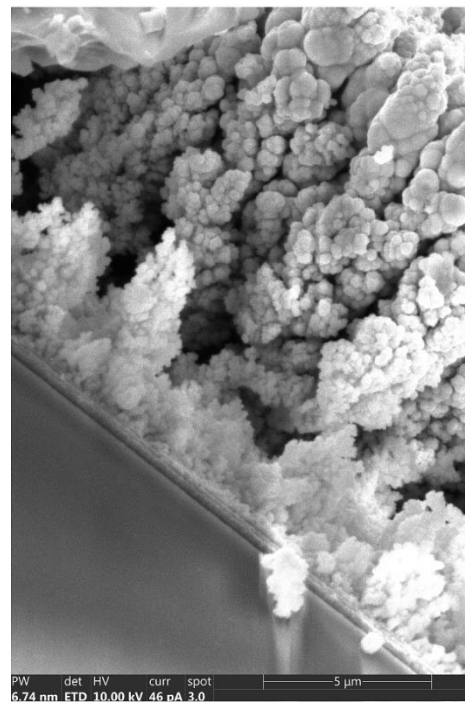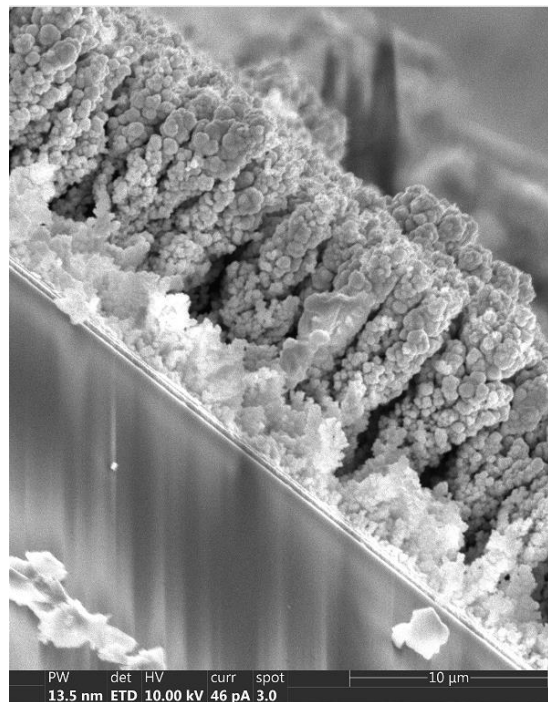***Figure 77***: *Edge-on SEM micrograph of electrochemically deposited Sb_2Se_3 on pre-deposited selenium seeds on MTI-produced FTO coated glass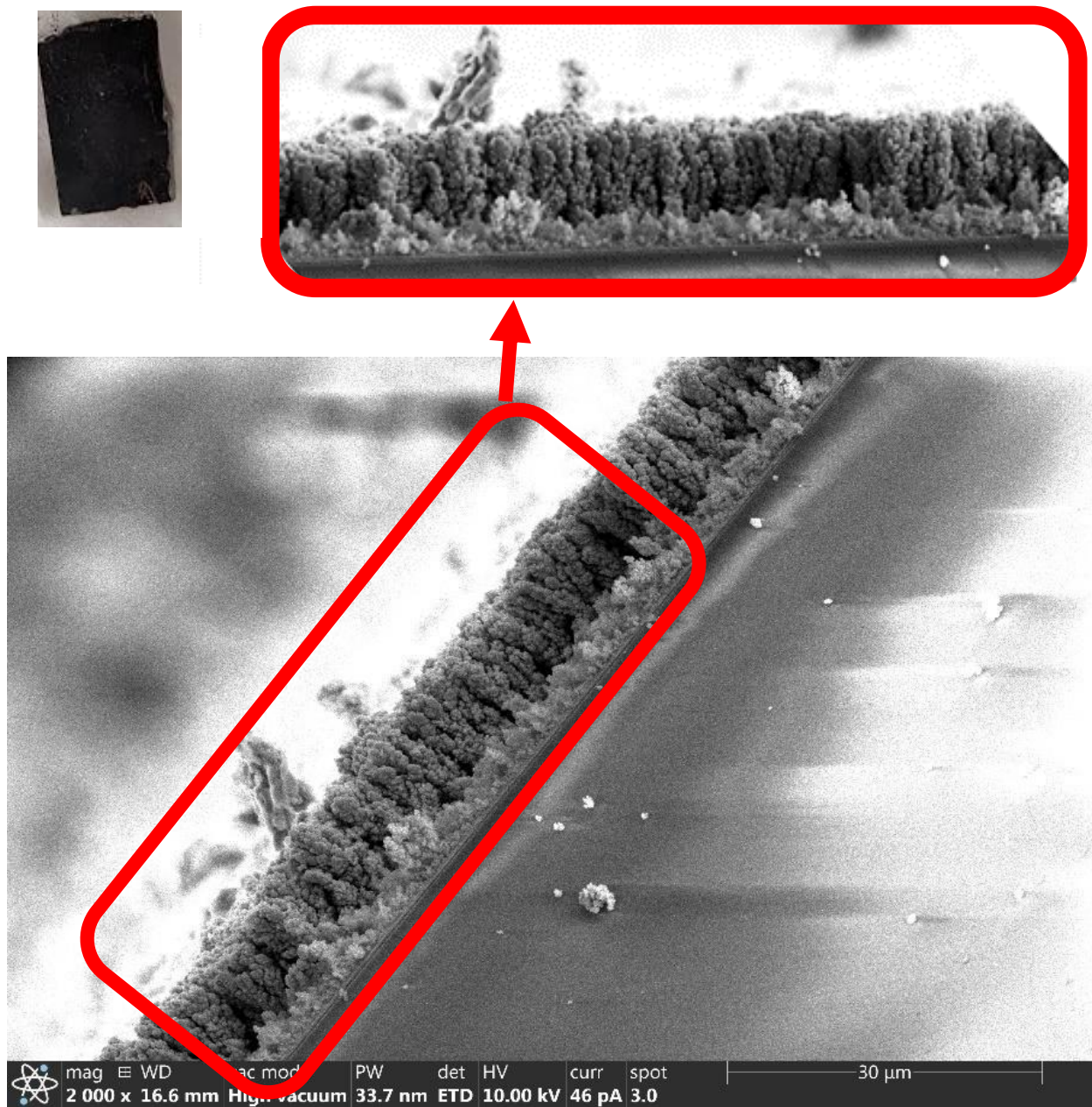. Film 17S (Naked-eye photo included). The inset shows a rotated magnification of the morphology shown in the red-circled area.*
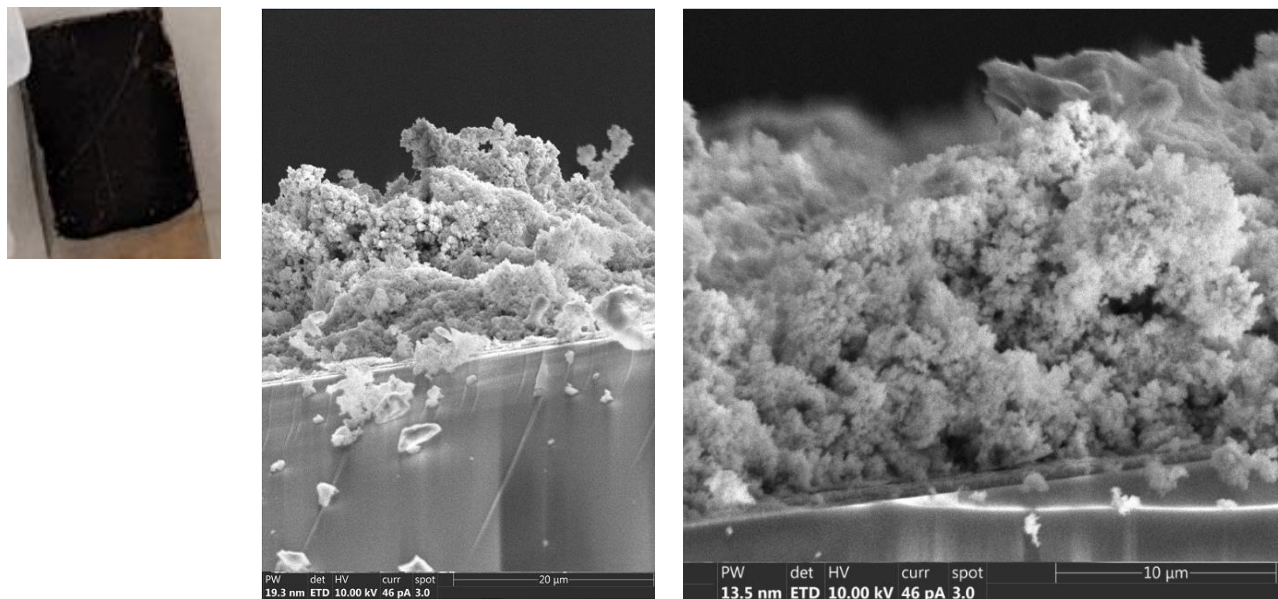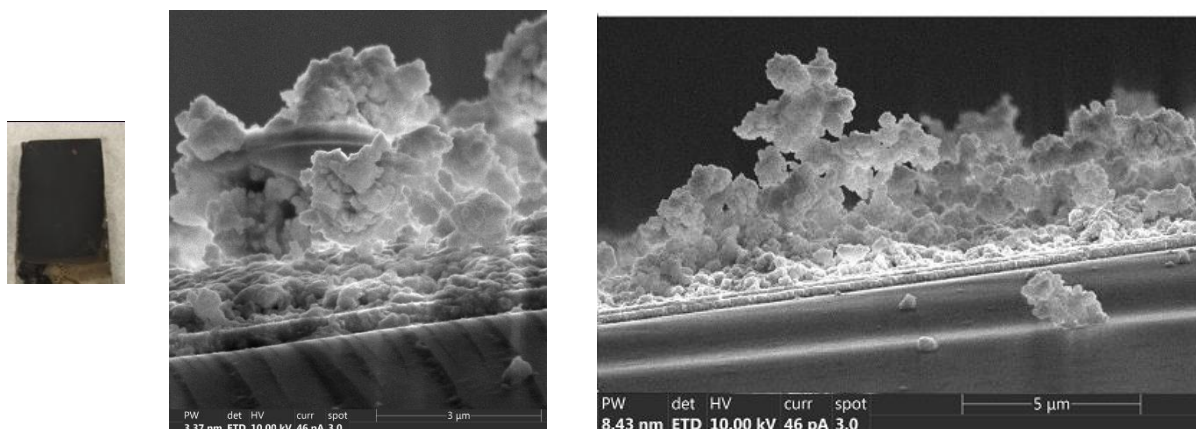
Figure 78: *Edge-on SEM micrograph of Sb$_2$Se$_3$ electrochemically deposited directly on MTI-produced FTO coated glass. Film 6 (Naked-eye photo included)*

The images shown in figure 71 through 78 allow for many comparisons. For example, these results show that regardless of the substrate supplier, the samples that underwent the seeding procedure were much thicker reaching thicknesses up to ~40 microns on seeds and only a maximum of ~21 microns for non-seeded samples

4.5.8 Experimental Results Table and Updated Energy Diagram:

The below table is the summation of data collected in this study. The experimental parameters and results are listed for each film sample. The average band gap determined for unseeded Se$_2$Sb$_3$ films was ~1.18 as shown in the energy band diagram in figure 66. This band gap is fully within the accepted bandgap range found in literature. The band diagram shown in figure 66 shows the comparison between the conduction band, valence band, and band gap energies of FTO and Sb$_2$Se$_3$. When selenium seeds were included in the synthesis process, the outcome of the UV-Vis (shown in figure 70) showed lower bandgaps than the samples with no seeds, but both types of

Sb$_2$Se$_3$ (seeded or not) showed band bending toward the positive energies is shown as a description

of the band bending of a p - type semiconductor. Figure 79 below shows an updated band diagram

showing the differences between the un-seeded and seeded bandgaps with respect to that of FTO.
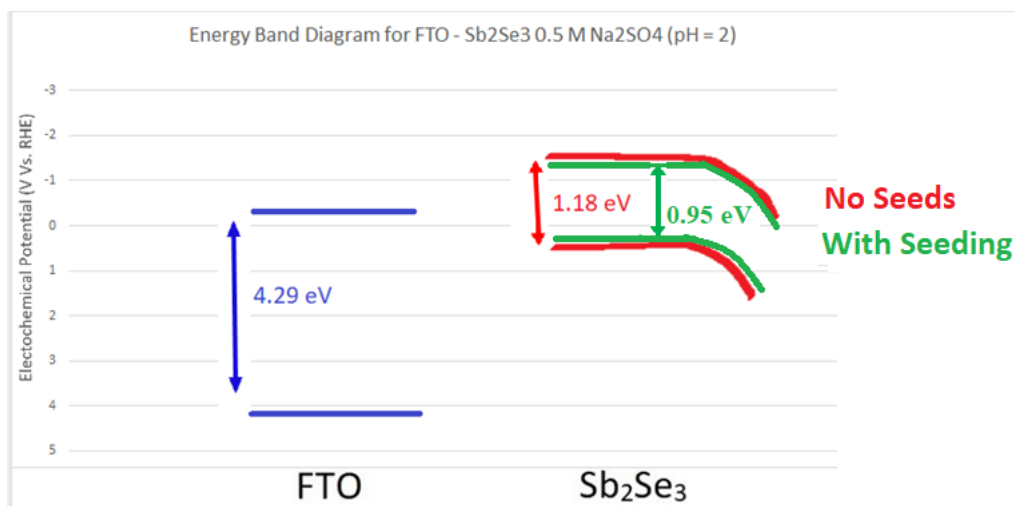
Figure 79: *Energy band diagram showing the conduction band, valence band, band gap of the working electrode coating (FTO), and the achieved target deposition material (Sb$_2$Se$_3$) on the FTO substrate alone and on selenium seeds. Sb$_2$Se$_3$ was shown to be a p-type semiconductor as expected from literature, so the diagram includes band bending towards positive energies.*

Table 3: **A record of the parameters chosen for each trial run and the resulting film thickness and estimated band gap**

Sample	Supplier	Potential (V vs. SCE)/ Duration/Temperature	Total Current (mC)	Film Thickness (μm)	Determined Band Gap (eV)
1	A	-0.6 / 10 min / 25°C	229.2	10	1.1-1.2
2	A	-0.6 / 26 min / 25°C	530.5	2.2	-
2 - PA	A	-	-	3.1	0.8-1.13
3	A	-0.6 / 29 min / 25°C	906.2	12	-
3 - PA	A	-	-	13.5	1.15-1.2
4	A	-0.7 / 27 min / 25°C	920.9	10.6	1.2 - 1.42
5	B	-0.79 / 27 min / 80°C	806.2	14.7	1.2 – 1.9
6 - PA	A	-0.8 / 20 min / 70°C	670.3	13.3	0.9 – 1.14
7 - PA	A	-0.7 / 36 min / 25°C	772.6	13.3	1.0 – 1.15
8	A	0.65 / 18 min / 70°C	549	5.4	1.2 – 1.26
9	A	-0.79 / 27 min / 70°C	430	21.1	1.16 – 1.5
10S	A	-0.79 / 34 min / 70°C	241.9	10.58	1.1–1.5
11S	A	-0.79 / 34 min / 70°C	553.6	19.5	1 – 1.1
12S	A	-0.79 / 34 min / 70°C	962.1	17.67	1.1-1.2
13S	A	-1.2 / 13.34 min / 80°C	1199	18.9	1 – 1.1
14S	A	-0.79 / 34 min / 70°C	425.9	37.5	0.96 – 1
15S	A	-0.79 / 30 min / 70°C	599	32.67	1 – 1.1
16S	B	-0.79 / 20 min / 70°C	875.2	20.4	0.95– 1.15
17S	B	-0.79 / 35 min / 70°C	690.5	39.75	1 - 1.05

4.6.0 Conclusion:

The deposition temperature, surface treatments, and post-deposition annealing all have effects on the morphology, composition, and performance. The increase in the deposition temperature (below 85°C to avoid holes in the film) works to produce a denser and more conformal film by allowing for more nucleation sites to deposit at the start of the deposition. The annealing treatment in an argon atmosphere with selenium powder when performed after the electrochemical deposition improved the density, coverage, and homogeneity of the morphology as well as the selenium content of the film. When the selenium anneal occurred before the electrochemical deposition it provided even more nucleation sites and increased surface selenium before the Sb_2Se_3 is deposited. The differences in the morphologies by presence of seeds and/or the FTO supplier are stark with the most promising of them being the MTI-brand FTO with selenium seeds, deposited at -0.79 V vs. SCE for 35 minutes at 70°. This trial passed 690.5 mC of charge which is extremely close to the 600 mC that Costa/Mascaro published previously.[127,139,140]

Via UV-Vis Kubelka Munk experiments and surface photovoltage experiments the bandgaps were determined while XRD and EDS confirmed that the target material of Sb_2Se_3 was achieved. Due to the strong oxidation and exfoliation of the pre-deposition $KMnO_4$ treatment, the bonding of the deposited film was stronger and achieved a more homogeneous field of separate globular nanoparticles (in the case of no initial seeding). Chopped light experiments confirmed that this material is indeed p-type as expected from literature and the combination of XRD and EDS confirmed the Sb_2Se_3 composition of all films grown for this dissertation.

The comparison of SEM micrographs of selenium seeded samples uncovered observable differences in resulting film morphologies also become evident in SEM. Both seeded samples showed more overall structure than the non-seeded samples. The films that were seeded and grown on MTI-brand FTO have a tree-like/forest like morphology from the top and globule columns from an edge-on view. The periodicity of this film as well as the thickness, density, and conformality is exciting in that while the columns are not as needle-like as the world record Sb_2Se_3 films of literature they do form a dense field with space in between the columns for possible light trapping for heightened efficiency. The seeded samples that began as Sigma Aldrich-brand FTO substrates produced a spongey or foam-like morphology which while more shapeless than the films on MTI-brand FTO, it did reach similar thicknesses and still maintains porosity which may allow for similar high surface area driven light trapping and thereby a potentially good efficiency. When the seeded samples are compared to the samples with no seeds, the non-seeded films were clearly less homogeneous, thinner, and less dense than the seeded samples.

The edge-on images of figure 78 show how little order or periodicity was achieved without seeds and the variety of morphologies achieved earlier in this dissertation in non-seeded samples (whether spheres, foam, disks, or globs) the homogeneity and density are nowhere near as great as those samples that were seeded before electrochemical deposition.

4.7.0 Proposed Future Work:

Specific Aim 1: Probe the effects of a pre-deposition selenium seeding heat treatment. Characterize the morphology and composition after the seeds are initially deposited and then again after the electrochemical deposition. Determine how the morphology of the FTO as

deposited on the glass by the supplier affects the resulting Sb_2Se_3 morphology. The performance and band gap will be analyzed to determine if this process creates a more conformal morphology with a Sb_2Se_3 composition via optimal microscopy, scanning electron microscopy (SEM), energy-dispersive X-ray spectroscopy (EDS), X-ray diffraction (XRD), and ultraviolet–visible (UV-Vis) spectroscopy for thorough surface characterization.

Specific Aim 2: Probe the effects of a pre-deposition antimony-seeding and the combination of selenium and antimony present during the heat treatment. Characterize the morphology and composition after the seeds are initially deposited and then again after the electrochemical deposition. Determine how the morphology of the FTO as deposited on the glass by the supplier affects the resulting Sb_2Se_3 morphology. The performance and band gap will be analyzed to determine if this process creates a more conformal morphology with a Sb_2Se_3 composition via optimal microscopy, scanning electron microscopy (SEM), energy-dispersive X-ray spectroscopy (EDS), X-ray diffraction (XRD), and ultraviolet–visible (UV-Vis) spectroscopy for thorough surface characterization.

Specific Aim 3: Probe the effects of layering the most successful process steps. For example: a seeding anneal followed by electrochemical bath deposition followed by another seeding anneal and so on. Characterize the morphology and composition after each never process step. The performance and band gap will be analyzed to determine if this process creates a more conformal morphology with a Sb_2Se_3 composition via optimal microscopy, scanning electron microscopy (SEM), energy-dispersive X-ray spectroscopy (EDS), X-ray diffraction (XRD), and ultraviolet–visible (UV-Vis) spectroscopy for thorough surface characterization.

Specific Aim 4: Using the most promising process steps and parameters, build a full device including, at minimum, a TiO$_2$ layer as a window layer, and drop-casted silver electrical contacts. Characterize the sample after each deposition using SEM, EDS, and XRD and observe the cell performance under real-world sunlight using 3-point probe and voltmeter electrical characterization. Characterization via grazing incidence x-ray diffraction (GIXRD) and atomic force microscopy (AFM) for thorough surface characterization.

The original design of experiments for the pre-deposition seeding trails was to do the same procedure not only for selenium powder, but also for antimony powder, and the combination of the two powders. Figure 80 below shows the experimental setup of the tube furnace with a crucible of pristine antimony powder. The preliminary experiments showed that using the same temperature and duration for annealing did not yield the same visible seeds as the selenium. The EDS compositional spectra and maps did show the presence of antimony equally all over the surface, but no actual particles were detected.
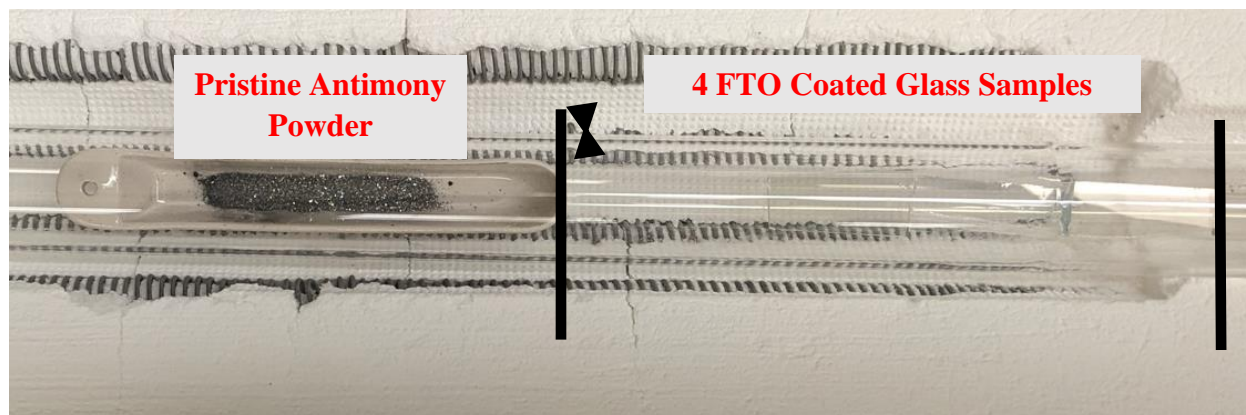
Figure 80: *Energy band diagram showing the conduction band, valence band, band gap of the working electrode coating (FTO), and the achieved target deposition material (Sb_2Se_3) on the FTO substrate alone and on selenium seeds. Sb_2Se_3 was shown to be a p-type semiconductor as expected from literature, so the diagram includes band bending towards positive energies.*

The next trials that would benefit this study would be to run the antimony in the tube furnace at a higher temperature than that of the selenium anneal. The melting point of selenium is 220.8 °C[194] which may what lead Costa/Mascaro to use 300 °C as their annealing temperature.[127,139,140] The melting point of antimony is 630.6 °C[195] so for the next trial it may make sense to use ~700 °C as the annealing temperature. Then, expanding on this, one could move forward in two ways:

1) Choose a temperature that may work to deposit both selenium and antimony at the same time.

2) Perform two annealing steps one after the other.

Another very interesting way future studies could go is to then perform the post-deposition anneal *and* the pre-deposition anneal. One could conceivably perform an anneal followed by an

electrochemical deposition repeated over and over as many times as desired. This may produce an extremely thick and conformal film, or it may not affect the second deposition at all.

In addition, work must be done to observe how these Sb_2Se_3 absorber layers affect the performance of a full PV device by depositing the additional window layer (perhaps TiO_2), back mirror layer, back surface field layer, and contacts (perhaps Ag) to determine if the performance of the full device is competitive with other devices accepted in academia and industry. One study that would be an amazing continuation of this work would be to electrochemically deposit a TiO_2 window layer and drop cast silver surface electrical contacts to complete a simple solar cell build. One could then characterize the sample after each deposition using SEM, EDS, and XRD and observe the cell performance under real-world sunlight using 3-point probe and voltmeter electrical characterization. Further useful forms of characterization might be grazing incidence x-ray diffraction (GIXRD) and atomic force microscopy (AFM) for thorough surface characterization. Also, more work needs to be explored with respect to electrochemical deposition of other layers included in a PV build. Novel absorber layer materials as well as other PV layer materials and their corresponding deposition methods will very likely continue to show improvement in PV production and optimized performance.

5. Acknowledgements:

The work that I was fortunate enough to be a part of at the University of California, Davis, was extremely rewarding. Both main projects discussed in this dissertation have the potential to lead to real change in the green energy sector. The underlying goal of both projects was to find cheaper methods to produce materials for energy harvesting and storage. The use of iron-based catalysts to assist in the production of alternative fuels and the electrochemical deposition of

absorber layers are both areas that will likely prove to be an amazing boon to energy production, harvesting, and storage.

By decreasing the cost of fuel electrolyzers, hydrogen production, solar cell materials, and deposition methods, and by using earth abundant materials and inexpensive manufacturing methods, we can get solar cells and alternative fuels to more consumers, ultimately adding to the effort of reducing the greenhouse gases and other pollution caused by the burning of fossil fuels.

Work like that discussed in this dissertation has incredible applications in industry and the energy sector as a whole. Electrochemistry provides options for easy to scale mass-production as one electrochemical bath, whether for alternative fuel production of PV film deposition, can be reused, and replenished with fresh electrolytes and precursors to afford multiple rounds of reactions per bath. It is this reusability of these baths that may propel these electrochemical methods to the forefront of manufacturing as a cheaper option compared to current vacuum based PV layer deposition or catalysis-free fuel production. I hope that this work can be continued as the results thus far have been extremely interesting and promising with a lot of possible options for how to continue from here.

Achieving this degree has been a long rocky road to say the least and there were times I thought it would never end and I would never accomplish my goal of earning a doctorate, but thanks to some encouragement from friends, family, and colleagues as well as healthy practices, I was able to come this far. The person who I would like to formally thank here is first and foremost, Dr. Subhash Risbud. He stuck with me on my team throughout this four-year degree and when I lost funding and needed to switch labs or when the depression was so great after breaking up with my partner of ten years, he never gave up on encouraging me to pick it all up and continue toward my goals. I am also so so grateful to my graduate student colleagues of the Material Science and

Engineering and Chemical Engineering departments who kept the social gatherings and happy hours going even in the worst of times such as wildfires, global pandemics, qualifying exams, and similar turmoil. Sometimes the grad student community was the only thing to keep me sane during the roughest moments of this degree.

In the Berben lab, I would like to thank Dr. Santanu Pattanayak, Dr. Leo Parsons, and Dr. Cody Carr for teaching me the ins and out of synthetic chemistry and in the Osterloh lab, I would like to acknowledge Tatiana Mamani, Samutr Assavachin, Hervin Errol Mendoza, Anna Kundmann, and Dr. Sahar Daemi, who found time to train me in electronic characterization and deposition methods. I definitely would also like to thank my mentees, Zoey Wiggins, Vyoma Bhanap, and Shirin Sidharta, who kept me motivated and ultimately helped me achieve the final results right on time to finish a PhD in four years. Another thank you goes to my employers, Dr. Risbud, and Dr. Kyle Crabtree for always making sure I had a teaching assistant position even when there were no research funds for me. I would be remised if I did not thank my family, Donna, Gary, Logan, and Jordan Brayfield, and friends in Connecticut and around the world who listened to me vent and offered love and support over the phone. Finally, I would like to thank my amazing dissertation committee, it is not every day that someone will agree to read a 250-page paper for me. Thank you so much for reading this dissertation, it has been a journey to perform this research and I am happy with how these studies concluded.

6. Resume and Publication Information

CASSONDRA BRAYFIELD

Cell: (860) 620-7042	*"I so much admire her enormous energy and passion."*
Email: cassie.brayfield@gmail.com	*"My best student in the 46 years of my academic career"*
Address: 417 Russell Park Apt 6, Davis CA 95616	*"One of the very few students who are actually Ph.D. quality!"*

EDUCATION

Sept 2019- *Present*   **PhD. in Material Science and Engineering (GPA: 3.6)**
Advisor: Prof. Subhash Risbud   University of California Davis, Davis, CA

Aug 2017- May 2019   **M.S. in Material Science and Engineering (GPA: 3.7)**
Advisor: Prof. Sefaattin Tongay   Arizona State University, Tempe, AZ

PROFESSIONAL EXPERIENCE

Mar. 2016 – July 2019 *Development*   **Intel Corporation,** Chandler, AZ
Metrology Tool Owner: R&D Engineer for Substrate Packaging Technology

- Managed recipe creation and troubleshooting for several metrology tools
- Characterized product defects using optical microscopy, SEM imaging, and EDS
- Created technical DOEs, BKMs, tool specifications, and statistical analyses (in JMP)
- Data analysis and yield engineering for all Client, Server, and Low-Cost Products

June 2015 – Aug. 2015   **Corning Inc.,** Corning, NY
Research Intern: Characterization Science - Failure Mode Analysis Lab, Fractography

- Designed and executed Stress wave fractography experiments to measure crack growth
- Performed surface fracture analysis for a variety of glass compositions and geometries
- **Side project:** invented and filed disclosure for new innovative glass composition

May 2014 – June 2015   **Smart Lighting ERC,** Troy, NY
Research Intern

- Developed experimental phosphor coating to produce multiphase full-spectra LEDs
- Final design achieved CRI of 90-98 in color temperatures of 4000-6000K
- Gained a working understanding of Color Science and Spectrophotometry

April 2014 – Nov. 2014   **BESS Tech,** Troy, NY
Research Intern

- Optimized time and temperature of deposition on experimental battery anodes
- Assembled batteries in vacuum environment for electronic performance testing
- Utilized Arbin tests, SEM imaging, Raman spectroscopy, and XRD for analysis

ACADEMIC RESEARCH

Nov 2021 – *Present*   **Electrochemical Methods for Deposition of Sb_2Se_3 Nanoparticles for Photovoltaics Solar Cell Assembly Production,** Davis CA

- Treatment of FTO glass and Mo foil substrates for PV layer electrodeposition
- CV, CPE, and electrochemistry techniques for Sb_2Se_3 deposition and characterization
- SEM, EDS, XRD, UV-VIS, Surface Photovoltage tests for compositional and morphological analysis

Jan 2019 – Nov 2021   **Engineering the Second Coordination Sphere of Iron Organometallic Catalysts for Facile Alternative Fuel Production,** Davis CA

- Cluster and ligand synthesis
- CV, CPE, and other electrochemistry for catalyst characterization
- NMR, IR, IR-SEC for catalyst and ligand characterization

Jan 2018 – May 2019   **GeSe Crystal Growth for Thermoelectronic Devices,** Tempe AZ

- SEM imaging, Compositional Analysis, EDS, and documentation

Sept. 2012 – June 2015	**Alzheimer's Disease Prevention Through Olfaction Training,** Troy, NY ◆ Led research team in investigating cure for Alzheimer's via use of olfactory stimulation ◆ Prototyped scent-identification brain training game designed to boost neural activity in brain

TECHNICAL SKILLS

Laboratory / Workshop
➢ Synthesis in hood and glove box
➢ Rotary evaporator
➢ X-Ray diffraction
➢ Machining, brazing, welding
  ➢ Production/Metrology tools for semiconductor packages

Synthesis
➢ Chemical synthesis and work up
➢ Polymer & metal extrusion
➢ Glass pouring
➢ Sputtering
➢ Chemical and Physical Vapor Deposition for crystal growth

Testing & Analysis
➢ NMR and Gas Chromatography
➢ IR, and IR-SEC
➢ Differential thermal analysis
➢ Hardness & tensile testing
➢ Finite element analysis
➢ SEM, EDS & TEM imaging

EXTRACURRICULAR AND OUTREACH

Mar. 2020 – *Present*	**Chemistry Outreach, Bodega Bay, STEM Squad/ESTEAM, Skype a Scientist Program, MANO/Fair Judge** ◆ Led several virtual/in-person science lessons/demonstrations/competitions for a variety of schools (K - 12)
Sept 2019 – *Present*	**Mentoring: Guardian Scholars, E-Prime, Society of Hispanic Professional Engineers, Sci Coaches, etc.** ◆ Funded to mentor scientists/engineers from many organizations from ex-foster children to industry engineers ◆ AACT Science Coach – Assisted High School Teacher build a new Mat Sci Curriculum for AP students
Aug. 2016 – June 2019	**Project Lead the Way (PLTW) STEM Outreach** Chandler, AZ ◆ Volunteered in Chandler elementary schools (K-6) ◆ Led lessons about science and technology and related careers
Aug. 2016 – June 2019	**Intel Hispanic Leadership Council (IHLC) Outreach,** Chandler, AZ ◆ Led science demonstrations and events for outstanding Hispanic females
March 2016 – *Present*	**Feed My Starving Children (FMSC)**, Mesa, AZ ◆ Fund raising and food packing for children in impoverished and war-torn areas
Sept. 2012 – June 2015	**Writer / Editor for RPI Magazine (Statler & Waldorf),** Troy, NY ◆ Wrote monthly advice column as well as journalism pieces on RPI social activities

PUBLICATIONS AND OTHER MEDIA

Articles:

Cassondra M. Brayfield, *"Toward a green community: Tuning electrochemical parameters to improve morphology of Sb_2Se_3 solar absorber Layers"* **American Ceramic Society Bulletin, Vol. 102, No. 5**

Cassondra M. Brayfield, Subhash Risbud et al *"Electrochemical Deposition of Sb2Se3 for Use in Photovoltaics"* Submitted to **Resolution and Discovery.**

Cassondra M. Brayfield, Cody R. Carr, Louise A. Berben et al "*Secondary Coordination Sphere Cations Break Scaling Relationships for Hydrogen Evolution Rate*" -Not yet submitted for publication.

Kentaro Yumigeta, **Cassondra Brayfield,** Sefaattin Tongay et al,. *"The Synthesis of Competing Phase GeSe and $GeSe_2$*

Ultrathin Materials" **RSC Advances, published by the Royal Society of Chemistry**
Kedi Wu, Bin Chen, Mark Blei, Lei Liu, Hui Cai, **Cassondra Brayfield**, David Wright et al. *"Phase transition across anisotropic superconducting NbS3 and direct gap semiconductor TiS3 at nominal titanium alloying limit."* **Advanced Materials**

Internal Industry Articles:

Cassondra M Brayfield, Hope Fenton, Scott Pitcher, Steven DeMartino, Jacob Rubendall, Ed Bernholtz, Timothy Smith, Jamie Westbrook, Ray Northrup, Steve Weckelman et al.(2015) Stress Wave Fractography as a Method to Measure Crack Velocity and Growth. **Corning Internal Library**.

Invention Disclosure (Corning):
Brayfield, Cassondra M. (PING) Phosphors IN Glass. Novel Phosphorescent Glass Compositions. Corning invention disclosure agreement filed, **Corning Internal Library**. August 20, 2015.

Poster and Symposium Presentations:

Brayfield, Cassondra M. (2018, September). Brains, Batteries, LEDs, and Broken Glass. SEMTE (School for Engineering of Matter, Transport and Energy) Symposium, Tempe AZ.

Videos, Socials, and In the Media:

- *Cassondra Brayfield Awarded Cadence Women in Technology Scholarship* by Matt Murphy*, (2023, Jan 13). https://engineering.ucdavis.edu/news/cassondra-brayfield-cadence-women-scholarship

- *How to Persevere* by Jocelyn Anderson*, *UC Davis Magazine* (2023, May 16) https://engineering.ucdavis.edu/news/how-persevere

- Brayfield, Cassondra M. [Cassie Brayfield]. (2015, April 30). Dip an LED in Liquid Nitrogen. You Won't Believe What Wide Bandgaps Can Do!!! Retrieved from [https://www.youtube.com/watch?v=tNphTlYvVt8].

- https://www.linkedin.com/in/cassondra-brayfield/

7. Supplemental Information

Figure S1: *Another micrograph of film 17S showing the morphology and thickness of the deposited film edge-on.*

8. References

1.) Environmental Protection Agency. (n.d.). EPA. https://www.epa.gov/ghgemissions/sources-greenhouse-gas-emissions

a. Special report on the ocean and Cryosphere in a changing climate. (n.d.). https://www.ipcc.ch/srocc/

b. WMO annual report highlights continuous advance of climate change. World Meteorological Organization. (2023, April 24). https://public.wmo.int/en/media/press-release/wmo-annual-report-highlights-continuous-advance-of-climate-change

2.) Mike Lockwood. (2009) "Solar Change and Climate: an update in the light of the current exceptional solar minimum," Proceedings of the Royal Society A, 2 December 2009, doi 10.1098/rspa.2009.0519;

3.)   Lindsey, R. (2021, October 7). Climate Change: Atmospheric Carbon Dioxide. Retrieved January 13, 2022, from https://www.climate.gov/news-features/understanding-climate/climate-change-atmospheric-carbon-dioxide

4.)   Kwon, Y. H., Kim, Y. B., Jeong, M., Do, H. W., Cho, H. K., & Lee, J. Y. (2017). Crystal growth direction-controlled antimony selenide thin film absorbers produced using an electrochemical approach and intermediate thermal treatment. *Solar Energy Materials and Solar Cells*, *172*, 11–17. https://doi.org/10.1016/j.solmat.2017.07.004

5.)   Kumar, M., Dubey, A., Adhikari, N., Venkatesan, S., & Qiao, Q. (2015). Strategic review of secondary phases, defects and defect-complexes in kesterite CZTS–SE solar cells. *Energy & Environmental Science*, *8*(11), 3134–3159. https://doi.org/10.1039/c5ee02153g

6.)   Costentin, C., Drouet, S., Robert, M., & Savéant, J.-M. (2012a). A local proton source enhances co   2   electroreduction to CO by a molecular Fe Catalyst. *Science*, *338*(6103), 90–94. https://doi.org/10.1126/science.1224581

7.)   Gordon, Z., Drummond, M. J., Matson, E. M., Bogart, J. A., Schelter, E. J., Lord, R. L., & Fout, A. R. (2017). Tuning the fe(ii/III) redox potential in nonheme Fe(II)–Hydroxo complexes through primary and secondary coordination sphere modifications. *Inorganic Chemistry*, *56*(9), 4852–4863. https://doi.org/10.1021/acs.inorgchem.6b03071

8.)   Kauffman, D. R., Alfonso, D., Matranga, C., Ohodnicki, P., Deng, X., Siva, R. C., Zeng, C., & Jin, R. (2014). Probing active site chemistry with differently charged AU25Q nanoclusters (q = −1, 0, +1). *Chemical Science*, *5*(8), 3151. https://doi.org/10.1039/c4sc00997e

        (b) Vasileff, A., Zhi, X., Xu, C., Ge, L., Jiao, Y., Zheng, Y., & Qiao, S.-Z. (2019). Selectivity control for electrochemical co2 reduction by charge redistribution on the surface of copper alloys. *ACS Catalysis*, *9*(10), 9411–9417. https://doi.org/10.1021/acscatal.9b02312

9.)   Ackermann, L. (2019). Metalla-electrocatalyzed C–H Activation by Earth-Abundant 3d Metals and Beyond. Accounts of Chemical Research, 53(1), 84-104. doi:10.1021/acs.accounts.9b00510

10.)   Carr, C. R.; Cluff, D. B.; Berben, L. A. (2020) Breaking Scaling Relationships in CO2 Electroreduction with Isoelectronic Analogs [Fe4N(CO)12]- and [Fe3MnO(CO)12]- Organometallics 2020, 39, 9, 1658–1663.https://doi.org/10.1021/acs.organomet.9b00848.s001

        (b) Loewen, N. D., Thompson, E. J., Kagan, M., Banales, C. L., Myers, T. W., Fettinger, J. C., & Berben, L. A. (2016). A pendant proton shuttle on [Fe4N(CO)12]− alters product selectivity in formate vs. H2 production via the hydride [H–Fe4N(CO)12]−. Chemical Science, 7(4), 2728-2735. doi:10.1039/c5sc03169a

11.) Carr, C. R., Taheri, A., & Berben, L. A. (2020). Fast Proton Transfer and Hydrogen Evolution Reactivity Mediated by [Co13C2(CO)24]4–. Journal of the American Chemical Society, 142(28), 12299-12305. doi:10.1021/jacs.0c04034

12.) Loewen, N. D.; Berben, L. A. unpublished results

13.) Elgrishi, N., Rountree, K. J., Mccarthy, B. D., Rountree, E. S., Eisenhart, T. T., & Dempsey, J. L. (2017). A Practical Beginner's Guide to Cyclic Voltammetry. Journal of Chemical Education, 95(2), 197-206. doi:10.1021/acs.jchemed.7b00361

14.) Martin, D. J., Johnson, S. I., Mercado, B. Q., Raugei, S., & Mayer, J. M. (2020). Intramolecular Electrostatic Effects on O2, CO2, and Acetate Binding to a Cationic Iron Porphyrin. Inorganic Chemistry, 59(23), 17402-17414. doi:10.1021/acs.inorgchem.0c02703

(b) Martin, D. J., Wise, C. F., Pegis, M. L., & Mayer, J. M. (2020). Developing Scaling Relationships for Molecular Electrocatalysis through Studies of Fe-Porphyrin-Catalyzed O2 Reduction. Accounts of Chemical Research, 53(5), 1056-1065. doi:10.1021/acs.accounts.0c00044

15.) Tsui, E. Y., & Agapie, T. (2013). Reduction potentials of heterometallic manganese–oxido cubane complexes modulated by redox-inactive metals. *Proceedings of the National Academy of Sciences*, *110*(25), 10084–10088. https://doi.org/10.1073/pnas.1302677110

(b) Tsui, E. Y., Tran, R., Yano, J., & Agapie, T. (2013). Redox-inactive metals modulate the reduction potential in heterometallic manganese–oxido clusters. *Nature Chemistry*, *5*(4), 293–299. https://doi.org/10.1038/nchem.1578.

(c) Lin, P.-H., Takase, M. K., & Agapie, T. (2014). Investigations of the effect of the Non-Manganese Metal in heterometallic-oxido cluster models of the oxygen evolving complex of Photosystem II: Lanthanides as substitutes for calcium. *Inorganic Chemistry*, *54*(1), 59–64. https://doi.org/10.1021/ic5015219.

16.) Carr, C. R., Taheri, A., & Berben, L. A. (2020). Fast Proton Transfer and Hydrogen Evolution Reactivity Mediated by [Co13C2(CO)24]4–. Journal of the American Chemical Society, 142(28), 12299-12305. doi:10.1021/jacs.0c04034

17.) Hosseinzadeh, P., & Lu, Y. (2016). Design and fine-tuning redox potentials of metalloproteins involved in electron transfer in Bioenergetics. *Biochimica et Biophysica Acta (BBA) - Bioenergetics*, *1857*(5), 557–581. https://doi.org/10.1016/j.bbabio.2015.08.006

18.) Gordon, Z., Drummond, M. J., Matson, E. M., Bogart, J. A., Schelter, E. J., Lord, R. L., & Fout, A. R. (2017a). Tuning the fe(ii/III) redox potential in nonheme Fe(II)–Hydroxo complexes through primary and secondary coordination sphere modifications. *Inorganic Chemistry*, *56*(9), 4852–4863. https://doi.org/10.1021/acs.inorgchem.6b03071

19.) Pegis, M. L., Martin, D. J., Wise, C. F., Brezny, A. C., Johnson, S. I., Johnson, L. E., . . . Mayer, J. M. (2019). Mechanism of Catalytic O2 Reduction by Iron Tetraphenylporphyrin. Journal of the American Chemical Society. doi:10.1021/jacs.9b02640

20.) Kauffman, D. R., Alfonso, D., Matranga, C., Deng, X., Ohodnicki, P., Siva, R., & Jin, R. (2014). Probing the active site chemistry of supported gold catalysts with charged au25 q nanoclusters (Q = -1, 0, +1). *ECS Meeting Abstracts*, *MA2014-01*(21), 948–948. https://doi.org/10.1149/ma2014-01/21/948

21.) Tsui, E. Y., & Agapie, T. (2013a). Reduction potentials of heterometallic manganese–oxido cubane complexes modulated by redox-inactive metals. *Proceedings of the National Academy of Sciences*, *110*(25), 10084–10088. https://doi.org/10.1073/pnas.1302677110

22.) Chantarojsiri, T., Ziller, J. W., & Yang, J. Y. (2018). Incorporation of redox-inactive cations promotes iron catalyzed aerobic C–H oxidation at mild potentials. *Chemical Science*, *9*(9), 2567–2574. https://doi.org/10.1039/c7sc04486k

23.) Mayneord, W. V. (1979). "John Alfred Valentine Butler, 14 February 1899 - 16 July 1977". Biographical Memoirs of Fellows of the Royal Society. 25: 144–178. doi:10.1098/rsbm.1979.0004. PMID 11615791. S2CID 1412298.

24.) Adler, S.B. (2016). "Chapter 11: Sources of cell and electrode polarisation losses in SOFCs". In Kendall, Kevin; Kendall, Michaela (eds.). High-Temperature Solid Oxide Fuel Cells for the 21st Century (2nd ed.). Academic Press. doi:10.1016/C2011-0-09278-5. ISBN 9780124104532

25.) Butler, J. A. (1924). Studies in heterogeneous equilibria. part ii.—the kinetic interpretation of the nernst theory of electromotive force. *Trans. Faraday Soc.*, *19*(March), 729–733. https://doi.org/10.1039/tf9241900729

26.) Butler, J. A. (1924a). Studies in heterogeneous equilibria. part III. A kinetic theory of reversible oxidation potentials at inert electrodes. *Transactions of the Faraday Society*, *19*(March), 734. https://doi.org/10.1039/tf9241900734

27.) Erdey-Grúz, T., & Volmer, M. (1930). Zur Theorie der Wasserstoff überspannung. *Zeitschrift Für Physikalische Chemie*, *150A*(1), 203–213. https://doi.org/10.1515/zpch-1930-15020

28.) Henstridge, M. C., Laborda, E., Rees, N. V., & Compton, R. G. (2012). Marcus–Hush–Chidsey theory of electron transfer applied to voltammetry: A review. Electrochimica Acta, 84, 12-20. doi:10.1016/j.electacta.2011.10.026

29.) Gourdon, A., & Jeannin, Y. (1992). The synthesis of phosphine derivatives of [fe4n(co)12]−: Crystal Structures of [fe4n(co)9(no)(pph3)2], [HFe4N (CO)11)PPH3)] and [(pph3)2n][fe4n(co)11(pme2ph)]. *Journal of Organometallic Chemistry*, *440*(3), 353–366. https://doi.org/10.1016/0022-328x(92)80214-i

(b) Zanello, P., Laschi, F., Cinquantini, A., Della Pergola, R., Garlaschelli, L., Cucco, M., Demartin, F., & Spalding, T. R. (1994). The redox behaviour of the cluster anion [fe4n(co)12]−. electron transfer chain catalytic substitution reactions. crystal structure of [fe4n(co)11pph3)]−. *Inorganica Chimica Acta*, *226*(1–2), 1–8. https://doi.org/10.1016/0020-1693(94)04061-3

30.) Dickinson, E. J., & Wain, A. J. (2020). The Butler-Volmer equation in electrochemical theory: Origins, value, and practical application. Journal of Electroanalytical Chemistry, 872, 114145. doi:10.1016/j.jelechem.2020.114145

31.) Butler, J. A. (1932). The mechanism of overvoltage and its relation to the combination of hydrogen atoms at metal electrodes. *Transactions of the Faraday Society*, *28*, 379. https://doi.org/10.1039/tf9322800379

32.) Andersen, T. N. (1968). Electrochemistry: *electrochemical kinetics*. theoretical and experimental aspects. Klaus J. Vetter. translated, with revisions by the author, from the German edition (Berlin, 1961) by Scripta Technica. Stanley Bruckenstein and Brian Howard, translation eds. academic press, New York, 1967. XXXIV + 788 pp., illus. $36. *Science*, *159*(3818), 970–970. https://doi.org/10.1126/science.159.3818.970.a

33.) A.J. Bard, L.R. Faulkner. (2001) Electrochemical Methods: Fundamentals and Applications, Second ed. John Wiley & Sons, Inc, Hoboken, NJ, 2001.

34.) J. Newman, K.E. Thomas-Alyea. (2004), Electrochemical Systems, Third ed. John Wiley & Sons, Inc, Hoboken, NJ, 2004.

35.) Crawford, E. (2021, February 15). Svante Arrhenius. Encyclopedia Britannica. https://www.britannica.com/biography/Svante-Arrhenius

36.) Strbac, S. B., & Adzic, R. R. (2014). Electrocatalysis, Fundamentals - Electron Transfer Process; Current-Potential Relationship; Volcano Plots. Encyclopedia of Applied Electrochemistry, 417-423. doi:10.1007/978-1-4419-6996-5_485

37.) Srinivasan, S. (2006). Electrode/electrolyte interfaces: Structure and kinetics of charge transfer. In *Fuel cells from fundamentals to applications*. essay, Springer US. ISBN 978-0-387-35402-6.

38.) Stock, J. T., & Orna, M. V. (1989). *Electrochemistry, past and present*. American Chemical Society. Columbus, OH: ISBN 978-0-8412-1572-6. OCLC 19124885

39.) Lim, C., & MZB. (2014). Reaction Kinetics Lecture 13: Butler-Volmer equation. Lecture presented at Reaction Kinetics Lecture 13: Butler-Volmer equation in MIT, Cambridge, Massachusetts. Spring 2014 Bai, P., & Bazant, M. Z. (2014). Charge transfer kinetics in lifepo4 porous electrodes: Butler-Volmer equation vs Marcus theory. ECS Meeting Abstracts, MA2014-01(1), 22–22. https://doi.org/10.1149/ma2014-01/1/22

40.) Matsuda, H., Ayabe, Y., The theory of the cathode-ray polarography of Randles-Sevcik, Zeitschrift fuer Elektrochmie and Angewandte Physikalische Chemie. 1955, 59, 494-503.

Matsuda, H., & Ayabe, Y. (1955). Zur Theorie der randles-sevčikschen kathodenstrahl-polarographie. *Zeitschrift Für Elektrochemie, Berichte Der Bunsengesellschaft Für Physikalische Chemie*, *59*(6), 494–503. https://doi.org/10.1002/bbpc.19550590605

41.) N. Aristov, A. Habekost. (2015) Cyclic Voltammetry - A Versatile Electrochemical Method Investigating Electron Transfer Processes. World Journal of Chemical Education. 2015; 3(5):115-119. doi: 10.12691/wjce-3-5-2.

42.) Henstridge, M. C., Wang, Y., Limon-Petersen, J. G., Laborda, E., & Compton, R. G. (2011). An experimental comparison of the Marcus–Hush and Butler–Volmer descriptions of electrode kinetics applied to cyclic voltammetry. The one electron reductions of europium (III) and 2-methyl-2-nitropropane studied at a mercury microhemisphere electrode. Chemical Physics Letters, 517(1-3), 29-35. doi:10.1016/j.cplett.2011.10.004

43.) IUPAC. Compendium of Chemical Terminology, 2nd ed. (the "Gold Book"). Compiled by A. D. McNaught and A. Wilkinson. Blackwell Scientific Publications, Oxford (1997). Online version (2019-) created by S. J. Chalk. ISBN 0-9678550-9-8. https://doi.org/10.1351/goldbook.

44.) Frumkin, A. N. & Florianovich, G. M. (1963). Dokl. Akad. nauk, SSSR 80 (1951) 907. *Deep Sea Research and Oceanographic Abstracts*, *10*(1–2), 122. https://doi.org/10.1016/0011-7471(63)90317-6

45.) Gabe, D. R. (2005). The centenary of Tafels equation. Transactions of the IMF, 83(3), 121-124. doi:10.1179/002029605x50191

46.) Tafel, J. (1905). Über die polarisation Bei Kathodischer Wasserstoffentwicklung. *Zeitschrift Für Physikalische Chemie*, *50U*(1), 641–712. https://doi.org/10.1515/zpch-1905-5043

47.) Tafel, J., & Naumann, K. (1905). Beziehungen zwischen kathodenpotential und Elektrolytischer Reduktionswirkung. *Zeitschrift Für Physikalische Chemie*, *50U*(1), 713–752. https://doi.org/10.1515/zpch-1905-5044

48.) Tafel, J., & Emmert, B. (1905). Über die Ursache der spontanen depression des kathodenpotentials bei der Elektrolyse Verdünnter schwefelsäure. *Zeitschrift Für Physikalische Chemie*, *52U*(1), 349–373. https://doi.org/10.1515/zpch-1905-5222

49.) Conway, B. E., & Greef, R. (1966). Theory and principles of Electrode Processes. *Journal of The Electrochemical Society*, *113*(12). https://doi.org/10.1149/1.2423843

50.) Costentin, C., Drouet, S., Robert, M., & Savéant, J.-M. (2012). Turnover numbers, turnover frequencies, and overpotential in molecular catalysis of electrochemical reactions. cyclic voltammetry and preparative-scale electrolysis. *Journal of the American Chemical Society*, *134*(27), 11235–11242. https://doi.org/10.1021/ja303560c

51.) Costentin, C., Robert, M., & Saveant, J. (2013). ChemInform Abstract: Catalysis of the Electrochemical Reduction of Carbon Dioxide. ChemInform, 44(24). doi:10.1002/chin.201324224

52.) Amatore, C., & Savéant, J. M. (1981). Product distribution in preparative scale electrolysis. *Journal of Electroanalytical Chemistry and Interfacial Electrochemistry*, *123*(2), 189–201. https://doi.org/10.1016/s0022-0728(81)80498-6

53.) Loewen, N. D., Neelakantan, T. V., & Berben, L. A. (2017). Renewable Formate from C–H Bond Formation with CO2: Using Iron Carbonyl Clusters as Electrocatalysts. Accounts of Chemical Research, 50(9), 2362-2370. doi:10.1021/acs.accounts.7b00302

54.) Roy, S., Sharma, B., Pécaut, J., Simon, P., Fontecave, M., Tran, P. D., . . . Artero, V. (2017). Molecular Cobalt Complexes with Pendant Amines for Selective Electrocatalytic Reduction of Carbon Dioxide to Formic Acid. Journal of the American Chemical Society, 139(10), 3685-3696. doi:10.1021/jacs.6b11474

55.) Jensen, William B. (2005). "The Origin of the Bunsen Burner" (PDF). Journal of Chemical Education. 82 (4): 518. Bibcode:2005JChEd..82..518J. doi:10.1021/ed082p518. Archived from the original (PDF) on 30 May 2005.

56.) Mr. Faraday. (1827). Lectures on Chemistry. *The Lancet*, *9*(222), 341–347. https://doi.org/10.1016/s0140-6736(01)75287-7

57.) Faraday, Michael (1821). "On two new Compounds of Chlorine and Carbon, and on a new Compound of Iodine, Carbon, and Hydrogen". Philosophical Transactions. 111: 47–74. doi:10.1098/rstl.1821.0007.

58.) Faraday, Michael (1859). Experimental Researches in Chemistry and Physics. London: Richard Taylor and William Francis. pp. 33–53. ISBN 978-0-85066-841-4.

59.) Williams, L. Pearce (1965). Michael Faraday: A Biography. New York: Basic Books. pp. 122–123. ISBN 978-0-306-80299-7.

60.) Faraday. (1823). Darstellung der chlorine und mehrerer Anderer Gasarten tropfbar-flüssig (ohne Wasser?). *Annalen Der Physik Und Der Physikalischen Chemie*, *75*(11), 335–338. https://doi.org/10.1002/andp.18230751108

61.) Faraday, Michael (1859). Experimental Researches in Chemistry and Physics. London: Richard Taylor and William Francis. pp. 81–84. ISBN 978-0-85066-841-4.

62.)   Ehl, Rosemary Gene; Ihde, Aaron (1954). "Faraday's Electrochemical Laws and the Determination of Eq electrochemical fundamentals ent Weights" (PDF). Journal of Chemical Education. 31 (May): 226–232. Bibcode:1954JChEd..31..226E. doi:10.1021/ed031p226.

63.)   Britannica, T. Editors of Encyclopaedia (2021, March 25). Faraday's laws of electrolysis. Encyclopedia Britannica. https://www.britannica.com/science/Faradays-laws-of-electrolysis

64.)   Kelly, N. (2014). Hydrogen production by water electrolysis. Advances in Hydrogen Production, Storage and Distribution, 159-185. doi:10.1533/9780857097736.2.159

65.)   Mavrikis, Sotirios; Perry, Samuel C.; Leung, Pui Ki; Wang, Ling; Ponce de León, Carlos (2021-01-11). "Recent Advances in Electrochemical Water Oxidation to Produce Hydrogen Peroxide: A Mechanistic Perspective". ACS Sustainable Chemistry & Engineering. 9 (1): 76–91. doi:10.1021/acssuschemeng.0c07263.

66.)   Jones, J. E.; et al. (1995). "Faradaic efficiencies less than 100% during electrolysis of water can account for reports of excess heat in 'cold fusion' cells". J. Phys. Chem. 99 (18): 6973–6979. doi:10.1021/j100018a033.

67.)   Shkedi, Z.; et al. (1995). "Calorimetry, Excess Heat, and Faraday Efficiency in Ni-H2O Electrolytic Cells". Fusion Technology. 28 (4): 1720–1731. doi:10.13182/FST95-A30436. ^ "Archived copy" (PDF). Archived from the original (PDF) on 2008-09-21. Retrieved 2008-10-08.

68.)   Shkedi, Z., McDonald, R. C., Breen, J. J., Maguire, S. J., & Veranth, J. (1995). Calorimetry, excess heat, and Faraday efficiency in ni-H2O electrolytic cells. *Fusion Technology*, *28*(4), 1720–1731. https://doi.org/10.13182/fst95-a30436

69.)   Libretexts. (2021, June 17). 14.3: Concentration and Rates (Differential Rate Laws). Retrieved from https://chem.libretexts.org/Bookshelves/General_Chemistry/Map:_Chemistry_The_Central _Science_(Brown_et_al.)/14:_Chemical_Kinetics/14.3:_Concentration_and_Rates_(Differ ential_Rate_Laws)

70.)   Peover, M. E., & White, B. S. (1967). The electro-oxidation of polycyclic aromatic hydrocarbons in acetonitrile studied by cyclic voltammetry. *Journal of Electroanalytical Chemistry and Interfacial Electrochemistry*, *13*(1–2), 93–99. https://doi.org/10.1016/0022-0728(67)80097-4

71.)   Koizumi, N., & Aoyagui, S. (1974). Kinetic parameters of the perylene+/perylene electrode reaction. *Journal of Electroanalytical Chemistry and Interfacial Electrochemistry*, *55*(3), 452–454. https://doi.org/10.1016/s0022-0728(74)80442-0

72.)   Kojima, H., & Bard, A. J. (1975). Determination of rate constants for the electroreduction of aromatic compounds and their correlation with homogeneous electron transfer rates.

Journal of the American Chemical Society, *97*(22), 6317–6324. https://doi.org/10.1021/ja00855a005

73.) Ibl, N. (1963). Elektrochemische Kinetik, Vonk. J. Vetter. Springer-Verlag. Berlin-Göttingen-Heidelberg 1961. 1. aufl., XV, 698 S., 342 abb., geb. DM 156.—. *Angewandte Chemie*, *75*(18), 879–879. https://doi.org/10.1002/ange.19630751837

74.) Erdey-Gruz, T., & Schwarzer, H. (1969). Grundlagen der Struktur der Materie. *Kristall Und Technik Band 4, Heft 2*, 331–332. https://doi.org/10.1515/9783112653685-019

75.) Whitehouse, D. R. (1966). P. Delahay, double layer and electrode kinetics. *Analytica Chimica Acta*, *36*, 412. https://doi.org/10.1016/0003-2670(66)80074-0

76.) Tanaka, N., & Tamamushi, R. (1964). Kinetic parameters of electrode reactions. *Electrochimica Acta*, *9*(7), 963–989. https://doi.org/10.1016/0013-4686(64)85045-3

77.) LINFORD, H. B. (1953). Electrochemical data. B. E. Conway. Amsterdam-houston: Elsevier, 1952. 374 pp. $8.75. *Science*, *118*(3077), 758–758. https://doi.org/10.1126/science.118.3077.758

78.) Holze, R. (2005). Piero Zanello: Inorganic electrochemistry: Theory, practice and applications. *Journal of Solid State Electrochemistry*, *10*(7), 512–513. https://doi.org/10.1007/s10008-005-0007-9

79.) Pine Research Instrumentation. (2020, October 27). Randles–Ševčík Equation. Retrieved from https://pineresearch.com/shop/kb/theory/fundamental-equations/randles-sevcik-equation/

80.) Barjat, H., Morris, G. A., Smart, S., Swanson, A. G., & Williams, S. C. R. (1995a). High-resolution diffusion-ordered 2D spectroscopy (HR-DOSY) - a new tool for the analysis of complex mixtures. *Journal of Magnetic Resonance, Series B*, *108*(2), 170. https://doi.org/10.1006/jmrb.1995.1118

81.) Barjat, H., Morris, G. A., Smart, S., Swanson, A. G., & Williams, S. C. R. (1995a). High-resolution diffusion-ordered 2D spectroscopy (HR-DOSY) - a new tool for the analysis of complex mixtures. *Journal of Magnetic Resonance, Series B*, *108*(2), 171-172. https://doi.org/10.1006/jmrb.1995.1118

82.) Morris, GA. (2009). Diffusion-Ordered Spectroscopy. Encyclopedia of Magnetic Resonance. DOI: 10.1002/9780470034590.emrstm0119.pub2Diffusion-ordered spectroscopy - morris - wiley online library. (n.d.-a). https://onlinelibrary.wiley.com/doi/pdf/10.1002/9780470034590.emrstm0119.pub2 .

83.)   Groves, P. (2017). Diffusion ordered spectroscopy (DOSY) as applied to polymers. Polymer Chemistry, 8(44), 6700-6708. doi:10.1039/c7py01577a

84.)   Tanner, J. E. (1970). Use of the stimulated echo in NMR diffusion studies. *The Journal of Chemical Physics*, *52*(5), 2523–2526. https://doi.org/10.1063/1.1673336

85.)   J. E. Tanner & E. O. Stejskal (2003). "Restricted Self-Diffusion of Protons in Colloidal Systems by the Pulsed-Gradient, Spin-Echo Method". The Journal of Chemical Physics. 49 (4): 1768. Bibcode:1968JChPh..49.1768T. doi:10.1063/1.1670306.

86.)   R. Kerssebaum and G. Salnikov, Topspin Man., 2.0.0, 1–32. Dosy and diffusion 2.0.0 - University of California, San Diego. (n.d.-b). http://sopnmr.ucsd.edu/assets/pdf/DOSY_and_Diffusion.pdf

87.)   Sinnaeve, D. (2012). The stejskal-tanner equation generalized for any gradient shape-an overview of most pulse sequences measuring free diffusion. *Concepts in Magnetic Resonance Part A*, *40A*(2), 39–65. https://doi.org/10.1002/cmr.a.21223 .

88.)   Vrvic, M. (2003). Comprehensive enzyme kinetics by V. Leskovac, published by Kluwer Academic/Plenum Plblisher New York, March 2003-11-17. *Journal of the Serbian Chemical Society*, *68*(12), 1011–1013. https://doi.org/10.2298/jsc0312011v

89.)   Bligaard, Thomas; Bullock, R. Morris; Campbell, Charles T.; Chen, Jingguang G.; Gates, Bruce C.; Gorte, Raymond J.; Jones, Christopher W.; Jones, William D.; Kitchin, John R.; Scott, Susannah L. (2016). "Toward Benchmarking in Catalysis Science: Best Practices, Challenges, and Opportunities". ACS Catalysis. 6 (4): 2590–2602. doi:10.1021/acscatal.6b00183.

90.)   Savéant, J. M., & Costentin, C. (2019). Hoboken, NJ: John Wiley & Sons. *Elements of Molecular and Biomolecular Electrochemistry*. https://doi.org/10.1002/9781119292364

91.)   Carr, C. R.; Cluff, D. B.; Berben, L. A.: Organometallics 2020, 39, 1658-1663 Hazari, N., Iwasawa, N., & Hopmann, K. H. (2020). Organometallic chemistry for enabling carbon dioxide utilization. Organometallics, 39(9), 1457–1460. https://doi.org/10.1021/acs.organomet.0c00229.

92.)   Carr, C. R., Cluff, D. B., & Berben, L. A. (2020). Breaking scaling relationships in co2 electroreduction with isoelectronic analogs [fe4n(co)12]− and [Fe3mno(co)12]−. Organometallics, 39(9), 1658–1663. https://doi.org/10.1021/acs.organomet.9b00848

93.)   Pattanayak, S., Loewen, N. D., & Berben, L. A. (2022). Using substituted [fe4n(co)12]− as a platform to probe the effect of cation and Lewis acid location on redox potential. Inorganic Chemistry. https://doi.org/10.1021/acs.inorgchem.2c01556

94.) Johnson, S. I., Nielsen, R. J., & Goddard, W. A. (2016). Selectivity for HCO2– over H2 in the electrochemical catalytic reduction of CO2 by (POCOP)IRH2. *ACS Catalysis*, *6*(10), 6362–6371. https://doi.org/10.1021/acscatal.6b01755

95.) Curtis, C. J., Miedaner, A., Ellis, W. W., & DuBois, D. L. (2002). Measurement of the hydride donor abilities of [hm(diphosphine)2]+ complexes (M = ni, pt) by heterolytic activation of hydrogen. *Journal of the American Chemical Society*, *124*(9), 1918–1925. https://doi.org/10.1021/ja0116829

96.) Vrvic, M. (2003a). Comprehensive enzyme kinetics by V. Leskovac, published by Kluwer Academic/Plenum Plblisher New York, March 2003-11-17. *Journal of the Serbian Chemical Society*, *68*(12), 1011–1013. https://doi.org/10.2298/jsc0312011v

97.) Bligaard, Thomas; Bullock, R. Morris; Campbell, Charles T.; Chen, Jingguang G.; Gates, Bruce C.; Gorte, Raymond J.; Jones, Christopher W.; Jones, William D.; Kitchin, John R.; Scott, Susannah L. (2016). "Toward Benchmarking in Catalysis Science: Best Practices, Challenges, and Opportunities". ACS Catalysis. 6 (4): 2590–2602. doi:10.1021/acscatal.6b00183.

98.) Tachikawa, M., Stein, J., Muetterties, E. L., Teller, R. G., Beno, M. A., Gebert, E., & Williams, J. M. (1980). Metal clusters with exposed and low-coordinate nitride nitrogen atoms. *Journal of the American Chemical Society*, *102*(21), 6648–6649. https://doi.org/10.1021/ja00541a084

(b) Nguyen, A. D., Rail, M. D., Shanmugam, M., Fettinger, J. C., & Berben, L. A. (2013). Electrocatalytic hydrogen evolution from water by a series of iron carbonyl clusters. *Inorganic Chemistry*, *52*(21), 12847–12854. https://doi.org/10.1021/ic4023882

99.) Savéant, J. M., & Su, K. B. (1984). Homogeneous redox catalysis of electrochemical reaction. *Journal of Electroanalytical Chemistry and Interfacial Electrochemistry*, *171*(1–2), 341–349. https://doi.org/10.1016/0022-0728(84)80125-4

100.) Savéant, J., & Costentin, C. (2019a). *Elements of Molecular and Biomolecular Electrochemistry*. https://doi.org/10.1002/9781119292364 .

101.) Carr, C. R., Cluff, D. B., & Berben, L. A. (2020a). Breaking scaling relationships in co2 electroreduction with isoelectronic analogs [fe4n(co)12]− and [Fe3mno(co)12]−. *Organometallics*, *39*(9), 1658–1663. https://doi.org/10.1021/acs.organomet.9b00848

102.) Otero, Y., Peña, D., Arce, A., Hissler, M., Réau, R., Sanctis, Y. D., . . . González, T. (2015). Fluxional behaviour of phosphole and phosphine ligands on triosmium clusters. Journal of Organometallic Chemistry, 799-800, 45-53. doi:10.1016/j.jorganchem.2015.08.026

103.) Wang, V., & Johnson, B. A. (2019). Interpreting the Electrocatalytic Voltammetry of Homogeneous Catalysts by the Foot of the Wave Analysis and Its Wider Implications. doi:10.26434/chemrxiv.7771217.v1

104.) Loewen, N. D., & Berben, L. A. (2019). Secondary Coordination Sphere Design to Modify Transport of Protons and CO2. Inorganic Chemistry, 58(24), 16849-16857. doi:10.1021/acs.inorgchem.9b03102

105.) Taheri, A., Carr, C. R., & Berben, L. A. (2018). Electrochemical methods for assessing kinetic factors in the reduction of CO2 to formate: Implications for improving electrocatalyst design. *ACS Catalysis*, *8*(7), 5787–5793. https://doi.org/10.1021/acscatal.8b01799

106.) Izutsu, K. Acid−Base Dissociation Constants in Dipolar Aprotic Solvents (IUPAC Chemical Data Series); Blackwell Science: Hoboken, NJ, 1990. Oxford ; Boston : Blackwell Scientific Publications ; Brookline Village, Mass. : Distributors, USA, Publishers' Business Services. (1990, January 1). Acid-base dissociation constants in dipolar aprotic solvents : Izutsu, Kosuke, 1933- : Free download, Borrow, and streaming. Internet Archive. https://archive.org/details/acidbasedissocia0000izut

(b) Fourmond, V., Jacques, P.-A., Fontecave, M., & Artero, V. (2010). H2 evolution and molecular electrocatalysts: Determination of overpotentials and effect of homoconjugation. *Inorganic Chemistry*, *49*(22), 10338–10347. https://doi.org/10.1021/ic101187v

107.) Savéant, J., & Costentin, C. (2019a). *Elements of Molecular and Biomolecular Electrochemistry*. https://doi.org/10.1002/9781119292364

108.)   Oxford ; Boston : Blackwell Scientific Publications ; Brookline Village, Mass. : Distributors, USA, Publishers' Business Services. (1990, January 1). Acid-base dissociation constants in dipolar aprotic solvents : Izutsu, Kosuke, 1933- : Free download, Borrow, and streaming. Internet Archive. https://archive.org/details/acidbasedissocia0000izut

109.) Taheri, A., Carr, C. R., & Berben, L. A. (2018). Electrochemical methods for assessing kinetic factors in the reduction of CO2 to formate: Implications for improving electrocatalyst design. *ACS Catalysis*, *8*(7), 5787–5793. https://doi.org/10.1021/acscatal.8b01799

110.) Savéant, J.-M. (2008). Molecular catalysis of electrochemical reactions. mechanistic aspects. *Chemical Reviews*, *108*(7), 2348–2378. https://doi.org/10.1021/cr068079z

(b) Costentin, C., & Savéant, J.-M. (2014). Multielectron, multistep molecular catalysis of electrochemical reactions: Benchmarking of homogeneous catalysts. *ChemElectroChem*, *1*(7), 1226–1236. https://doi.org/10.1002/celc.201300263

111.) Savéant, J., & Costentin, C. (2019a). *Elements of Molecular and Biomolecular Electrochemistry*. https://doi.org/10.1002/9781119292364

112.) Chantarojsiri, T., Ziller, J. W., & Yang, J. Y. (2018). Incorporation of redox-inactive cations promotes iron catalyzed aerobic C–H oxidation at mild potentials. *Chemical Science*, *9*(9), 2567–2574. https://doi.org/10.1039/c7sc04486k

(b)Chantarojsiri, T., Reath, A. H., & Yang, J. Y. (2018). Cationic charges leading to an inverse free-energy relationship for N−N bond formation by Mn   vi   nitrides. *Angewandte Chemie International Edition*, *57*(43), 14037–14042. https://doi.org/10.1002/anie.201805832

(c) Kang, K., Fuller, J., Reath, A. H., Ziller, J. W., Alexandrova, A. N., & Yang, J. Y. (2019). Installation of internal electric fields by non-redox active cations in transition metal complexes. *Chemical Science*, *10*(43), 10135–10142. https://doi.org/10.1039/c9sc02870f

(d) Azcarate, I., Costentin, C., Robert, M., & Savéant, J.-M. (2016). Through-space charge interaction substituent effects in molecular catalysis leading to the design of the most efficient catalyst of CO2-to-Co electrochemical conversion. *Journal of the American Chemical Society*, *138*(51), 16639–16644. https://doi.org/10.1021/jacs.6b07014

113.) Savéant, J.-M. (2008a). Molecular catalysis of electrochemical reactions. mechanistic aspects. *Chemical Reviews*, *108*(7), 2348–2378. https://doi.org/10.1021/cr068079z

114.) Costentin, C., & Savéant, J.-M. (2014a). Multielectron, multistep molecular catalysis of electrochemical reactions: Benchmarking of homogeneous catalysts. *ChemElectroChem*, *1*(7), 1226–1236. https://doi.org/10.1002/celc.201300263

115.) Savéant, J. M., & Su, K. B. (1984). Homogeneous redox catalysis of electrochemical reaction. *Journal of Electroanalytical Chemistry and Interfacial Electrochemistry*, *171*(1–2), 341–349. https://doi.org/10.1016/0022-0728(84)80125-4

116.) Margarit, C. G., Asimow, N. G., Gonzalez, M. I., & Nocera, D. G. (2020). Double Hangman Iron Porphyrin and the Effect of Electrostatic Nonbonding Interactions on Carbon Dioxide Reduction. The Journal of Physical Chemistry Letters, 11(5), 1890-1895. doi:10.1021/acs.jpclett.9b03897

117.) Tashiro, Y., Hirano, S., Matson, M. M., Atsumi, S., & Kondo, A. (2018). Electrical-biological hybrid system for CO2 reduction. Metabolic Engineering, 47, 211-218. doi:10.1016/j.ymben.2018.03.015

118.) Desai, S. H., Rabinovitch-Deere, C. A., Fan, Z., & Atsumi, S. (2015). Isobutanol production from cellobionic acid in Escherichia coli. Microbial Cell Factories, 14(1). doi:10.1186/s12934-015-0232-6

119.) How a solar cell works. American Chemical Society. (n.d.). Retrieved September 4,2022 https://www.acs.org/content/acs/en/education/resources/highschool/chemmatters/past-

issues/archive-2013-2014/how-a-solar-cell-works.htmlGreenwood, Norman N.; Earnshaw, Alan (1997). Chemistry of the Elements (2nd ed.). Butterworth-Heinemann. pp. 751–752. ISBN 978-0-08-037941-8

120.) Fernandez, A. (n.d.). How a solar cell works. American Chemical Society. Retrieved April 21, 2023, from https://www.acs.org/education/resources/highschool/chemmatters/past-issues/archive-2013-2014/how-a-solar-cell-works.html

121.) Standard atomic weights (2013). (2014). *CRC Handbook of Chemistry and Physics*, 2663–2663. https://doi.org/10.1201/b17118-26

122.) Wood-Black, F. (2000). NIOSH pocket guide to Chemical Hazards and other databases DHHS (NIOSH) publication no. 99-115. *Chemical Health & Safety*, *7*(2), 52–52. https://doi.org/10.1016/s1074-9098(99)00094-5

123.)   Antimony triselenide. American Chemical Society. (n.d.). Retrieved July 27, 2022, from https://www.acs.org/content/acs/en/molecule-of-the-week/archive/a/antimony-triselenide.html

124.) Li, Z., Liu, H., Luo, W., Minceva-Sukarova, B., Pfrommer, B. G., Bilgin, I., Butt, F. K., Chang, H.-W., Chen, G.-Y., Chen, G., Clark, S. J., Dan, Y., Deng, Y., Efthimiopoulos, I., Fan, X., Gong, C., Guo, L., Hamrouni, R., Hao, S., … Lin, M.-L. (2022, January 23). *Two-dimensional antimony selenide (SB2SE3) nanosheets prepared by hydrothermal method for visible-light photodetectors*. Solar Energy. https://www.sciencedirect.com/science/article/abs/pii/S0038092X22000226

125.) Tideswell, N. W., Kruse, F. H., & McCullough, J. D. (1957). The crystal structure of antimony selenide, SB2SE3. *Acta Crystallographica*, *10*(2), 99–102. https://doi.org/10.1107/s0365110x57000298

126.) Niclas. (2022, April 21). Energy band gap of Solar Cells. Energy Band Gap of Solar cells. Retrieved March 24, 2023, from https://sinovoltaics.com/learning-center/solar-cells/energy-band-gap-of-solar-cells/

(a) William Shockley; Hans J. Queisser (March 1961). "Detailed Balance Limit of Efficiency of p-n Junction Solar Cells" (PDF). Journal of Applied Physics. 32 (3): 510–519. Bibcode:1961JAP....32..510S. doi:10.1063/1.1736034.

(b) "Hans Queisser". Computer History Museum. Retrieved 17 January 2017. Oral history of Hans Queisser - Computer history museum. (n.d.-a). http://archive.computerhistory.org/resources/text/Oral_History/Queisser_Hans/Queisser_Hans_1.oral_history.2006.102658051.pdf

(c) A. De Vos & H. Pauwels (1981). "On the Thermodynamic Limit of Photovoltaic Energy Conversion". Appl. Phys. 25 (2): 119–125. Bibcode:1981ApPhy..25..119D. doi:10.1007/BF00901283. S2CID 119693148.

(d) De Vos, A. (1980). "Detailed balance limit of the efficiency of tandem solar cells". Journal of Physics D: Applied Physics. 13 (5): 839–846. Bibcode:1980JPhD...13..839D. doi:10.1088/0022-3727/13/5/018. S2CID 250782402.

127.) Costa, M. B., Lucas, F. W., & Mascaro, L. H. (2019). Electrodeposition conditions effect SB2se3thin-film properties. ChemElectroChem, 6(11), 2937–2944. https://doi.org/10.1002/celc.201900457

128.) FTO glass substrates, unpatterned: TEC 8, TEC 10, TEC 15 FTO. Ossila. (n.d.). Retrieved April 21, 2023, from https://www.ossila.com/en-us/products/fto-glass-unpatterned#:~:text=There%20are%20several%20properties%20of,a%20wide%20range%20of%20chemicals.

129.) Way, A., Luke, J., Evans, A. D., Li, Z., Kim, J.-S., Durrant, J. R., Hin Lee, H. K., & Tsoi, W. C. (2019). Fluorine doped tin oxide as an alternative of indium tin oxide for bottom electrode of semi-transparent organic photovoltaic devices. AIP Advances, 9(8), 085220. https://doi.org/10.1063/1.5104333

130.) Bhattacharyya, B. (2015). Electrochemical micromachining setup. *Electrochemical Micromachining for Nanofabrication, MEMS and Nanotechnology*, 83–100. https://doi.org/10.1016/b978-0-323-32737-4.00005-0

131.) Arulmani, S., Anandan, S., & Ashokkumar, M. (2018). Introduction to advanced nanomaterials. Nanomaterials for Green Energy, 1–53. https://doi.org/10.1016/b978-0-12-813731-4.00001-1

132.) De Alwis, A. C., Atapattu, H. Y., & De Silva, D. S. (2018). Influence of the type of conducting glass substrate on the properties of electrodeposited cds and CdTe thin films. Journal of Materials Science: Materials in Electronics, 29(14), 12419–12428. https://doi.org/10.1007/s10854-018-9358

133.) Kim, J., Yang, W., Oh, Y., Lee, H., Lee, S., Shin, H., Kim, J., & Moon, J. (2017). Self-oriented Sb2Se3 nanoneedle photocathodes for water splitting obtained by a simple spin-coating method. Journal of Materials Chemistry A, 5(5), 2180–2187. https://doi.org/10.1039/c6ta09602f

134.) Versavel, M. Y., & Haber, J. A. (2007). Structural and optical properties of amorphous and crystalline antimony sulfide thin-films. *Thin Solid Films*, *515*(18), 7171–7176. https://doi.org/10.1016/j.tsf.2007.03.043

135.) Kumar, P., & Thangaraj, R. (2006). Electrical conduction and optical properties of amorphous (sb2se3)100−xsnx thin films. *Solid State Communications*, *140*(11–12), 525–528. https://doi.org/10.1016/j.ssc.2006.09.029

136.) Vedeshwar, A. G. (1995). Optical properties of amorphous and Polycrystalline Stibnite (SB2s3) films. *Journal de Physique III*, *5*(8), 1161–1172. https://doi.org/10.1051/jp3:1995183

137.) Kashif, M., Jaafar, E., Bhadja, P., Wah Low, F., Kudnie Sahari, S., Hussain, S., Kai Loong, F., Ahmad, A., Saad AlGarni, T., Shafa, M., Asghar, H., & Al-Tamrah, S. A. (2021). Effect of potassium permanganate on morphological, structural and electro-optical properties of graphene oxide thin films. Arabian Journal of Chemistry, 14(2), 102953. https://doi.org/10.1016/j.arabjc.2020.102953

138.) Yang, Y., Wu, J., Liu, X., Guo, Q., Wang, X., Liu, L., Ding, Y., Dai, S., & Lin, J.-Y. (2019). Dual functional doping of KMNO4 in spiro-ometad for highly effective planar perovskite solar cells. *ACS Applied Energy Materials*, *2*(3), 2188–2196. https://doi.org/10.1021/acsaem.8b02219

139.) Costa, M. B., de Souza Lucas, F. W., & Mascaro, L. H. (2017). Electrodeposition of fe-doped Sb2Se3 thin films for photoelectrochemical applications and study of the doping effects on their properties. Journal of Solid State Electrochemistry, 22(5), 1557–1562. https://doi.org/10.1007/s10008-017-3768-z

140.) Costa, M. B., de Souza Lucas, F. W., & Mascaro, L. H. (2017). Thermal treatment effects on electrodeposited SB2se3photovoltaic thin films. ChemElectroChem, 4(10), 2507–2514. https://doi.org/10.1002/celc.201700511

141.) Li, Z., Liang, X., Li, G., Liu, H., Zhang, H., Guo, J., Chen, J., Shen, K., San, X., Yu, W., Schropp, R. E., & Mai, Y. (2019). 9.2%-efficient core-shell structured antimony selenide nanorod array solar cells. Nature Communications, 10(1). https://doi.org/10.1038/s41467-018-07903-6

142.) Zhu, J., Yu, Z., Burkhard, G. F., Hsu, C.-M., Connor, S. T., Xu, Y., Wang, Q., McGehee, M., Fan, S., & Cui, Y. (2009). Optical absorption enhancement in amorphous silicon nanowire and nanocone arrays. *Nano Letters*, *9*(1), 279–282. https://doi.org/10.1021/nl802886y

143.) Chen, C., Bobela, D. C., Yang, Y., Lu, S., Zeng, K., Ge, C., Yang, B., Gao, L., Zhao, Y., Beard, M. C., & Tang, J. (2017). Characterization of basic physical properties of SB2SE3 and its relevance for photovoltaics. *Frontiers of Optoelectronics*, *10*(1), 18–30. https://doi.org/10.1007/s12200-017-0702-z

144.) Gobet, J., & Tannenberger, H. (1988). ChemInform Abstract: Electrodeposition of Silicon from a Nonaqueous Solvent. ChemInform, 19(18). doi:10.1002/chin.198818016

145.) Torane, A. P., Rajpure, K. Y., & Bhosale, C. H. (1999). Preparation and characterization of electrodeposited SB2SE3 thin films. *Materials Chemistry and Physics*, *61*(3), 219–222. https://doi.org/10.1016/s0254-0584(99)00160-1

146.) Ghosh, S., Moreira, M. V. B., Fantini, C., & González, J. C. (2020). Growth and optical properties of nanocrystalline SB2SE3 thin-films for the application in solar-cells. Solar Energy,211,613–621. https://doi.org/10.1016/j.solener.2020.10.00.

147.)   Wei, H., Gong, H., Wang, Y., Hu, X., Chen, L., Xu, H., . . . Cao, B. (2011). Three kinds of Cu2O/ZnO heterostructure solar cells fabricated with electrochemical deposition and their structure-related photovoltaic properties. CrystEngComm, 13(20), 6065. doi:10.1039/c1ce05540b

148.)   Pham, B., Willinger, D., Mcmillan, N. K., Roye, J., Burnett, W., Dachille, A., . . . Sherman, B. D. (2021). Tin(IV) oxide nanoparticulate films for aqueous dye-sensitized solar cells. Solar Energy, 224, 984-991. doi:10.1016/j.solener.2021.06.067

149.)   Chappel, S., & Zaban, A. (2002). Nanoporous SNO2 electrodes for dye-sensitized solar cells: Improved cell performance by the synthesis of 18nm sno2 colloids. Solar Energy Materials and Solar Cells, 71(2), 141–152. https://doi.org/10.1016/s09270248(01)00050-2

150.)   Dong, C., Xiang, W., Huang, F., Fu, D., Huang, W., Bach, U., Cheng, Y.-B., Li, X., & Spiccia, L. (2014). Controlling interfacial recombination in aqueous dye-sensitized solar cells by octadecyltrichlorosilane surface treatment. *Angewandte Chemie International Edition*, *53*(27), 6933–6937. https://doi.org/10.1002/anie.201400723

151.)   Lin, R. Y.-Y., Wu, F.-L., Li, C.-T., Chen, P.-Y., Ho, K.-C., & Lin, J. T. (2015). High-performance aqueous/organic dye-sensitized solar cells based on sensitizers containing triethylene oxide methyl ether. *ChemSusChem*, *8*(15), 2503–2513. https://doi.org/10.1002/cssc.201500589

152.)   Bella, F., Porcarelli, L., Mantione, D., Gerbaldi, C., Barolo, C., Grätzel, M., & Mecerreyes, D. (2020). A water-based and metal-free dye solar cell exceeding 7% efficiency using a cationic poly(3,4-ethylenedioxythiophene) derivative. *Chemical Science*, *11*(6), 1485–1493. https://doi.org/10.1039/c9sc05596g

153.)   Mathews, N. R. (2009). Chemically and Electrochemically Deposited Thin Films of Tin Sulfide for Photovoltaic Structures. MRS Proceedings, 1165. doi:10.1557/proc-1165-m08-35

        (a) Cheng, S., Chen, Y., He, Y., & Chen, G. (2007a). The structure and properties of SNS thin films prepared by pulse electro-deposition. *Materials Letters*, *61*(6), 1408–1412. https://doi.org/10.1016/j.matlet.2006.07.067

        (b) Avellaneda, D., Nair, M. T., & Nair, P. K. (2008). Polymorphic tin sulfide thin films of zinc blende and orthorhombic structures by chemical deposition. *Journal of The Electrochemical Society*, *155*(7). https://doi.org/10.1149/1.2917198

154.)   Ramakrishna Reddy, K. T., Koteswara Reddy, N., & Miles, R. W. (2006). Photovoltaic properties of SNS based solar cells. *Solar Energy Materials and Solar Cells*, *90*(18–19), 3041–3046. https://doi.org/10.1016/j.solmat.2006.06.012

155.) Reddy, N. K., Reddy, K. T., Fisher, G., Best, R., & Dutta, P. K. (1999). The structural behaviour of layers of SNS grown by spray pyrolysis. *Journal of Physics D: Applied Physics*, *32*(9), 988–990. https://doi.org/10.1088/0022-3727/32/9/307

156.) Gunasekaran, M., & Ichimura, M. (2007). Photovoltaic cells based on pulsed electrochemically deposited SNS and photochemically deposited cds and cd1−xznxs. *Solar Energy Materials and Solar Cells*, *91*(9), 774–778. https://doi.org/10.1016/j.solmat.2006.10.026

157.) Sato, N., Ichimura, M., Arai, E., & Yamazaki, Y. (2005). Characterization of electrical properties and photosensitivity of SNS thin films prepared by the electrochemical deposition method. *Solar Energy Materials and Solar Cells*, *85*(2), 153–165. https://doi.org/10.1016/j.solmat.2004.04.014

158.) Xi, D., Zhang, H., Furst, S., Chen, B., & Pei, Q. (2008). Electrochemical Synthesis and Photovoltaic Property of Cadmium Sulfide−Polybithiophene Interdigitated Nanohybrid Thin Films. The Journal of Physical Chemistry C, 112(49), 19765-19769. doi:10.1021/jp807868j

159.) Gorer, S., Ganske, J. A., Hemminger, J. C., & Penner, R. M. (1998). Size-selective and epitaxial electrochemical/chemical synthesis of sulfur-passivated cadmium sulfide nanocrystals on graphite. *Journal of the American Chemical Society*, *120*(37), 9584–9593. https://doi.org/10.1021/ja981676l

160.) Gorer, S., & Penner, R. M. (1999). "multipulse" electrochemical/chemical synthesis of cds/s core/shell nanocrystals exhibiting Ultranarrow photoluminescence emission lines. *The Journal of Physical Chemistry B*, *103*(28), 5750–5753. https://doi.org/10.1021/jp991141u

161.) Li, Q., & Penner, R. M. (2005). Photoconductive cadmium sulfide hemicylindrical shell nanowire ensembles. *Nano Letters*, *5*(9), 1720–1725. https://doi.org/10.1021/nl050994x

162.) Hu, H., Kung, S., Yang, L., Nicho, M., & Penner, R. M. (2009). Photovoltaic devices based on electrochemical–chemical deposited CdS and poly3-octylthiophene thin films. Solar Energy Materials and Solar Cells, 93(1), 51-54. doi:10.1016/j.solmat.2008.03.011

163.) Ji, W., & Ichimura, M. (2019). Fabrication of photovoltaic FeSxOy/ZnO heterostructures by electrochemical deposition. Japanese Journal of Applied Physics, 58(5), 050922. doi:10.7567/1347-4065/ab1975

164.) Yao, L., Ao, J., Jeng, M.-J., Bi, J., Gao, S., He, Q., Zhou, Z., Sun, G., Sun, Y., Chang, L.-B., & Chen, J.-W. (2014). CZTSe solar cells prepared by electrodeposition of Cu/Sn/Zn Stack Layer followed by Selenization at low se pressure. Nanoscale Research Letters, 9(1). https://doi.org/10.1186/1556-276x-9-678

165.) Jeon, J.-O., Lee, K. D., Seul Oh, L., Seo, S.-W., Lee, D.-K., Kim, H., Jeong, J.-hyun, Ko, M. J., Kim, B. S., Son, H. J., & Kim, J. Y. (2014). Highly efficient copper-zinc-tin-selenide

(CZTSe) solar cells by electrodeposition. ChemSusChem, 7(4), 1073–1077. https://doi.org/10.1002/cssc.201301347

166.) Lee, K. D., Seo, S.-W., Lee, D.-K., Kim, H., Jeong, J., Ko, M. J., Kim, B., Kim, D. H., & Kim, J. Y. (2013). Preparation of CU2ZNSNS4 thin films via electrochemical deposition and rapid thermal annealing. *Thin Solid Films*, *546*, 294–298. https://doi.org/10.1016/j.tsf.2013.02.051

167.) Araki, H., Kubo, Y., Jimbo, K., Maw, W. S., Katagiri, H., Yamazaki, M., Oishi, K., & Takeuchi, A. (2009). Preparation of cu2znsns thin films by sulfurization of co-electroplated cu-zn-sn precursors. *Physica Status Solidi c*, *6*(5), 1266–1268. https://doi.org/10.1002/pssc.200881182 .

168.) Bär, M., Schubert, B.-A., Marsen, B., Krause, S., Pookpanratana, S., Unold, T., Weinhardt, L., Heske, C., & Schock, H.-W. (2011). Native oxidation and Cu-poor surface structure of thin film CU2ZNSNS4 solar cell absorbers. *Applied Physics Letters*, *99*(11). https://doi.org/10.1063/1.3637574

169.) Mandati, S., Misra, P., Boosagulla, D., Rao, T. N., & Sarada, B. V. (2020). Economic pulse electrodeposition for flexible Cuinse2 Solar Cells. Materials for Renewable and Sustainable Energy, 9(3). https://doi.org/10.1007/s40243-020-00177-3

170.) Luo, M., Leng, M., Liu, X., Chen, J., Chen, C., Qin, S., & Tang, J. (2014). Thermal evaporation and characterization of superstrate cds/SB2SE3 solar cells. *Applied Physics Letters*, *104*(17). https://doi.org/10.1063/1.4874878

171.) Zhou, Y., Wang, L., Chen, S., Qin, S., Liu, X., Chen, J., Xue, D.-J., Luo, M., Cao, Y., Cheng, Y., Sargent, E. H., & Tang, J. (2015). Thin-film SB2SE3 photovoltaics with oriented one-dimensional ribbons and benign grain boundaries. *Nature Photonics*, *9*(6), 409–415. https://doi.org/10.1038/nphoton.2015.78

172.) Messina, S., Nair, M. T., & Nair, P. K. (2009). Antimony selenide absorber thin films in all-chemically deposited solar cells. *Journal of The Electrochemical Society*, *156*(5). https://doi.org/10.1149/1.3089358

173.) *Inorganic crystal structure database – ICSD*. Inorganic Crystal Structure Database – ICSD | FIZ Karlsruhe. (n.d.). http://www.fiz-karlsruhe.de/icsd.html for Inorganic Crystal Structure Database (last accessed January 2018).

174.) de Souza Lucas, F. W., & Zakutayev, A. (2018). Research update: Emerging Chalcostibite absorbers for thin-film solar cells. APL Materials, 6(8), 084501. https://doi.org/10.1063/1.5027862

175.) Tang, A., Long, M., & He, Z. (2014). Electrodeposition of SB 2 SE 3 on tio 2 nanotube arrays for catalytic reduction of P -nitrophenol. *Electrochimica Acta*, *146*, 346–352. https://doi.org/10.1016/j.electacta.2014.09.027

176.) Lai, Y., Han, C., Lv, X., Yang, J., Liu, F., Li, J., & Liu, Y. (2012). Electrodeposition of antimony selenide thin films from aqueous acid solutions. *Journal of Electroanalytical Chemistry*, *671*, 73–79. https://doi.org/10.1016/j.jelechem.2012.02.018

177.) Yang, J., Zhu, W., Gao, X., Bao, S., Fan, X., Duan, X., & Hou, J. (2006). Formation and characterization of SB2te3 nanofilms on PT by electrochemical atomic layer epitaxy. *The Journal of Physical Chemistry B*, *110*(10), 4599–4604. https://doi.org/10.1021/jp0565498

178.) Chen, Y., Wang, L., Pradel, A., Merlen, A., Ribes, M., & Record, M.-C. (2015). Underpotential deposition of selenium and antimony on gold. *Journal of Solid State Electrochemistry*, *19*(8), 2399–2411. https://doi.org/10.1007/s10008-015-2881-0

179.) Shi, X., zhang, X., Tian, Y., Shen, C., Wang, C., & Gao, H.-J. (2012). Electrodeposition of SB2SE3 on indium-doped tin oxides substrate: Nucleation and growth. Applied Surface Science, 258(6), 2169–2173. https://doi.org/10.1016/j.apsusc.2011.02.097

180.) Krumm, R., Guel, B., Schmitz, C., & Staikov, G. (2000). Nucleation and growth in electrodeposition of metals on n-si(111). *Electrochimica Acta*, *45*(20), 3255–3262. https://doi.org/10.1016/s0013-4686(00)00418-7

181.) Gunawardena, G., Hills, G., Montenegro, I., & Scharifker, B. (1982). Electrochemical Nucleation. *Journal of Electroanalytical Chemistry and Interfacial Electrochemistry*, *138*(2), 225–239. https://doi.org/10.1016/0022-0728(82)85080-8

182.) Scharifker, B., & Hills, G. (1983). Theoretical and experimental studies of multiple nucleation. *Electrochimica Acta*, *28*(7), 879–889. https://doi.org/10.1016/0013-4686(83)85163-9

183.) Sadale, S. (2004). Nucleation and growth of bismuth thin films onto fluorine-doped tin oxide-coated conducting glass substrates from nitrate solutions. *Solid State Ionics*, *167*(3–4), 273–283. https://doi.org/10.1016/j.ssi.2004.01.017

184.) Harrick Scientific Products, Inc. |. (n.d.). What is Kubelka-Munk? - California Institute of Technology. California Institute of Technology. https://mmrc.caltech.edu/FTIR/Literature/Diff%20Refectance/Kubelka-Munk.pdf

185.) Kubelka, Paul; Munk, Franz (1931). "An article on optics of paint layers" (PDF). Z. Tech. Phys. 12: 593–601. An article on optics of Paint Layers - Cornell University. (n.d.-a). http://www.graphics.cornell.edu/~westin/pubs/kubelka.pdf

186.) "Kubelka–Munk Theory – an overview". www.sciencedirect.com. Retrieved 22 February 2021. *Kubelka-Munk theory*. Kubelka-Munk Theory - an overview | ScienceDirect Topics. (n.d.). https://www.sciencedirect.com/topics/engineering/kubelka-munk-theory

187.) Brill, M. H., & Vik, M. (2014). Kubelka, paul. *Encyclopedia of Color Science and Technology*, 1–3. https://doi.org/10.1007/978-3-642-27851-8_300-1

188.) Westin, Stephen (2011). "Autobiographical Sketch: Paul Kubelka". Autobiographical sketch: Paul Kubelka. (n.d.). https://www.graphics.cornell.edu/~westin/pubs/kubelka-autobio.html

189.) Schroder, Dieter K. (2006). Semiconductor Material and Device Characterization. Wiley-IEEE Press. ISBN 978-0-471-73906-7.

190.) Schroder, Dieter K. (2001). "Surface voltage and surface photovoltage: history, theory and applications". Meas. Sci. Technol. 12 (3): R16–R31. Bibcode:2001MeScT..12R..16S. doi:10.1088/0957-0233/12/3/202.

191.) Kronik, L.; Shapira, Y. (1999). "Surface photovoltage phenomena: theory, experiment, and applications" (PDF). Surface Science Reports. 37 (1): 1–206. Bibcode:1999SurSR..37....1K. CiteSeerX 10.1.1.471.8047. doi:10.1016/S0167-5729(99)00002-3. Archived from the original (PDF) on 2005-03-12. Retrieved 2008-07-03.

192.) Light-induced charge separation and surface photovoltage. (2020). *Surface Photovoltage Analysis of Photoactive Materials*, 1–46. https://doi.org/10.1142/9781786347664_0001

193.) Ko, T.-Y., Shellaiah, M., & Sun, K. W. (2016). Scientific Reports, 6(1). https://doi.org/10.1038/srep35086

194.) (2021, November 26). Selenium - melting point - boiling point. Nuclear Power. https://www.nuclear-power.com/selenium-melting-point-boiling-point/ *Selenium - element information, properties and uses: Periodic Table*. Selenium - Element information, properties and uses | Periodic Table. (n.d.). https://www.rsc.org/periodic-table/element/34/Selenium

195.) *The Royal Society of Chemistry*. Royal Society of Chemistry. 2023 Registered charity number: 207890. (n.d.). Antimony - element information, properties and uses: Periodic Table. Antimony - Element information, properties and uses | Periodic Table. (n.d.). https://www.rsc.org/

196.) Quantitative EDS explained: How to achieve great results - 2021 - wiley ... (n.d.-c). https://analyticalscience.wiley.com/do/10.1002/was.0004000113

197.) Nanakoudis, A. (2023, June 12). EDX analysis with sem: How does it work?. Advancing Materials. https://www.thermofisher.com/blog/materials/edx-analysis-with-sem-how-does-it-work

198.) Dutrow, B. L., & Clark, C. M. (2023, July 31). X-ray powder diffraction (XRD). Techniques.
https://serc.carleton.edu/research_education/geochemsheets/techniques/XRD.html

199.) Stoddart, Charlotte (1 March 2022). "Structural biology: How proteins got their close-up". Knowable Magazine. doi:10.1146/knowable-022822-1

200.) Libretexts. (2022, July 8). Bragg's law. Chemistry LibreTexts.
https://chem.libretexts.org/Bookshelves/Analytical_Chemistry/Supplemental_Modules_(Analytical_Chemistry)/Instrumentation_and_Analysis/Diffraction_Scattering_Techniques/Bragg's_Law